PMFSEL 95-2
APRIL 1995

DEVELOPMENT OF ANALYTICAL MODELS FOR EARTHQUAKE ANALYSIS OF STEEL MOMENT FRAMES

By

Keedong Kim
Michael D. Engelhardt

with support from
The National Science Foundation and
the American Institute of Steel Construction, Inc.

Development of Analytical Models for Earthquake Analysis of Steel Moment Frames

by

Keedong Kim

Michael D. Engelhardt

Supported by the National Science
Foundation and the American Institute of
Steel Construction, Inc.

Abstract

Moment resisting steel frames (MRFs) designed according to current building codes are expected to deform well into the inelastic range during severe earthquake ground motions. Inelastic deformations of MRFs are typically concentrated in critical regions at the ends of girders and columns, and in column panel zones. The accurate prediction of the mechanical behavior of the structure during earthquake excitations depends on the development of reliable analytical models which describe the hysteretic behavior of the critical regions. The development of such analytical models is the subject of this study.

The multi-linear hinge element (a one component series hinge type model), nonlinear panel zone element (a rotational spring element), and composite beam element (a one component series hinge type model) were developed to model bare steel beams and columns, column panel zones, and composite beams. The multi-linear hinge element employes multilinear force deformation relationships, and accounts for the effects of beam end connection type, for the case of fully welded as well as welded flange-bolted web type connections. The element also models plastic axial deformations and changes in axial stiffness due to hinge formation under combined bending and axial force. Hardening rules handle monotonic, cyclic or random loading. In the hysteretic models of the nonlinear panel zone element and the composite beam element, a smooth transition from the elastic stage to the inelastic stage was considered. In the composite beam element, the capability to account for a moving inflection point was implemented. The member behavior predicted by the developed elements match well with available experimental results and with predictions made by a fiber model.

The multi-linear hinge element, the nonlinear panel zone element, and the composite beam element were combined into thirteen steel subassemblages and five steel frames to investigate their local and overall response. The analytically predicted overall responses matched reasonably well with experimental data. The analyses by the multi-linear hinge elements and the nonlinear panel zone elements produced better overall and local response predictions than the analyses by existing bilinear hinge elements and bilinear panel zone elements.

Acknowledgment

The writers gratefully acknowledge financial support provided for this work by the National Science Foundation Young Investigator Award (Grant No. CMS-9358186) and by the American Institute of Steel Construction, Inc.

Table of Contents

List of Figures

List of Tables

Chapter 1: INTRODUCTION

1.1 General

Moment resisting steel frames (MRFs) have been a very widely used building system for seismic resistant design in the western U.S. and in other areas of the world. This system is made of beams rigidly connected to columns, resisting lateral load through bending and shear of these members. MRFs provide architectural and functional advantages by permitting large spaces that are not obstructed by walls or bracing. Further, prior to the 1994 Northridge Earthquake, steel MRFs were widely viewed as being among the most ductile and safe of all structural systems for earthquake applications.

MRFs designed according to current building codes are expected to deform well into the inelastic range during severe earthquake ground motions. Therefore, the framing must provide sufficient ductility to sustain the inelastic activity without collapse. Inelastic deformations of MRFs are typically concentrated in critical regions at the ends of girders and columns, and in column panel zones. The accurate prediction of the mechanical behavior of the structure during earthquake excitations depends on the development of reliable analytical models which describe the hysteretic behavior of the critical regions. The development of such analytical models is the subject of this study.

The determination of the structural properties of MRFs is an essential step in the evaluation of earthquake response. Typically, initial stiffness, ultimate capacity, and global and local ductility demands are some of the parameters included in this assessment. A complete assessment of the seismic resistant design of structures often requires a nonlinear dynamic analysis. Due to the complex interactions between the various components of real structures, their dynamic characteristics up to failure cannot be identified solely from dynamic tests of scale models. Moreover, the cost of such tests is often substantial, particularly for large scale specimens.

Historically these difficulties have been overcome by static tests on components and on reduced-scale subassemblages of structures under cyclic load reversals. Results from these tests are then used in the development and calibration of hysteretic models that permit the extrapolation of the limited test data to other cases and to the dynamic response of complete structures. In this study, several models for the nonlinear response analysis of structures have been developed.

Many analytical models have been developed in the past two decades. These models can be divided into three categories in accordance with an increasing level of refinement and complexity.

The first category is global models, in which the nonlinear response of a structure is concentrated at selected degrees of freedom. For example, the response of a multistory building may be represented as a system with one lateral degree of freedom at each floor. Each degree of freedom has the hysteretic characteristics of the inter story shear-lateral drift response. Such models are useful in the preliminary design phase for estimating inter story drifts and global displacement ductility demands. The recovery of internal member forces and local inelastic deformation demands from the limited number of degrees of freedom is not possible.

The second category is discrete element models, in which the structure is modeled as an assembly of interconnected elements that describe the hysteretic behavior of structural members. Material nonlinearity is either introduced at the element level in an average sense or at the section level. Correspondingly, two types of element formulation are possible: lumped plasticity models and distributed plasticity models.

The third category is the microscopic finite element models, in which members and joints are discretized into a large number of finite elements. Material and geometrical nonlinearity is typically described at the stress-strain level or averaged over a finite region.

Global models yield little information on the forces and deformations in the members and joints of the structure. Microscopic finite element models permit the most accurate study of critical regions, but are often computationally prohibitively expensive for large scale nonlinear dynamic analyses. The present study concentrates on the second class of models. The discrete member models represent a reasonable compromise between simplicity and accuracy in nonlinear seismic response studies, and represent the simplest class of models that still allows significant insight into the seismic response of members and of the entire structure.

1.2 Literature Review of Discrete Member Models

A review of existing analytical models relevant to the nonlinear analysis of steel frame members is presented in this section. Lumped plasticity models are presented first and distributed plasticity models follow. Analytical models for column panel zones and for composite beams will be reviewed later in chapters 5 and 6.

1.2.1 Lumped Plasticity Models

Under seismic excitation, the inelastic activity in moment resisting frames often concentrates at the ends of girders and columns. In a lumped model, following from this observation, plastification is assumed to occur at a plastic hinge at the end of the frame member, while the remainder of the member remains elastic. Lumped models typically consist of several springs that are connected in series or in parallel. Each spring or "component" has a predetermined force-deformation response. An element is then constructed by connecting the components in parallel or in series. The force-deformation response of the resulting element is a combination of the component responses.

A parallel component element was introduced by Clough and Benuska (1966) and allowed for a bilinear moment-rotation relation. The element consists of two components; a fully elastic component to represent strain hardening and an elasto-perfectly plastic component to represent yielding. The stiffness matrix of the member is the sum of the stiffnesses of the components.

Kanaan and Powell (1973) used a modification of Clough's parallel component model for their beam column element. The reduction of section plastic moment capacity due to an axial force was introduced by using an interaction formula. However, the variation of axial stiffness with progressive yielding was neglected in their formulation. This model has been very widely used in the inelastic analysis of multistory building frames.

The one component series model was formally introduced by Giberson (1969), although it had been reportedly used earlier. The element consists of a linear elastic element with one equivalent nonlinear rotational spring attached to each end. Although the model has several components in series, the name "one component model" is used commonly in the literature. In a parallel component model two components participate in modeling inelastic behavior at each end of a member, whereas in the one component series model only a single nonlinear rotational spring takes part in modeling the inelastic behavior at a member end. The inelastic deformations of the member are lumped into the end springs. This model is more versatile than the parallel component models, since it can describe more complex hysteretic behavior by the selection of appropriate moment-rotation relations for the end springs. This makes the model attractive for the phenomenological representation of the hysteretic behavior of composite and of reinforced concrete members.

Otani (1974) developed inelastic models for reinforced concrete beam members. In the derivation of the element stiffness matrix, independent hysteretic rules were used for the moment-free end displacement and for the moment-free end rotation relations. The use of two different hysteretic rules resulted in an unsymmetric element stiffness matrix. To overcome this lack of symmetry of the stiffness matrix, Otani assumed that the inelastic deformations were lumped in two equivalent springs at the ends of the member, thus reducing his inelastic beam element to the one component series model proposed by Giberson.

In the model introduced by Soleimani (1979), a zone of inelastic deformation gradually spreads from the member end into the member as a function of loading history, while the rest of beam remains elastic. The model was developed for reinforced concrete members. The length of the inelastic segments at the member ends is determined from the moment diagram and the level of the yield moment at a particular loading step. The total member end rotations of the element are the sum of the member end rotations for the elastic beam and those for the plastic segments. In this sense, it can be considered that the plastic hinges, which account for a change in the inelastic length, are inserted at the member ends. Therefore, even though a change in the length of the plastic segment is considered in the element formulation, it can also be considered that the model belongs to the family of lumped plasticity models. The yielding in the model is concentrated at the ends of the member under the assumption of an anti-symmetric moment distribution, as in the series and parallel models. The flexibility matrix of the plastic segments is obtained by using the principle of virtual work and the effective stiffness of the plastic segments, which is the average of the section stiffnesses of the moment-curvature relations at the two ends of the plastic segment.

A very similar model to Soleimani's model was developed for reinforced concrete members by Meyer (1983). The flexibility coefficients of the model are identical to those proposed by Soleimani. A slightly different method of calculating the stiffness of the plastic zone during reloading was proposed. The original model was later extended by Roufaiel and Meyer (1987) to include the effect of shear and axial forces on the flexural hysteretic behavior based on a set of empirical rules. Although the axial forces in the columns vary in time as the result of the overturning moment and vertical accelerations due to earthquake motions, in the model the axial forces are assumed to remain constant and equal to the gravity load effect present at the beginning of earthquake excitations.

Another variation of Soleimani's model was introduced for the analysis of reinforced concrete members by Keshavarzian and Schnobrich (1985). The main modification is that this model includes the effect of changing axial force on the element stiffness as well as on the yield moment. The axial force is assumed to be a linear function only of the average axial strain, while the bending moment is assumed to be a function of both curvature and axial force. The stiffness of the moment-curvature relation at the member end is calculated by introducing appropriate shifts between the members of the family of moment-curvature relations for various constant axial forces. Although being one of the most promising among the family of Soleimani models, the model neglects the effect of bending moments on the axial stiffness and employs complex procedures to account for the effect of axial force on the member stiffness and the yield moment.

Chen and Powell (1982) developed a lumped plasticity beam-column element, where it is assumed that inelastic behavior is concentrated in plastic hinges at the element ends and the remaining part of the element remains elastic. In this model, inelastic interaction between bending moments, torque and axial force has been considered by means of four dimensional yield interaction surfaces and a flow rule of plasticity theory. In this model, four multilinear force-deformation relationships are required for plastic hinges. Subsequent yield surfaces are not geometrically similar to the initial yield surface and the overlapping of yield surfaces is allowed, causing potential difficulties in the algorithm for computer implementation. To account for the different shape of yield surfaces, a modified Mroz kinematic hardening rule is employed for post-yield behavior. In this model it is difficult to establish the general parameters required for the force-deformation relationships and the four dimensional yield surfaces, which are governed by the cross-sectional dimensions and the hysteretic force-deformation characteristic of the member material.

As a simple extension of the one component model, Hsu (1974), and Takayanagi and Schnobrich (1979) proposed a multiple spring model for analyzing wall members. The member is divided into several subelements along its axis, each represented by a nonlinear spring. The flexural properties of each of the subelements is defined by a trilinear moment-rotation primary curve, and a set of hysteresis rules is used to describe the unloading and load reversal stages. In this model it may be difficult to define an appropriate set of phenomenological rules that govern the interaction of flexural and axial deformations. Although the multi-spring model can represent the behavior of a frame element subjected to a relatively general moment distribution along its length, it still does not directly account for the effect of axial load on member behavior.

1.2.2 Distributed Plasticity Models

A more accurate description of the inelastic behavior of frame members is possible with distributed plasticity models. In contrast to lumped plasticity models, material nonlinearity can take place at any element section and the element behavior is derived by weighted integration of the section response. In practice, since the element integrals are evaluated numerically, only the behavior of selected sections at the integration points is monitored. The constitutive behavior of the cross-section is explicitly derived by discretization of the cross-section into fibers. A common assumption of these models is that plane sections remain plane, such that the strains are linearly distributed over the cross-section.

In fiber models, the element is subdivided into longitudinal fibers. The geometric characteristics of the fiber are its location in the cross-section and the fiber area. The constitutive relation of the cross-section is not specified explicitly, but is derived by integration of the response of the fibers, which follow the uniaxial stress-strain relation of the particular material. Many fiber models have been proposed. These fiber models can be divided into two categories in accordance with the procedure employed in the derivation of the element stiffness matrix.

In the first category, fiber models are based on the finite element displacement approach using cubic Hermitian polynomials to approximate the deformations along the element. Using this fixed shape function during the analysis, Kang and Scordelis (1980) developed two dimensional fiber model for reinforced and prestressed concrete members. Later, Mari and Scordelis (1982) extended the formulation to include three dimensional behavior of frame members. Firmansjah and Hanson (1992) proposed a three dimensional fiber model for steel members. A major limitation of the finite element displacement approach is the assumption of cubic shape functions, which results in a linear curvature distribution along the element. When the structural member undergoes significant yielding, the curvature distribution becomes highly nonlinear in the inelastic region. This requires the use of a very fine discretization of fiber elements in the inelastic region.

In the second category, the element stiffness is formulated based on the section flexibility matrix and the force interpolation functions, which relate the member end forces to the section forces. Latona and Roesset (1970) proposed the fiber model based on force interpolation functions. Adams (1973) extended the formulation to include second order effects and the change of geometry for steel frame members. Later, Mark (1976) applied the fiber model to reinforced concrete members. B äcklund (1976) developed the fiber model based on force interpolation functions and showed the comparison with the model based on the finite element displacement approach. Kaba and Mahin (1984) applied a two dimensional fiber model based on force interpolation functions to reinforced concrete members. In the model, flexibility dependent shape functions, which are continuously updated during the analysis as inelastic deformations spread into the member, are employed to relate the member deformations to the section deformations in obtaining the member resisting forces. Later, Taucer and Filippou (1992) extended the model to account for three dimensional behavior of reinforced concrete members. Carol and Murcia (1988), and Moon (1994) applied two dimensional fiber models to prestressed concrete members. In their models, the flexibility dependent shape functions are employed to relate the section forces to the member resisting forces.

1.3 Objective and Scope

Ideally, analytical models should be based on an accurate representation of material behavior taking into account the controlling states of stress or strain and identifying the main factors which influence the hysteretic behavior of each critical region in any structural component during the earthquake response. At the same time these models should be computationally efficient.

In practice, it is very difficult to find an analytical model satisfying both an accurate representation of material behavior and computational efficiency. Although lumped plasticity models sacrifice accuracy to some degree, these models have the capability to provide a reasonable compromise between simplicity and accuracy in nonlinear seismic response studies. Hinge type models for frame members and rotational spring models for joints are widely used in the evaluation of earthquake response of steel moment resisting frames due to their computational efficiency. However, they are highly simplified and have been subjected to inadequate verification by comparison with experiments or other sophisticated analytical models. In this study, the investigation will be mainly focused on lumped plasticity models due to their computational efficiency. Fiber models and finite element models are used for the calibration of hysteretic rules and the verification of lumped plasticity models.

The objective of this research is to develop a library of analytical models for frame members and joints for the inelastic dynamic analysis of steel moment resisting frames. Existing simple analytical models will be examined by making comparisons with experimental data or with other analytical models. Where these comparisons show poor performance of the existing models, the model will be improved or new models will be developed. The study will include analytical models for bare steel beams and columns, composite beams, and column panel zones. The developed models will be added to ANSR 1 computer program (Mondkar and Powell 1975) for the analysis of nonlinear structural response, the element library of which includes the bilinear beam-column element and the bilinear panel zone element for the analysis of steel moment resisting frames.

1.4 Outline of Study

The bare steel beam-column element, based on an one-component series model, is developed in chapter 2, and is calibrated and verified in chapter 4. Multilinear hysteretic models, which are calibrated to experimental data, are employed and the influence of beam connection type (fully welded versus welded flange-bolted web) is taken into account. The element has the capability to model plastic axial deformation and employs hardening rules to handle monotonic, cyclic or random loading. In chapter 3, a fiber element is presented which will be used for the calibration and verification of the bare steel beam-column element.

After reviewing previous research on column panel zones and existing models for monotonic and cyclic loading, an improved panel zone model is presented in chapter 5. Response predictions of the model are compared with finite element results and with available experimental results.

Based on observations from the experimental behavior of composite beams, and on existing composite beam models, an improved one component series model for composite beams is developed in chapter 6. The model accounts for the influence of a moving inflection point on the beam element stiffness. The results predicted by the model are compared with existing experimental data.

The elements developed for bare steel beam-columns, column panel zones and composite beams are combined into subassemblages, bare steel frames and frames with concrete slabs in chapter 7. Analytical results are compared with the experimental data. Finally, conclusions are presented in chapter 8.

Chapter 2: DEVELOPMENT OF BEAM-COLUMN ELEMENT

2.1 General

In this chapter, a beam-column element is developed for modeling bare steel members in moment resisting frames. This element models members subject to cyclic bending moment, shear force and axial force. Inelastic response under bending and axial force is considered using a lumped plasticity approach. This element is intended to represent the clear span portion of beams and columns in moment frames. Beam-column joints will be modeled with a joint element that will be presented in Chapter 5.

The current design philosophy for seismic resistant steel MRFs adopted by building codes in the western U.S. (Uniform Building Code 1994; SEAOC 1990) discourages the formation of plastic hinges in the clear span portion of columns, while encouraging the formation of hinges in beams or in beam-column joints. Thus, accurate modeling of cyclic inelastic response of members subject to bending, but without significant axial force (i.e., beams), is essential for accurate modeling of MRF response. However, models for inelastic response of members subject to both bending and significant axial force (i.e., columns) is needed to investigate frames where the code philosophy is not achieved in the design or to investigate alternate design philosophies that permit plastic hinges in columns. The beam-column element developed in this study is intended for both purposes, i.e., to model members with purely flexural yielding, as well as members with yielding under combined flexure and axial force.

An overview of beam-column elements proposed by previous researchers was given in Chapter 1. Among these, the model proposed by Kanaan and Powell (1973) has been among the most widely used for inelastic dynamic analysis of steel MRFs. This model employs a bilinear moment-rotation relationship, and incorporates the effects of axial force by adjusting the yield moment according to a moment-axial force interaction relationship. The model does not, however, consider any change in axial stiffness due to inelastic action. This bilinear hinge model has been used in several recent analytical studies of steel MRF behavior in earthquakes (Tsai 1988; Schiff 1988; Schneider 1991).

Despite the common use of the bilinear hinge element, there appears to have been little scrutiny by past researchers on the accuracy of this element for predicting actual inelastic steel beam or beam-column response. The accuracy of this model can be evaluated, for example, by comparison with experimental results, or by comparison with the results of more sophisticated models. In the following paragraph, the performance of the bilinear element is briefly investigated.

Figure 2.1 compares an analytical prediction using Kanaan and Powell's bilinear element with an experimentally determined cyclic load-deflection response for a cantilever. The experiment was conducted on a W21x57 beam (Engelhardt 1992), with a fully welded connection to a column. The yield moment for the model was taken as the actual plastic moment of the beam (based on actual reported material yield stress). The post-yield stiffness of the model was taken as 3% of the initial elastic stiffness, a common assumption in MRF modeling. Figure 2.1 shows that the analytical model captures some of the general characteristics of the inelastic response, but also misses some potentially important aspects of the real response. For example, the model underestimates the actual strength by about 20%. The bilinear model, of course, also provides a poor representation of the actual curvilinear load deformation response. The significance of these inaccuracies depends on the objectives of the analysis. Past researchers have pointed out that rather significant changes in hinge model parameters often result in little change in the predicted global frame response. For example, Tsai (1988) observed that a 100% change in post yield stiffness had little effect on overall displacement of the model. Thus, if the analysis goal is to predict global frame response, expending a great deal of effort in refining the frame element models may not be justified. On the other hand, if the analysis goal is to study local response characteristics, e.g. hinge rotations, the accuracy of the element model may be of greater significance.

Figure 2.2 considers the response of a cantilever subject to a cyclic lateral force combined with constant axial compression. The purpose of this analysis is to illustrate the behavior of the bilinear hinge element when used to model a member under combined flexure and axial force. Very little experimental data is available for such loading conditions. Consequently, the hinge model predictions are compared with the predictions of a more sophisticated model; in this case, the fiber model. The fiber model permits more accurate modeling of beam-column elements, and is discussed in detail later in Chapter 3. For the analysis shown in Figure 2.2, the parameters to define the cyclic stress-strain rules for the fiber model (see section 3.8) was first calibrated to the experimental results in Figure 2.1, for the case of zero axial load. This calibrated fiber model was then used for the analysis in Figure 2.2 for the case of applied axial force. The hinge model parameters were the same as above. A typical simplified moment-axial force interaction relationship (AISC Specification 1989) was used. Comparing the results of the bilinear hinge model with the predictions of the fiber model leads to similar conclusions as above. The hinge model captures general characteristics of the inelastic response, but misses much of the detailed response. In this case, the hinge model underestimates the strength predicted by the fiber model by 30%.

The comparisons in Figures 2.1 and 2.2 were shown to suggest that the commonly used bilinear hinge model, while perhaps suitable for many analyses objectives, nonetheless leaves considerable room for improvement. In particular, it appears that considerable improvement may be possible in the prediction of the detailed force-deformation response and overall strength response of the element, as well as in the treatment of axial force effects.

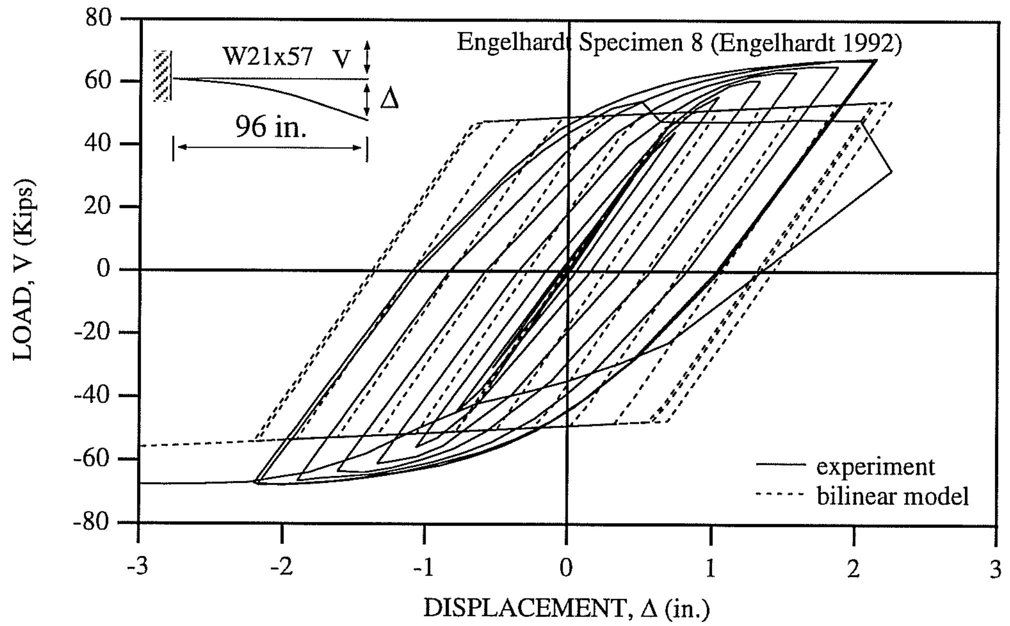

Fig. 2.1: Comparison of Kanaan's Hinge Model with Experiment

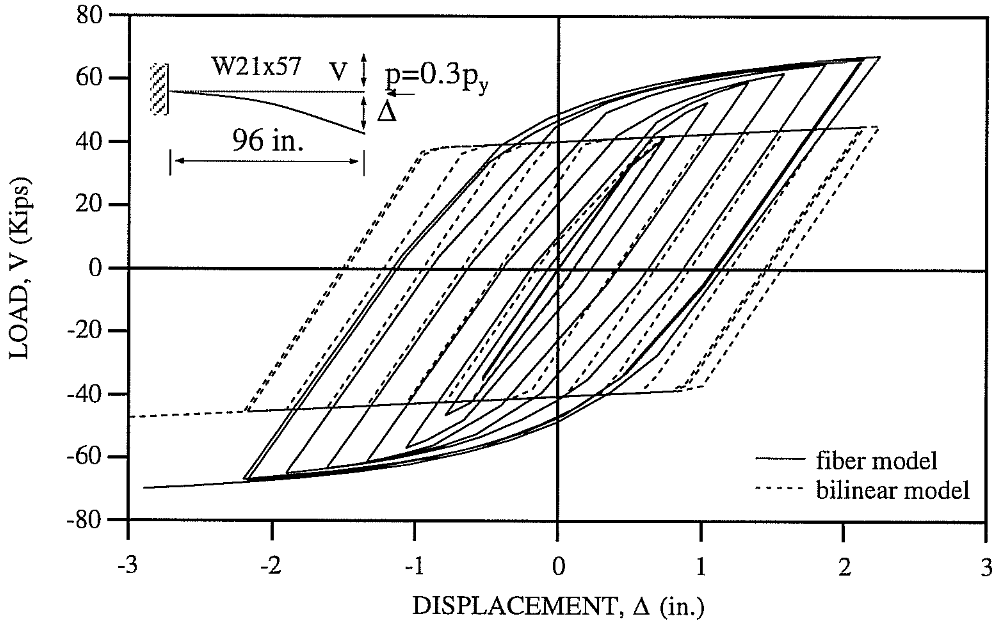

Fig. 2.2: Comparison of Kanaan's Hinge Model with Fiber Model

In this chapter, an improved bare steel beam-column element is developed. The element can be considered as an one-component series hinge type model. It employs multilinear force deformation relationships, and accounts for the effects of beam end connection types, for the case of fully welded as well as welded flange-bolted web type connections. The element also models plastic axial deformations and changes in axial stiffness due to hinge formation under combined bending and axial force. Hardening rules are developed to handle monotonic loading and random cyclic loading.

The general formulation of the element is developed in Section 2.2. The element is then calibrated in Chapter 4, by comparison with experimental results and by comparison with fiber model predictions. These comparisons also illustrate the limitations of this new element. Since the fiber model will be used as a basis of comparison, Chapter 3 provides a description of the fiber model.

2.2 General Description

In the remainder of this chapter, the development of a two dimensional beam-column element is described. Some of the basic features, assumptions, and simplifications that characterize this model are listed below.

1) The element will model the response of members subject to moment, axial force and shear. Inelastic response due to yielding under moment and/or axial force is modeled using a lumped plasticity approach, i.e., a plastic hinge approach. Inelastic effects due to shear are not modeled. No interaction is considered between shear and moment, or between shear and axial force in the development of yield surfaces. Elastic shear deformations are modeled.

2) The element models bare steel members only, and the influence of a composite concrete deck is not considered. Composite beam response is considered later in Chapter 6.

3) The element models inelastic response using multilinear force-deformation relationships, in an attempt to more closely mimic experimentally observed behavior.

4) For the case of beam members (no axial force), the element models the effects of beam-to-column connection type. Two common connection types are considered: all-welded beam-to-column connections, and welded flange-bolted web beam-to-column connections.

5) For members yielding under combined axial force and moment, the element model changes in both flexural and axial stiffness.

6) The element employs hardening rules to model response under monotonic, symmetric cyclic, and random loadings.

7) The effects of local buckling or lateral-torsional buckling are not considered.

8) The element employs a simplified geometric stiffness to approximately model second-order frame effects, i.e., P-Δ effects.

The two dimensional beam-column element consists of a linear elastic beam-column element with a nonlinear hinge at each end, as shown in Fig. 2.3a. To facilitate the discussion, this element will be referred to as the "complete element," consisting of both hinges and the elastic beam-column element. The hinges are considered to have a zero length. Inelastic behavior of the element is concentrated in the hinges, where each hinge is affected by axial force and moment. Both hinges are assumed to be initially rigid. Therefore the initial stiffness of the complete element is that of only the elastic beam-column element. As the forces at the element ends increase, the hinges can yield, resulting in a reduced stiffness of the complete element.

Each hinge possesses two rigid-plastic force-deformation relationships; the moment-rotation relationship and the axial force-extension relationship. Each hinge has several yield surfaces to account for the interaction between bending moment and axial force, where the yield surfaces of the hinge are arranged in a consecutive manner as shown qualitatively in Fig. 2.4 for a two-dimensional force space. To produce multilinear relationships for the complete element, the rigid plastic force-deformation relationships for a hinge are combined with the linear force-deformation relationships for the elastic beam-column element. Under increasing deformation, the hinges strain harden, following the multilinear force-deformation relationships as shown in Figs. 2.4a and 2.4b. Strain hardening results in a translation and expansion of the yield surfaces, as shown in Fig.2.4c.

The basic Mroz kinematic hardening theory for yielding of metals is implemented numerically and combined with an isotropic hardening rule to extend its modeling capabilities for arbitrary loading. These hardening rules are required to establish tangent stiffness relationships between the forces and deformations of a yielded hinge. The tangent stiffness of the hinges is then combined with the stiffness of the elastic beam-column element to produce the tangent stiffness of the complete element. If the forces at a hinge decrease, the hinge becomes rigid again as unloading occurs. Under such conditions the stiffness of the complete element is equal to that of the elastic beam-column element.

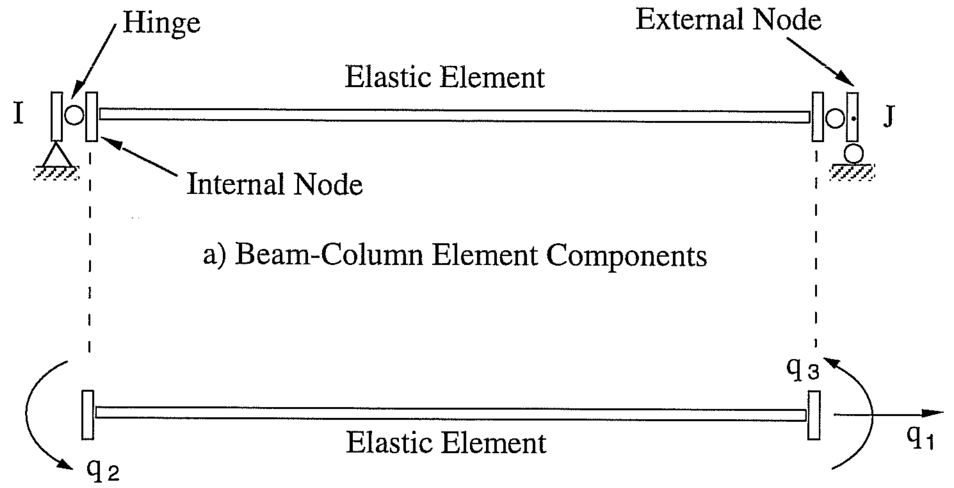

a) Beam-Column Element Components

b) Deformation Degrees of Freedom of Elastic Element

Fig. 2.3: Element Components and Degrees of Freedom of Elastic Element

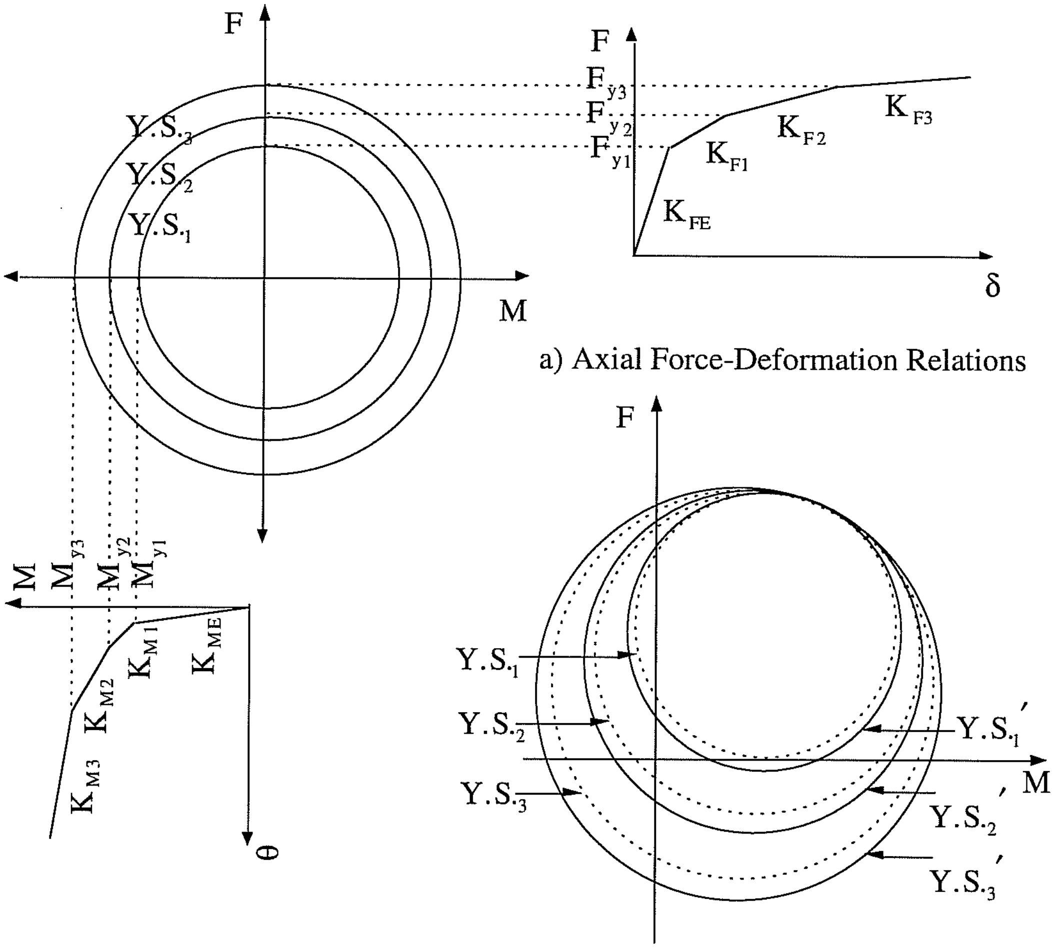

a) Axial Force-Deformation Relations

b) Moment-Rotation Relations c) Translation and Expansion of Yield Surfaces

Fig. 2.4: Strain Hardening Behavior of Hinges

2.3 Degrees of Freedom

The complete element has two external nodes and two internal nodes, as shown in Fig. 2.3a. The internal nodes exist at the end of the elastic element. The hinges connect the internal nodes with the external nodes. The external nodes connect to the global structure and have three degrees of freedom each, namely translations and rotation in the local coordinate system, as shown in Fig. 2.5. Nodal forces are indicated by R_1 to R_6. Nodal displacements are indicated by U, V, and θ at the "I" and "J" ends of the member. In the local coordinate system, if the rigid body motions are removed, the element can be considered as a simply supported beam. The resulting element deformations in the local coordinate system can be represented by three relative deformations (v_1, v_2, and v_3) and three relative forces (s_1, s_2, and s_3) as shown in Fig. 2.5.

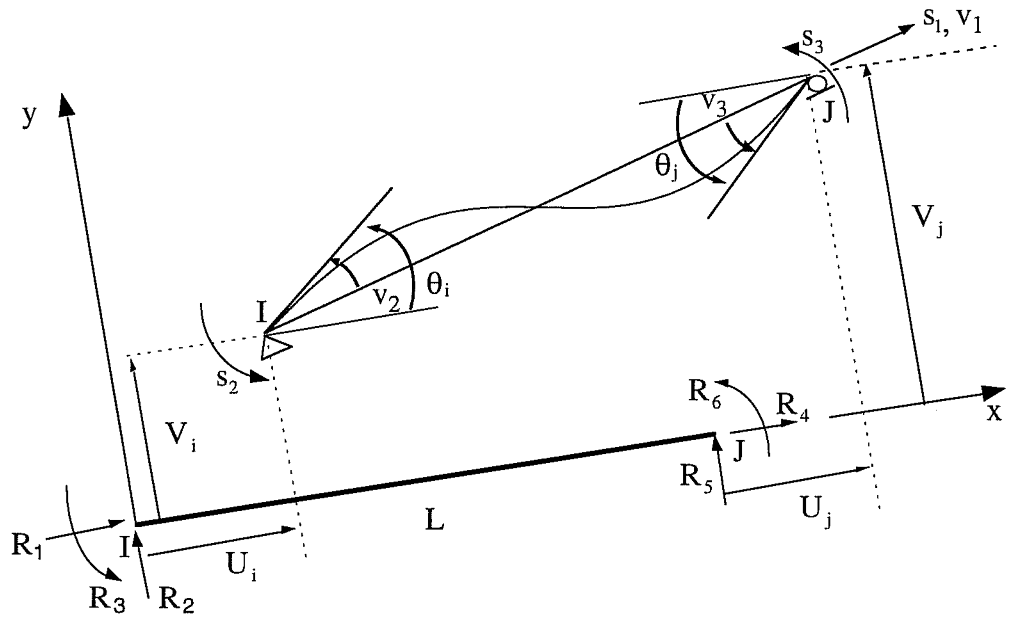

Fig. 2.5: Element Relative Forces and Deformations in Local Coordinate System

On the basis of equilibrium, all the components of local nodal forces **R** can be computed from the values of relative forces **s**. The transformation from the nodal forces **R** to relative forces **s** is defined as

$$\mathbf{R} = \mathbf{A}\cdot\mathbf{s} = \begin{bmatrix} -1 & 0 & 0 \\ 0 & 1/L & 1/L \\ 0 & 1 & 0 \\ 1 & 0 & 0 \\ 0 & -1/L & -1/L \\ 0 & 0 & 1 \end{bmatrix} \begin{Bmatrix} s_1 \\ s_2 \\ s_3 \end{Bmatrix} \tag{2.1a}$$

where

$$\mathbf{R}^T = \{R_1, R_2, R_3, R_4, R_5, R_6\} \tag{2.1b}$$

From geometry, the transformation from the local displacements **r** to the relative deformations **v** is accomplished by

$$\mathbf{v} = \mathbf{A}^T \cdot \mathbf{r} \tag{2.2a}$$

where $$\mathbf{r}^T = \{U_i, V_i, \theta_i, U_j, V_j, \theta_j\} \tag{2.2b}$$

and $$\mathbf{v}^T = \{v_1, v_2, v_3\} \tag{2.2c}$$

The elastic element has degrees of freedom **q** which act at the internal nodes, as shown Fig. 2.3b, and are defined as

$$\mathbf{q}^T = \{q_1, q_2, q_3\} \tag{2.3}$$

The hinges at nodes I and J have deformation degrees of freedom $\mathbf{w}_p^I$ and $\mathbf{w}_p^J$, respectively, where

$$\mathbf{w}_p^I = \{(v_1 - q_1)^I, (v_2 - q_2)\} \tag{2.4a}$$

and $$\mathbf{w}_p^J = \{(v_1 - q_1)^J, (v_3 - q_3)\} \tag{2.4b}$$

The hinge deformations $\mathbf{w}_p^I$ and $\mathbf{w}_p^J$ represent the plastic deformations of the complete element. The axial hinge deformation is shared between the hinges at nodes I and J, hence:

$$v_1 - q_1 = (v_1 - q_1)^I + (v_1 - q_1)^J \tag{2.5}$$

The remaining terms in $\mathbf{w}_p^I$ and $\mathbf{w}_p^J$ represent plastic rotational deformations. The deformations **v** of the complete element are obtained by summing the deformations of the elastic element and deformations of both hinges as follows.

$$\mathbf{v} = \mathbf{q} + \mathbf{w}_p \tag{2.6}$$

where $\mathbf{w}_p$ includes the deformations of both hinges defined as

$$\mathbf{w}_p^T = \{(v_1 - q_1), (v_2 - q_2), (v_3 - q_3)\} \tag{2.7}$$

2.4 Complete Element Stiffness

A flexibility matrix is first formed for the elastic element in terms of degrees of freedom **q**. Thus, the elastic element stiffness relationship in matrix form can be written as

$$\mathbf{s} = \mathbf{k} \cdot \mathbf{q} \tag{2.8a}$$

where **s** and **k**, respectively, are the nodal force vector and stiffness matrix for the elastic beam-column element, in which

$$\mathbf{s}^T = \{F, M^I, M^J\} = \{s_1, s_2, s_3\} \tag{2.8b}$$

and $$\mathbf{k} = \begin{bmatrix} \frac{EA}{L} & 0 & 0 \\ 0 & \frac{EI}{L}k_{ii} & \frac{EI}{L}k_{ij} \\ 0 & \frac{EI}{L}k_{ji} & \frac{EI}{L}k_{jj} \end{bmatrix} \tag{2.8c}$$

where EI = bending rigidity about z axis,
EA = axial rigidity,
$k_{ii} = k_{jj} = 4$ and $k_{ij} = 2$ for an uniform member
F and M = axial force and moment about local z axis, respectively.

The stiffness matrix expressed by Eq. 2.8c is inverted to obtain a flexibility matrix for the elastic beam-column element. Elastic shear deformations are accounted for by adding a shear flexibility matrix $\mathbf{f}_s$ to the flexibility matrix of the elastic element, where

$$\mathbf{f}_s = \frac{1}{GA_sL}\begin{bmatrix} 0 & 0 & 0 \\ 0 & 1 & 1 \\ 0 & 1 & 1 \end{bmatrix} \tag{2.9}$$

in which GA_s is the effective shear rigidity associated with shear deformations about the z axis.

Thus, the elastic element flexibility relationship is obtained which includes the effects of shear, as follows;

$$\mathbf{q} = \mathbf{f} \cdot \mathbf{s} \tag{2.10a}$$

or in the incremental form

$$\mathbf{dq} = \mathbf{f} \cdot \mathbf{ds} \tag{2.10b}$$

where **dq** and **ds**, respectively, are the deformation increment and action increment at the internal nodes, and **f** is the flexibility matrix for the elastic element defined as

$$\mathbf{f} = \begin{bmatrix} \frac{L}{EA} & 0 & 0 \\ 0 & \frac{L}{EI}F_{ii} + \frac{1}{GA_sL} & -\frac{L}{EI}F_{ij} + \frac{1}{GA_sL} \\ 0 & -\frac{L}{EI}F_{ij} + \frac{1}{GA_sL} & \frac{L}{EI}F_{jj} + \frac{1}{GA_sL} \end{bmatrix} \tag{2.10c}$$

where $F_{ii} = F_{jj} = 1/3$ and $F_{ij} = 1/6$ for an uniform member. This elastic flexibility matrix **f** is modified by adding the flexibility of the hinges, resulting in the flexibility matrix for the complete element.

In two-dimensional action space, each hinge has a 2x2 flexibility matrix $\mathbf{f}_p^h$ in terms of its axial deformation and flexural deformation. A hinge flexibility relationship can be written as

$$\mathbf{dw}_p^h = \mathbf{f}_p^h \cdot \mathbf{ds}^h \tag{2.11}$$

where $\mathbf{dw}_p^h$ and $\mathbf{f}_p^h$, respectively, are the deformation increment and the flexibility matrix of a hinge, and $\mathbf{ds}^h$ is the action increment acting on the hinge, defined as

$$\mathbf{ds}^{hT} = \{dF,\ dM^h\} \tag{2.12}$$

The superscript h refers to the hinge at the I or J end of the member.

Before yielding of a hinge occurs, the flexibility matrix of the hinge is null and therefore has no effect on the flexibility of the complete element. For the hinge at node I, the incremental action-deformation relationship can be expressed as

$$\mathbf{dw}_p^I = \begin{Bmatrix} (dv_1 - dq_1)^I \\ dv_2 - dq_2 \end{Bmatrix} = \begin{Bmatrix} d\delta_p^I \\ d\theta_p^I \end{Bmatrix} = \mathbf{f}_p^I \cdot \begin{Bmatrix} dF \\ dM^I \end{Bmatrix} \tag{2.13a}$$

Likewise, for the hinge at node J

$$\mathbf{dw}_p^J = \begin{Bmatrix} (dv_1 - dq_1)^J \\ dv_3 - dq_3 \end{Bmatrix} = \begin{Bmatrix} d\delta_p^J \\ d\theta_p^J \end{Bmatrix} = \mathbf{f}_p^J \cdot \begin{Bmatrix} dF \\ dM^J \end{Bmatrix} \tag{2.13b}$$

where

$\mathbf{dw}_p^I$, $\mathbf{dw}_p^J$ = vectors of plastic hinge deformations at node I and J,

$d\delta_p^I$, $d\delta_p^J$ = incremental plastic axial deformations at node I and J,

$d\theta_p^I$, $d\theta_p^J$ = incremental plastic rotations at node I and J,

$\mathbf{f}_p^I$, $\mathbf{f}_p^J$ = hinge or plastic flexibility matrices at node I and J.

As can be noted from Eqs. 2.13a and 2.13b, the hinge at node I affects the degrees of freedom v_1 and v_2, while the hinge at node J affects the degrees of freedom v_1 and v_3. Therefore, the hinge flexibility coefficients of $\mathbf{f}_p^I$ and $\mathbf{f}_p^J$ can be simply added to the appropriate coefficients of the elastic element flexibility matrix $\mathbf{f}$ in order to obtain the tangent flexibility matrix $\mathbf{F}_t$ for the complete element.

$$\mathbf{F}_t = \mathbf{f} + \mathbf{f}_p \tag{2.14a}$$

where

$$\mathbf{f}_p = \mathbf{f}_p^I + \mathbf{f}_p^J = \begin{bmatrix} f_{11}^I + f_{11}^J & f_{12}^I & f_{13}^J \\ f_{12}^I & f_{22}^I & 0 \\ f_{13}^J & 0 & f_{33}^J \end{bmatrix} \tag{2.14b}$$

$$\mathbf{F}_t = \begin{bmatrix} \frac{L}{EA} + f_{11}^I + f_{11}^J & f_{12}^I & f_{13}^J \\ f_{12}^I & \frac{L}{EI}F_{ii} + \frac{1}{GA_sL} + f_{22}^I & -\frac{L}{EI}F_{ij} + \frac{1}{GA_sL} \\ f_{13}^J & -\frac{L}{EI}F_{ij} + \frac{1}{GA_sL} & \frac{L}{EI}F_{jj} + \frac{1}{GA_sL} + f_{33}^J \end{bmatrix} \tag{2.14c}$$

Thus, using Eqs. 2.10b, 2.13a, and 2.13b, the action-deformation relationship is obtained for the complete element expressed in terms of the degrees of freedom $\mathbf{v}$.

$$\mathbf{dv} = \mathbf{dq} + \mathbf{dw}_p = \mathbf{F}_t \cdot \mathbf{ds} \tag{2.15}$$

where
$$\mathbf{dw}_p = \mathbf{f}_p \cdot \mathbf{ds} \tag{2.16a}$$

$$\mathbf{dq} + \mathbf{dw}_p = \begin{Bmatrix} dq_1 + (dv_1 - dq_1)^I + (dv_1 - dq_1)^J \\ dq_2 + (dv_2 - dq_2) \\ dq_3 + (dv_3 - dq_3) \end{Bmatrix} = \begin{Bmatrix} dv_1 \\ dv_2 \\ dv_3 \end{Bmatrix} \tag{2.16b}$$

and

$$\mathbf{ds}^T = \left\{dF,\ dM^I,\ dM^J\right\} \tag{2.17}$$

Having determined the 3x3 tangent flexibility matrix $\mathbf{F}_t$, this matrix is inverted to obtain a 3x3 tangent stiffness matrix $\mathbf{K}_t$. That is

$$\mathbf{K}_t = \mathbf{F}_t^{-1} \tag{2.18}$$

2.5 Hinge Flexibility

The vector of actions $\mathbf{s}^h$ affecting the deformations of a hinge is defined as

$$\mathbf{s}^{hT} = \left\{F,\ M^h\right\} \tag{2.19}$$

As the action $\mathbf{s}^h$ increases, the hinge can yield, which is assumed to be initially rigid. After the hinge yields, the increment of action $\mathbf{ds}^h$ produces the plastic deformation increment of the hinge. Let $\mathbf{dw}_p^h$ be the vector of the increment of plastic deformations, where

$$\mathbf{dw}_p^{hT} = \left\{d\delta_p^h,\ d\theta_p^h\right\} \tag{2.20}$$

in which $d\delta_p^h$ and $d\theta_p^h$, respectively, are the axial and rotational plastic deformations of the hinge. It is necessary to obtain for the hinge a flexibility relationship of the form

$$\mathbf{dw}_p^h = \mathbf{f}_p^h \cdot \mathbf{ds}^h \tag{2.21}$$

where $\mathbf{f}_p^h$ is the hinge flexibility matrix. To achieve this, the following assumptions are made:

- i) Let $\Phi(s^h)$ be the yield function defining a surface which translates in action space due to strain hardening. After some amount of hardening has taken place, the yield function is $\Phi(s^h - \alpha)$, where α is the vector defining the location of the origin of the yield surface. This is illustrated in Fig. 2.6 for a two dimensional action space. The direction of translation is governed by the hardening rule, to be discussed later.
- ii) Drucker's postulate (Drucker 1960) that the work done on the increments of strain by the corresponding increments of stress is nonnegative, applies in two dimensional action space. Consequently, the following holds:
  - a) The yield surface is convex for a stable work-hardening material.
  - b) Any increment of plastic deformation is perpendicular to the yield surface.
  - c) An increment of plastic deformation is linearly related to the action increment.

If the action point is on the yield surface, continued loading generates an increment of plastic deformation $\mathbf{dw}_p^h$. According to Drucker's postulate, this deformation is perpendicular to the yield surface as shown in Fig. 2.6b, hence:

$$\mathbf{dw}_p^h = \mathbf{n} \cdot \lambda \tag{2.22}$$

where **n** is an outward normal unit vector from the yield surface at the point of action, and λ is a scalar defining the magnitude of plastic deformation of the hinge. Because the yield surface is considered to be a plastic potential function, the direction of the outward normal to the yield surface is the gradient of the yield function. Hence:

$$\mathbf{n} = \frac{\Phi_{,s}}{\sqrt{\Phi_{,s}^{T} \cdot \Phi_{,s}}} = \begin{Bmatrix} n_f \\ n_m \end{Bmatrix} \tag{2.23}$$

in which $\Phi_{,s}$ is the gradient of the yield function. That is:

$$\Phi_{,s}^{T} = \left\{ \frac{\partial \Phi}{\partial F}, \frac{\partial \Phi}{\partial M} \right\} \tag{2.24}$$

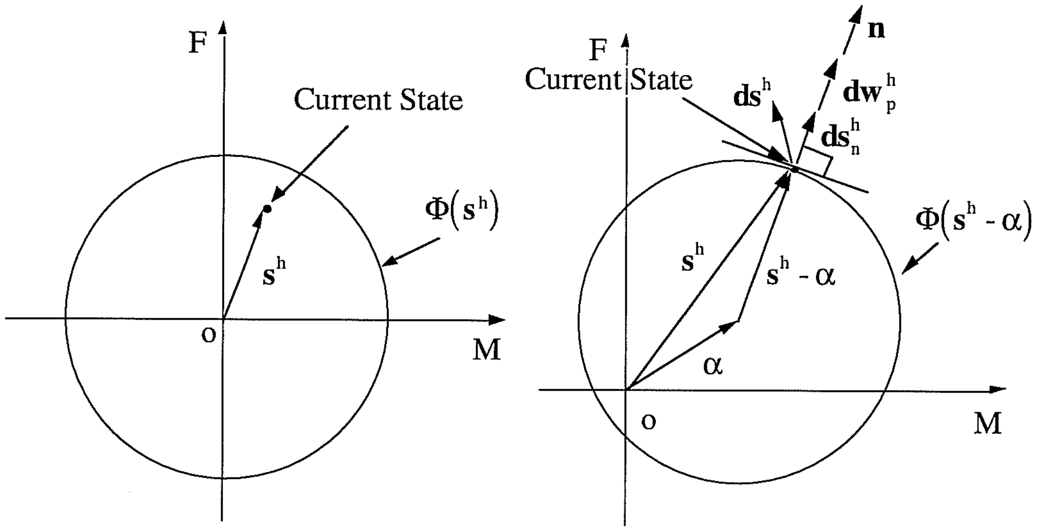

a) Initial Position of Yield Position b) Translated Yield Surface

Fig. 2.6: Translation of Yield Surface and Normal Vector to Yield Surface

Consider an increment of action $\mathbf{ds}^h$ shown in Fig. 2.6. The component of $\mathbf{ds}^h$ in the direction of **n** is $\mathbf{ds}_n^h$, and is defined by

$$\mathbf{ds}_n^h = \mathbf{n} \cdot \left(\mathbf{n}^T \cdot \mathbf{ds}^h \right) \tag{2.25}$$

Since, by Drucker's postulate, the plastic deformation increment is linearly related to the action increment, assume that

$$\mathbf{ds}_n^h = \mathbf{K}_p \cdot \mathbf{dw}_p^h \tag{2.26}$$

in which $\mathbf{K}_p$ is a diagonal plastic stiffness matrix from the individual action-deformation relationships for the hinge. That is, the off diagonal terms in $\mathbf{K}_p$ are zero, with the diagonal terms defined as

$$\mathbf{K}_p = \begin{bmatrix} k_{pf} & 0 \\ 0 & k_{pm} \end{bmatrix} \tag{2.27}$$

The selection of diagonal terms must be carefully specified in order to provide appropriate post-yield stiffness of the complete element. This will be discussed later.

If Eqs. 2.22 and 2.25 are substituted into Eq. 2.26, and the result premultiplied by $\mathbf{n}^T$, it follows that

$$\mathbf{n}^T \cdot \mathbf{ds}^h = \mathbf{n}^T \cdot \mathbf{K}_p \cdot \mathbf{n} \cdot \lambda \tag{2.28}$$

Therefore,

$$\lambda = \frac{\mathbf{n}^T \cdot \mathbf{ds}^h}{\mathbf{n}^T \cdot \mathbf{K}_p \cdot \mathbf{n}} \tag{2.29}$$

With λ now defined, the increment of plastic deformation for the hinge can be computed due to an increment of action. Upon substituting for λ into Eq. 2.22,

$$\mathbf{dw}_p^h = \frac{\mathbf{n} \cdot \mathbf{n}^T}{\mathbf{n}^T \cdot \mathbf{K}_p \cdot \mathbf{n}} \mathbf{ds}^h \tag{2.30}$$

Therefore, by referring to Eq. 2.21, the required flexibility matrix of a yielded hinge is obtained as follows.

$$\mathbf{f}_p^h = \frac{\mathbf{n} \cdot \mathbf{n}^T}{\mathbf{n}^T \cdot \mathbf{K}_p \cdot \mathbf{n}} = \frac{1}{n_f^2 k_{pf} + n_m^2 k_{pm}} \begin{bmatrix} n_f^2 & n_f n_m \\ n_f n_m & n_m^2 \end{bmatrix} \tag{2.31}$$

2.6 Yield Surfaces

The moment and axial force interact with each other to produce initial yield of the hinge. The interaction is determined by a yield surface. First yield is governed by the initial yield surface. The shape of the yield surface is generally chosen to be similar to an axial force-moment interaction diagram for a fully plastic cross-section. For each change of stiffness, there is a corresponding yield surface as shown in Fig. 2.7. These surfaces are assumed to have a shape similar to that of the initial yield surface. Either the multi-linear (piecewise-linear) or the nonlinear shape shown in Fig. 2.7 can be employed as the yield surface. If the action point is on a yield surface, continued loading generates translation of the yield surface. When the yield surface is a nonlinear shape, the current action point is not on the yield surface after translation of the yield surface. The drift of the action point outward from the nonlinear yield surface will be discussed later. In this study, the AISC approximate moment-axial force interaction equations (AISC Specification 1989) and the exact interaction equations for wide flange sections subjected to strong axis bending, respectively, are chosen as the multi-linear and nonlinear initial yield surfaces. Each of these two types of yield surfaces consists of eight line segments as shown in Fig. 2.7. For the upper right quadrant of yield surfaces shown in Fig. 2.7, the equation of the yield surface 'i' is defined as

$$\frac{1}{a_2} \cdot (M - \alpha_M) + \frac{a_1}{a_2} \cdot (F - \alpha_F) + \frac{a_3}{a_2} \cdot (F - \alpha_F)^2 = 1 \tag{2.32}$$

where α_M and α_F are the moment and axial force coordinates of the origin of the yield surface, respectively. Therefore, the yield function is expressed by

$$\Phi = \frac{1}{a_2} \cdot (M - \alpha_M) + \frac{a_1}{a_2} \cdot (F - \alpha_F) + \frac{a_3}{a_2} \cdot (F - \alpha_F)^2 \tag{2.33a}$$

The coefficients of the yield function for the multi-linear yield surface are defined as

$$a_1 = \frac{M_{y1}}{0.85 F_{y1}}, \quad a_2 = \frac{M_{yi}}{0.85}, \quad a_3 = 0 \qquad \text{for } F \geq 0.15 F_{y1} \frac{M_{yi}}{M_{y1}} \tag{2.33b}$$

and

$$a_1 = 0\,,\ a_2 = M_{yi}\,,\ a_3 = 0 \qquad \text{for } F \le 0.15F_{y1}\frac{M_{yi}}{M_{y1}} \qquad (2.33c)$$

For the nonlinear yield surface, the coefficients are

$$a_1 = \frac{A_o}{2b_f}\,,\ a_2 = \frac{A_{to}}{4b_f}F_{yi}\,,\ a_3 = \frac{A}{4b_fF_{yi}} \qquad \text{for } F \ge \frac{A_w}{A}F_{y1}\frac{M_{yi}}{M_{y1}} \qquad (2.33d)$$

and

$$a_1 = 0\,,\ a_2 = M_{yi}\,,\ a_3 = \frac{A}{4t_wF_{yi}} \qquad \text{for } F \le \frac{A_w}{A}F_{y1}\frac{M_{yi}}{M_{y1}} \qquad (2.33e)$$

where $A_o = b_fd - A$,
$A_{to} = 2b_fd - A$,
A = section area,
A_w = section web area,
b_f = section flange width,
d = section depth,
t_w = section web thickness.

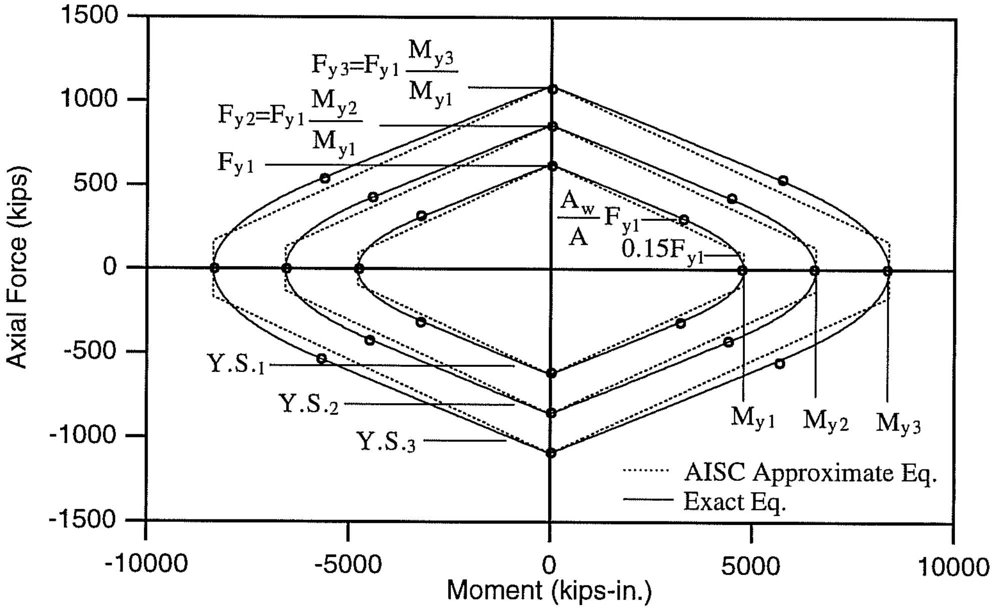

Fig. 2.7: Initial and Subsequent Yield Surfaces

The gradient of the yield function $\Phi_{,s}$ can be represented by

$$\Phi_{,s}^{T} = \left\{\frac{\partial\Phi}{\partial F},\ \frac{\partial\Phi}{\partial M}\right\} = \left\{\frac{2\cdot a_3\cdot(F-\alpha_F)}{a_2},\ \frac{1}{a_2}\right\} \qquad (2.34)$$

and the outward normal unit vector **n** to the yield surface is expressed in terms of a_1 and a_2 as follows:

$$\mathbf{n} = \frac{\Phi,_{s}}{\sqrt{\Phi,_{s}^{T} \cdot \Phi,_{s}}} = \begin{Bmatrix} n_f \\ n_m \end{Bmatrix} = \frac{|a_2|}{\sqrt{1+x^2}} \begin{Bmatrix} \dfrac{x}{a_2} \\ \dfrac{1}{a_2} \end{Bmatrix} \qquad (2.35)$$

where $x = a_1 + 2 \cdot a_3 \cdot (F - \alpha_F)$. The normal unit vector at a vertex of the yield surface will be discussed later. By substituting Eq. 2.35 into Eq. 2.31 the flexibility matrix of a yielded hinge $\mathbf{f}_p^h$ is also obtained by

$$\mathbf{f}_p^h = \frac{1}{x^2 \cdot k_{pf} + k_{pm}} \begin{bmatrix} x^2 & x \\ x & 1 \end{bmatrix} \qquad (2.36)$$

2.7 Hardening Rule

In the hardening model, it is assumed that the stress-strain curve continues to rise after yielding. For a strain-hardening material, the yield function changes progressively. The hardening rule defines how this function changes. Several hardening rules have been proposed in the past; these include the classical isotropic hardening theory of Hill (1950), the kinematic hardening theory of Prager (1956), the series and parallel formulations of Iwan (1967), the constant plastic moduli of Mroz (1967; 1969), and the bounding surface models of Dafalias-Popov (1973; 1975) and Peterson-Popov (1977; 1978). In the study by Mosaddad and Powell (1982), it was concluded that the Mroz model is the most flexible model for numerical implementation. Based on this model, they developed an extended model suitable for an arbitrary cyclic loading.

The hardening rule originally proposed by Mroz is basically a kinematic hardening model. This model corresponds to the translation of the yield surface without changes in size and shape, and the general stress-strain behavior is approximated by a series of yield surfaces with constant hardening moduli. Each yield surface is represented by two constants, yield stress and plastic modulus. In uniaxial tension, the stress-strain relationship for the Mroz model is approximated by a multilinear curve.

The kinematic model is generally incorrect for predicting material behavior under cyclic loading. This model predicts a steady-state cyclic behavior for constant cyclic strain, whereas for actual materials, steady-state hysteresis loops are reached only after a period of transition. The nature and duration of this transition varies for different materials and may depend on a variety of parameters, including loading path, temperature, manufacturing process, etc. On the other hand, the isotropic model predicts elastic shakedown under cyclic loading, which is incorrect. The actual material behavior under cyclic loading generally can be represented by two limiting states, the virgin state and the saturated state as shown in Fig. 2.8. The virgin state represents the strength and hardening properties of the material for the first half-cycle of loading. The saturated state represents the strength and hardening properties of the material when it reaches the steady state cyclic behavior. As the plastic strain accumulates, the properties of a metal migrate from the virgin state toward the saturated state.

To account for cyclic behavior, the concept of the constant hardening model of Mroz is extended to a variable field model proposed by Mosaddad and Powell (1982). In their model, the transition from the virgin state to the fully saturated state is controlled by a weighting function, which is based on the accumulated plastic strain. In this study, this extended Mroz hardening rule is applied to the force-deformation relationships.

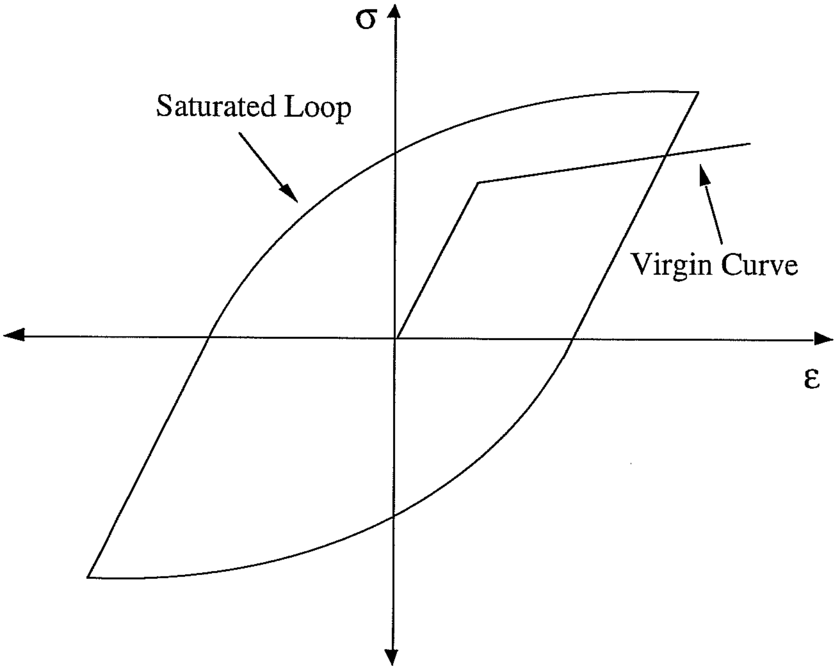

Fig. 2.8: Saturated Curve and Virgin Curve

After the initial yielding occurs, the behavior of a hinge is assumed to obey the Mroz hardening rule for yield in metals. The location of the initial yield surface for the hinge is plotted in a two-dimensional action space as shown in Fig. 2.9. Assume the current state, defined by s_1^h, has reached a point P_1 on the yield surface $Y.S._1$, causing the hinge to yield. Continued loading will cause yield surface $Y.S._1$ to translate toward yield surface $Y.S._2$, in the direction defined by a vector from P_1 to the corresponding point P_2 (see Fig. 2.10). The point P_2 lies on yield surface $Y.S._2$ and is defined by s_2^h. For points P_1 and P_2 to be corresponding, their outward normals must be parallel, i.e., $\mathbf{n}_1^T \cdot \mathbf{n}_2 = 1$, and the direction of vector $s_1^h - \alpha_1$ should be the same as that of $s_2^h - \alpha_2$. Therefore, the vector of actions s_2^h at point P_2 can be determined knowing the sizes and current positions of yield surfaces $Y.S._1$ and $Y.S._2$. In two-dimensional space this is defined as

$$s_2^h = \frac{M_{y2}}{M_{y1}}\left(s_1^h - \alpha_1\right) + \alpha_2 \tag{2.37}$$

in which α_1 and α_2, respectively, are the current positions of the origins of the yield surfaces $Y.S._1$ and $Y.S._2$.

The translation of yield surface $Y.S._1$ is depicted in Fig. 2.10. Yield surface $Y.S._2$ does not begin to translate until yield surface $Y.S._1$ reaches yield surface $Y.S._2$. Observing that the vector $s_2^h - s_1^h$ defines a vector from point P_1 to P_2 in Fig. 2.10, it follows that the increment of translation $\mathbf{d}\alpha_1$ of the yield surface $Y.S._1$ is equal to

$$\mathbf{d}\alpha_1 = \left(s_2^h - s_1^h\right) \cdot dm_1 \tag{2.38}$$

where dm_1 is a scalar defining the magnitude of translation of yield surface $Y.S._1$. To determine dm_1, Eq. 2.37 is substituted into Eq. 2.38 to obtain

$$\mathbf{d\alpha}_1 = \left(\left(\frac{M_{y2}}{M_{y1}} - 1\right)\cdot \mathbf{s}_1^h - \left(\frac{M_{y2}}{M_{y1}}\cdot \alpha_1 - \alpha_2\right)\right)\cdot dm_1 \qquad (2.39)$$

From the definition of the yield function, point P_1 lies on yield surface $Y.S._1$ when

$$\Phi(\mathbf{s}_1^h - \alpha_1) = 1 \qquad (2.40)$$

The fact that the action point P_1 must remain on the yield surface $Y.S._1$ during translation, requires that

$$d\Phi = \Phi,_s^T\cdot(\mathbf{ds}_1^h - \mathbf{d\alpha}_1) = 0 \qquad (2.41)$$

Upon substituting Eq. 2.39 into 2.41,

$$\Phi,_s^T\,\mathbf{ds}_1^h - \Phi,_s^T\cdot\left(\left(\frac{M_{y2}}{M_{y1}} - 1\right)\cdot \mathbf{s}_1^h - \left(\frac{M_{y2}}{M_{y1}}\cdot \alpha_1 - \alpha_2\right)\right)\cdot dm_1 = 0 \qquad (2.42)$$

Hence,

$$dm_1 = \frac{\Phi,_s^T\,\mathbf{ds}_1^h}{\Phi,_s^T\cdot\left(\left(\frac{M_{y2}}{M_{y1}} - 1\right)\cdot \mathbf{s}_1^h - \left(\frac{M_{y2}}{M_{y1}}\cdot \alpha_1 - \alpha_2\right)\right)} \qquad (2.43)$$

Thus, yield surface $Y.S._1$ undergoes an increment of translation $\mathbf{d\alpha}_1$ due to an increment of action $\mathbf{ds}_1^h$, where

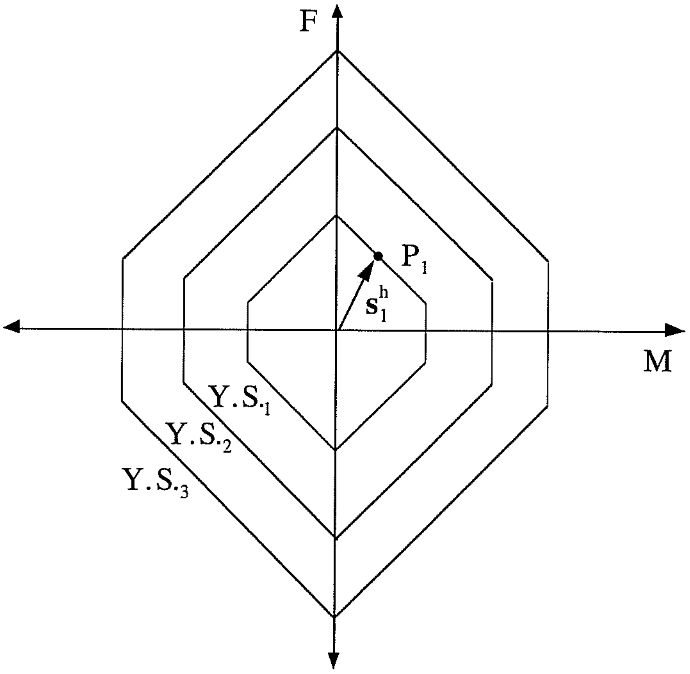

Fig. 2.9: Yield Surfaces Prior to Yielding

$$\mathbf{d}\alpha_1 = \frac{\left(\left(\frac{M_{y2}}{M_{y1}} - 1\right)\cdot s_1^h - \left(\frac{M_{y2}}{M_{y1}}\cdot\alpha_1 - \alpha_2\right)\right)\cdot \Phi,_s^T\,\mathbf{ds}_1^h}{\Phi,_s^T\cdot\left(\left(\frac{M_{y2}}{M_{y1}} - 1\right)\cdot s_1^h - \left(\frac{M_{y2}}{M_{y1}}\cdot\alpha_1 - \alpha_2\right)\right)} \qquad (2.44a)$$

or

$$\mathbf{d}\alpha_1 = \frac{\mathbf{n}_1^T\cdot\mathbf{ds}_1^h}{\mathbf{n}_1^T\cdot\left(s_2^h - s_1^h\right)}\cdot\left(s_2^h - s_1^h\right) \qquad (2.44b)$$

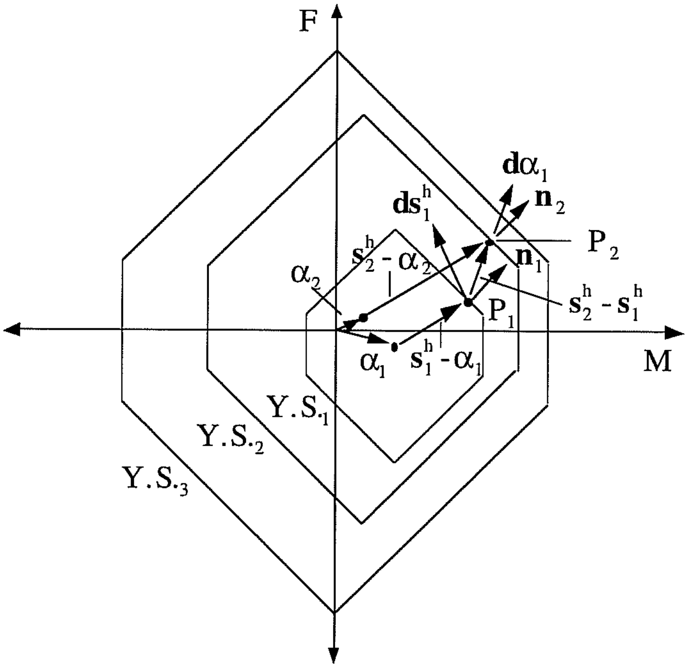

Fig. 2.10: Translation of Initial Yield Surface

The Mroz hardening rule requires that yield surfaces never overlap and that the point of contact be the current action point P_2 as shown in Fig. 2.11, rather than some other points. When several yield surfaces are in contact, therefore, a hardening rule is needed to be employed for only the outermost yield surface of contacted yield surfaces. If by the increment of action the yield surface $Y.S._1$ translates toward and reaches the yield surface $Y.S._2$, yield surfaces $Y.S._1$ and $Y.S._2$ will translate together toward a corresponding point P_3 on yield surface $Y.S._3$. This situation is illustrated in Fig. 2.11.

In the general case where the yield surface $Y.S._i$ translates toward yield surface $Y.S._j$, the translation increment $\mathbf{d}\alpha_i$ is defined as

$$\mathbf{d}\alpha_i = \frac{\left(\left(\frac{M_{yj}}{M_{yi}} - 1\right)\cdot s_i^h - \left(\frac{M_{yj}}{M_{yi}}\cdot\alpha_i - \alpha_j\right)\right)\cdot \Phi,_s^T\,\mathbf{ds}_i^h}{\Phi,_s^T\cdot\left(\left(\frac{M_{yj}}{M_{yi}} - 1\right)\cdot s_i^h - \left(\frac{M_{yj}}{M_{yi}}\cdot\alpha_i - \alpha_j\right)\right)} \qquad (2.45a)$$

or

$$d\alpha_i = \frac{\mathbf{n}_i^T \cdot \mathbf{ds}_i^h}{\mathbf{n}_i^T \cdot \left(s_j^h - s_i^h\right)} \cdot \left(s_j^h - s_i^h\right) \qquad (2.45b)$$

An exception to this rule occurs when the outermost yield surface $Y.S._3$ is reached. For this situation the direction of translation is obtained by assuming that an additional infinitely large yield surface exists. Thus, the term $\frac{M_{y4}}{M_{y3}}$ in Eq. 2.45a is infinite, and it can be shown that the translation of yield surface $Y.S._3$ is equal to

$$d\alpha_3 = \frac{\left(s_3^h - \alpha_3\right) \cdot \Phi,_s^T \cdot \mathbf{ds}_3^h}{\Phi,_s^T \cdot \left(s_3^h - \alpha_3\right)} \qquad (2.46a)$$

or

$$d\alpha_3 = \frac{\mathbf{n}_3^T \cdot \mathbf{ds}_3^h}{\mathbf{n}_3^T \cdot \left(s_3^h - \alpha_3\right)} \cdot \left(s_3^h - \alpha_3\right) \qquad (2.46b)$$

The translation of yield surface $Y.S._3$ represented by Eq. 2.46b occurs along the radial direction connecting the origin α_3 of $Y.S._3$ to the current action point s_3^h, as shown in Fig. 2.12. This is what is known as Ziegler's hardening rule (Ziegler 1959).

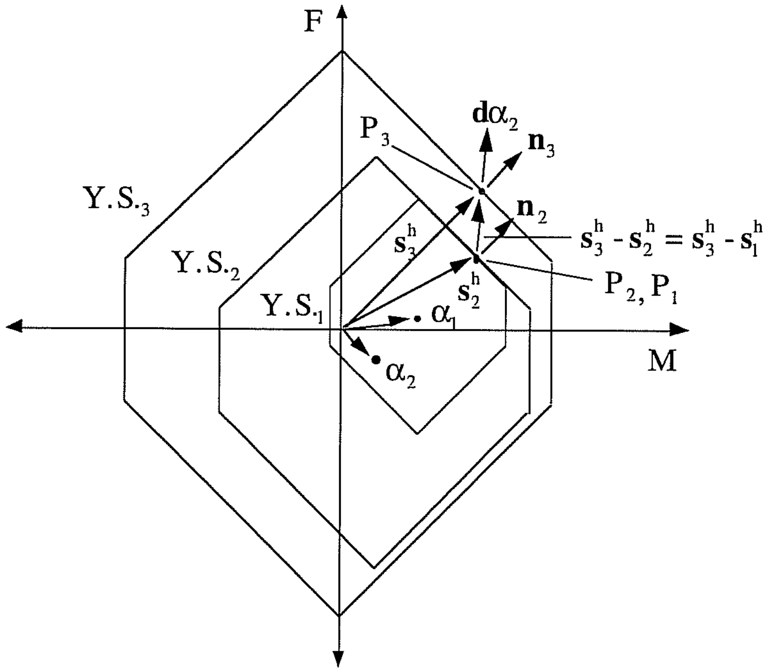

Fig. 211: Translation of Contacted Yield Surfaces

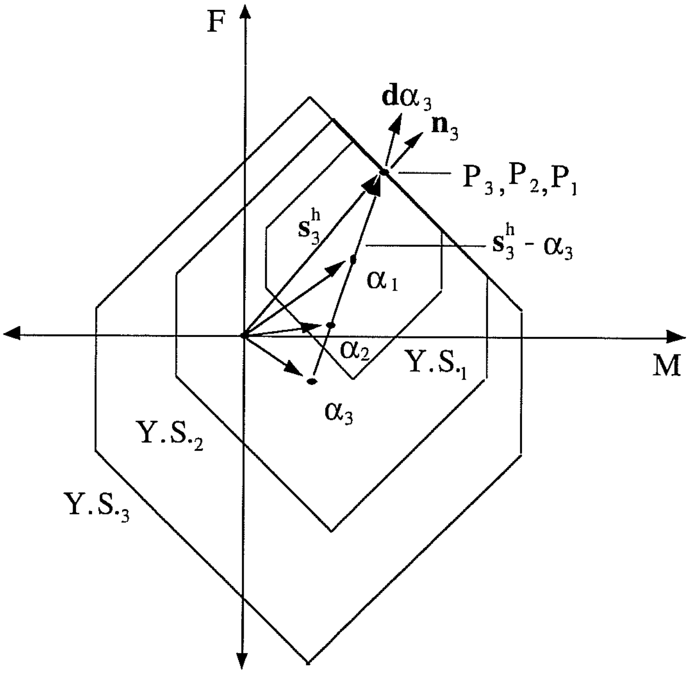

Fig. 2.12: Translation of the Outmost Yield Surface

To account for general cyclic behavior, the Mroz model extended by Mosaddad and Powell (1982) is applied to the action-deformation relationships. In their model, the transition from the virgin state to the fully saturated state is controlled by a weighting function, which is based on the accumulated plastic strain. As plastic deformations accumulate, the properties of the material deviate from those in the virgin state and tend toward those in the saturated state. During this transition, the yield surfaces both expand (or contract) and translate in action space. When the accumulated plastic deformations reach a specified value, the transition stage is complete, and the subsequent behavior follows a pure kinematic hardening rule, governed by the saturated properties. Typical moment-rotation curves for the virgin and saturated state, together with a typical weight function are shown in Fig. 2.13. During the transition, the instantaneous values of M_{yi} and F_{yi} are assumed to be

$$M_{yi} = \omega \cdot M_{yi}^{v} + (1-\omega) \cdot M_{yi}^{s} \qquad (2.47a)$$

and

$$F_{yi} = \omega \cdot F_{yi}^{v} + (1-\omega) \cdot F_{yi}^{s} \qquad (2.47b)$$

where

M_{yi}^{v} and F_{yi}^{v} = virgin state yield moment and axial force of yield surface i

M_{yi}^{s} and F_{yi}^{s} = saturated state yield moment and axial force of yield surface i

ω = weighting factor, which is a function only of accumulated plastic rotation in this work. That is, $\omega = \omega\left(\sum\theta_p\right)$, $0 \le \omega \le 1$ (2.48)

in which $\sum\theta_p$ is the accumulated plastic rotation.

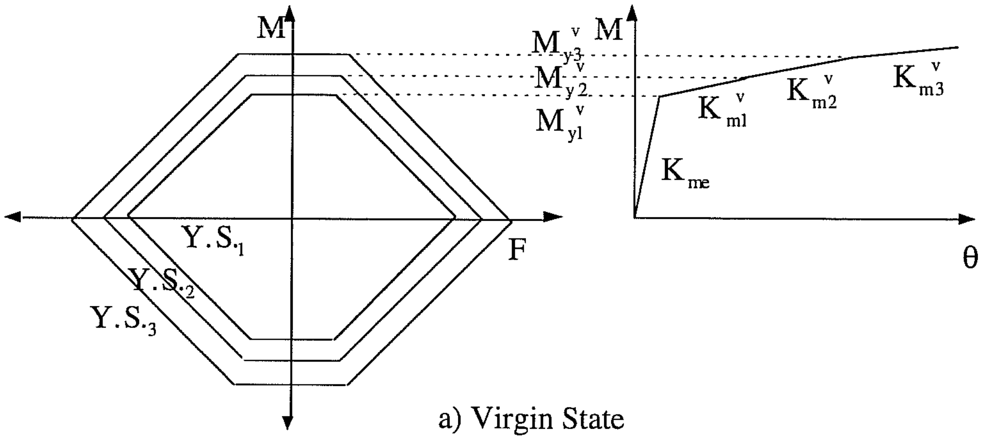

a) Virgin State

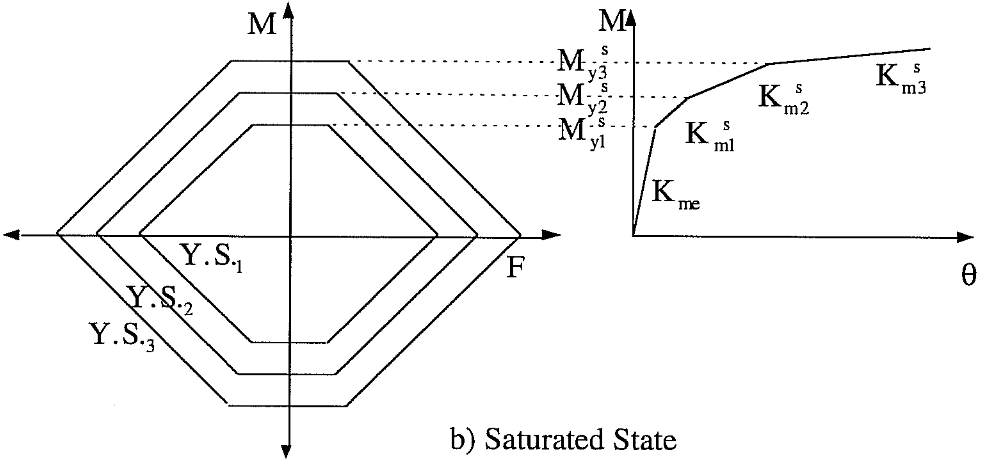

b) Saturated State

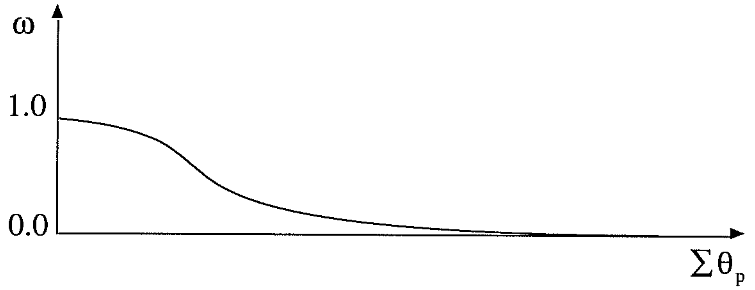

c) Weighting Function

Fig. 2.13: Typical Moment-Rotation Curves for Two Limiting States

The plastic stiffness K_{pmi}^{v} and K_{pmi}^{s} of moment-rotation relationships for the virgin and saturated state can be determined according to the following equation.

$$K_{pmi}^{v} = \frac{K_{me} \cdot K_{mi}^{v}}{K_{me} - K_{mi}^{v}} \quad , \quad K_{pmi}^{s} = \frac{K_{me} \cdot K_{mi}^{s}}{K_{me} - K_{mi}^{s}} \tag{2.49}$$

Likewise, the plastic stiffness K_{pfi}^{v} and K_{pfi}^{s} of axial force-deformation relationships can be determined for the virgin and saturated state, respectively. From the plastic stiffness obtained from Eq. 2.49 , the plastic stiffness during transition is calculated as follows.

$$K_{pmi} = \omega \cdot K_{pmi}^{v} + (1-\omega) \cdot K_{pmi}^{s} \tag{2.50a}$$

and

$$K_{pfi} = \omega \cdot K^{v}_{pfi} + (1-\omega)\cdot K^{s}_{pfi} \tag{2.50b}$$

For the action increment $\mathbf{ds}^h$, the current yield surface is first translated without change in size, according to Eqs. 2.45 and 2.46. The sizes of all surfaces are then updated to correspond to the new value of ω, according to Eq. 2.47. Figure 2.14 illustrates the procedure. Surface $Y.S._i$ is the current yield surface, after translation toward the next yield surface $Y.S._{i+1}$. The vector s^h_i defines the state of action at the end of action increment $\mathbf{ds}^h$, and α_i and α_{i+1} locate the origins of surfaces $Y.S._i$ and $Y.S._{i+1}$. The updating of the surfaces $Y.S._{i+1}$ and $Y.S._{i+2}$,..., etc. involves only expansion or contraction, with no translation. For example, surface $Y.S.'_{i+1}$ is the updated yield surface of surface $Y.S._{i+1}$. Surfaces $Y.S._1$, $Y.S._2$,..., $Y.S._i$, which pass through the current action point P_i, must, however, be kept tangent to each other at P_i (only $Y.S._{i-1}$ and $Y.S._i$ are shown in Fig. 2.14 for simplicity) and hence must be expanded (or contracted) such that they remain tangent to each other at P_i. This requires that the centers of these surfaces, as well as their sizes, be adjusted. The new coordinates of centers of these surfaces can be determined by simple geometry to be

$$\alpha'_k = \alpha_i + \left(1 - \frac{M'_{yk}}{M_{yi}}\right)\cdot\left(s^h_i - \alpha_i\right) \quad \text{for } k = 1,\ 2,\ \ldots,\ i \tag{2.51}$$

in which α'_k locates the origin of updated surface $Y.S.'_k$, and M_{yi} and M'_{yk} are the sizes of surface $Y.S._i$ and $Y.S.'_k$, respectively.

Computational difficulties may arise if surface $Y.S._{i+1}$ contracts to such an extent that surfaces $Y.S.'_i$ and $Y.S.'_{i+1}$ overlap, as shown in Fig. 2.15. In Mosaddad and Powell's model, if this happens, surface $Y.S.'_{i+1}$ is translated to bring the corresponding point P_{i+1} on surface $Y.S.'_{i+1}$ into contact with surface $Y.S.'_i$ at the current action point P_i. However, if the overlapping of two yield surfaces occurs and the current action point P_i is within yield surface $Y.S.'_{i+1}$ as shown in Fig. 2.16, their model can not detect the overlapping of yield surfaces. To overcome this problem a new procedure is developed.

To detect the overlapping of yield surfaces the inner bounding surface $Y.S._{\alpha i}$ of surface $Y.S.'_{i+1}$ is employed, as shown in Fig. 2.16. This surface $Y.S._{\alpha i}$ represents the limit of position of the vector α'_i locating the origin of surface $Y.S.'_i$, such that updated surfaces $Y.S.'_{i+1}$ and $Y.S.'_i$ never overlap. Whenever α'_i is within the surface $Y.S._{\alpha i}$, therefore, the overlapping of yield surfaces $Y.S.'_i$ and $Y.S.'_{i+1}$ never occurs. The equation for the surface $Y.S._{\alpha i}$ is determined by simple geometry as follows.

$$\Phi_{\alpha i} = \left(1 - \frac{M'_{yi}}{M'_{yi+1}}\right)\cdot\Phi'_{i+1} \tag{2.52}$$

where Φ'_{i+1} = yield function of updated yield surface $Y.S.'_{i+1}$

M'_{yi} and M'_{yi+1} = the sizes of updated surfaces $Y.S.'_i$ and $Y.S.'_{i+1}$.

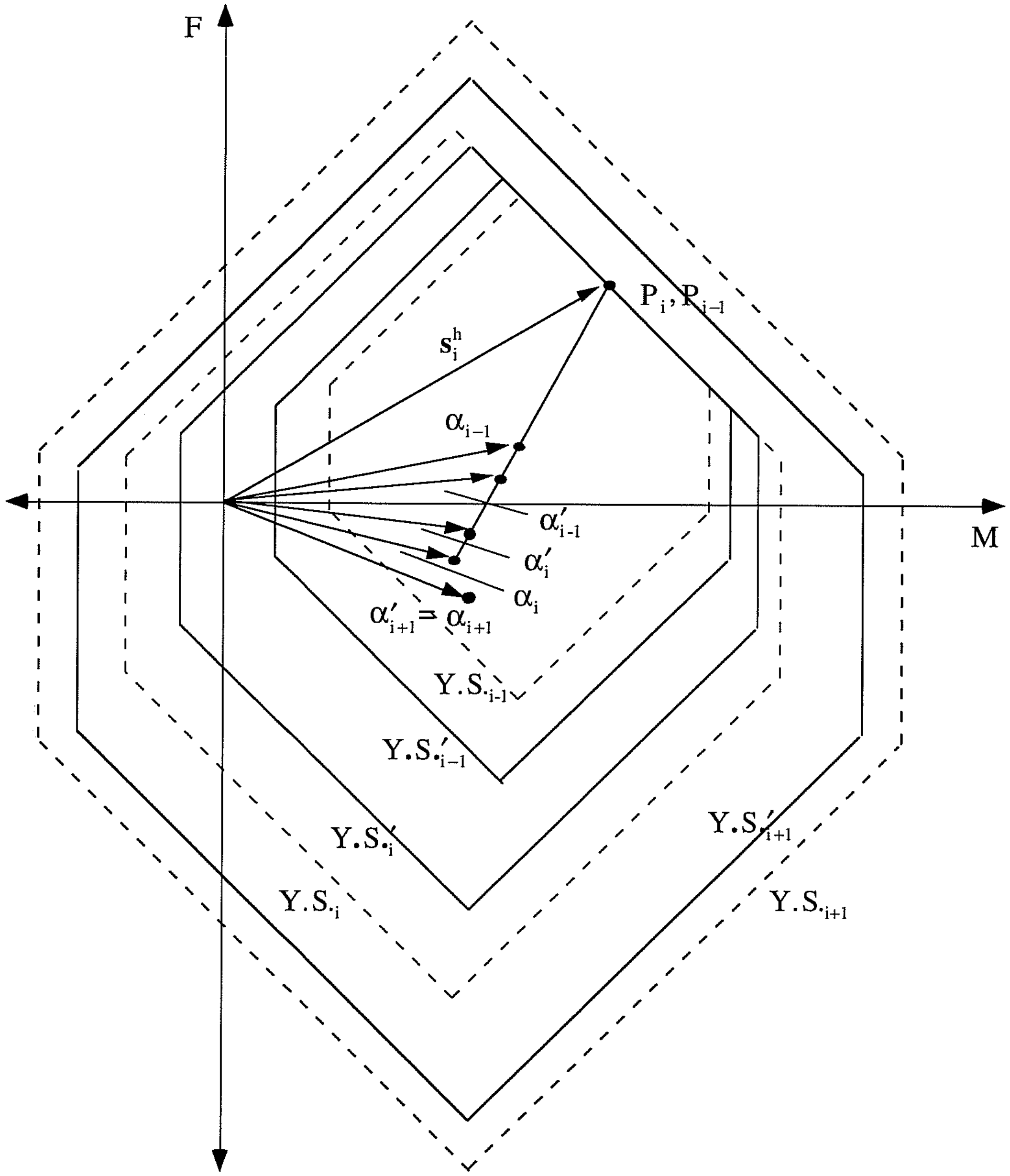

Fig. 2.14: Updating Yield Surfaces

When the overlapping of updated yield surfaces $Y.S.'_i$ and $Y.S.'_{i+1}$ occurs, the yield surface $Y.S.'_{i+1}$ is translated in the direction of a vector $(\alpha'_i - \alpha'_{i+1})$ such that it contacts with updated surface $Y.S.'_i$ as shown in Fig. 2.16. Surfaces $(Y.S.'_{i+1})_{tr}$ and $(Y.S._{\alpha i})_{tr}$ are the translated locations of surfaces $Y.S.'_{i+1}$ and $Y.S._{\alpha i}$, and the vector $(\alpha'_{i+1})_{tr}$ locates the origins of surfaces $(Y.S.'_{i+1})_{tr}$ and $(Y.S._{\alpha i})_{tr}$. The vector $(\alpha'_{i+1})_{tr}$ can be determined from the following equation.

$$(\alpha'_{i+1})_{tr} = \alpha'_{i+1} + \mu \cdot (\alpha'_i - \alpha'_{i+1}) \tag{2.53}$$

where $\mu\cdot$is a proportion of the magnitude of the vector $(\alpha_i' - \alpha_{i+1}')$ such that the vector α_i' lies on the surface $(Y.S._{\alpha i})_{tr}$, which is the location of surface $Y.S._{\alpha i}$ translated by a vector $\mu\cdot(\alpha_i' - \alpha_{i+1}')$. This approach is more reasonable in that it can always detect the overlapping of updated yield surfaces and that the overlapping can be prevented by translating updated yield surface $Y.S._{i+1}'$ by the possible shortest distance $\mu\cdot(\alpha_i' - \alpha_{i+1}')$.

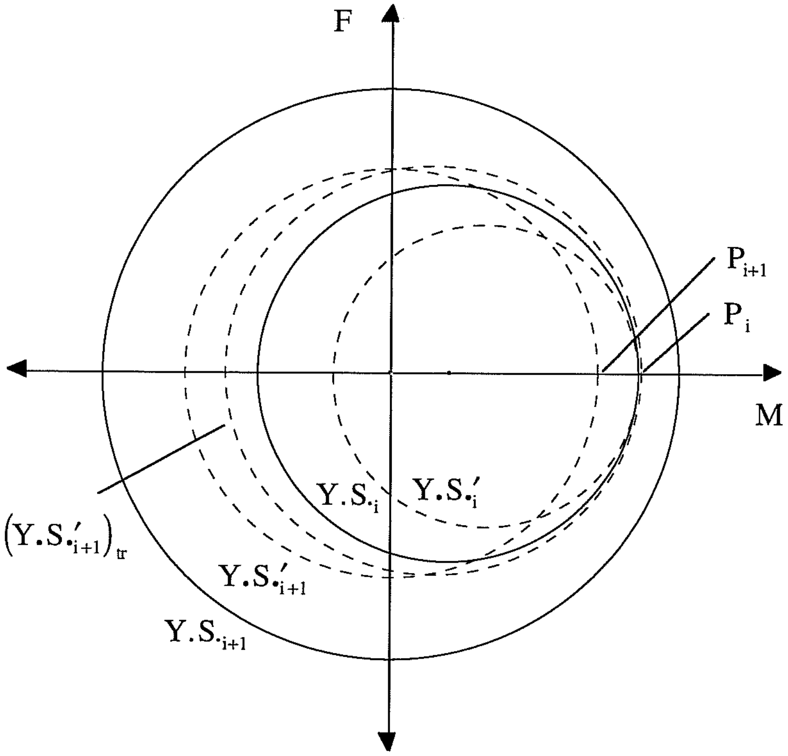

Fig. 2.15: Yield Surface Overlap and Correction in Mosaddad's Model

2.8 Updating Options

The basic Mroz theory requires that yield surfaces which are in contact at the current action point be translated together for a given action increment, while remaining tangent to each other at the current action point. Computationally, however, it is not necessary to move all the yield surfaces. Instead, the state can be obtained more efficiently by translating only the current yield surface. That is, if yield surfaces $Y.S._1$ through $Y.S._i$ are contacted at the current action point, only surface $Y.S._i$ needs to be translated toward surface $Y.S._{i+1}$ as long as loading continues. If loading continues until yield surface $Y.S._{i+1}$ is reached, the surface $Y.S._i$ can also be left alone, and only the motion of surface $Y.S._{i+1}$ needs to be monitored. Ultimately, with this procedure, it is necessary to restore the material "memory", by translating surfaces $Y.S._1$ through $Y.S._i$ to their final positions, as shown in Fig. 2.14 (only surfaces $Y.S._{i-1}$ and $Y.S._i$are shown for simplicity). However, this needs to be done only when unloading occurs. Equations similar to Eq. 2.51 are used for this purpose.

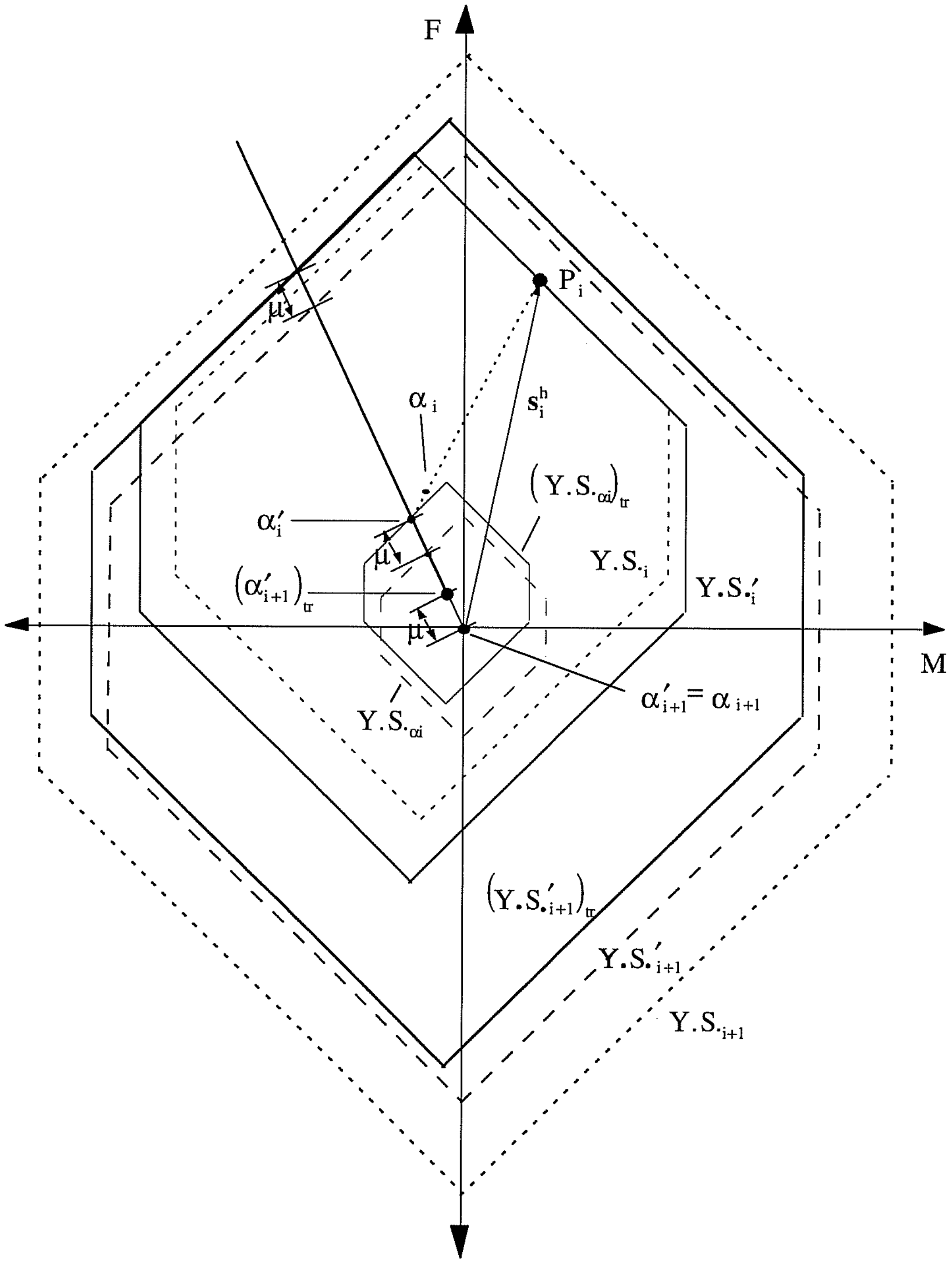

Fig. 2.16: Detection and Correction of the Overlapping of Yield Surface

For the extended model, when the action point lies on surface $Y.S._i$, updating of the properties can similarly be carried out by updating the sizes and plastic stiffnesses only for yield surfaces $Y.S._i$, $Y.S._{i+1}, \ldots, Y.S._n$ as long as loading occurs, using Eqs. 2.47 and 2.50. When unloading occurs, the properties for all yield surfaces are updated. With the continuous updating option, the properties are updated at the end of every inelastic subincrement of a state determination process. With this option the multilinear nature of the action-deformation relationships is no longer preserved, and the element tangent stiffness matrix changes continuously. With the discontinuous updating option, the properties are updated only when unloading occurs and are otherwise kept constant along each loading path. For most practical applications, the cyclic behavior of beam-column element can be modeled sufficiently and accurately using this option. It has the advantages of being more efficient computationally and of preserving the multilinear nature of the action-deformation relationships. Therefore, in this study the discontinuous updating option is implemented into the computer program.

2.9 Loading-Unloading Criteria

The loading-unloading criteria must differentiate between plastic flow and elastic unloading from any current plastic state for any specified deformation increment. The procedure used herein is based on the criterion that the magnitude of plastic deformation defined by λ (Eq. 2.29) must be positive during continued loading from the yield surface.

Hence, given that the current state $\mathbf{s}^h$ is on the yield surface, the loading of a hinge continues to occur if the increment of action is such that

$$\lambda = \frac{\mathbf{n}^T \cdot \mathbf{ds}^h}{\mathbf{n}^T \cdot \mathbf{K}_p \cdot \mathbf{n}} \geq 0 \qquad (2.54a)$$

while unloading of the hinge occurs if

$$\lambda = \frac{\mathbf{n}^T \cdot \mathbf{ds}^h}{\mathbf{n}^T \cdot \mathbf{K}_p \cdot \mathbf{n}} < 0 \qquad (2.54b)$$

Since the diagonal matrix $\mathbf{K}_p$ is always positive definite, the scalar $\mathbf{n}^T \cdot \mathbf{K}_p \cdot \mathbf{n}$ is always positive. Hence, the loading-unloading criterion is expressed in simple form. Continued loading occurs if

$$\mathbf{n}^T \cdot \mathbf{ds}^h \geq 0 \qquad (2.55a)$$

while unloading occurs if

$$\mathbf{n}^T \cdot \mathbf{ds}^h < 0 \qquad (2.55b)$$

2.10 Drift Control and Normal Vectors at a Vertex of Yield Surface

Suppose that the shape of the yield surface consists of two vertical lines and the Mroz hardening rule is applied to this yield surface. For this case, since the direction of the yield surface translation is the same as that of normal vector at the current action point, the increment in translation of the yield surface is equal to the increment of action causing the translation. This is a property of the Mroz hardening rule, where a surface with a constant gradient will have the action point remain on the yield surface. For a curved yield surface, such as an ellipse, the gradient is not constant and as a result the action point will drift outside the translated yield surface. From Fig. 2.17, it can be seen that if a finite sized action increment $\mathbf{ds}_i^h$ is taken, the final action point P_i', corresponding to $\mathbf{s}_i^{h'}$, may depart from the yield surface. This discrepancy can be practically eliminated by ensuring that the load increments considered in the solution are sufficiently small. However the point P_i' can be returned to the yield surface by simply scaling the vector $s_i^{h'} - \alpha_i'$ in the radial direction. From the geometry shown in Fig. 2.17 and the yield function (Eq. 2.32), the appropriate scaling factor RF is readily seen to be

$$RF = \frac{-R_b \pm \sqrt{R_b^2 + 4a_2a_3(F - \alpha_F)^2}}{2a_3(F - \alpha_F)^2} \tag{2.56a}$$

where $$R_b = (M^h - \alpha_M) + a_1(F - \alpha_F) \tag{2.56b}$$

The reduced action vector $s_i^{h'}$ can be written as

$$s_i^{h'} = \alpha_i' + RF \cdot (s_i^{h'} - \alpha_i') \tag{2.57}$$

If relatively large load increment sizes are to be permitted, the process described above can lead to an inaccurate prediction of the final point P_i' on the yield surface if the action point is in the vicinity of a region of large curvature of the yield surface. This is illustrated in Fig. 2.17 where the action point P_i' is scaled down to the yield surface to give point P_i''. Greater accuracy can be achieved by scaling the action vector $s_i^{h'}$ to the yield surface in several stages.

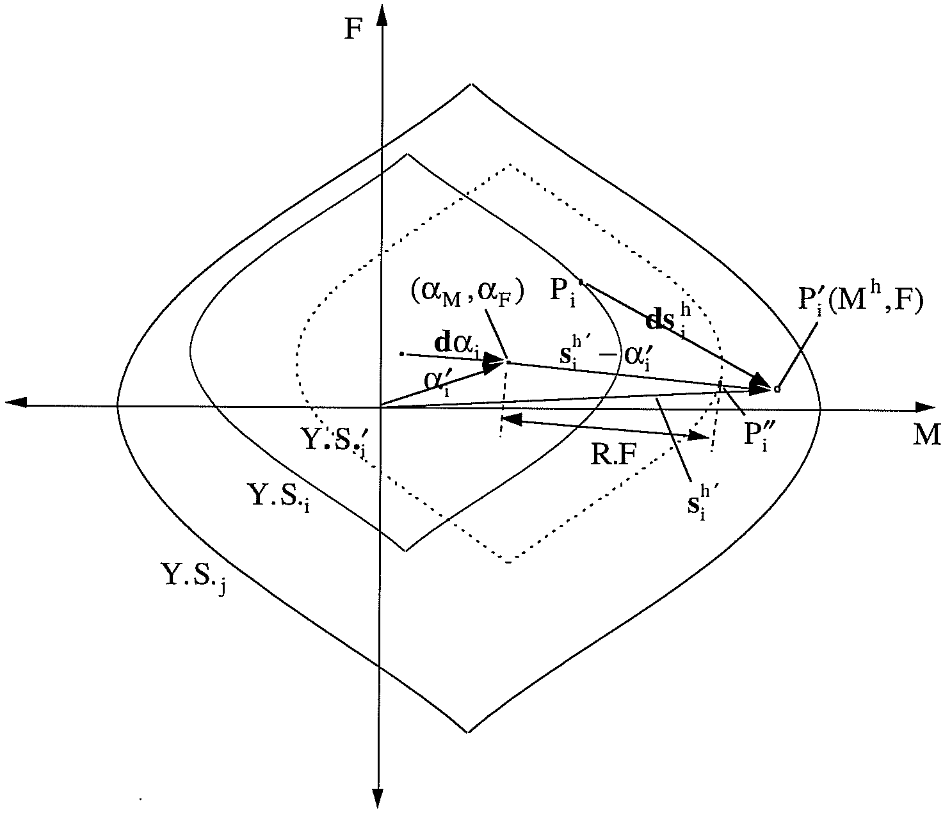

Fig. 2.17: Scaling the Action Point to the Yield Surface

To scale the action vector $s_i^{h'}$ to the yield surface in several stages, the element deformation increment is divided into several equal parts and each deformation subincrement is used to calculate the hinge action subincrement. At the end of each of the hinge action subincrements, the action vector is scaled down to the translated yield surface. Obviously the greater the number of steps into which the deformation increment is divided, the greater the accuracy. However the amount of computation for each step is relatively large since the normal vector **n** and the element tangent stiffness matrix $\mathbf{K}_t$ have to be calculated at each stage. Clearly a balance must be sought and in this study the following criterion is adopted. The element deformation increment is divided into *m* parts where *m* is given by the nearest integer which is less than

$$\left(\frac{dM^h}{M_{y2}-M_{y1}}\right)\cdot 10 + 1 \tag{2.58}$$

where dM^h is the moment component of the hinge action increment $\mathbf{ds}_i^h$ and $M_{y2}-M_{y1}$ is the difference between the moment sizes of the yield surfaces 1 and 2. This criterion can be readily amended by the user.

When the yield surface is a multi-linear shape, there may also be a possibility that the action point will be outside the translated yield surface. This situation is illustrated in Fig. 2.18. The inside of the dotted circle in Fig. 2.18 is enlarged in detail in Fig. 2.19. In Figs. 2.18 and 2.19, the translation increment $\mathbf{d\alpha}_i$ of yield surface $Y.S._i$ was calculated by using Eq. 2.45b for a given action increment $\mathbf{ds}_i^h$. From these figures, it can be found that the action point P_i' defined by a vector $s_i^{h'}$ is not on translated yield surface $Y.S._i'$ because the action increment vector $\mathbf{ds}_i^h$ intersects the vector $\mathbf{P}_{ji}$, which has the origin at the vertex V and is parallel to the vector $\mathbf{d\alpha}_i$.

To prevent the action point from being outside the yield surface, a proportion of deformation increment η, shown in Fig. 2.19, is determined such that the reduced action increment $\eta\mathbf{ds}_i^h$ corresponding to the proportioned deformation increment reaches the vector $\mathbf{P}_{ji}$. Thus, from the geometry of Fig. 2.19, a proportion of deformation increment η is expressed as

$$\eta = \frac{(M^j - M^i)(F^v - F^i) + (F^j - F^i)(M^i - M^v)}{(M^j - M^i)dF - (F^j - F^i)dM} \tag{2.59}$$

For the reduced action increment $\eta\mathbf{ds}_i^h$, the action point P_i' will always be at a vertex of translated yield surface $Y.S._i'$, as shown in Fig. 2.20. Then, the remaining action increment $(1-\eta)\mathbf{ds}_i^h$ which is calculated by using a tangent stiffness updated at a vertex and the deformation increment left over, is applied at a vertex.

When the action point lies at a vertex of a yield surface, the determination of the yield surface translation becomes complicated if the Mroz hardening rule is applied directly to the two dimensional action space. Firstly, the gradient at the corners of yield surface can not be computed from the yield function. Secondly, unless the action increment $\mathbf{ds}_i^h$ is in the direction of the yield surface translation , depicted in Fig. 2.21 as being the vector $\mathbf{s}_2^h$ - $\mathbf{s}_1^h$ defined by points P_i and P_j, the action point may drift off the yield surface. Thirdly, the loading-unloading criteria, which depend on the normal vector at the current action point, must be able to differentiate between plastic flow and elastic unloading from any plastic state for any specified deformation increment. These criteria may fail to differentiate between plastic flow and elastic unloading because there is no normal vector to satisfy these criteria regardless of the direction of the action increment.

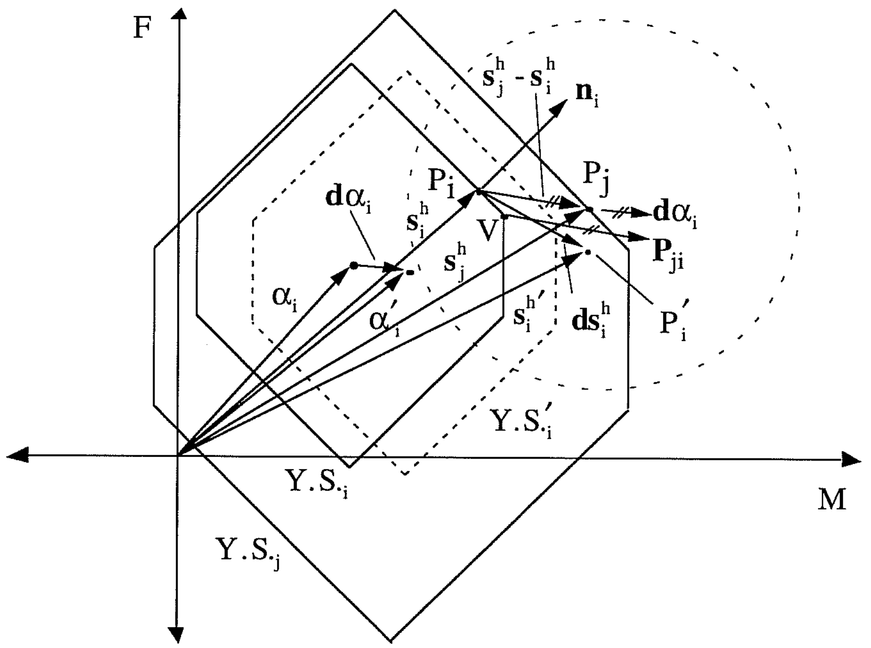

Fig. 2.18: Action Point Outside of Yield Surface

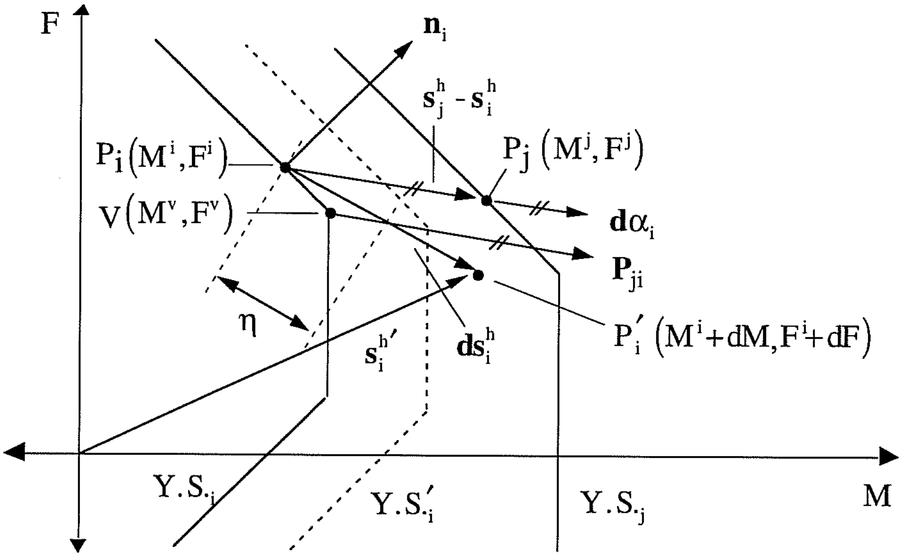

Fig. 2.19: A Proportion of Deformation Increment

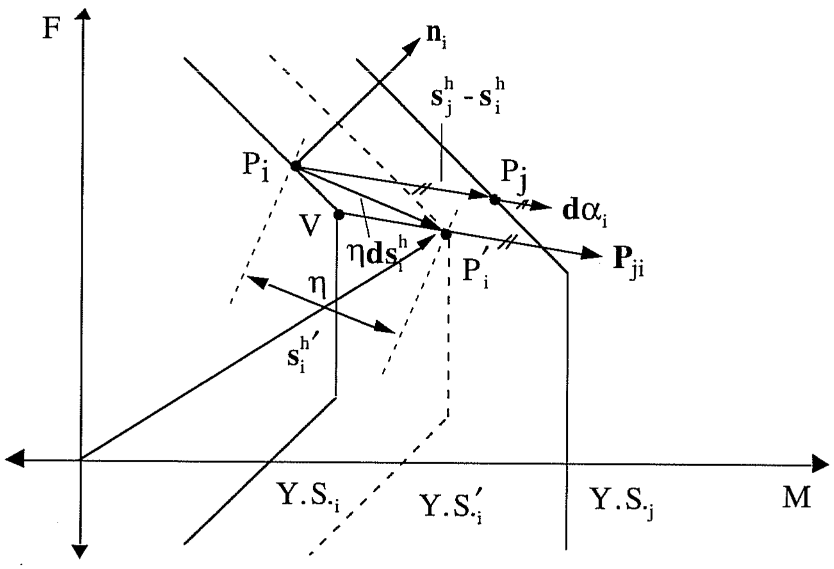

Fig. 2.20: Reduced Action Increment to Make Action Point Remain on Yield Surface

To overcome the complexity of the problems at the corners of a yield surface, in this study, two unit normal vectors at a vertex are applied for different purposes. The first normal vector is used to determine the element tangent stiffness and plastic deformations. The second one is applied to the translation of the yield surface and the loading-unloading criteria.

The first normal vector is determined from the sum of two unit vectors $\mathbf{n}_i^1$ and $\mathbf{n}_i^2$, which are normal to the facets $\underline{1}$ and $\underline{2}$ of a vertex shown in Fig. 2.21. Thus, the normal vector $\mathbf{n}_i^a$ which is used to determine the element tangent stiffness and plastic deformations, is expressed as

$$\mathbf{n}_i^a = \frac{1}{\left|\mathbf{n}_i^1 + \mathbf{n}_i^2\right|} \cdot \left(\mathbf{n}_i^1 + \mathbf{n}_i^2\right) \tag{2.60}$$

This normal vector $\mathbf{n}_i^a$ realistically models the unit normal vector at the corresponding point of a higher order yield surface which accounts for the moment-force interaction more exactly, and plays a transitional role to keep the tangent stiffness and the direction of plastic deformation at a plastic state from changing abruptly.

The second normal vector is chosen according to the direction of the action increment, such that the action point always remains on the yield surface during the translation and the loading-unloading criteria are always able to differentiate between plastic flow and elastic unloading. One of the unit vectors $\mathbf{n}_i^1$ and $\mathbf{n}_i^2$ shown in Fig. 2.21 is chosen as the normal vector according to the direction of the action increment as follows. When the Z component of cross product $\left(\mathbf{s}_j^h - \mathbf{s}_i^h\right) \times \mathbf{ds}_i^h$ is positive in the rectangular coordinate system shown in Fig. 2.21, the normal vector is the unit vector which produces the larger of the Z components of the cross products $\left(\mathbf{s}_j^h - \mathbf{s}_i^h\right) \times \mathbf{n}_i^1$ and $\left(\mathbf{s}_j^h - \mathbf{s}_i^h\right) \times \mathbf{n}_i^2$. Otherwise, the normal vector is the unit vector which gives the smaller Z component of the cross product $\left(\mathbf{s}_j^h - \mathbf{s}_i^h\right) \times \mathbf{n}_i^k$, where the superscript k is 1 and 2. For example, when the action increment is represented by a vector $\mathbf{ds}_i^{h2}$ shown in Fig. 2.21, the Z component of cross product $\left(s_j^h - s_i^h\right) \times \mathbf{ds}_i^{h2}$ is positive. Thus, the normal vector is the unit vector $\mathbf{n}_i{}^2$, which gives the larger Z component of cross product $\left(s_j^h - s_i^h\right) \times \mathbf{n}_i{}^k$. When the action increment is represented by the vector $\mathbf{ds}_i^{h1}$ which produces the negative Z component of cross product $\left(s_j^h - s_i^h\right) \times \mathbf{ds}_i^{h1}$, the normal vector is the unit vector $\mathbf{n}_i{}^1$, which gives the smaller Z component of cross product $\left(s_j^h - s_i^h\right) \times \mathbf{n}_i{}^k$. The unit normal vector chosen by this approach always makes the action point remain on the translated yield surface. When this chosen vector is applied to the loading-unloading criteria using the scalar product of the normal vector and the action increment vector, the distinction between plastic flow and elastic unloading is always accomplished correctly.

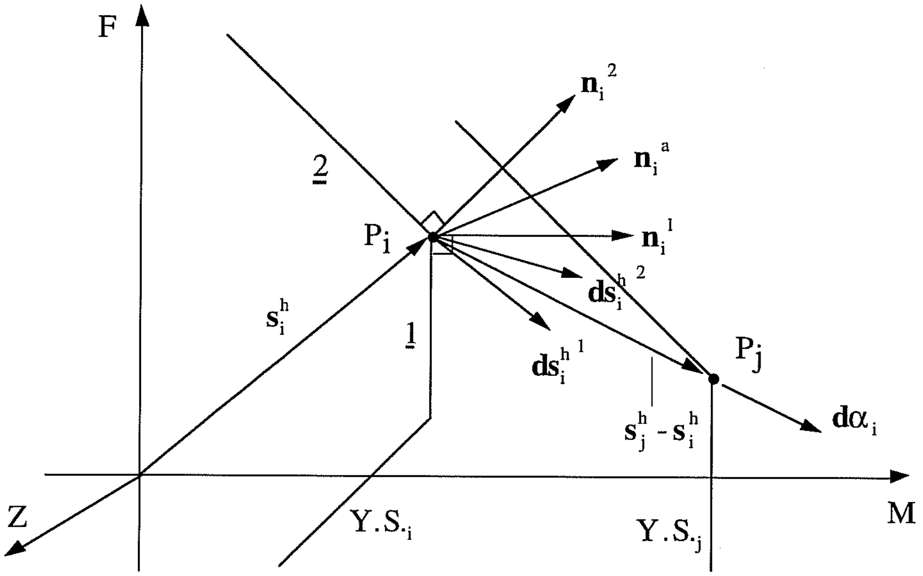

Fig. 2.21: Normal Vector at a Vertex of Yield Surface

2.11 Determination of Plastic Stiffness

As noted previously, the post yield behavior of the complete element is governed by the diagonal plastic stiffness matrix $\mathbf{K}_p$ of each hinge. For each hinge, the determination of the diagonal terms of $\mathbf{K}_p$ requires a knowledge of the complete action-deformation relationships. Since the matrix $\mathbf{K}_p$ is diagonal, each action-deformation relationship is uncoupled. Thus the individual terms in $\mathbf{K}_p$ for a hinge can be obtained from separate applied actions, as indicated in Figs. 2.22 and 2.23. The relationship for axial load is straightforward because the corresponding internal force is constant along the length of the member. In the hinge model, it is assumed that each hinge at the member ends shares the plastic axial deformations evenly. Consequently, the axial force-deformation relationship is obtained for each half of the element, as shown in Fig. 2.22.

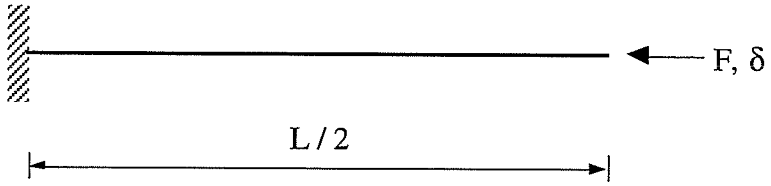

a) Beam Under Axial Force

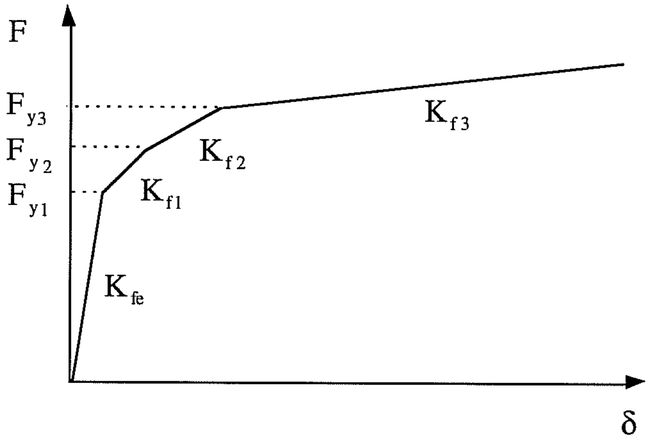

b) Axial Force-Deformation Relationship

Fig. 2.22: Axial Force-Deformation Relationship

In specifying the flexural plastic stiffness, however, a complication arises from the fact that moment-curvature nonlinearities are being modeled by using concentrated hinges. In an actual beam the moment typically varies along the length, and plastic deformations occur over finite regions. Consequently, the flexural stiffness depends on the moment variation along the beam. In a concentrated hinge model, it is not possible to account for all possible moment variations which may occur, and hence, some assumptions must be made in specifying the hinge properties. Under seismic loading, beams and columns of steel moment resisting frames typically have a linear variation of bending moment over the element length, with equal and opposite values at the member ends, as shown in Fig. 2.23a. Thus, one could consider obtaining a moment-rotation relationship for an equivalent cantilever representing each half of the element, as shown in Figs. 2.23b and 2.23c.

To determine the plastic stiffness coefficient of $\mathbf{K}_p$ for a hinge, the reciprocal of the slope of the action-deformation relationship for the current state is equated to the combined flexibilities of the elastic cantilever beam and the hinge. Thus, if the hinge yields due to the axial force exceeding the yield strength F_{y1}, then

$$\frac{1}{K_{f1}} = \frac{1}{K_{fe}} + \frac{1}{K_{pf1}} \tag{2.61}$$

Thus, the plastic stiffness coefficient K_{pf1} for the hinge associated with axial force is given as

$$K_{pf1} = \frac{K_{fe}K_{f1}}{K_{fe} - K_{f1}} \tag{2.62}$$

where K_{fe} and K_{f1}, respectively, are the axial stiffness of the elastic beam, and the slope of the axial force-deformation relationship between the strengths F_{y1} and F_{y2}, as shown in Fig. 2.22. If the axial force of the hinge exceeds the yield strength F_{yi}, then

$$K_{pfi} = \frac{K_{fe}K_{fi}}{K_{fe} - K_{fi}} \tag{2.63}$$

Similarly, if the bending moment of the hinge exceeds the yield moment M_{yi} shown in Fig. 2.23c, the plastic coefficient K_{pmi} for the hinge associated with bending moment is expressed as

$$K_{pmi} = \frac{K_{me}K_{mi}}{K_{me} - K_{mi}} \tag{2.64}$$

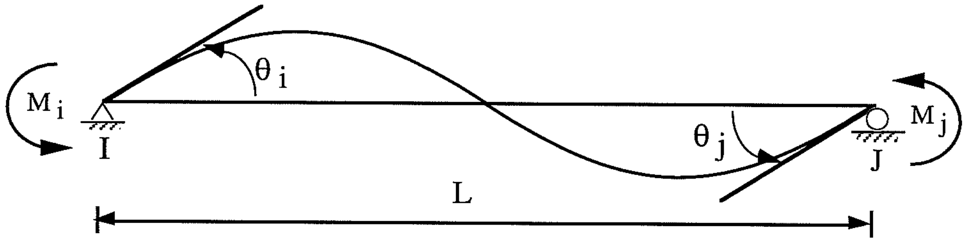

a) Beam with Equal End Moments

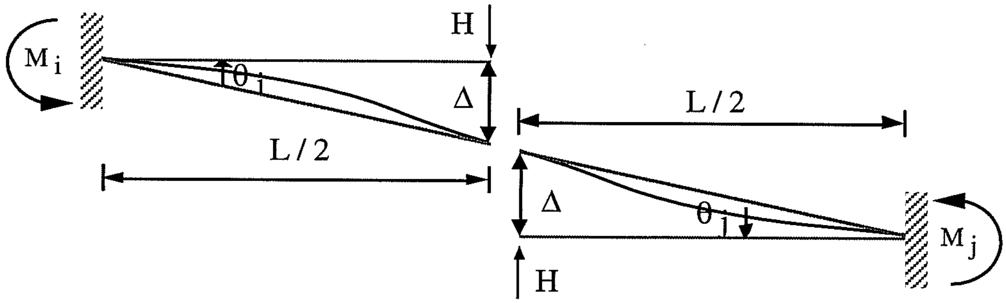

b) Equivalent Cantilevers

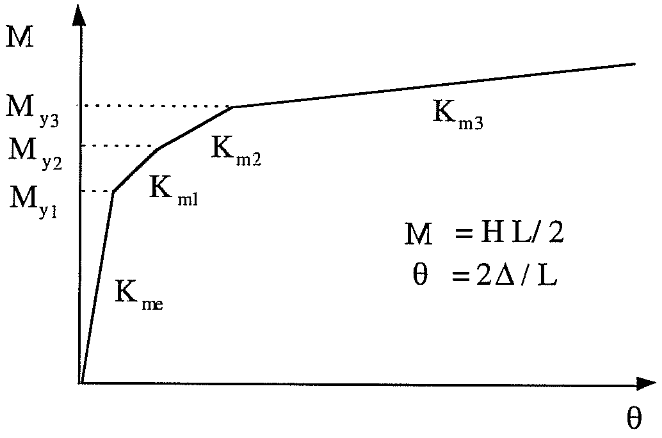

c) Moment-Rotation Relationship

Fig. 2.23: Moment-Rotation Relationship for Equivalent Cantilever Beam

2.12 State Determination

When the inelastic analysis of a structure is performed, it is necessary to carry out a state determination after computing the increment in local element displacements **dr,** in order to determine the updated internal resisting forces $\mathbf{R}^{I}$ of the elements. As a result, the unbalanced global nodal loads $\mathbf{R}^{U}$ can be determined for the current state, where

$$\mathbf{R}^{U} = \mathbf{R}^{E} - \mathbf{R}^{I} \tag{2.65}$$

in which $\mathbf{R}^{E}$ is the external applied loads. If the specified norm of $\mathbf{R}^{U}$ is greater than an allowable tolerance, then an iteration scheme is required to satisfy equilibrium to within the allowable tolerance.

Having computed the increment of local displacements **dr** for the element, it is necessary to compute resisting forces $\mathbf{R}^{I}$ due to the associated element deformations $\mathbf{dv}$. The computation procedure is as follows:

i) Calculate the element deformation increment $\mathbf{dv}$:

$$\mathbf{dv} = \mathbf{A}^{T} \cdot \mathbf{dr} \tag{2.66}$$

where $\mathbf{dv}$ = vector of element deformation increment,
$\mathbf{A}^{T}$ = displacement transformation matrix,
$\mathbf{dr}$ = vector of local nodal displacement increment.

ii) Calculate linear action increments for the element $\mathbf{ds}$:

$$\mathbf{ds} = \mathbf{K}_{t} \cdot \mathbf{dv} \tag{2.67}$$

where $\mathbf{K}_{t}$ = element tangent stiffness, which, in general, varies during the increment.

iii) Determine hinge action increment $\mathbf{ds}^{h}$ from $\mathbf{ds}$ according to Eq.2.12.
* The following procedure is implemented only for the nonlinear yield surface.

a) If the moment component dM^{h} of $\mathbf{ds}^{h}$ is less than the criterion $CM = \frac{M_{y2} - M_{y1}}{10}$ used in Eq. 2.58, go to the next step iv.

b) Otherwise, the element deformation increment $\mathbf{dv}$ is divided into m parts by using Eq. 2.58 and for each deformation subincrement the hinge action increment is calculated.

iv) Check for the occurrence of an event for each hinge, and calculate the corresponding event factor FAC for each hinge as a proportion of the deformation increment. Possible events are:

a) If the current state is elastic, calculate the proportion of deformation increment FAC to reach the initial yield surface as shown in Fig. 2.24. From the geometry of Fig. 2.24, the proportion FAC is calculated as follows:

$$\mathrm{FAC} = \frac{\sqrt{\left(M^{Y} - M^{h}\right)^{2} + \left(F^{Y} - F\right)^{2}}}{\sqrt{\left(dM^{h}\right)^{2} + (dF)^{2}}} \tag{2.68}$$

If this proportion FAC is greater than 1.0, the state continues to be elastic and event factor is 1.0. Otherwise, an event occurs and the event factor is set equal to the calculated proportion FAC.

b) If the current state is plastic, calculate loading-unloading criterion $\mathbf{n}^T \cdot \mathbf{ds}^h$. If the value exceeds zero, continued loading is indicated.

1) For continued loading, two types of events will be possible. Firstly, to check whether the action point reaches the next yield surface at the end of action increment, the yielding factor FAC is calculated by using an equation similar to Eq. 2.68. Secondly, the drift control factor η is calculated to prevent the action point from drifting outside the yield surface by using Eq. 2.59. Select the smallest factor from factors FAC and η. If the smallest factor is greater than 1.0, the state does not change and the event factor is 1.0. Otherwise, an event occurs and the event factor is set equal to the calculated smallest factor.

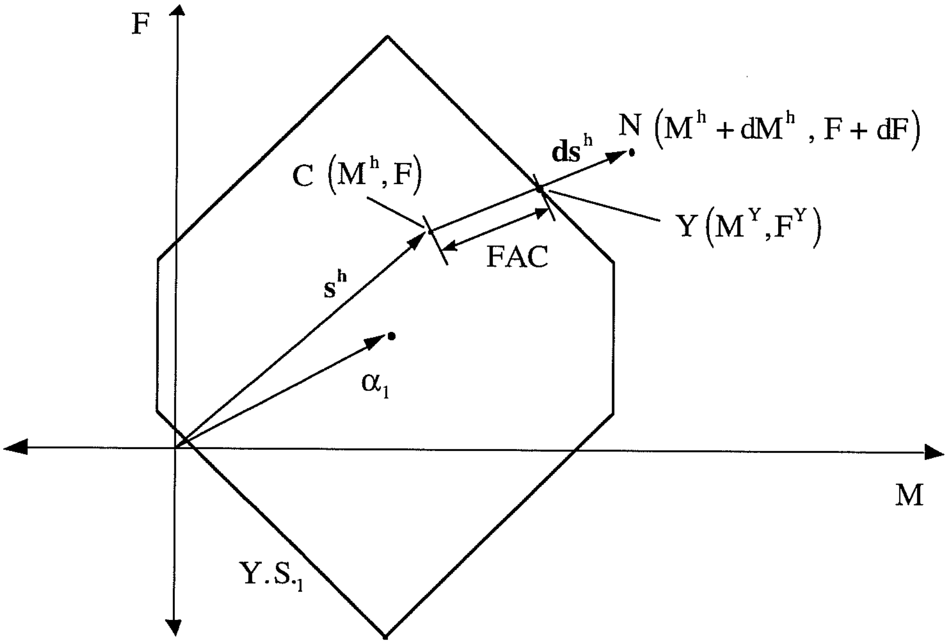

Fig. 2.24: Determination of Yielding Event Factor

2) If unloading occurs, the stiffness matrix is reformed as the elastic stiffness, and the calculation proceeds from step ii after the following procedure is performed.
   - Calculate the weight function ω for the accumulated plastic deformation $\Sigma\theta_p$
   - Adjust the sizes and the plastic stiffnesses for all yield surfaces according to Eqs. 2.47 and 2.50.
   - Adjust the center coordinates α's for the initial yield surface Y.S.$_1$ through the current yield surface Y.S.$_i$ according to Eq. 2.51.

- Check the overlapping of yield surfaces $Y.S._k$ and $Y.S._{k+1}$ for k = i, i+1, ..., n-1, using α'_k and Eq. 2.52. In case of overlapping, the center α'_{k+1} of surface $Y.S._{k+1}$ will be adjusted according to Eq. 2.53.

v) Calculate the element plastic deformations $\mathbf{dw}_p$, using Eq. 2.16a.

vi) Select the smallest event factor, FACT, from the event factors for two hinges at the element ends.

vii) Use the event factor FACT, to compute new hinge forces, new total plastic deformations, and a new origin for the current yield surface, as follows:

$$\mathbf{s}^h = \mathbf{s}^h + \mathrm{FACT} \cdot \mathbf{ds}^h \tag{2.69a}$$

$$\mathbf{w}_p = \mathbf{w}_p + \mathrm{FACT} \cdot \mathbf{dw}_p \tag{2.69b}$$

$$\alpha_i = \alpha_i + \mathrm{FACT} \cdot \mathbf{d}\alpha_i \tag{2.69c}$$

* Only for the nonlinear yield surface the new hinge forces are scaled to the yield surface by using Eqs. 2.56 and 2.57.

viii) Calculate the complement of the event factor as:

$$\mathrm{CF} = 1 - \mathrm{FACT} \tag{2.70}$$

ix) Reform the tangent stiffness matrix for the element if any event has occurred.

x) If all of the deformation increment for the element has been used up, go to step xii. Otherwise, continue to the next step.

xi) Calculate the remaining element deformation increment for the next cycle from:

$$\mathbf{dv} = \mathrm{CF} \cdot \mathbf{dv} \tag{2.71}$$

Then go to step ii.

xii) Obtain the element actions, $\mathbf{s}$, using the hinge forces $\mathbf{s}^h$'s determined in step vii.

xiii) Calculate the internal resisting force for the element, $\mathbf{R}_e^I$, using:

$$\mathbf{R}_e^I = \mathbf{A} \cdot \mathbf{s} \tag{2.72}$$

Chapter 3: FIBER ELEMENT

3.1 General

Later in this report, the beam-column hinge type element developed in Chapter 2 will be calibrated and verified by comparison with experimental data or by comparison with response predictions made using a fiber element analysis. This chapter provides a description of the fiber element.

The fiber element is a beam-column type element for modeling the response of structural members subjected to bending moment and axial force. Unlike the hinge type element, which lumps inelastic effects into nonlinear springs at the member ends, the fiber element more realistically models the spread of yielding, both over the depth of the cross-section and over the length of the member. Whereas the user of a hinge type element must specify the properties of a hypothetical hinge, the user of a fiber element must only specify the cross-sectional geometry of the member and the uniaxial stress-strain behavior of the material. The response of the fiber element is derived from the fundamental kinematic assumption that plane sections remain plane.

In the fiber model, the element is subdivided into longitudinal fibers or layers. The geometric characteristics of a fiber are its location in the cross section and its area. Material nonlinearity is introduced at any element section and the element behavior is derived by the weighted integration of the section response. In practice, since the element integrals are evaluated numerically, only the behavior of selected sections at the integration points is monitored. The constitutive behavior of the cross section is not specified explicitly, but is derived by integration of the response of the fibers or layers, which follow the uniaxial stress-strain relation of the particular material.

Many fiber models have been proposed in the past two decades. These fiber models can be divided into two categories in accordance with the procedure employed in the derivation of the element stiffness matrix.

The first category of fiber models is based on the finite element displacement approach using cubic Hermitian polynomials to approximate the deformations along the length of the element. A major limitation of the finite element displacement approach is the assumption of cubic interpolation functions, which results in a linear curvature distribution along the element. When the structural member undergoes significant yielding, the curvature distribution becomes highly nonlinear in the inelastic region. This requires the use of a fine discretization in the inelastic region of fiber elements.

In the second category of fiber models the element stiffness is formulated based on the section flexibility matrix and on force interpolation functions, which relate the member end forces to the section forces. The curvature distribution is determined from the section forces and the section flexibility matrix, which is continuously updated during the analysis as the inelastic deformations spread into the member. Therefore, the curvature distribution can be determined in a more exact manner without being restricted by the fixed shape function, as in the finite element approach. In this study this flexibility-based approach is adopted to formulate the element stiffness and the section deformations. The mathematical formulation is based on the approaches suggested by Carol and Murcia (1989), and Moon (1994), with some modifications for shear deformations.

The general formulation is based on the assumption that plane cross-sections perpendicular to the element axis always remain plane and perpendicular to the element axis after deformation. Shear deformations are separately taken into account by using the effective shear rigidity GA_s, where A_s is the effective shear area. With these assumptions, the basic formulation is derived for the undeformed position of the element. Later, second-order effects are considered by satisfying equilibrium in the deformed position. The change of geometry is accounted for by continuously changing the local coordinate system at every step. Thus, the joint displacements are added to the old joint coordinates, and a new set of rotation matrices and lengths are computed for each member.

3.2 Equilibrium Equations

Cross-sectional forces (N,Q) and moment (M), and distributed applied load (P^*) acting on a differential beam slice placed in its undeformed position are shown in Fig. 3.1. From equilibrium of the beam slice, the well known system of differential equilibrium equations can be obtained. These differential equations result in the following solution:

$$N(x) = s_1 \tag{3.1a}$$

$$M(x) = M^* + s_2 \cdot \left(\frac{x}{L} - 1 \right) + s_3 \cdot \frac{x}{L} \tag{3.1b}$$

$$Q(x) = - \left(\frac{dM^*}{dx} + \frac{s_2}{L} + \frac{s_3}{L} \right) \tag{3.1c}$$

where s_1, s_2 and s_3 are three independent forces shown in Fig. 3.2. In these equations, M^* is a particular solution of Eqs. 3.1 for the distributed load $P^*(x)$. This particular solution has been chosen for zero values of s_1, s_2 and s_3 at the ends, which lets M^* correspond to the solution of the simply supported beam with applied distributed load $P^*(x)$. Therefore, the section forces **C** can also be written in a matrix form as

$$\begin{Bmatrix} N \\ Q \\ M \end{Bmatrix} = \begin{bmatrix} 1 & 0 & 0 \\ 0 & -1/L & -1/L \\ 0 & (x/L-1) & x/L \end{bmatrix} \begin{Bmatrix} s_1 \\ s_2 \\ s_3 \end{Bmatrix} + \begin{Bmatrix} 0 \\ -\dfrac{dM^*}{dx} \\ M^* \end{Bmatrix} \tag{3.2}$$

or, in a more compact notation,

$$\mathbf{C} = \mathbf{b} \cdot \mathbf{s} + \mathbf{C}_p \tag{3.3}$$

This expression can be considered as an exact interpolation for cross-sectional forces **C** within the element. It depends on the independent forces **s** and on particular solution $\mathbf{C}_p$.

3.3 Strain-Displacement Relationships

Having assumed that plane cross-sections perpendicular to the element axis remain plane and perpendicular, the longitudinal strain ε of any fiber placed in the cross-section at a distance y over the reference axis can be written as a linear function of the reference fiber strain ε_r and the curvature Φ as

$$\varepsilon = \varepsilon_r + y \cdot \Phi \tag{3.4}$$

These two variables ε_r and Φ therefore represent the entire cross-section strain state, and can be related to the axis displacements U,V and rotation of reference axis θ shown in Fig. 3.2 by the equation.

$$\varepsilon_r = \frac{dU}{dx} \tag{3.5a}$$

$$\Phi = \frac{d^2V}{dx^2} \tag{3.5b}$$

$$\theta = \frac{dV}{dx} \tag{3.5c}$$

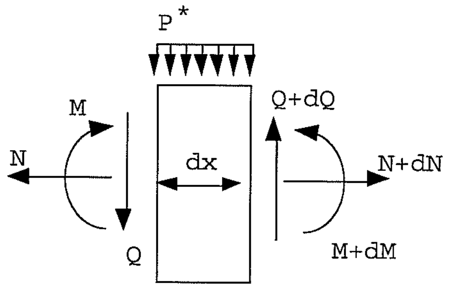

Fig. 3.1: First-Order Equilibrium of a Beam Slice

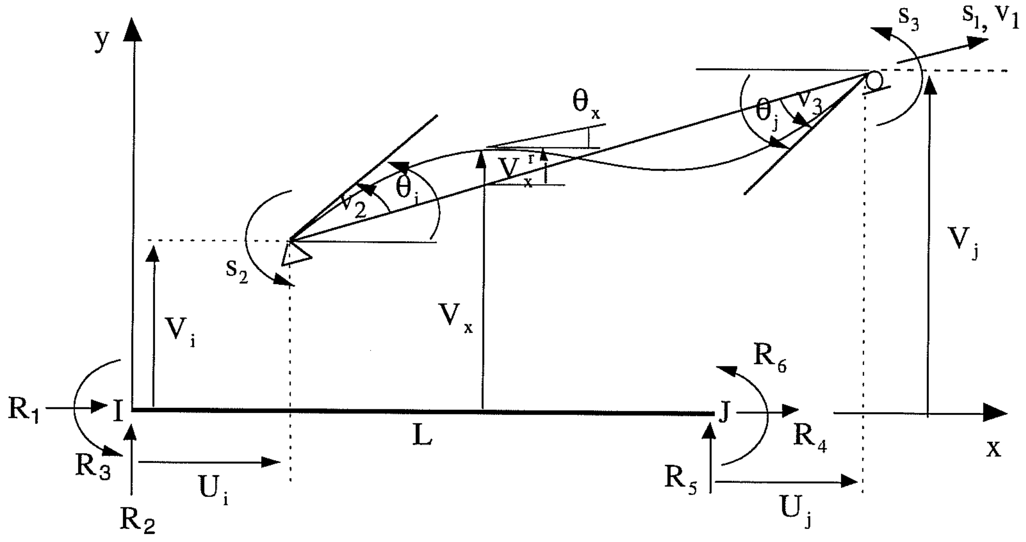

Fig. 3.2: Relative Displacements and Transverse Deflections

The previous strain-displacement relationships can also be expressed in the following integral form

$$U_j = U_i + \int_0^L \varepsilon_r \, dx \tag{3.6a}$$

$$V_j = V_i - \theta_i \cdot L - \int_0^L \Phi \cdot (L - x) \, dx \tag{3.6b}$$

$$\theta_j = \theta_i + \int_0^L \Phi \, dx \tag{3.6c}$$

Equations 3.6 can be written in matrix form as

$$\begin{Bmatrix} U_j - U_i \\ \theta_i - \left(V_j - V_j\right)/L \\ \theta_j - \left(V_j - V_j\right)/L \end{Bmatrix} = \int_0^L \begin{bmatrix} 1 & 0 \\ 0 & (x/L-1) \\ 0 & x/L \end{bmatrix} \cdot \begin{Bmatrix} \varepsilon_r \\ \Phi \end{Bmatrix} dx \tag{3.7}$$

or, in a more compact notation,

$$\mathbf{v} = \int_0^L \mathbf{b}_b^T \cdot \mathbf{e}_b \, dx \tag{3.8}$$

where $\mathbf{v}$ is the vector of relative displacements shown in Fig. 3.2, $\mathbf{b}_b$ is the same matrix as in Eq. 3.2 with the exception that the row associated with the shear is omitted, and $\mathbf{e}_b$ is the generalized strain vector for the cross-section.

When the shear deformations are separately accounted for by using the effective shear rigidity GA_s, the principle of virtual forces can be used to derive the strain-displacement relationships. The work done by virtual forces during the actual displacements is called the complementary virtual work. The virtual section forces $\delta \mathbf{C}$ must satisfy the equation of internal section force equilibrium, and the virtual member forces $\delta \mathbf{s}$ must satisfy equations for boundary equilibrium. The section strains derived from the virtual section forces $\delta \mathbf{C}$ need not necessarily satisfy the equations of compatibility.

The complementary virtual work done by the virtual forces $\delta \mathbf{s}$ corresponding to the actual relative displacements $\mathbf{v}$ can be written as

$$\delta W^*_{ext} = \mathbf{v}^T \cdot \delta \mathbf{s} \tag{3.9}$$

The complementary virtual internal work can be found to be

$$\delta W^*_{int} = \int \mathbf{e}^T \cdot \delta \mathbf{C} \tag{3.10}$$

in which $\mathbf{C}$ is the section force vector defined by Eq. 3.2 or Eq.3.3, and $\mathbf{e}$ is the cross-section strain vector including the shear strain γ expressed as

$$\mathbf{e}^T = \{\varepsilon_r, \gamma, \Phi\} \tag{3.11}$$

Substituting $\mathbf{C} = \mathbf{b} \cdot \mathbf{s}$ into Eq. 3.10 and equating the resulting equation to Eq.3.9 lead to

$$\mathbf{v}^T \cdot \delta \mathbf{s} = \left(\int \mathbf{e}^T \cdot \mathbf{b}\right) \cdot \delta \mathbf{s} \tag{3.12}$$

Since the virtual forces $\delta \mathbf{s}$ are arbitrary, then

$$\mathbf{v} = \int \mathbf{b}^T \cdot \mathbf{e} \tag{3.13}$$

This equation implies that the relative displacement $\mathbf{v}$ including the shear deformation effects can also be determined by using the interpolation matrix $\mathbf{b}$ relating the relative forces $\mathbf{s}$ to the section forces $\mathbf{C}$.

3.4 Constitutive Equations

The uniaxial stress-strain relationship of a fiber can be generally written as

$$d\sigma = E_t \cdot d\varepsilon \tag{3.14}$$

where

$$d\varepsilon = d\varepsilon_r + y \cdot d\Phi \tag{3.15}$$

E_t is the tangent stiffness and y is a distance from the reference axis to a fiber. From these equations, the incremental section forces **dC** can be related to the incremental section strain vector **de** as follows:

$$\begin{Bmatrix} dN \\ dQ \\ dM \end{Bmatrix} = \begin{bmatrix} \int E_t dA & 0 & \int yE_t dA \\ 0 & GA_s & 0 \\ \int yE_t dA & 0 & \int y^2 E_t dA \end{bmatrix} \cdot \begin{Bmatrix} d\varepsilon_r \\ d\gamma \\ d\Phi \end{Bmatrix} \tag{3.16}$$

where GA_s is the effective shear rigidity. This equation can be written in a more compact notation

$$\mathbf{dC} = \mathbf{D} \cdot \mathbf{de} \tag{3.17}$$

in which **D** is the cross-section stiffness matrix. This equation is used as the cross sectional constitutive equation.

3.5 Governing Differential Equation

The governing equation for the element behavior can be derived from the equilibrium equations, the strain-displacement relationship, and the constitutive equation. The strain-displacement relationship is expressed in an incremental form

$$\mathbf{dv} = \int \mathbf{b}^T \cdot \mathbf{de}\, dx \tag{3.18}$$

The constitutive equation can be rewritten in terms of the section flexibility matrix $\mathbf{D}^{-1}$:

$$\mathbf{de} = \mathbf{D}^{-1} \cdot \left(\mathbf{C}_i^k - \mathbf{C}_{i-1}\right) = \mathbf{D}^{-1} \cdot \left(\mathbf{b} \cdot \mathbf{s} + \mathbf{C}_p - \mathbf{C}_{i-1}\right) \tag{3.19}$$

in which the incremental section forces are written as the difference between the section forces $\mathbf{C}_i^k$ at the current iteration k of the load step i and the section forces $\mathbf{C}_{i-1}$ at the previous load step i-1, in order to take into account the second order effects later. Therefore, the incremental relative displacements are expressed as

$$\mathbf{dv} = \mathbf{F}_r \cdot \mathbf{s} + \int \mathbf{b}^T \cdot \mathbf{D}^{-1} \cdot \left(\mathbf{C}_p - \mathbf{C}_{i-1}\right) dx \tag{3.20a}$$

and

$$\mathbf{F}_r = \int \mathbf{b}^T \cdot \mathbf{D}^{-1} \cdot \mathbf{b}\, dx \tag{3.20b}$$

in which $\mathbf{F}_r$ is the element flexibility matrix. This equation can be written as

$$\mathbf{s} + \mathbf{F}_r^{-1} \cdot \int \mathbf{b}^T \cdot \mathbf{D}^{-1} \cdot \left(\mathbf{C}_p - \mathbf{C}_{i-1}\right) dx = \mathbf{F}_r^{-1} \cdot \mathbf{dv} \tag{3.21}$$

in which the two terms in the left-hand side of Eq. 3.21 represent the incremental nodal forces due to the applied joint forces and member loads. This equation can be rewritten in the local coordinate system, using Eqs. 2.1a and 2.2a.

$$\mathbf{R} + \mathbf{A} \cdot \mathbf{F}_r^{-1} \cdot \int \mathbf{b}^T \cdot \mathbf{D}^{-1} \cdot \left(\mathbf{C}_p - \mathbf{C}_{i-1}\right) dx = \mathbf{K}_e \cdot \mathbf{dr} \tag{3.22a}$$

and

$$\mathbf{K}_e = \mathbf{A} \cdot \mathbf{F}_r^{-1} \cdot \mathbf{A}^T \tag{3.22b}$$

where $\mathbf{K}_e$ is the element stiffness matrix, **R** is the nodal force vector in the local coordinate system, and **dr** is the corresponding incremental nodal displacement vector.

3.6 Second Order Effects

A differential beam slice placed in its deformed position is presented in Fig. 3.3, with the cross-sectional forces and external applied loads acting on it. Although they are considered to move together with the cross-section, the axial and shear forces will be considered in this work as having the direction of the initial axis of the beam. The basic assumption made herein concerning the magnitude of deformations is that $dV \ll dx$, which is equivalent to assuming that the slope of the deflected axis of the beam is small. With this assumption, Eqs. 3.5 and 3.13 remain valid.

The differential equilibrium equations obtained from Fig. 3.3 result in the following:

$$N(x) = s_1 \tag{3.23a}$$

$$M(x) = M^* + s_2 \cdot \left(\frac{x}{L} - 1 \right) + s_3 \cdot \frac{x}{L} + s_1 \cdot V_x^r \tag{3.23b}$$

$$Q(x) = -\left(\frac{dM^*}{dx} + \frac{s_2}{L} + \frac{s_3}{L} - s_1 \cdot \frac{V_j - V_i}{L} \right) \tag{3.23c}$$

in which V_x^r is the deflection along the reference axis, but measured from the straight line connecting the deformed position of ends I and J, as shown in Fig. 3.2. Compared to the corresponding first order solution, Eqs. 3.1, two new terms appear in the 2nd order solution. The first is a new term in the expression of moments, and corresponds to a moment increment proportional to s_1 and to V_x^r. This term accounts for 2nd order effects resulting from member deflections relative to a chord connecting the member ends. These are often referred to as "P-δ" effects. The second new term in Eq. 3.23c, accounts for 2nd order effects resulting from the deflection of one member end with respect to the other end. These are often referred to as "P - Δ" effects.

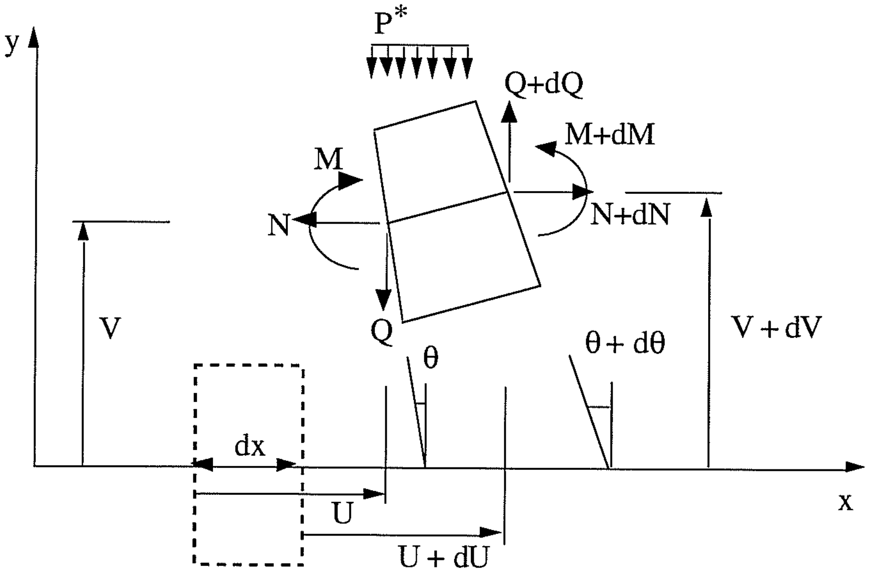

Fig. 3.3: Second Order Equilibrium of a Beam Slice

The section forces **C** can also be written in matrix form as

$$\begin{Bmatrix} N \\ Q \\ M \end{Bmatrix} = \begin{bmatrix} 1 & 0 & 0 \\ 0 & -1/L & -1/L \\ 0 & x/L-1 & x/L \end{bmatrix} \begin{Bmatrix} s_1 \\ s_2 \\ s_3 \end{Bmatrix} + \begin{Bmatrix} 0 \\ -\dfrac{dM^*}{dx} \\ M^* \end{Bmatrix} + \begin{Bmatrix} 0 \\ s_1 \cdot \dfrac{V_j - V_i}{L} \\ s_1 \cdot V_x^r \end{Bmatrix} \tag{3.24}$$

or, in a more compact notation,

$$\mathbf{C} = \mathbf{b} \cdot \mathbf{s} + \mathbf{C}_p + \mathbf{C}_s \tag{3.25}$$

Substituting Eq. 3.25 into Eqs. 3.19 and 3.18 results in

$$\mathbf{s} + \mathbf{F}_r^{-1} \cdot \int \mathbf{b}^T \cdot \mathbf{D}^{-1} \cdot \left(\mathbf{C}_p + \mathbf{C}_s - \mathbf{C}_{i-1}\right) dx = \mathbf{F}_r^{-1} \cdot \mathbf{dv} \tag{3.26}$$

Premultiplying this equation by the transformation matrix **A** gives the incremental governing equation in the local coordinate system

$$\mathbf{R} + \mathbf{A} \cdot \mathbf{F}_r^{-1} \cdot \int \mathbf{b}^T \cdot \mathbf{D}^{-1} \cdot \left(\mathbf{C}_p + \mathbf{C}_s - \mathbf{C}_{i-1}\right) dx = \mathbf{K}_e \cdot \mathbf{dr} \tag{3.27}$$

3.7 Numerical Integration

In the previous section, the governing equation for the nonlinear behavior of an element was formulated. However, the equation consists of many integrals that cannot be evaluated in a closed form. Therefore, it is necessary to employ some numerical schemes to evaluate the integrals. Furthermore, when the second order effects are taken into account, a suitable numerical scheme should also be applied for the computation of transverse deformations within the element, because the structural analysis gives only the nodal displacements of the element.

The element properties are characterized by the integrated values of cross sectional variables at a certain number of points which are distributed along the axis of the element. The cross sectional variables include axial stiffness, flexural stiffness, internal forces, etc. For purposes of integration, each cross section at integration points is subdivided into layers over its height as shown in Fig.3.4. A uniaxial state of stress is assumed for each layer. The geometric characteristics of the layer are its location in the cross-section and the layer area.

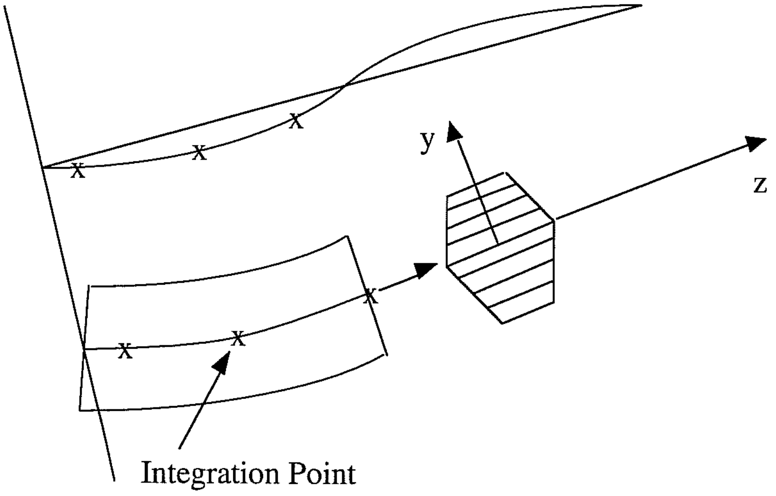

Fig. 3.4: Idealization of Cross-Section at an Integration Point

To determine the sectional stiffness matrix **D** (Eq. 3.16) at an integration point, Simpon's rule (Bäcklund 1976) can be employed for the integration over the height of the cross-section. The restrictions of Simpon's rule are that an odd number of integration points should be equally spaced and the number of integration points must be greater than two. Simpon's rule gives an exact value of area and moment of inertia if the shape of the section is rectangular or trapezoidal.

The Gaussian integration method is employed to integrate the element flexibility matrix $\mathbf{F}_r$ (Eq. 3.20b) along the axis of the element. To employ the Gaussian integration method efficiently, the element can be divided into a certain number of segments. If a short segment is placed on the region where yielding occurs, as shown in Fig. 3.5, a better distribution of integration points within the element is obtained and the element flexibility matrix can be more exactly obtained by summing its integrated values over the segments.

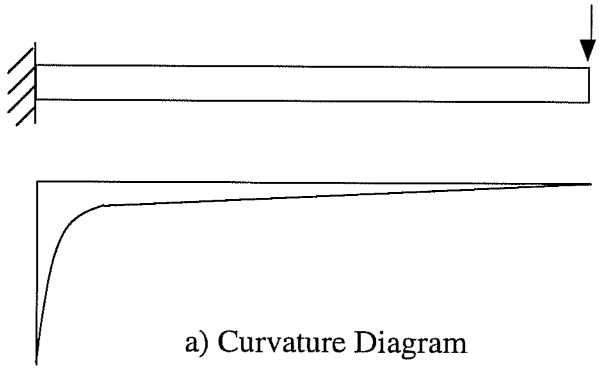

a) Curvature Diagram

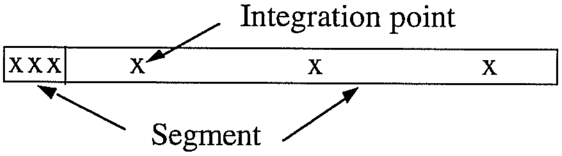

b) Distribution of Integration Points

Fig. 3.5: Distribution of Integration Points Along Segments

To account for the second order effects, it is necessary to compute the transverse deformations V_x^r at integration points along the element (see Eq. 3.24). The moment area method and the finite difference method are applied to determine these transverse deformations. The moment area method can provide theoretically exact transverse deformations at the ends of segments, using the curvatures obtained from the section forces at the Gaussian integration points as follows.

$$V_B^r = v_2 \cdot x_B - \int_0^{x_B} x \cdot \Phi \, dx \tag{3.28}$$

where V_B^r is the transverse deformation at the end B of the segment shown in Fig. 3.6 and v_2 is the relative rotation at the end I shown in Fig. 3.2.

To determine the transverse deformations V_i^r at the Gaussian integration points shown in Fig. 3.6, the finite difference method is employed. In this method the deformations V_A^r and V_B^r at the end of segment are used as the boundary values and the curvatures Φ_i at the Gaussian integration points are used as the basic known variables. The finite difference method is usually employed for equally spaced intervals. Therefore, the typical interpolation coefficients for uniform intervals are modified by the Lagrangian interpolation function because the Gaussian method does not allow uniform intervals. The modified coefficients are expressed as

$$h_{i-1} = -\frac{(x - x_i)(x - x_{i+1})}{(x_{i-1} - x_i)(x_{i+1} - x_{i-1})} \tag{3.29a}$$

$$h_i = -\frac{(x - x_{i-1})(x - x_{i+1})}{(x_{i-1} - x_i)(x_i - x_{i+1})} \tag{3.29b}$$

$$h_{i+1} = -\frac{(x - x_{i-1})(x - x_i)}{(x_{i+1} - x_{i-1})(x_i - x_{i+1})} \tag{3.29c}$$

By using the second derivatives of Eqs. 3.29 with respect to the distance x, the curvature can be written as

$$-\Phi_x = \ddot{h}_{i-1}V^r_{i-1} + \ddot{h}_i V^r_i + \ddot{h}_{i+1}V^r_{i+1} \tag{3.30}$$

Applying Eq. 3.30 to each integration point within a segment leads to the transverse deformations V^r_i at integration points as follows.

$$\begin{Bmatrix} V^r_1 \\ V^r_2 \\ V^r_3 \end{Bmatrix} = \begin{bmatrix} \ddot{h}_1 & \ddot{h}_2 & 0 \\ \ddot{h}_1 & \ddot{h}_2 & \ddot{h}_3 \\ 0 & \ddot{h}_2 & \ddot{h}_3 \end{bmatrix} \cdot \begin{Bmatrix} -\Phi_1 - \ddot{h}_A V^r_A \\ -\Phi_2 \\ -\Phi_3 - \ddot{h}_B V^r_B \end{Bmatrix} \tag{3.31}$$

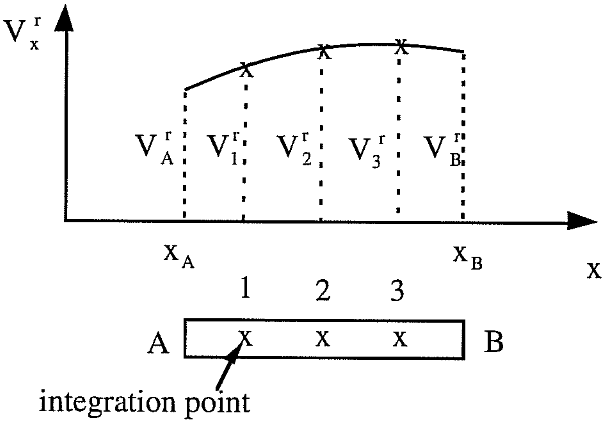

Fig. 3.6: Deformations at Integration Points Within a Segment

3.8 Uniaxial Stress-Strain Relationships for Steel

When steel is subjected to complex cyclic loading in the inelastic range, an accurate stress-strain model is needed for a correct assessment of behavior. However, an accurate description of material behavior under random cyclic loading becomes complicated due to the effects of prior load history and the complex characteristics of the cyclic loading phenomenon. Cofie and Krawinkler (1985) proposed a cyclic stress-strain relationship based on the concept of the bounding surface model developed by Dafalias and Popov (1975; 1976). In their model it was suggested that the cyclic behavior of structural steel is governed by two reference curves; the monotonic stress-strain curve and the cyclic steady state stress-strain curve (see Fig.3.7). In this work Cofie's model is adopted to describe uniaxial stress-strain relationships of steel under random cyclic loading.

From cyclic uniaxial tension tests, it has been found that the material always progresses towards the cyclic steady state curve during the course of the loading history. The cyclic steady state stress-strain curve is defined as the curve through the locus of tips of the saturation stresses at various strain amplitudes. If steel is subjected to constant strain amplitude cycling, the shape and size of the stress-strain hysteretic loops stabilize as the number of load cycles increases. After the loops have stabilized, the peak stress achieved at the peak strain is referred to as the saturation stress. Cyclic hardening refers to the phenomenon in which the stress level between two particular strain limits increases with the number of reversals. Cyclic softening, as opposed to cyclic hardening, is associated with a decrease in the stress amplitude as the number of reversals is increased at a particular strain amplitude. It has been observed that after steel has been worked at a higher strain amplitude, it softens when cycled at a smaller amplitude. The rate of cyclic hardening generally significantly exceeds the rate of softening. Mean stress is defined as the average of the stresses at the peaks of two successive reversals. Mean stress relaxation is observed in steel under cyclic loading. It refers to the phenomenon in which a mean stress, if present, decreases as the number of reversals increases.

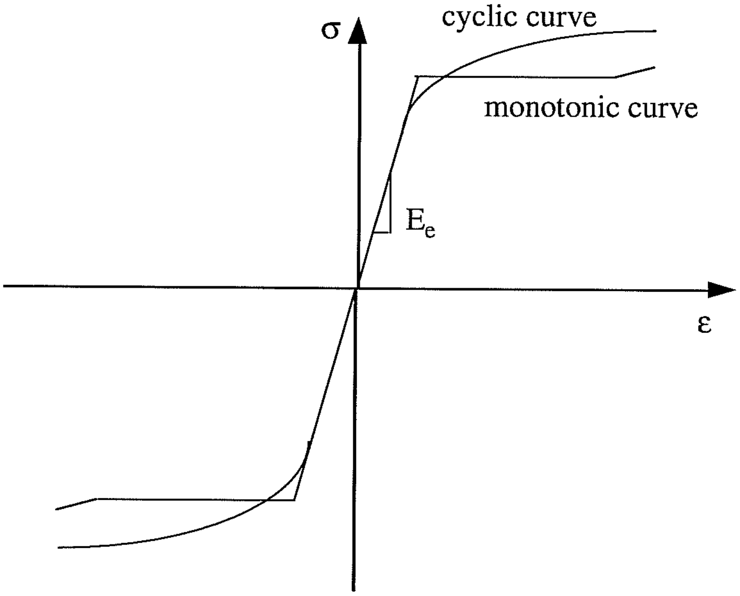

Fig. 3.7: Monotonic and Cyclic Stress-Strain Curves

In Cofie's model three basic cyclic loading parameters are employed to describe cyclic hardening, cyclic softening, and mean stress relaxation. The difference $\Delta\sigma$ between the stress amplitude σ_a of excursion A-B and the corresponding saturation stress σ_s, as shown in Fig. 3.8, is an indication of how far the material is from saturation. The hardening factor F_H describes the rate at which the available hardening $\Delta\sigma$ is used up in each excursion. The softening factor F_S identifies the rate at which the material softens back to the saturation stress if previous cycling has caused a stress amplitude that exceeds the corresponding saturation stress ($\Delta\sigma<0$). Unless the mean stress of an excursion is zero, cyclic hardening or softening is accompanied by mean stress relaxation. Similar to the hardening and softening factors, a mean stress relaxation factor F_R can be defined to describe the rate at which the mean stress relaxes to zero. The main feature of Cofie's model is that these cyclic loading parameters are applied to move the bound line such that the material works its way towards the steady state curve during cyclic deformation.

After any excursion of a loading history (e.g., excursion A-B in Fig. 3.8), a positive and a negative bound exist whose position is a function of the past loading history. One of the two bounds is updated after the excursion in order to account for the hardening or softening and mean stress relaxation that are expected to occur during the next excursion. The procedure for updating the bound line is presented as follows;

i) Whenever load reversal occurs, the mean values and the amplitudes of the current excursion A-B shown in Fig.3.8, are calculated.

$$\sigma_m = 0.5(\sigma_A + \sigma_B) \quad ; \quad \varepsilon_m = 0.5(\varepsilon_A + \varepsilon_B) \tag{3.32a}$$

$$\sigma_a = 0.5|\sigma_A - \sigma_B| \quad ; \quad \varepsilon_a = 0.5|\varepsilon_A - \varepsilon_B| \tag{3.32b}$$

where the subscripts 'm' and 'a' stand for a mean value and an amplitude, respectively.

ii) Calculate the difference between the stress amplitude σ_a and the saturation stress σ_s on the cyclic steady state curve corresponding to the strain amplitude ε_a

$$\Delta\sigma = \sigma_s - \sigma_a \tag{3.33}$$

iii) If $\Delta\sigma>0$, cyclic hardening is predicted to take place in the next excursion. Update the bound by moving it outward by an amount equal to $2F_H\Delta\sigma$, where F_H is the hardening factor.

$$(\sigma_{bl})_{new} = (\sigma_{bl})_{old} - 2F_H\Delta\sigma \tag{3.34}$$

iv) If $\Delta\sigma<0$, cyclic softening is predicted to take place in the next excursion. Update the bound by moving it inward by an amount equal to $2F_S\Delta\sigma$, where F_S is the softening factor.

$$(\sigma_{bl})_{new} = (\sigma_{bl})_{old} - 2F_S\Delta\sigma \tag{3.35}$$

v) Further move the bound line by an amount equal to $F_R\sigma_m$, where F_R is the mean value relaxation factor.

$$(\sigma_{bl})_{new} = (\sigma_{bl})_{new} - F_R\sigma_m \tag{3.36}$$

The initial positive bound for the first excursion (monotonic deformation) is determined by drawing a horizontal line at the end of the monotonic loading to have an intersection with the stress axis, and by rotating the line about its intersection point to have the predetermined slope E_p^{bl} of the bound line. At the first reversal, the negative bound has the intersection at $-\sigma_y$. on the stress axis.

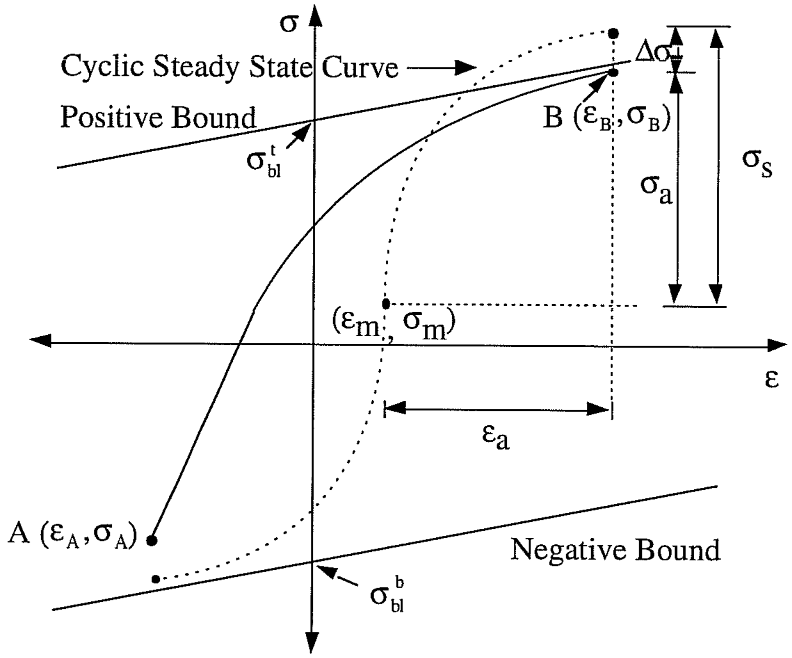

Fig. 3.8: Movement of Bound Line

For the first excursion, the monotonic stress-strain curve is represented by three branches shown in Fig.3.7, and is described by the following equations;

$$\sigma = E_e \varepsilon \qquad \text{for } 0 \le \varepsilon \le \varepsilon_y \tag{3.37a}$$

$$\sigma = \sigma_y \qquad \text{for } \varepsilon_y \le \varepsilon \le \varepsilon_{sh} \tag{3.37b}$$

$$\varepsilon/\varepsilon_y = \sigma/\sigma_y + \left(\sigma/\left(k_m \sigma_y\right)\right)^{n_m} \qquad \text{for } \varepsilon \ge \varepsilon_{sh} \tag{3.37c}$$

The parameters k_m and n_m are obtained from curve fitting to experimental data.

The cyclic steady state curve shown in Fig. 3.7 is obtained from multiple step tests. In a multiple step test, a specimen is subjected to step-wise increasing strain amplitude cycles with a sufficient number of cycles performed at each amplitude to attain a stabilization of peak stresses. The curve can be described by the expression similar to the third branch of the monotonic stress-strain curve as follows.

$$\varepsilon/\varepsilon_y = \sigma/\sigma_y + \left(\sigma/\left(k_c \sigma_y\right)\right)^{n_c} \tag{3.38}$$

in which the parameters k_c and n_c are obtained from curve fitting.

A hysteresis curve, which describes the stress-strain response for an excursion, consists of the elastic range with a stiffness equal to the monotonic elastic stiffness and a nonlinear portion that approaches the stress bound line asymptotically, as shown in Fig. 3.9. The elastic range $\alpha\sigma_y$ is assumed to remain constant for each excursion. A model proposed by Dafalias and Popov is used to describe the nonlinear portion of the hysteresis curve. In this model the bound line is used as an asymptote that is approached by the hysteresis curve. In the nonlinear range, the plastic modulus is defined by the following equation

$$E_p = \frac{\partial\sigma}{\partial\varepsilon_p} = E_p^{bl}\cdot\left[1+\hat{h}\cdot\delta/(\delta_{in}-\delta)\right] \qquad (3.39)$$

in which E_p is the plastic modulus; ε_p is the plastic strain; E_p^{bl} is the plastic modulus associated with the bound; δ_{in} is the distance from the yield point to the bound, measured along the stress axis (see Fig.3.9); δ is the distance between the instantaneous stress and the bound; $\hat{h}$ is the shape factor chosen to fit the experimental data. This equation describes a plastic modulus that decreases continuously in the manner shown in Fig. 3.9. The relationship between the tangent modulus E_t and the plastic modulus E_p is given by the equation

$$1/E_t = 1/E_e + 1/E_p \qquad (3.40)$$

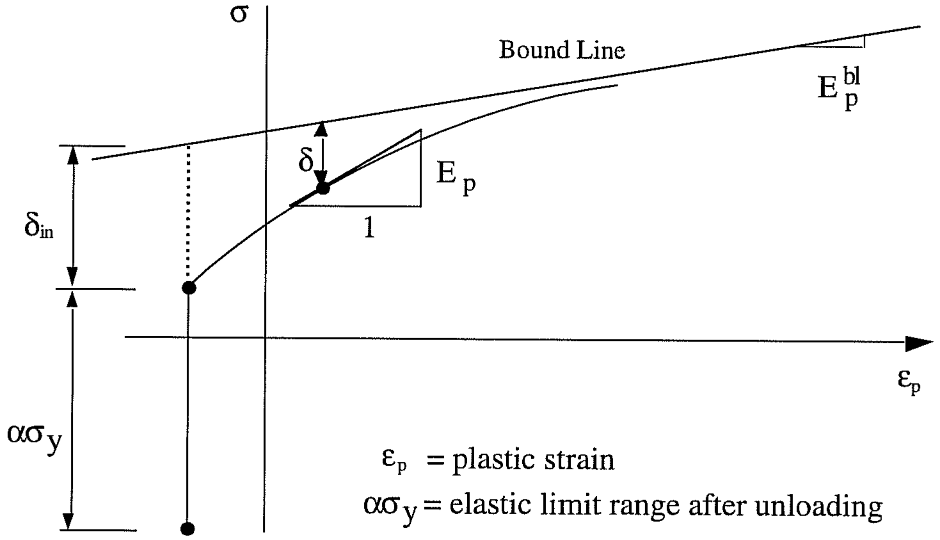

Fig. 3.9: Dafalias-Popov Model for Hysteresis Curve.

Cofie (1985) provided a comparison between the predicted and the experimentally obtained results for a multiple step test, as shown in Fig. 3.10. Cofie also compared his model for several irregular strain histories for which experimental results were available. The comparisons are presented in Figs. 3.11 and 3.12 The agreement is satisfactory in all cases except for the first one or two excursions following the monotonic loading and excursions with small strain amplitudes. Although the predictions at the small amplitudes are not very accurate, the model is able to predict fairly accurately the cyclic response for subsequent large excursions.

The parameters used to obtain the analytical results in Figs. 3.10, 3.11, and 3.12 are listed in Table 3.1. The steel used to generate the experimental data was classified as ASTM A36 steel. Note that the parameters needed for a cyclic stress-strain model cannot be fully determined from a typical monotonic tensile coupon test. Cyclic testing is required.

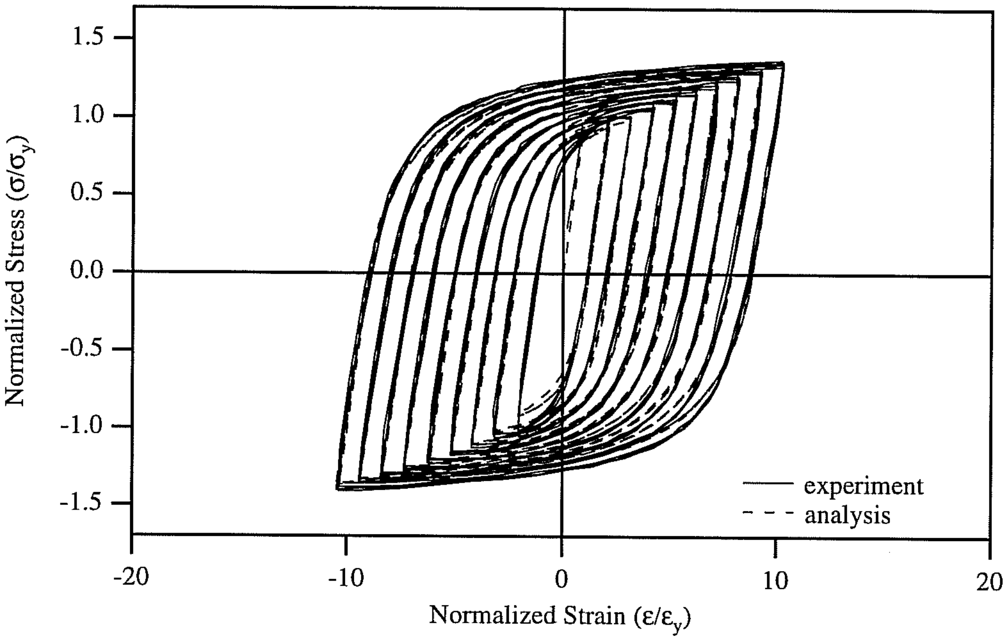

Fig. 3.10: Comparison of Analytical and Experimental Results for Multiple Step Test (Cofie 1985).

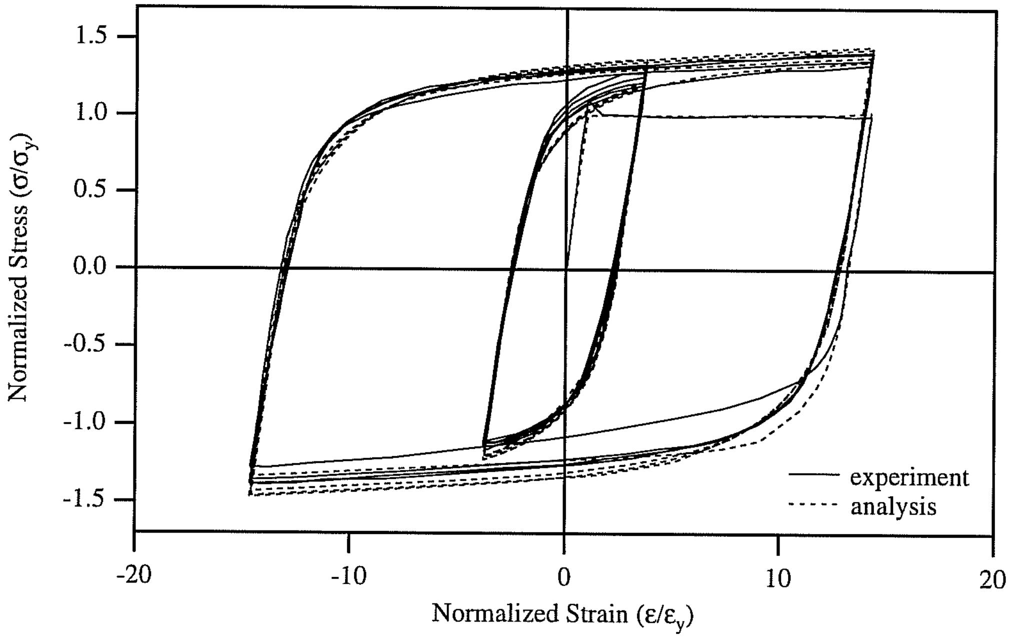

Fig. 3.11: Comparison of Analytical and Experimental Results for Strain History 2 (Cofie 1985).

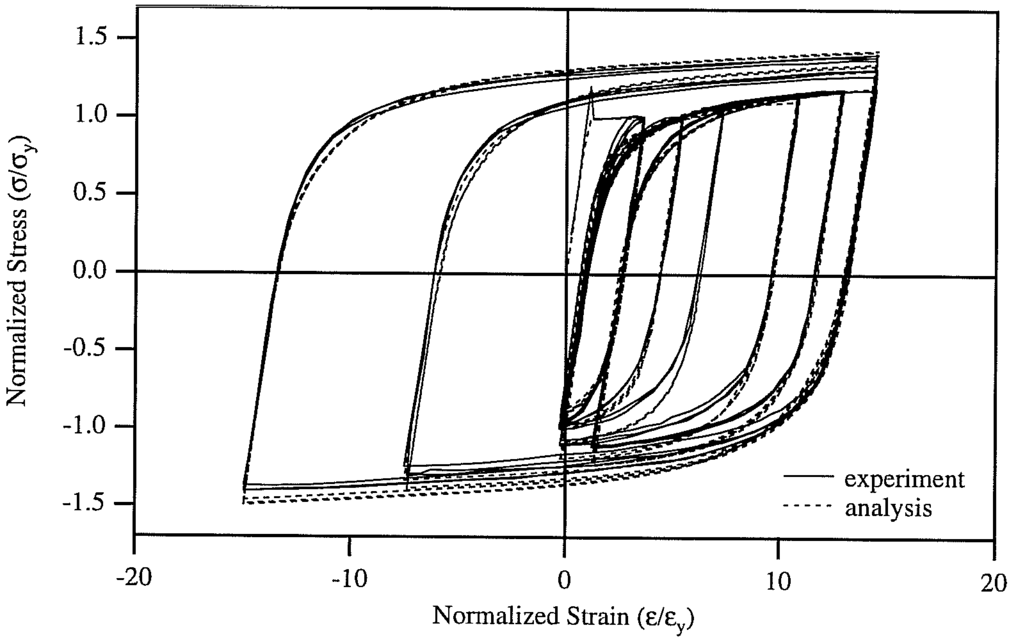

Fig. 3.12: Comparison of Analytical and Experimental Results for Strain History 3 (Cofie 1985).

σ_y	ε_{sh}	E_e	E_p^{bl}	$\hat{h}$	$\alpha\sigma_y$
45.6 ksi	$12\varepsilon_y$	29000 ksi	$0.0075E_p^{bl}$	45	$1.2\sigma_y$

k_m	n_m	k_c	n_c	F_H	F_S	F_R
0.51	0.23	0.9	0.19	0.45	0.07	0.05

Table 3.1: Stress-Strain Parameters for Cofie's Model

Chapter 4: CALIBRATION OF BEAM-COLUMN ELEMENT

4.1 Introduction

In this chapter the action-deformation relationships, used in the development of the multi-linear hinge model in Chapter 2 are calibrated to experimental results and to results predicted by the fiber model. In the multi-linear hinge model, the action-deformation relationships are required for each of two limiting states, i.e., the virgin state and the saturated state, shown in Fig. 2.13. To account for the transition from the virgin state to the saturated state, a weighting factor is determined by calibration to results predicted by the fiber model under various cyclic displacement histories.

To verify the multi-linear hinge model employing the calibrated action-deformation relationships, the model is applied to the analyses of beams and columns of bare steel frames in this chapter. In Chapter 7, the model will be applied to the analyses of subassemblages, bare steel frames and frames with composite concrete slabs. To investigate the performance of the model as a bare steel beam element, the model is compared to available experimental data for test specimens subjected to no axial force. The model is also applied to cantilever beams subjected to combined flexure and axial force, to investigate the performance of the model as a bare steel column element. The results predicted by the multi-linear hinge model are compared with results predicted by the fiber model. Second order effects are included in the analyses of columns by both the multi-linear hinge model and fiber model.

4.2 Calibration of Multi-Linear Hinge Model for Members Without Axial Force

In this section, the response of the multi-linear hinge model is investigated for modelling bare steel beams without axial force. The hinge model response will be calibrated against or compared with experimental results. Since the amount of experimental data is limited, hinge model response will also be compared with fiber model response predictions. For these comparisons, the fiber model will first be calibrated against experimental results. The calibrated fiber model will then be used to predict beam response under loading conditions for which no experimental data is available.

Available experimental data suggests that the cyclic inelastic response of beams in steel moment frames is dependent on the beam-to-column connection details. This study will consider two common connection types: fully welded beam-to-column connections and welded flange-bolted web connections. In fully welded connections, both beam flange and the beam web are welded directly to the column. In the welded flange-bolted web connection, the beam flanges are welded directly to the column. The beam web, however, is bolted to a single plate shear tab, which is in turn welded to the column. In some cases, additional fillet welds are provided between the beam web and the shear tab to supplement the bolts. In the following sections, both connection types will be considered. Response predictions will be investigated for cantilever beams subjected to monotonic and cyclic tip loads. The cantilever was chosen because the majority of experiments have been conducted on cantilever type test specimens. Model predictions for more complex subassemblages and for complete frames will be investigated later in this report.

4.2.1 Calibration to Experimental and Analytical Results for Fully Welded Connections

The parameters that control the response of the multi-linear hinge model were calibrated against experimental results and fiber model predictions for cantilevers with fully-welded end connections. Parameters for the virgin state were calibrated to the monotonic responses of cantilever beams. Parameters for the saturated state were calibrated to the cyclic steady state load-displacement curves obtained from symmetric cyclic loading experiments. The cyclic steady state load-displacement curve is defined as the curve through the locus of tips of the peak loads at various displacement amplitudes.

The calibration process resulted in the multi-linear hinge model parameters listed in Table 4.1. In this table, M_p and K_{me} are the section plastic moment and the elastic flexural stiffness of the cantilever beam (moment per unit rotation). The superscrips v and s refer to the virgin and saturated state models. The parameters listed in Table 4.1 were chosen to provide the best match, on average, to the experimental or fiber model results used in the calibration process. In the remainder of this section, the response of the multi-linear hinge model, using the parameters in Table 4.1, is compared with experimental and fiber model results.

The moment-rotation relationship for the virgin state is presented in terms of the tip load-displacement relationship of a W21x57 cantilever, similar to Engelhardt Specimen 8 (Engelhardt 1992), in Fig. 4.1. To obtain the prediction made by the fiber model, the yield stress of specimen 8 shown in Table 4.2 is used, along with the monotonic stress-strain parameters listed in Table 3.1. From Fig. 4.1, it can be seen that even though there is some difference between the multi-linear hinge and fiber models in the vicinity of initial yielding, the predictions made by the hinge model are reasonable when the simplicity of the model is considered.

M^v_{y1}	M^v_{y2}	M^v_{y3}	M^s_{y1}	M^s_{y2}	M^s_{y3}
$1.0M_p$	$1.1M_p$	$1.2M_p$	$0.8M_p$	$1.1M_p$	$1.25M_p$
K^v_{m1}	K^v_{m2}	K^v_{m3}	K^s_{m1}	K^s_{m2}	K^s_{m3}
$0.02K_{me}$	$0.01K_{me}$	$0.001K_{me}$	$0.3K_{me}$	$0.1K_{me}$	$0.03K_{me}$

Table 4.1: Parameters Defining Moment-Rotation Relationships for Fully Welded Connections.

Specimen	Beam Section	Beam Length	Flange Yield Stress	Web Yield Stress
Popov # 2	W18X50	83”	45 ksi	47 ksi
Popov # 7	W24X76	83”	36 ksi	37 ksi
Tsai # 9	W18X46	62.9”	37.2 ksi	41.5 ksi
Tsai # 11	W21X44	63.2”	37.2 ksi	41.5 ksi
Engelhardt # 8	W21X57	96”	38.4 ksi	36.5 ksi

Table 4.2: Material Properties and Beam Sections of Test Specimens with Fully Welded Connections (Popov 1972, Tsai 1988, and Engelhardt 1992)

In this work, no attempt is made to further evaluate the monotonic predictions made by the multi-linear hinge model, because the cyclic behavior of the hinge model is the primary concern of this research. The parameters for the virgin state shown in Table 4.1 are mainly of interest to define member response in the early inelastic stages of a cyclic loading history.

In the remainder of this chapter, the cyclic loading predictions made by the multi-linear hinge model are compared with experimental data or with fiber model predictions. For fiber model comparisons, the same yield stress is used in the multi-linear hinge model (to compute M_p) as for the fiber model. The cyclic stress-strain parameters for the fiber model were chosen by calibration to the cyclic experimental response of Engelhardt Specimen 8. Based on this calibration, the resulting parameters are the same as those listed in Table 3.1, except that the cyclic steady state curve parameter, n_c, is taken as 0.18. The predictions made by the fiber model are compared with the experimental response of specimen 8 in Fig. 4.2.

Several researchers such as Popov (1972), Tsai (1988), and Engelhardt (1992) conducted cyclic tests on large scale cantilever beams to investigate the performance of fully welded connections. To compare the cyclic moment-rotation relationships of the developed hinge model with experimental results, the hinge model is applied to test specimens with fully welded connections. The test beams are attached to a heavy column stub, and a portion of the beam tip displacement is due to column deformations. For that case, the analytical results are compared with the test data that are obtained by subtracting the beam tip displacement due to the column deformations from the original experimental data. The material properties and beam sections of the test specimens with all welded connections are listed in Table 4.2.

In Figs. 4.3 and 4.4, the transverse load-displacement relationships obtained by Kanaan's bilinear model are compared with the experimental results. As expected, the bilinear model can not provide the smooth transition of stiffness from the elastic range to the strain hardening range and underestimates the strength considerably.

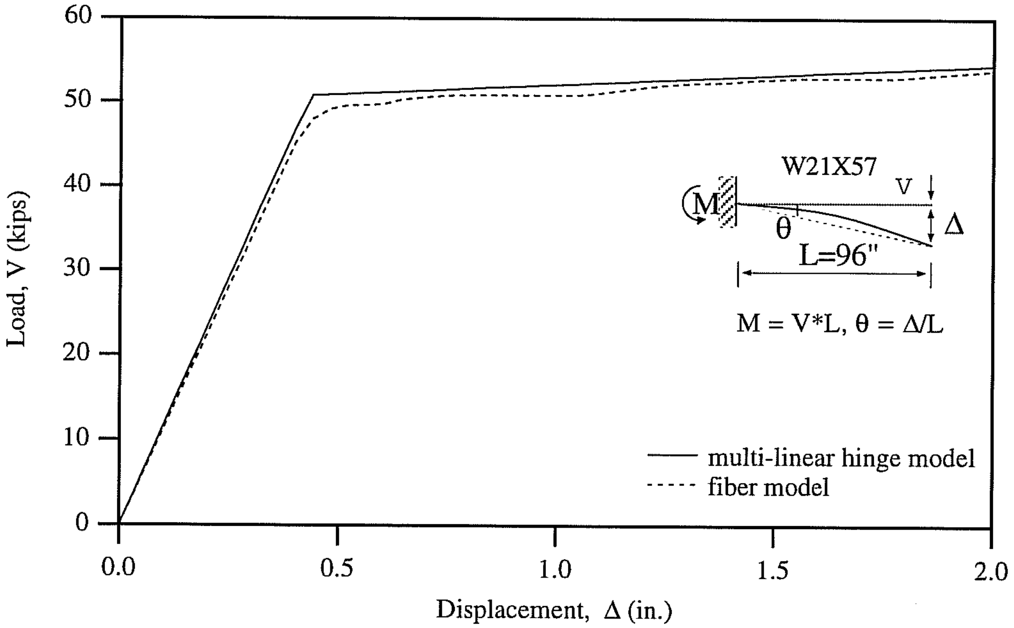

Fig. 4.1: Comparison of Multi-Linear Hinge Model and Fiber Model for Monotonic Vertical Loading.

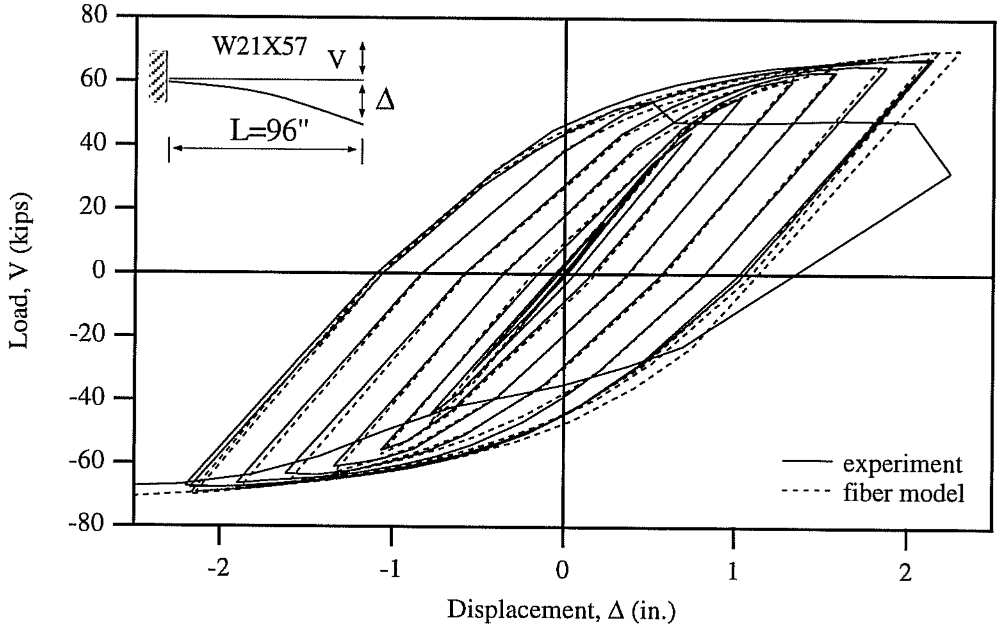

Fig. 4.2: Comparison of Experimental Results and Predictions Made by the Fiber Model for Engelhardt Specimen 8.

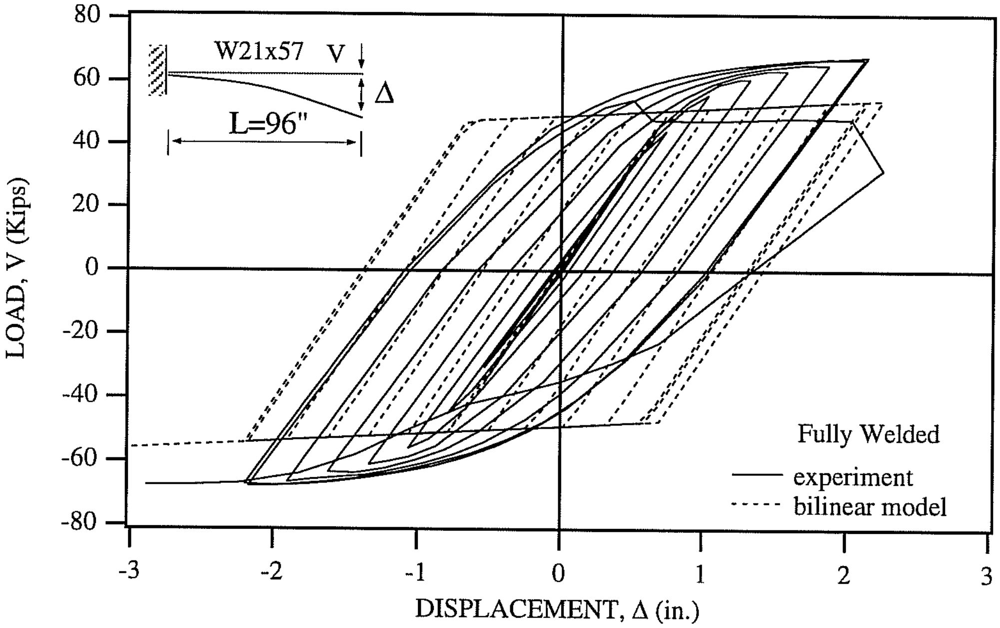

Fig. 4.3: Comparison of Experimental Results and Predictions Made by Bilinear Model for Engelhardt Specimen 8.

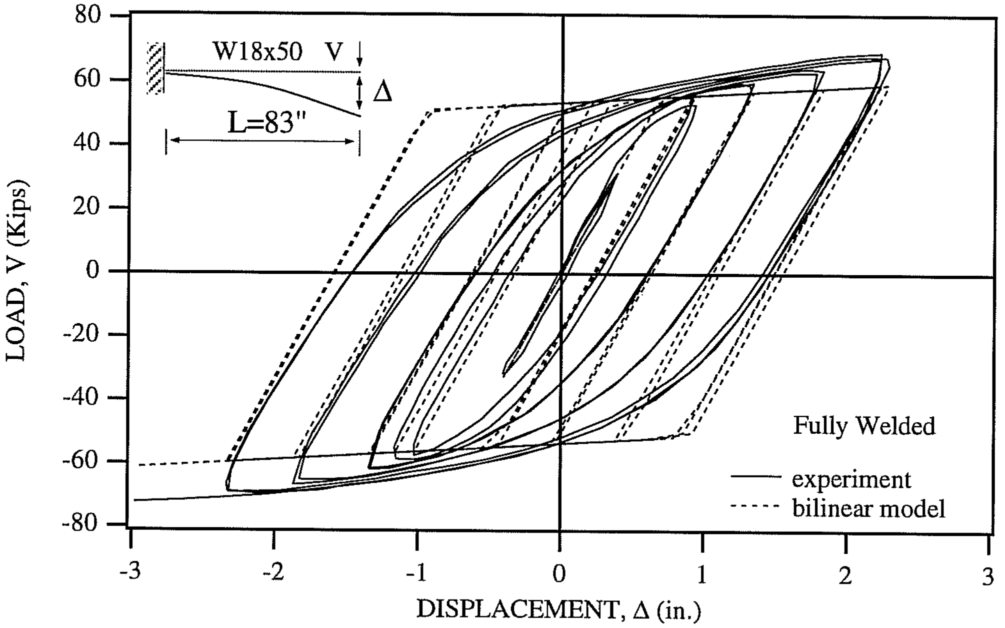

Fig. 4.4: Comparison of Experimental Results and Predictions Made by Bilinear Model for Popov Specimen 2.

In Figs. 4.5 and 4.6, the results predicted by the multi-linear hinge model are compared with the experimental results by Tsai. The match is good before local buckling occurs. In Fig. 4.7, comparison is made with Popov Specimen 2. From this figure, it can be seen that the match between the analytical results and test results is satisfactory. The comparison of the analytical and experimental results for Popov Specimen 7 is shown in Fig. 4.8. The match is good on the negative load side, but the model underestimates the strength on the positive side. Note that test results are not symmetrical on the positive and negative sides. Figure 4.9 shows the comparison of the responses obtained by the model and test for Engelhardt Specimen 8. Even though the model underestimates the strength, the agreement between model prediction and test results is reasonable.

The developed multi-linear hinge model has been compared to five specimens with fully welded connections to investigate the cyclic moment-rotation relationships. When compared to the bilinear hinge model, the multi-linear hinge model showed significantly better agreement. Note that in the above comparisons, the same model parameters (Table 3.1) were used in each case. For any one of these five cases, better agreement between analysis and experiment would have been possible by tuning the model parameters to match the specific experimental result. Such a process, however, may not lead to a broadly applicable model. For modeling a MRF, experimental data will generally not be available for the particular member sizes and frame geometries being modeled. Consequently, the data will not be available to tune model parameters. A single set of model parameters which appear to satisfactorily predict, on average, a broad range of experimental results leads to a more generally applicable and useful model.

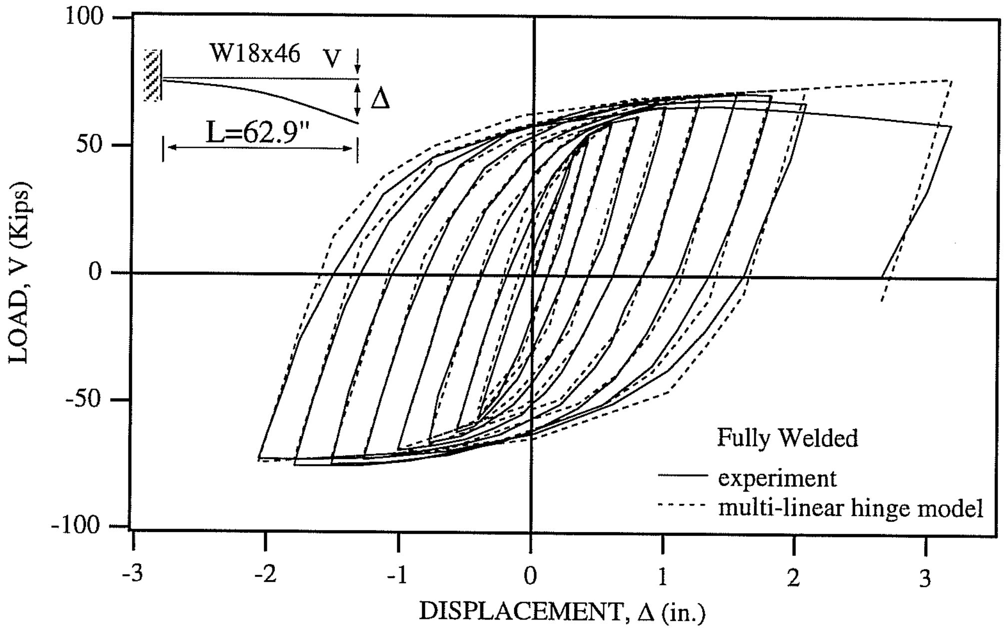

Fig. 4.5: Comparison of Experimental Results and Predictions Made by the Multi-Linear Hinge Model for Tsai Specimen 9.

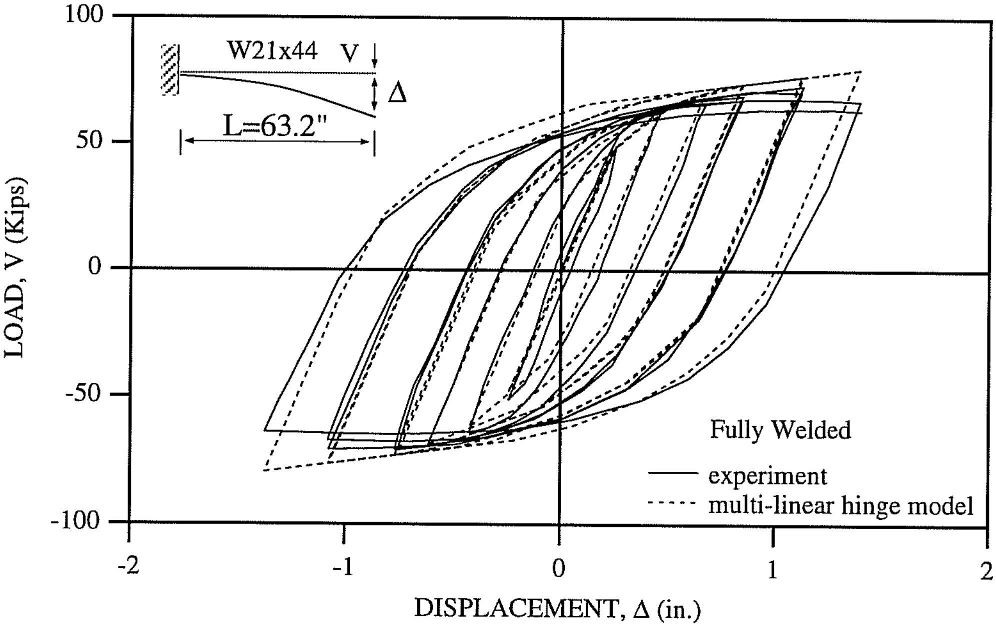

Fig. 4.6: Comparison of Experimental Results and Predictions Made by the Multi-Linear Hinge Model for Tsai Specimen 11.

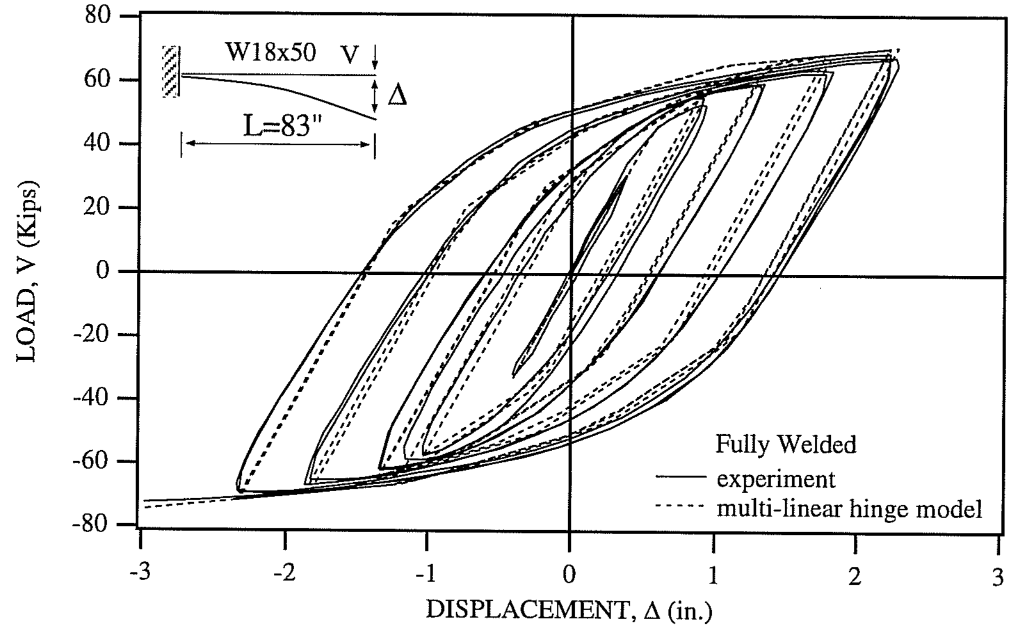

Fig. 4.7: Comparison of Experimental Results and Predictions Made by the Multi-Linear Hinge Model for Popov Specimen 2.

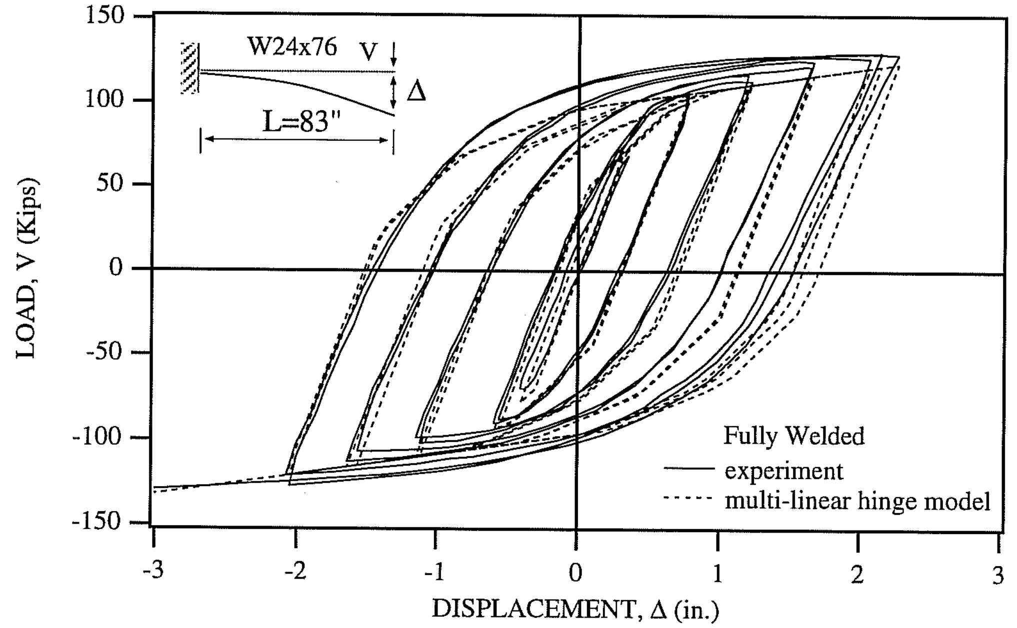

Fig. 4.8: Comparison of Experimental Results and Predictions Made by the Multi-Linear Hinge Model for Popov Specimen 7.

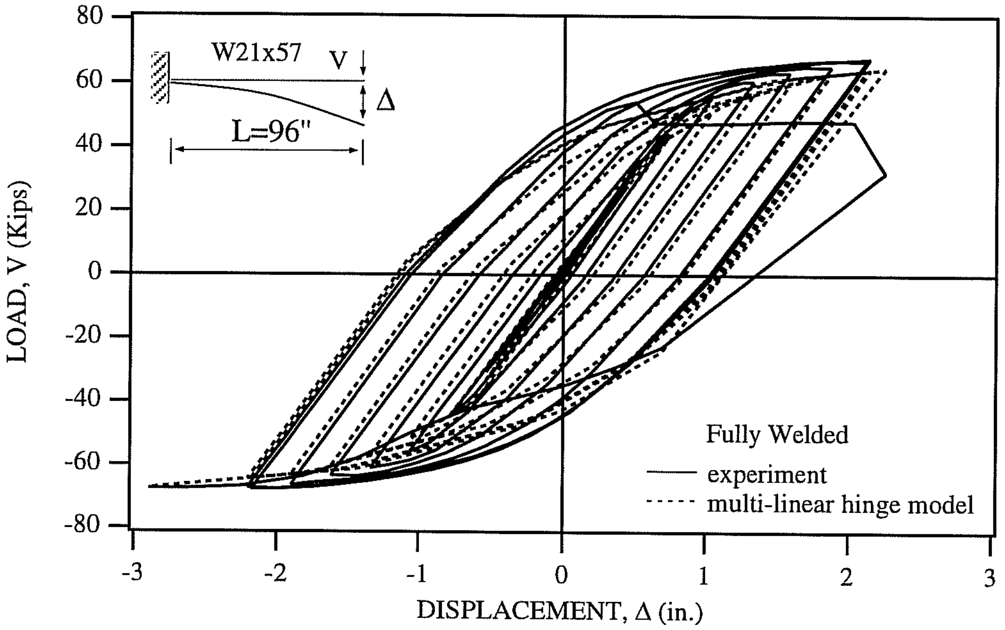

Fig. 4.9 Comparison of Experimental Results and Predictions Made by the Multi-Linear Hinge Model for Engelhardt Specimen 8.

4.2.2 Calibration to Experimental and Analytical Results for Welded Flange-Bolted Web Connections

A connection detail that has been widely used in U.S. practice is the welded flange-bolted web type connection. The strength, stiffness and ductility of this moment connection under cyclic loading has been studied in several experimental investigations using large scale test specimens (Popov 1972; Tsai 1988; Engelhardt 1992). The important conclusions that can be drawn by studying the available cyclic test data on welded flange-bolted web details, are presented as follows.

As far as the stiffness is concerned, welded flange-bolted web connections develop slightly smaller stiffness than that of all welded connections. However, the discrepancy is negligible as shown in Figs. 4.10 and 4.11. In this study, therefore, it is assumed that the stiffness of welded flange-bolted web connections can be defined by the stiffness parameters presented in Table 4.1, which are used to describe the moment-rotation relationships of fully welded connections.

It has been shown that connections with bolted webs sometimes develop less ductility and less strength than connections with welded webs. The performance of bolted web connections has been erratic, with some specimens performing well and others performing poorly. The large variability in the experimental observations can perhaps be related to the large number of design and detailing variables that may influence the performance of these connections. The factors which may have an influence on the strength and ductility of the welded flange-bolted web connection, are described in the research report by Engelhardt (1992).

As far as the strength is concerned, it is believed that the relative flexural contribution of the beam web to the full moment capacity of the beam plays an important role on the reduction of strength of bolted web connections when compared to all welded connections. The relative flexural contribution of the web can be evaluated in terms of the ratio Z_f/Z, where Z_f is the plastic modulus of the flanges only and Z is the plastic modulus of the entire beam section. In Figs. 4.10 and 4.11, the experimental data for bolted web connections are compared with those for fully welded connections. From these figures, it can be seen that for the relatively large ratio Z_f/Z=0.75 the strength of the bolted web connection matches well with that of all welded connection. For the smaller ratio Z_f/Z=0.68 the bolted web connection develops noticeably smaller strength than the all welded connection.

Cyclic tests on welded flange-bolted web connections often show little or no yielding of the web, indicating that the bolted web connection does not develop the flexural capacity of the beam web in the vicinity of the connection. To model this phenomenon by using the fiber model, portions of the web area are eliminated in the vicinity of the bolted web connection, as shown in Fig. 4.12. The portion of the web to be eliminated is determined by trial and error such that the analytical results match well with the experimental data. For test specimens with these reduced web areas, the predictions made by the fiber model are compared with the experimental data in Figs. 4.13, 4.14, and 4.15. To investigate the influence of the ratio Z_f/Z on the reduction of strength of the bolted web connection, the analytical results for test specimens without reduced web areas are also obtained by the fiber model and are compared with those for test specimens with reduced web areas in Figs. 4.16, 4.17, and 4.18. From these figures, it appears that for the relatively large ratio Z_f/Z=0.75, the strength of the beam with the reduced web area is essentially the same as that without the reduced web area. However, as the ratio Z_f/Z becomes smaller, the difference between the strengths of beams with and without the reduced web area becomes larger.

To account for this influence of the ratio Z_f/Z on the reduction of strength of the bolted web connection, the moment-rotation relationships for welded flange-bolted web connections are reduced by multiplying the moment-rotation relationships for fully welded connections by an reduction factor *RF*, which is a function of the ratio Z_f/Z. Thus, the yield moments $\mathrm{M}_{\mathrm{yi}}^{\mathrm{bw}}$ to define the moment-rotation relationships for welded flange-bolted web connections, can be written as

$$\mathrm{M}_{\mathrm{yi}}^{\mathrm{bw}} = RF \cdot \mathrm{M}_{\mathrm{yi}}^{\mathrm{fw}} \tag{4.1a}$$

where

$$RF = 1 \qquad \text{for } \frac{Z_f}{Z} \geq 0.75 \tag{4.1b}$$

$$RF = \left(1.6\frac{Z_f}{Z} - 0.2\right) \qquad \text{for } \frac{Z_f}{Z} \leq 0.75 \tag{4.1c}$$

$\mathrm{M}_{\mathrm{yi}}^{\mathrm{fw}}$ = yield moments to define the moment-rotation relationships for fully welded connections shown in Table 4.1.

The reduction factor *RF* is empirically determined from the calibration to the experimental and analytical results.

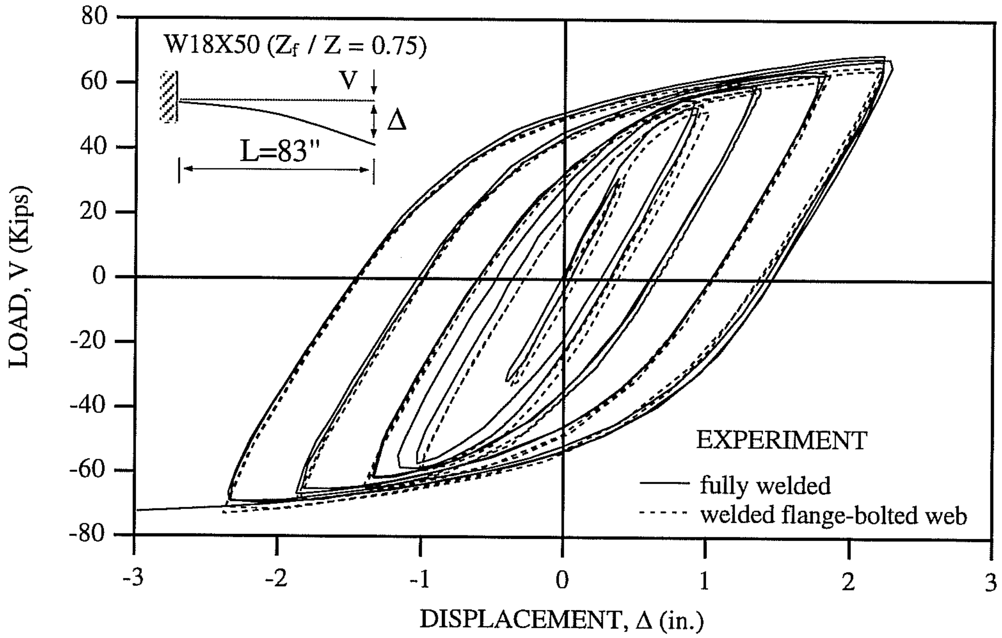

Fig. 4.10: Comparison of the Experimental Results for Popov Specimens 2 and 4.

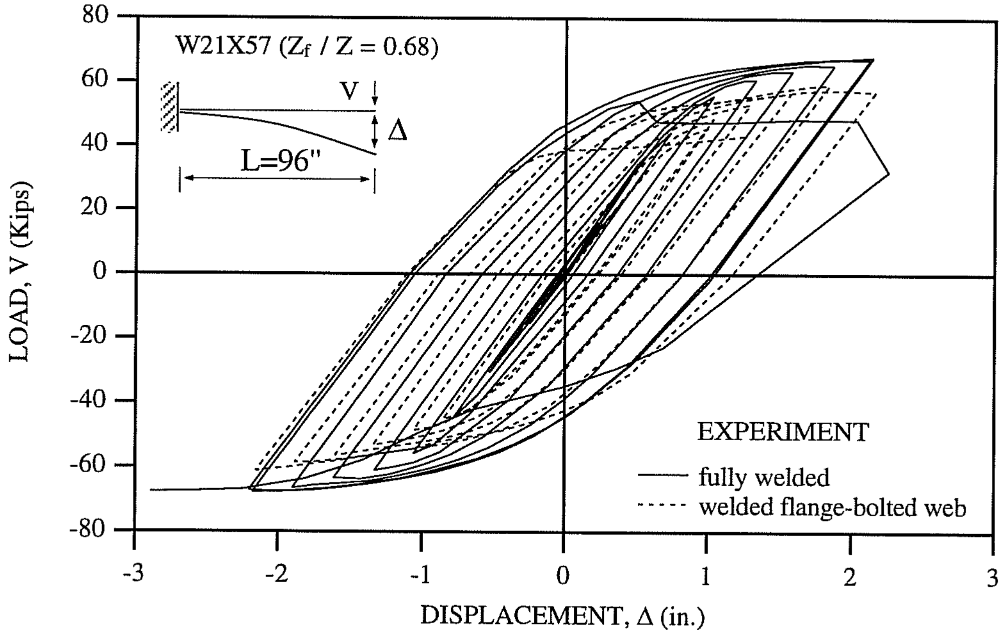

Fig. 4.11: Comparison of the Experimental Responses for Engelhardt Specimens 8 and 6.

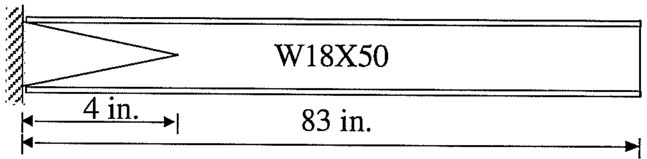

a) Popov Specimen #4 ($Z_f/Z=0.75$)

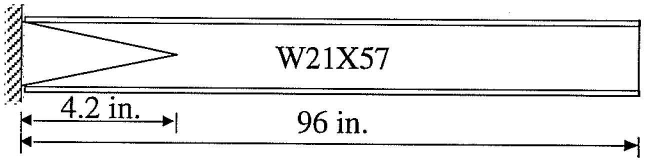

b) Engelhardt Specimen #6 ($Z_f/Z=0.68$)

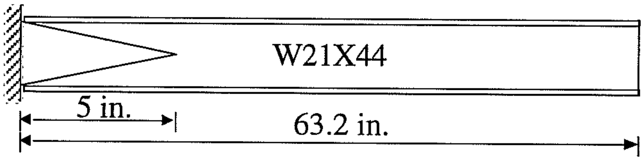

c) Tsai Specimen #18 ($Z_f/Z=0.62$)

Fig 4.12: Test Specimens with the Reduced Web Area

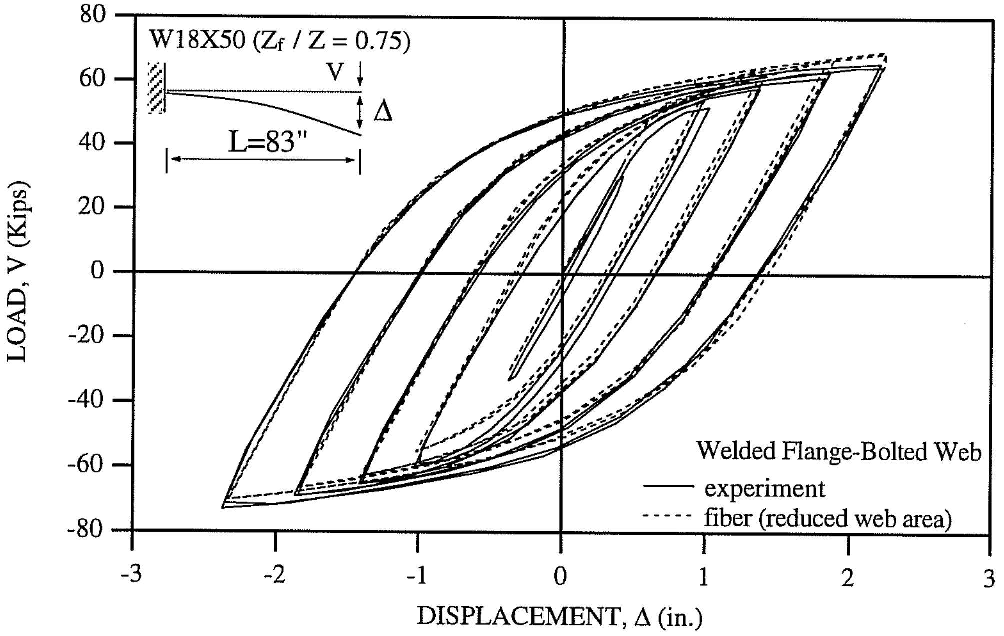

Fig. 4.13: Comparison of Experimental Results and Predictions Made by the Fiber Model for Popov Specimen 1.

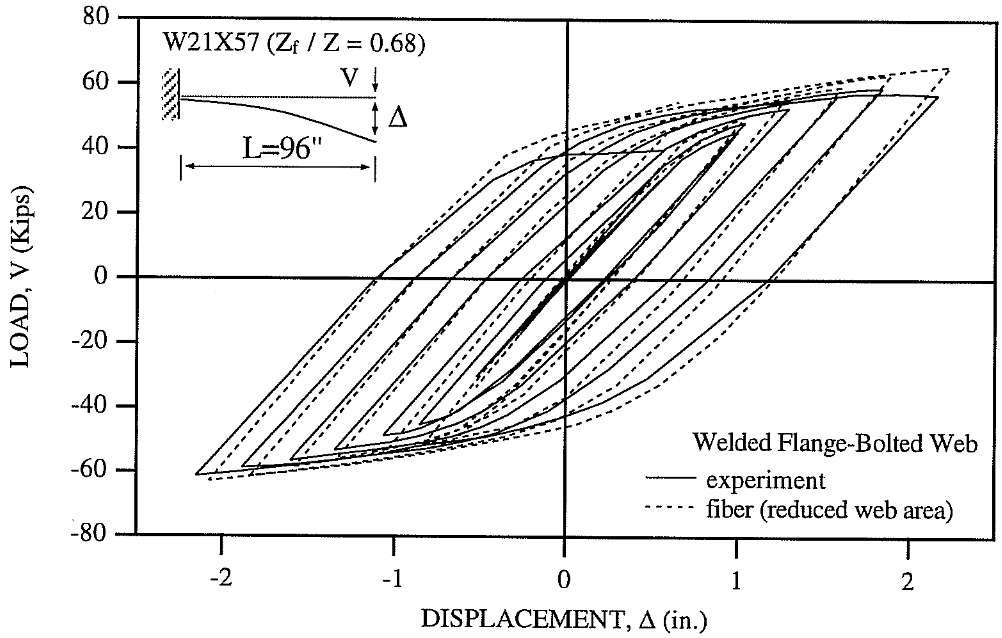

Fig. 4.14: Comparison of Experimental Results and Predictions Made by the Fiber Model for Engelhardt Specimen 6.

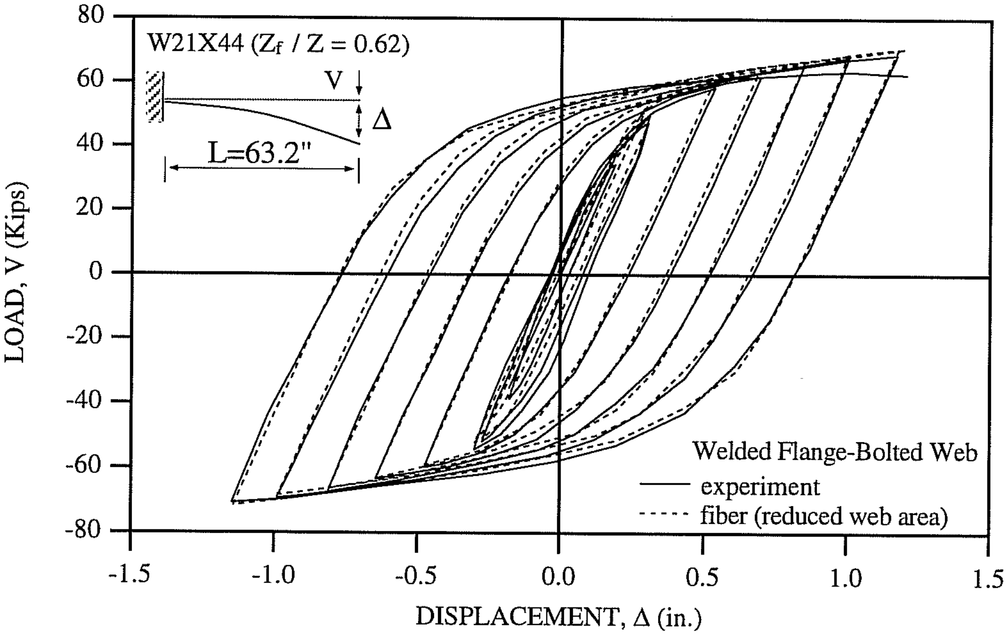

Fig. 4.15: Comparison of Experimental Results and Predictions Made by the Fiber Model for Tsai Specimen 18.

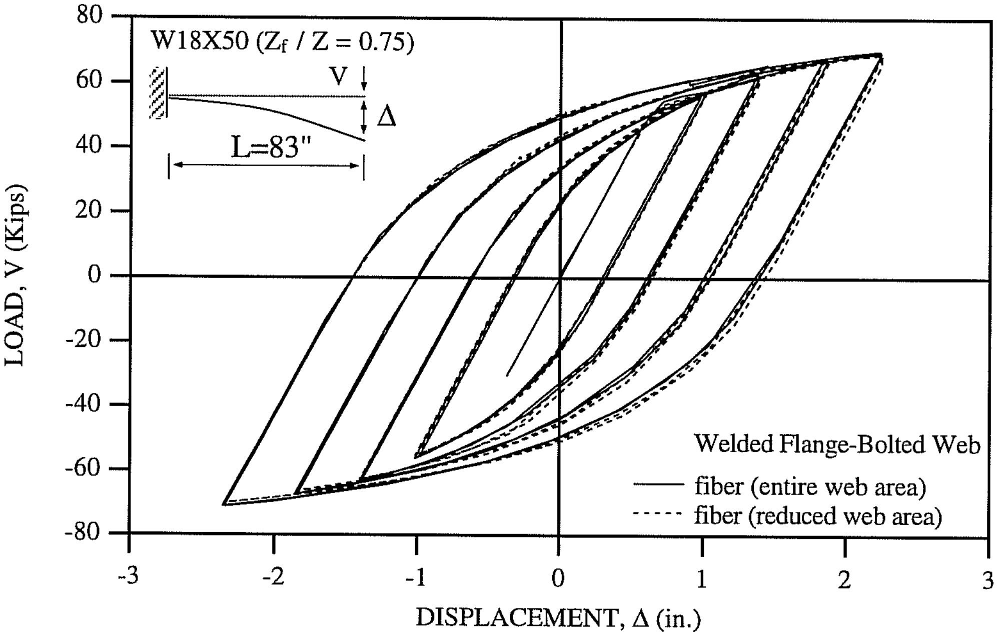

Fig. 4.16: Comparison of the Predictions Made by the Fiber Model for Popov Specimen 1 With and Without the Reduced Web Area.

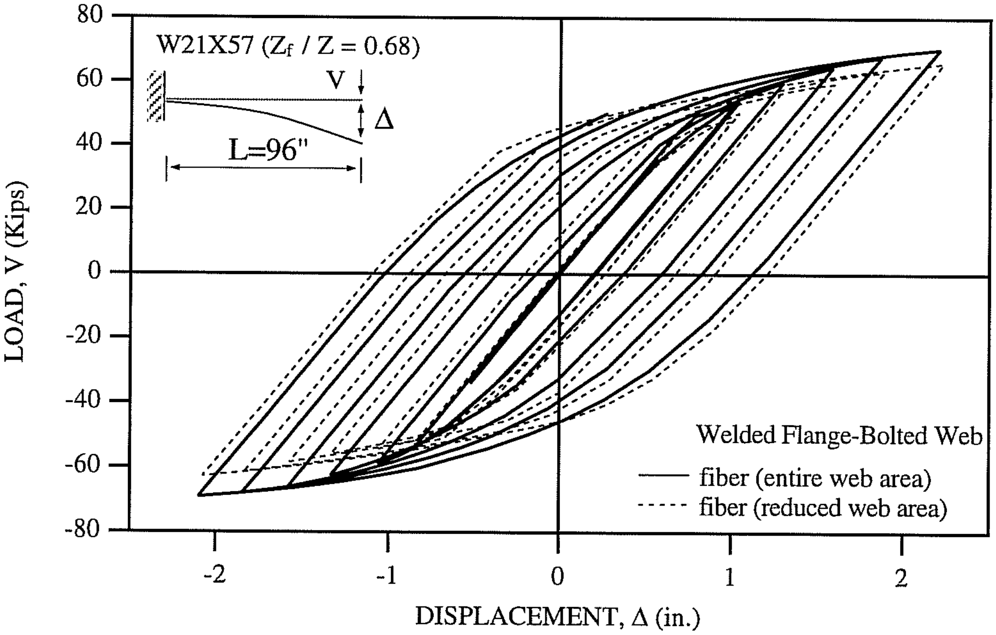

Fig. 4.17: Comparison of the Predictions Made by the Fiber Model for Engelhardt Specimen 6 With and Without the Reduced Web Area.

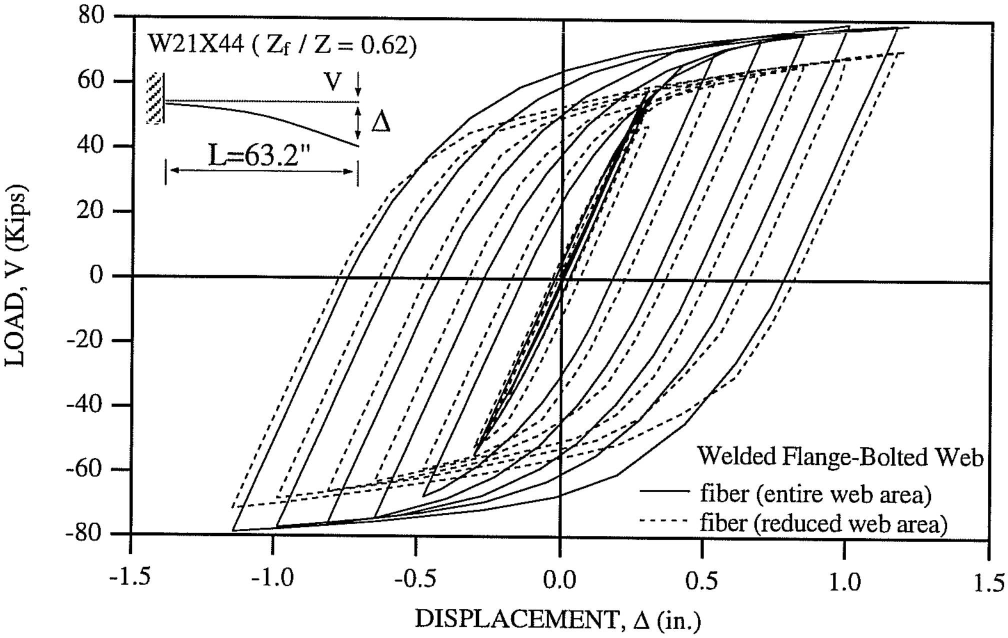

Fig. 4.18: Comparison of the Predictions Made by the Fiber Model for Tsai Specimen 18 With and Without the Reduced Web Area.

Several researchers (Popov 1972; Tsai 1988; Engelhardt 1992) conducted cyclic tests on large scale cantilever beams to investigate the performance of welded flange-bolted web connections. To compare the cyclic moment-rotation relationships for welded flange-bolted web connections of the developed model with experimental data, the developed model is applied to test specimens with welded flange-bolted web connections. The material properties and beam sections of the test specimens with welded flange-bolted web connections are presented in Table 4.3.

In Figs. 4.19 and 4.20, the transverse load-displacement relationships obtained by the bilinear hinge model are compared with the experimental data. As expected, the bilinear model can not provide the smooth transition of stiffness from the elastic range to strain hardening range. Further, for low values of Z_f/Z, the bilinear model may overestimate strength.

Specimen	Beam Section	Beam Length	Flange Yield Stress	Web Yield Stress
Popov # 1	W18X50	83”	45 ksi	47 ksi
Popov # 4	W18X50	83”	45 ksi	47 ksi
Popov # 5	W24X76	83”	36 ksi	37 ksi
Popov # 6	W24X76	83”	36 ksi	37 ksi
Tsai # 17	W18X35	63.2”	46.3 ksi	55.7 ksi
Tsai # 18	W21X44	63.2”	42 ksi	42 ksi
Engelhardt # 5	W18X60	96”	40.9 ksi	43 ksi
Engelhardt # 6	W21X57	96”	38.4 ksi	36.5 ksi

Table 4.3: Material Properties and Beam Sections of Test Specimens with Welded Flange-Bolted Web Connections

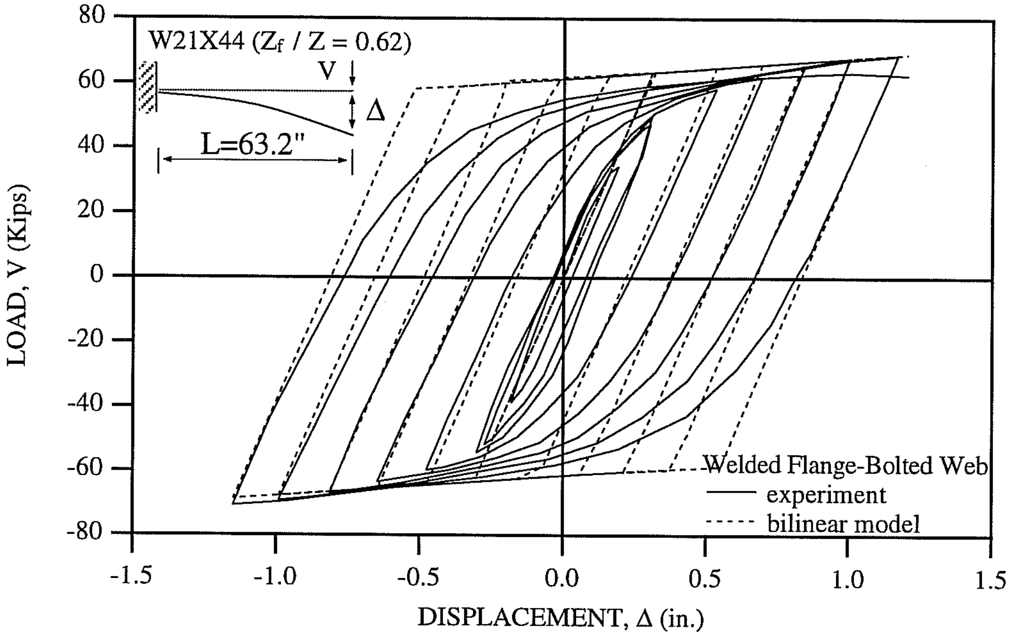

Fig. 4.19: Comparison of Experimental Results and Predictions Made by Bilinear Model for Popov Specimen 4.

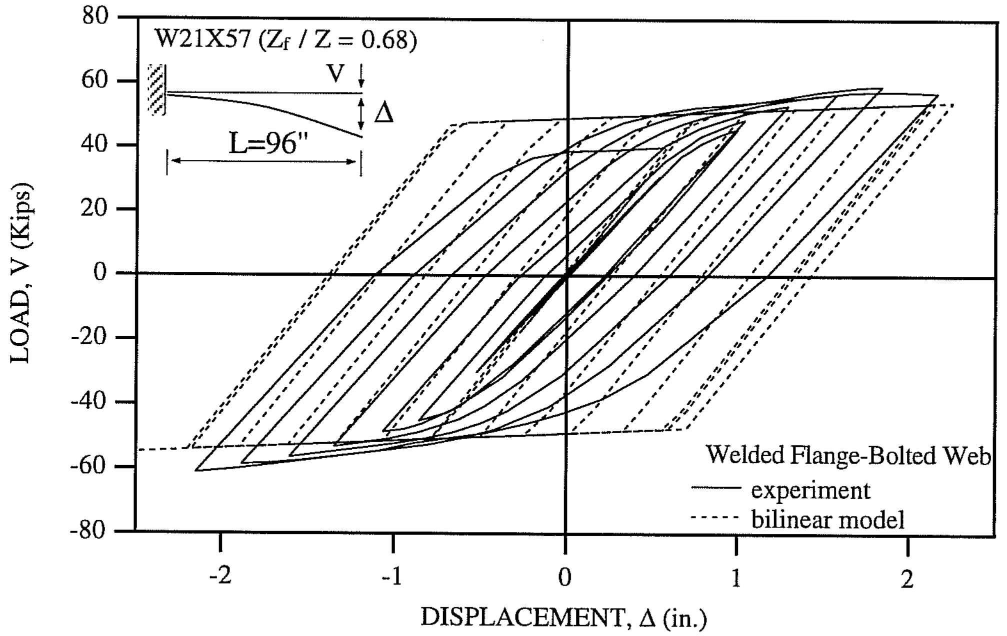

Fig. 4.20: Comparison of Experimental Results and Predictions Made by Bilinear Model for Engelhardt Specimen 6.

In Figs. 4.21 through 4.28, the predictions made by the developed model are compared with the experimental responses. The analytical responses for Popov Specimens 1 and 4 are plotted against the experimental results in Figs. 4.21 and 4.22. Popov Specimens 1 and 4 use the same W18X50 (Z_f/Z=0.75) wide flange section. The only difference between the specimens 1 and 4 is that five 7/8" diameter A325 bolts are used in web connection of specimen 1, whereas four 3/4" diameter A325 bolts are used in specimen 4. Although the model can not account for the difference of the beam web connection details, the correlation of the analytical and experimental results is reasonable. For these specimens, the same yield moments as those for all welded connections are employed in the developed model because the ratio Z_f/Z has the relatively large value of 0.75. The analytical results for Popov Specimens 5 and 6 are compared with the experimental data in Figs. 4.23 and 4.24. Popov Specimens 5 and 6 use the same W24X76 (Z_f/Z=0.72) wide flange section, but employ different beam web connection details. The match of the analytical and experimental results for Popov Specimen 5 is reasonable. However, for Popov Specimen 6 the developed model overestimates the strength on the positive load side.

In Figs. 4.25 and 4.26 the correlation of the predictions made by the developed model and the test results for Tsai Specimens 17 and 18 is presented. Tsai Specimens 17 and 18, respectively, use wide flange sections W18X35 (Z_f/Z=0.66) and W21X44 (Z_f/Z=0.62). From these figures, it can be seen that the match between the analytical results and test results is good.

The comparison of the analytical and experimental results for Engelhardt Specimens 5 and 6 is shown in Figs. 4.27 and 4.28. Engelhardt Specimens 5 and 6, respectively, use wide flange sections W18X60 (Z_f/Z=0.76) and W21X57 (Z_f/Z=0.68). For Specimen 5, the same yield moments as those for all welded connections are employed in the developed model because the ratio Z_f/Z has the relatively large value of 0.76. From these figures, it can be found that the match is satisfactory.

The developed model has been applied to eight specimens with welded flange-bolted web connections to investigate the cyclic moment-rotation relationships. When compared to the bilinear model, the developed multi-linear hinge model showed significantly better performance. Reasonable agreement has been established between model predictions and test results. As before, the agreement has been achieved using a single set of model parameters.

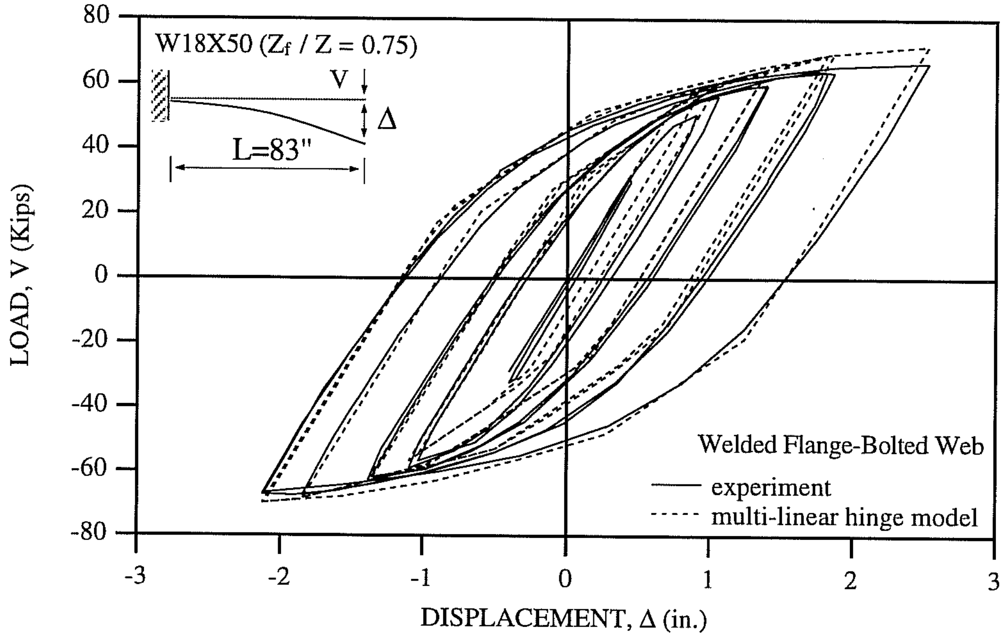

Fig. 4.21: Comparison of Experimental Results and Predictions Made by the Multi-Linear Hinge Model for Popov Specimen 1.

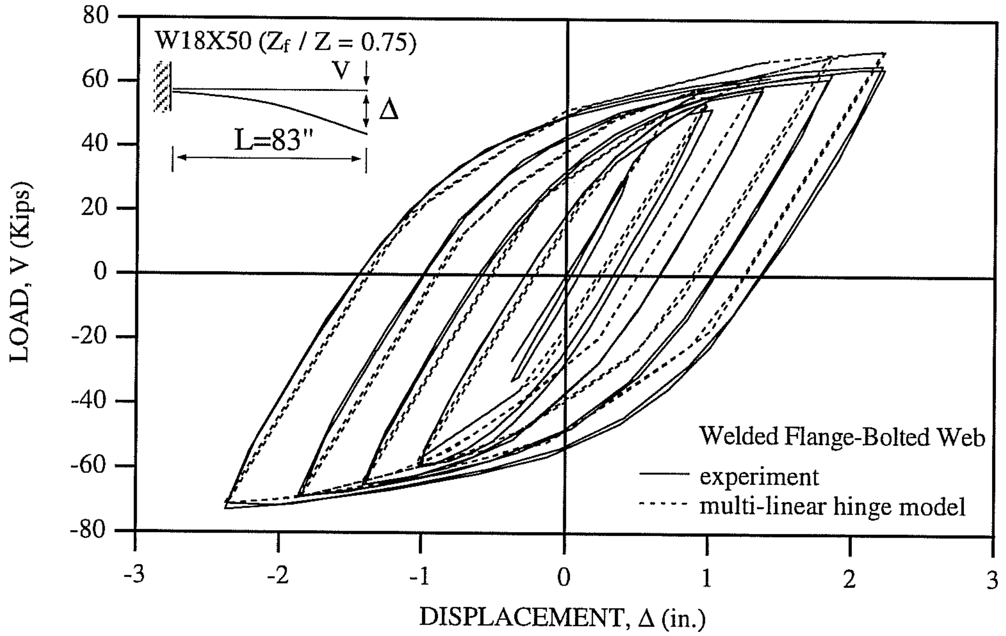

Fig. 4.22: Comparison of Experimental Results and Predictions Made by the Multi-Linear Hinge Model for Popov Specimen 4.

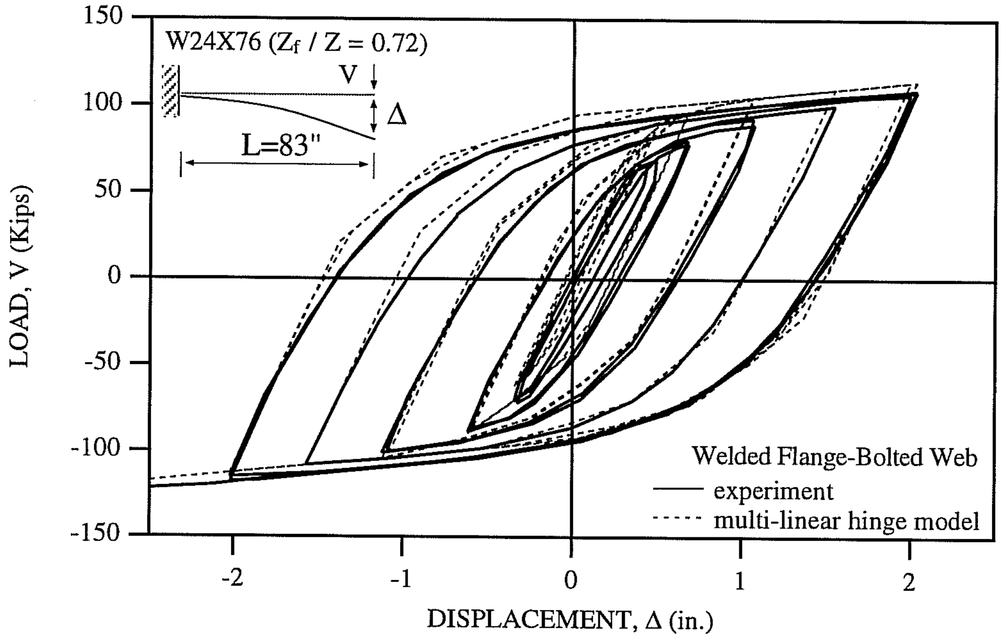

Fig. 4.23: Comparison of Experimental Results and Predictions Made by the Multi-Linear Hinge Model for Popov Specimen 5.

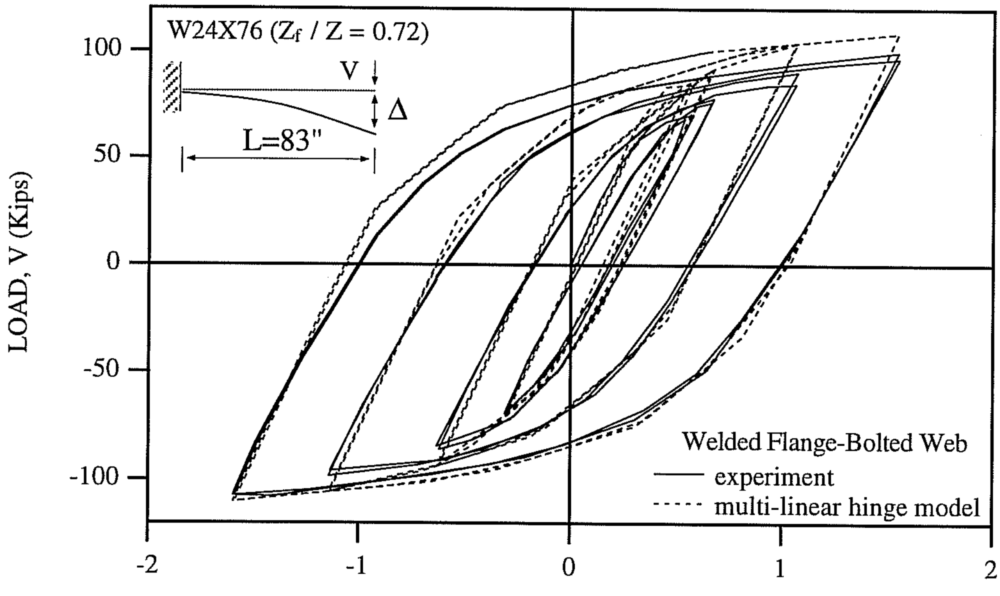

Fig. 4.24: Comparison of Experimental Results and Predictions Made by the Multi-Linear Hinge Model for Popov Specimen 6.

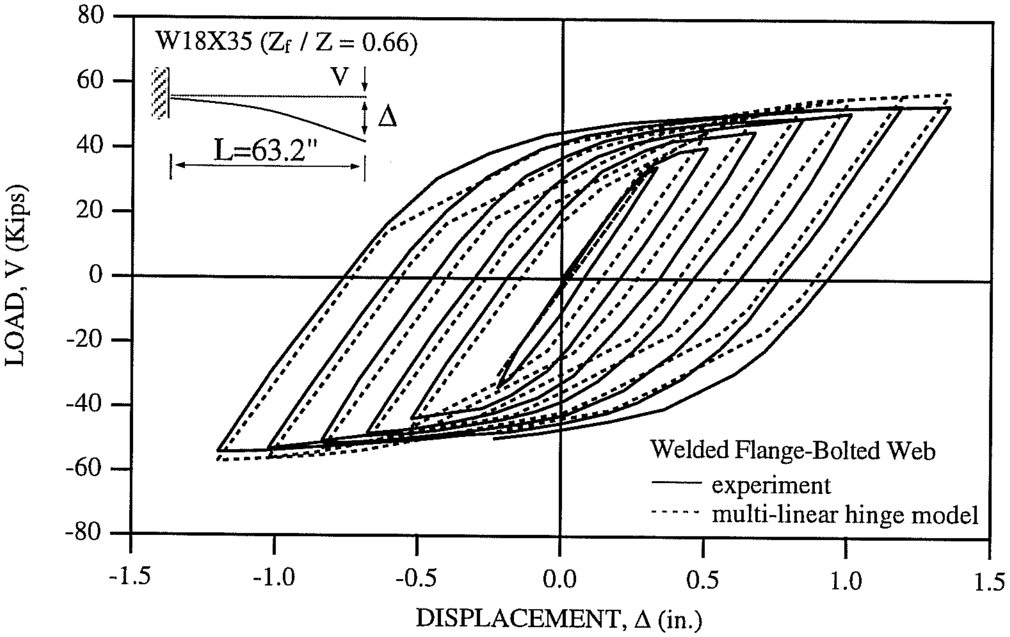

Fig. 4.25: Comparison of Experimental Results and Predictions Made by the Multi-Linear Hinge Model for Tsai Specimen 17.

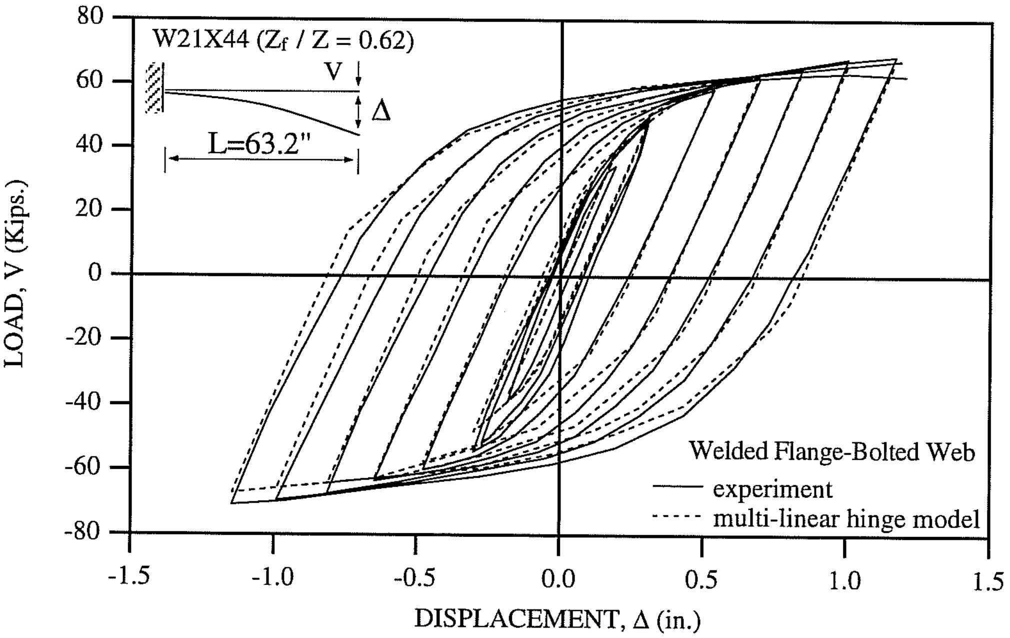

Fig. 4.26: Comparison of Experimental Results and Predictions Made by the Multi-Linear Hinge Model for Tsai Specimen 18.

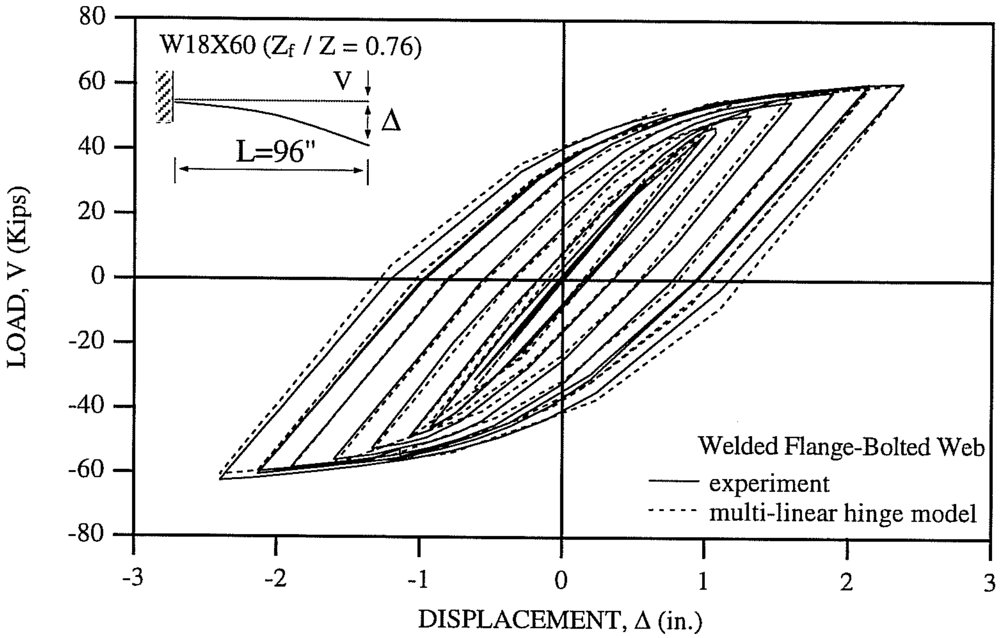

Fig. 4.27: Comparison of Experimental Results and Predictions Made by the Multi-Linear Hinge Model for Engelhardt Specimen 5.

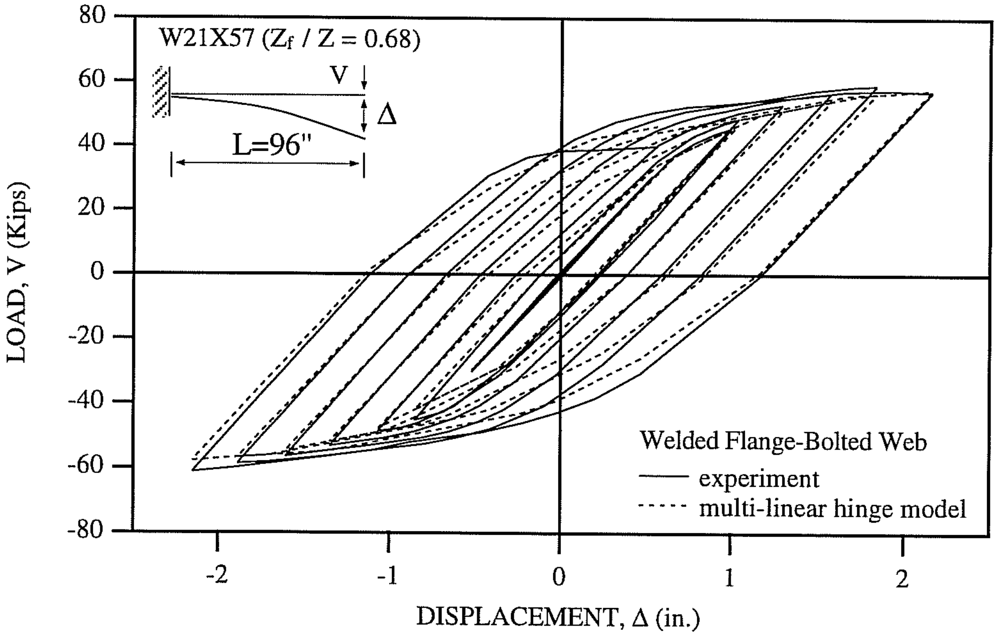

Fig. 4.28: Comparison of Experimental Results and Predictions Made by the Multi-Linear Hinge Model for Engelhardt Specimen 6.

4.3 Weighting Factor

To account for general cyclic behavior, the transition from the virgin state to the fully saturated state is controlled by a weighting factor (Eq.2.48), which is based on the accumulated plastic rotation. This weighting factor is empirically determined from calibration to experimental results and analytical results obtained by the fiber model under various cyclic loading histories. In this study the weighting factor is expressed by the implicit function of the accumulated plastic deformation. The procedure to obtain the weighting factor is presented as follows.

i) When the loading follows the curve a-b, the virgin state, in Fig. 4.29, the weighting factor ω_{ab} for the virgin state is equal to one.

ii) When unloading occurs at the point b of the loading path a-b in Fig. 4.29, the weighting factor for the path b-c is computed as follows.

a) First, the positive bound line for the virgin state is obtained in the following manner. The position of bound line is determined by drawing the line with the slope K^s_{m3} at the last yield moment M^s_{y3} on the saturated moment-rotation relationships and by making the resulting line have a intercept on the moment axis. The bound line is rotated about its intersection point with the moment axis to have a slope of K^v_{m3}, where K^v_{m3} is the last slope of the virgin moment-rotation relationships.

b) Second, the distances δ^p_i from the point of yield to the bound and δ^p_b between the point b and the bound are measured along the moment axis. The weighting factor for the path b-c is determined by the following equation.

$$\omega_{bc} = \omega_{ab} \cdot \left\{ 1 - e^{\left(-\alpha \cdot \delta^p_b / \left(\delta^p_i - \delta^p_b\right)\right)} \right\} \tag{4.2}$$

c) If a displacement reversal occurs in the elastic range b-b_u while approaching the negative bound line, the moment-rotation behavior is elastic until the moment is reached on the previous moment-rotation curve a-b and deformation continues along this curve a-b-b_r. The previous ω_{bc} is discarded in this case.

iii) When unloading occurs at the point c of the loading path b-c in Fig. 4.29, the weighting factor for the path c-d is computed as follows.

a) The negative bound line has the intercept with the moment axis, which is opposite to the intersection point of the positive bound line with the moment axis, and has a slope of K^{bc}_{m3}, where K^{bc}_{m3} is the last slope of the moment-rotation relationships to describe the path b-c in Fig. 4.29.

b) The weighting factor is written as

$$\omega_{cd} = \omega_{bc} \cdot \left\{ 1 - e^{\left(-\alpha \cdot \delta^n_c / \left(\delta^n_i - \delta^n_c\right)\right)} \right\} \tag{4.3}$$

iv) When unloading occurs at the point d of the path c-d, the positive bound line is rotated about its intersection point with the moment axis to have a slope of K_{m3}^{cd}, where K_{m3}^{cd} is the last slope of the moment-rotation relationships to describe the path c-d in Fig. 4.29. The weighting factor for the following loading path can be determined by the similar equation to Eq. 4.2

v) In this study, the value of $\alpha=1$ is applied to Eqs. 4.2 and 4.3. It should be noted that when a smaller value of α is applied, the moment-rotation relationships reach the saturated moment-rotation relationships more rapidly.

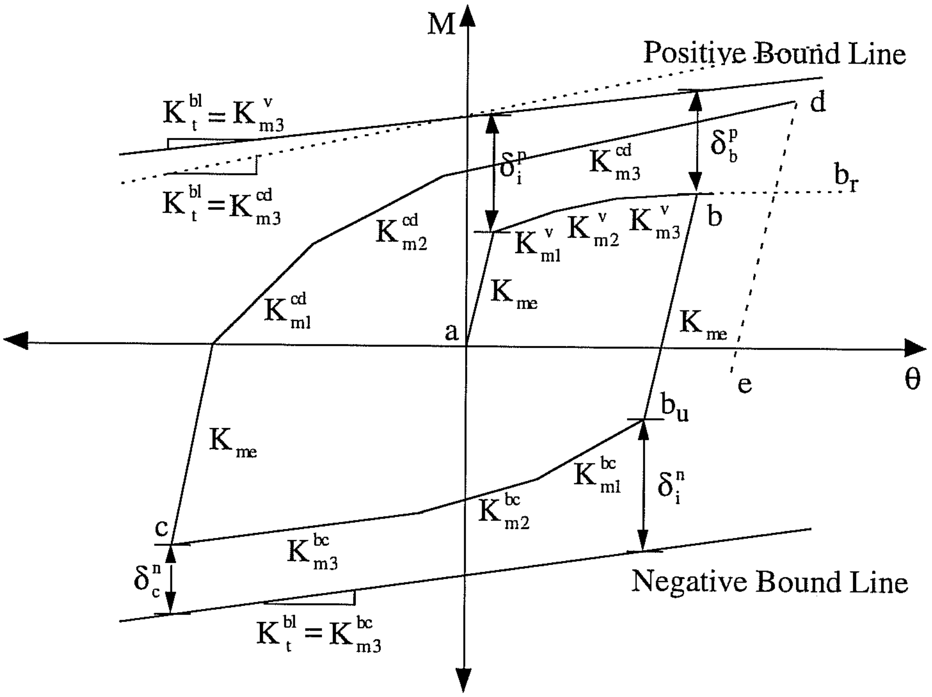

Fig. 4.29: Procedure for Weighting Factor

The developed multi-linear hinge model employing the weighting factor is tested on a W21x57 cantilever similar to Engelhardt Specimen 8, subjected to various displacement histories. The prediction results made by the developed model are compared with the analytical results obtained by the fiber model and by the bilinear hinge model in Figs. 4.30 to 4.35.

In Fig. 4.30, the developed model is tested on repetitive load reversals under the virgin state and is compared with the fiber model. The agreement is satisfactory. The bilinear model develops larger strength because it employes a strain hardening ratio which is intended to model cyclic behavior.

In Fig. 4.31, the comparison for constant displacement amplitude cycles is presented. From this figure, it can be seen that the transition from the virgin state to saturated state is reasonably accomplished by the weighting factor. As the number of cycles increases, the prediction made by the developed model matches better with the fiber model results. The bilinear model shows the same performance regardless of the number of cycles.

For several cycles of small displacement amplitude after a relatively large displacement in one direction, the performance of the developed model is shown in Figs. 4.32 and 4.33. The correlation of predicted results by the developed model and the fiber model is reasonable. However, the performance of the bilinear model is rather poor after a relatively large displacement in one direction.

The developed model is tested on a couple of large displacement amplitude cycles after several small displacement amplitude cycles and is compared to the fiber model and bilinear model in Figs. 4.34 and 4.35. The agreement is reasonable. From these figures, it can be found that for several small displacement amplitude cycles, the developed model produces the gradual transition from the virgin state to saturated state by using the weighting factor. After small displacement cycles, the behavior of the develop d model is close to the saturated state and easily reaches that of the fiber model for large displacement cycles.

The developed multi-linear hinge model has been tested on several irregular displacement histories. It has been shown that the developed model can produce a smooth transition from the virgin state to the saturated state by using the weighting factor. When compared to the bilinear model, the developed model shows significantly better performance.

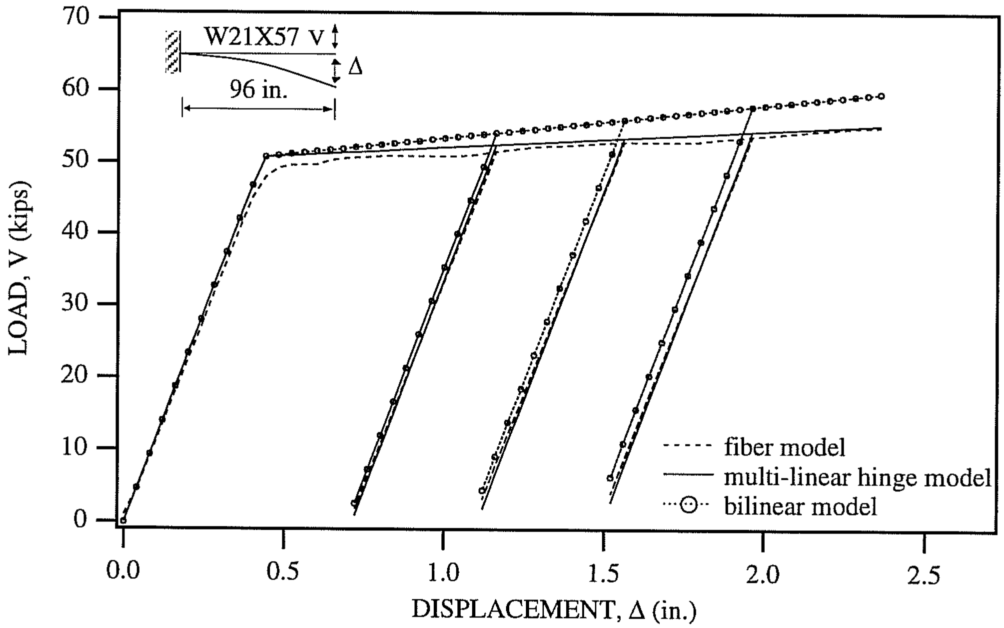

Fig. 4.30: Comparison of the Multi-Linear Hinge Model and Other Models for Displacement History No. 1

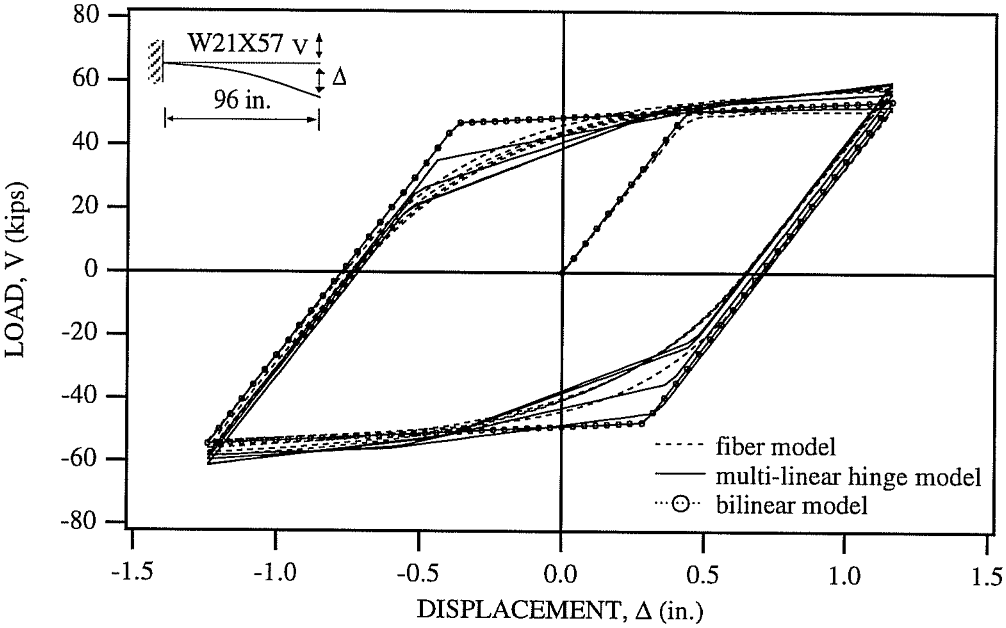

Fig. 4.31: Comparison of the Multi-Linear Hinge Model and Other Models for Displacement History No. 2

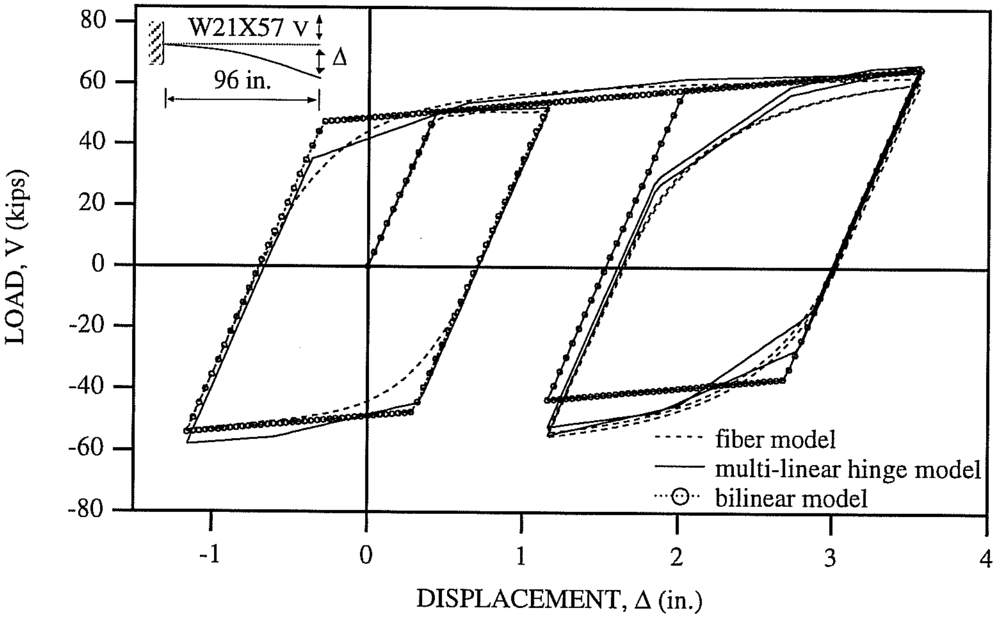

Fig. 4.32: Comparison of the Multi-Linear Hinge Model and Other Models for Displacement History No. 3

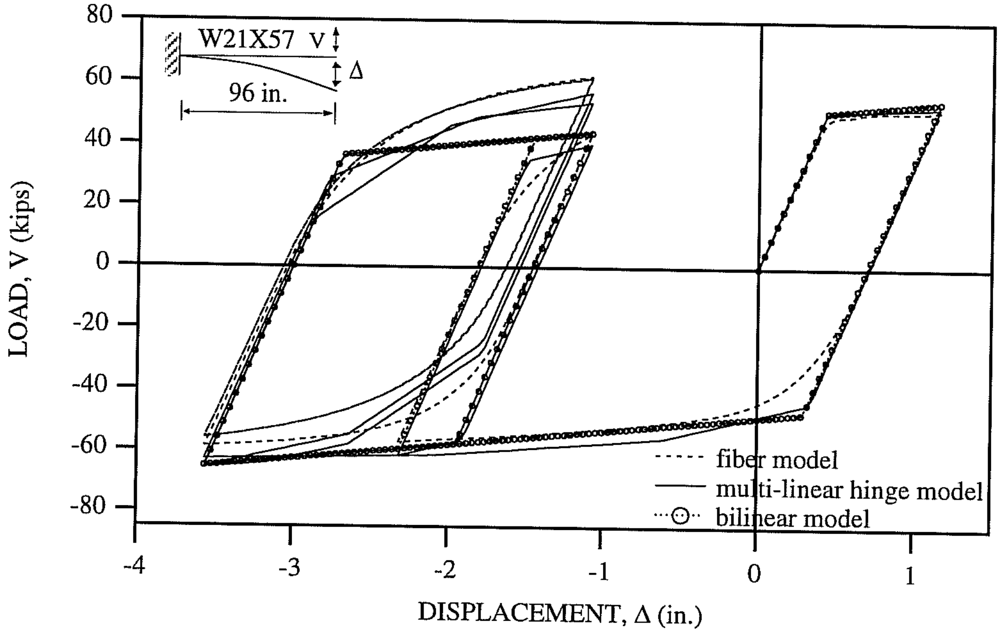

Fig. 4.33: Comparison of the Multi-Linear Hinge Model and Other Models for Displacement History No. 4

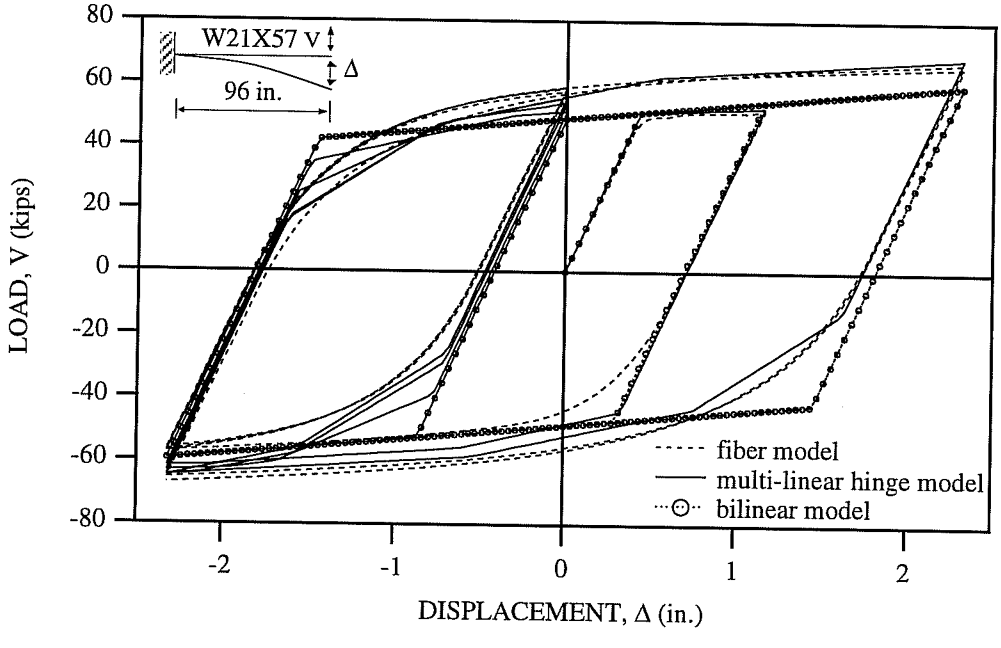

Fig. 4.34: Comparison of the Multi-Linear Hinge Model and Other Models for Displacement History No. 5

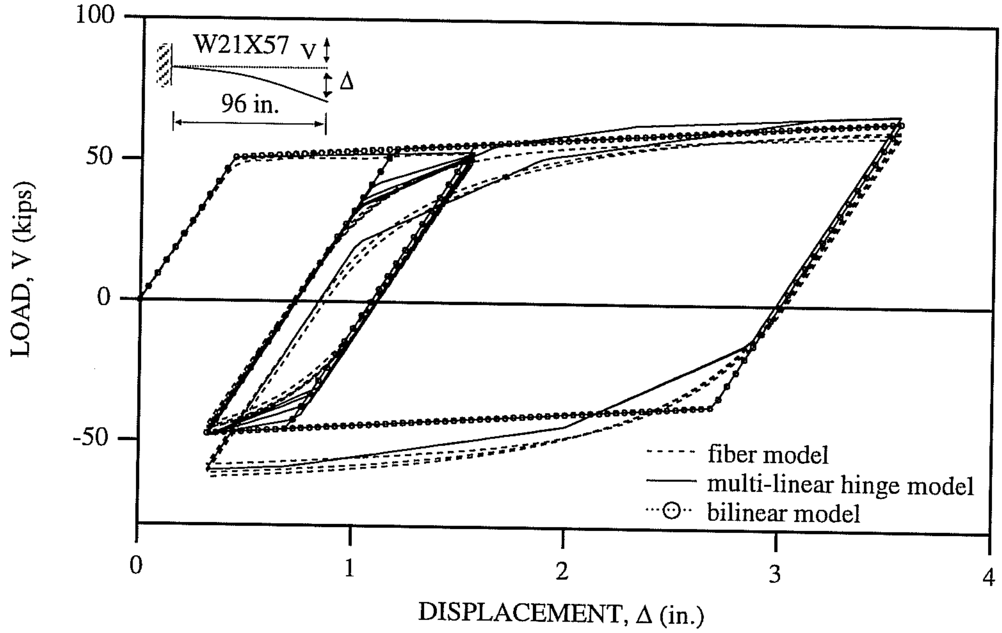

Fig. 4.35: Comparison of the Multi-Linear Hinge Model and Other Models for Displacement History No. 6

4.4 Calibration of Multi-Linear Hinge Model for Members with Axial Force

4.4.1 Plastic Axial Stiffness

In this section, the response of the multi-linear hinge model is investigated for modeling bare steel members under combined bending and axial force. The axial force-deformation relationships for the multi-linear hinge model were calibrated to the fiber model predictions for an equivalent cantilever, representing each half of a member, as shown in Fig. 2.22. The axial force-deformation relationships for the virgin state were calibrated to the monotonic response of cantilever beams. The axial force-deformation relationships for the saturated state were obtained by calibrating to the envelop curve through the tips of the saturated forces at various displacement amplitudes. This calibration process resulted in the axial stiffness parameters listed in Table 4.4. The superscripts v and s refer to the virgin and saturated state models. In Table 4.4, K_{fe} is the elastic axial stiffness of the equivalent cantilever beam (axial force per unit axial displacement). When the initial yield axial force F_{y1}^{v} for the virgin state is known, the remaining yield axial forces F_{yi}'s of the axial force-deformation relationships for two limiting states can be determined from the yield functions (Eq. 2.32) and yield moment parameters presented in Table 4.1. In this work, the section yield force, equal to AF_y, is used as the initial yield axial force F_{y1}^{v}. Combined with the parameters listed in Table 4.1, the parameters presented in Table 4.4 can be used to describe the moment-rotation and axial force-deformation relationships employed in the multi-linear hinge model as a bare steel beam-column element.

In Figs. 4.36 and 4.37, the developed multi-linear hinge model using the calibrated parameters is compared with the fiber model for a W21x57 cantilever similar to Engelhardt Specimen 8, under monotonic and cyclic axial loadings. It can be seen that the chosen parameters for the axial force-deformation relationships are reasonable. Note that the conventional bilinear hinge model is completely incapable of modeling plastic axial deformations.

K_{f1}^{v}	K_{f2}^{v}	K_{f3}^{v}	K_{f1}^{s}	K_{f2}^{s}	K_{f3}^{s}
$0.001K_{fe}$	$0.001K_{fe}$	$0.005K_{fe}$	$0.3K_{fe}$	$0.1K_{fe}$	$0.03K_{fe}$

Table 4.4: Parameters Defining Axial Force-Deformation Relationships

Suppose that a cantilever beam is subjected to constant axial force smaller than the section yield force. When vertical load is then imposed at the free end of this beam, yielding due to the bending moment starts to occur at the member support. As the vertical load is further increased, the yielding spreads over a finite region at the support. The yielding over the finite region reduces not only the flexural stiffness, but also the axial stiffness.

The reduction of axial stiffness due to the yielding on the finite region caused by the bending moment, can not be properly described by the axial force-deformation parameters presented in Table 4.4. To overcome this difficulty, the length of an equivalent cantilever beam, for which the plastic axial stiffness of the axial force-deformation relationships is obtained, is varied according to the level of axial force. To vary the length of equivalent cantilever beam according to the level of axial force, empirical relationships were determined from calibration to the fiber model results. The length L_{eq} of equivalent beam for the nonlinear yield surface is expressed as

$$L_{eq} = L/\left\{40 + 27850 \cdot e^{(-38 \cdot \beta)}\right\} \quad \text{for} \quad 0 < \beta \le 0.2 \qquad (4.4a)$$

$$L_{eq} = L/\left\{4.2 + 998 \cdot e^{(-15 \cdot \beta)}\right\} \quad \text{for} \quad 0.2 \le \beta \le 0.5 \qquad (4.4b)$$

$$L_{eq} = L/(7 - 5\beta) \quad \text{for} \quad 0.5 \le \beta \le 1 \qquad (4.4c)$$

where L and β are the element length and the ratio F/F_y of axial force to the section yield force. For the multi-linear yield surface, the length of equivalent cantilever beam is written as

$$L_{eq} = L/\left\{3 + 200 \cdot e^{(-8 \cdot \beta)}\right\} \quad \text{for} \quad 0 < \beta \le 0.5 \qquad (4.5a)$$

$$L_{eq} = L/(12 - 10 \cdot \beta) \quad \text{for} \quad 0.5 \le \beta \le 1 \qquad (4.5b)$$

From Eqs. 4.4 and 4.5, it can be found that when the axial force is equal to the section yield force, the length of equivalent cantilever beam is half of the element length, and as the value of axial force approaches zero, the length becomes very short and the plastic axial stiffness becomes very large. For a zero value of axial force, the plastic axial force is infinite and there is no plastic axial deformation.

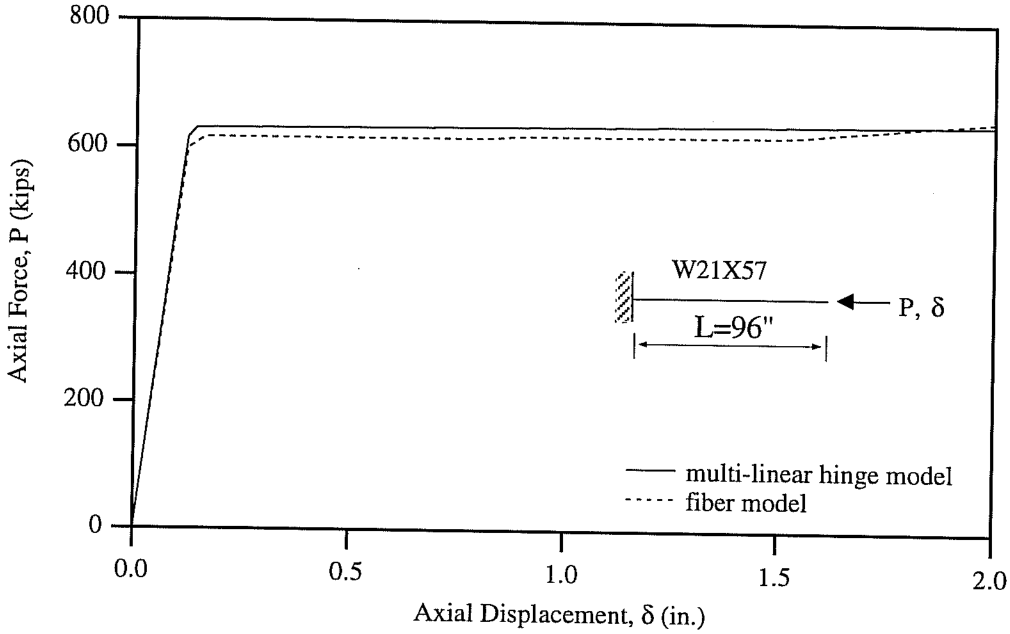

Fig. 4.36: Comparison of Multi-Linear Hinge Model and Fiber Model for Monotonic Axial Loading

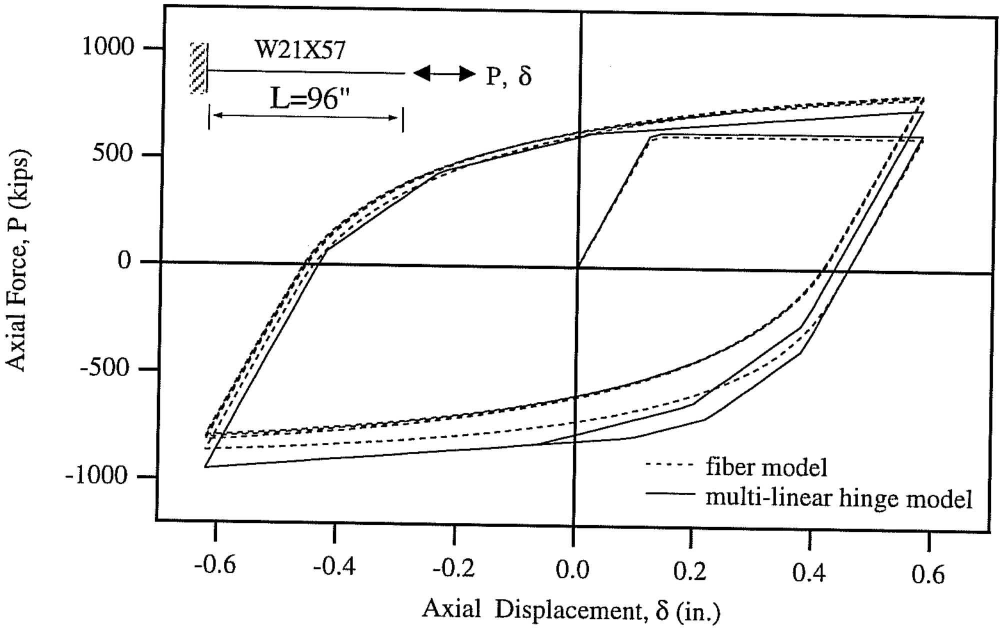

Fig. 4.37: Comparison of Multi-Linear Hinge Model and Fiber Model for Cyclic Axial Loading

4.4.2 Monotonic Behavior

The bending moment-axial force interaction of the developed model for the virgin state is shown in Fig. 4.38. In this figure, 'm.l.y.s.' and 'n.l.y.s.' denote the multi-linear and nonlinear yield surfaces, respectively. The developed model using the multi-linear yield surface matches well with the fiber model under low axial forces, but underestimates the strength for relatively large axial forces. The developed model using the nonlinear yield surface matches well with the fiber model regardless of the level of axial force, except that as the axial force increases, the discrepancy between the predicted initial yielding force by both models increases. The developed model with the multi-linear yield surface produces initial yielding at a smaller load for relatively large axial forces than the developed model with the nonlinear yield surface. This can be attributed to the fact that the multi-linear yield surface has a smaller yield moment for relatively large axial force than the nonlinear yield surface, as shown in Fig. 2.7.

Even though there is some difference between the developed and fiber models, the predicted results by the developed model with the nonlinear yield surface are reasonable.

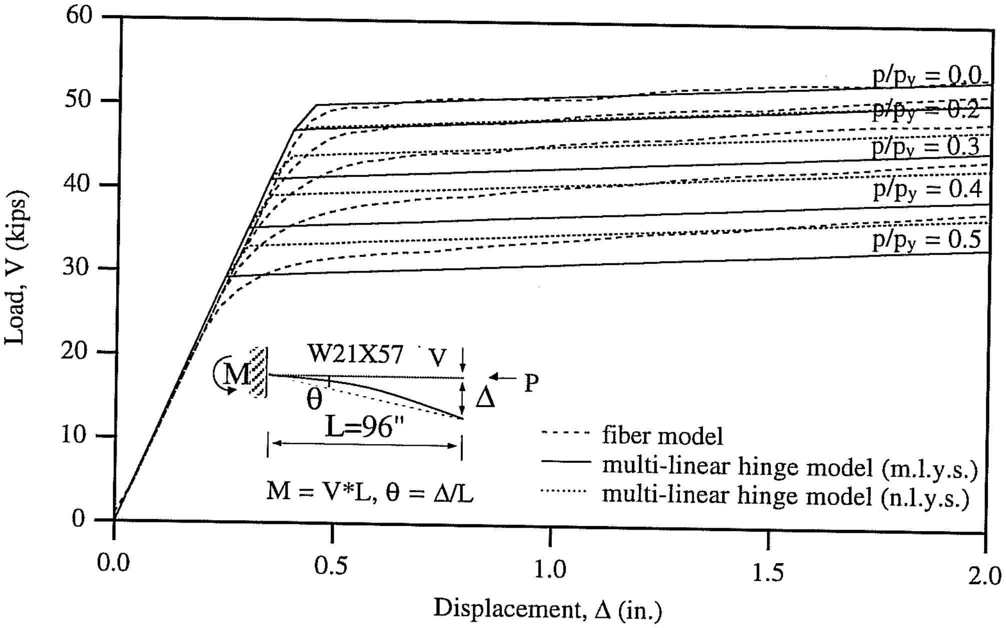

Fig. 4.38 : Bending Moment-Axial Force Interaction of Multi-Linear Hinge Model for Monotonic Loading with Constant Axial Force

4.4.3 Cyclic Behavior

To investigate the bending moment-axial force interaction during cyclic loading, the developed model is applied to Engelhardt specimen 8 subjected to various constant axial forces and cyclic transverse loading. Since it is difficult to obtain cyclic experimental data for test specimens subjected to constant axial force, the predicted results by the developed model are compared with the analytical results obtained by the fiber model.

Figures. 4.39 through 4.42 present predictions made by the developed multi-linear hinge model and the fiber model for the cantilever beam subjected to various constant axial forces and cyclic transverse loading. The response for first order analyses are shown in these figures. The legend “n.p.a.d.” indicates that plastic axial deformations are not considered during the analyses. This is accomplished by forcing the direction of the normal vector to the yield surface to always follow the direction of the moment axis in action space. The results with the legend “n.p.a.d.” are obtained by the multi-linear hinge model with the multi-linear yield surface. The legends "m.l.y.s." and "n.l.y.s." stand for the multi-linear and nonlinear yield surfaces, respectively. The response plots with these legends include the influence of plastic axial deformations.

The transverse load-displacement relationships obtained from first order analyses for various constant axial forces are shown in Figs. 4.39. to 4.42. From these figures, it can be seen that the developed model considering plastic axial deformations matches well with the fiber model regardless of the level of axial force, and that as the level of axial force increases, the developed model neglecting plastic axial deformations shows increasingly poor performance. As the level of axial force increases, the developed model neglecting plastic axial deformations exhibits more flexible bending behavior than the other models because the yielding is not shared properly by the axial and bending stiffness, but concentrated only on the bending stiffness. When plastic axial deformations are considered in the developed multi-linear hinge model with multi-linear or nonlinear yield surfaces, performance improves as the level of axial force increases. The model with the multi-linear yield surface predictes somewhat higher strength compared to the model with the nonlinear yield surface. This may be explained by the observation that the normal vector to the multi-linear yield surface is constant during the loading histories, but the normal vector to the nonlinear yield surface varies and has smaller slope than that to the multi-linear yield surface. As the direction of normal vector to the yield surface gradually approaches the direction of the moment axis, a greater portion of the yielding affects the flexural stiffness, and consequently reduces the bending stiffness.

In Figs. 4.39d to 4.42d, the transverse load-axial deformation relationships for various constant axial forces are presented. The developed model neglecting plastic axial deformations produces only the initial elastic axial deformation due to the constant axial force regardless of the level of transverse load. However, when plastic axial deformations are considered in the multi-linear hinge model, the axial deformation oscillates and increases beyond the initial elastic axial deformation as the transverse load is imposed cyclically and yielding spreads over a finite region at the member support. The axial deformations obtained by the model with the multi-linear yield surface stop oscillating and increasing after several cycles of loading. As the level of axial force increases, the number of cycles increases after which the axial deformations stop oscillating and increasing. This can be attributed to the fact that the current action point moves along the yield surface during strain hardening and finally settles on the portion of multi-linear yield surface (Eq. 2.32c) to which the direction of the normal vector is that of the moment axis. The axial deformations obtained by the model with the nonlinear yield surface is larger during the initial cycles of loading than those by the fiber model, but becomes smaller than those by the fiber model as the number of cycles increases. Although there is some difference between the predicted transverse load-axial deformation relationships by the two models, the agreement is reasonable when the simplicity of the multi-linear hinge model is considered.

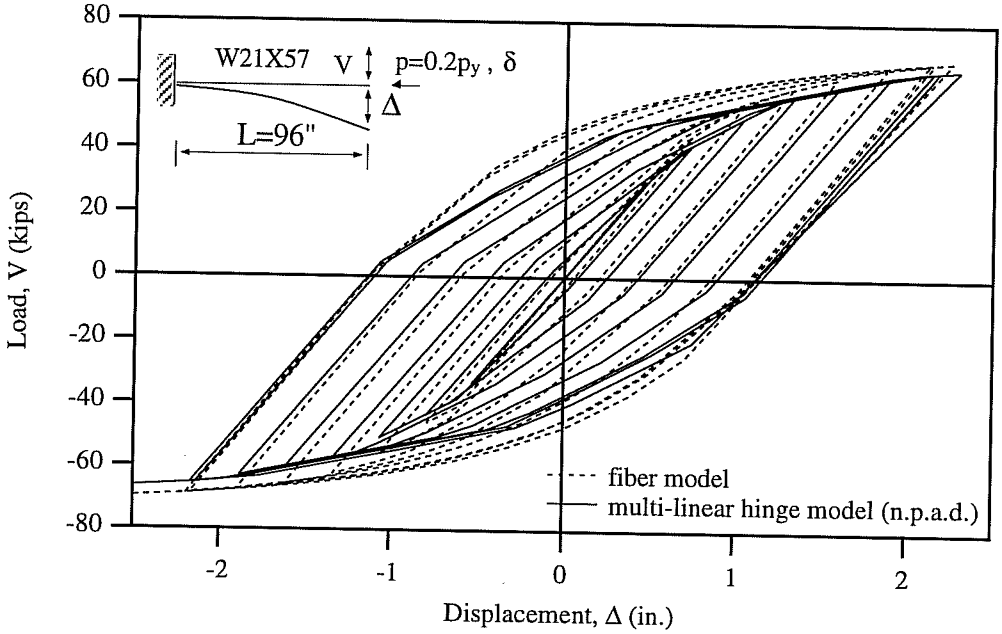

Fig. 4.39a: Comparison of Predicted Results by Fiber Model and Multi-Linear Hinge Model Neglecting Plastic Axial Deformation Under $P = 0.2P_y$

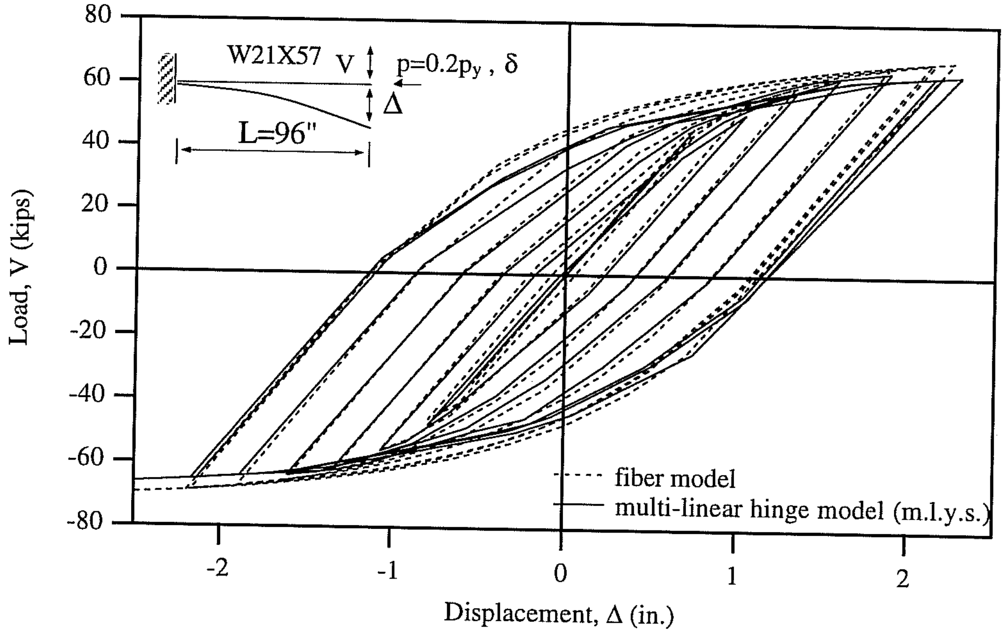

Fig. 4.39b: Comparison of Predicted Results by Fiber Model and Multi-Linear Hinge Model With Multi-linear Yield Surface Under $P = 0.2P_y$

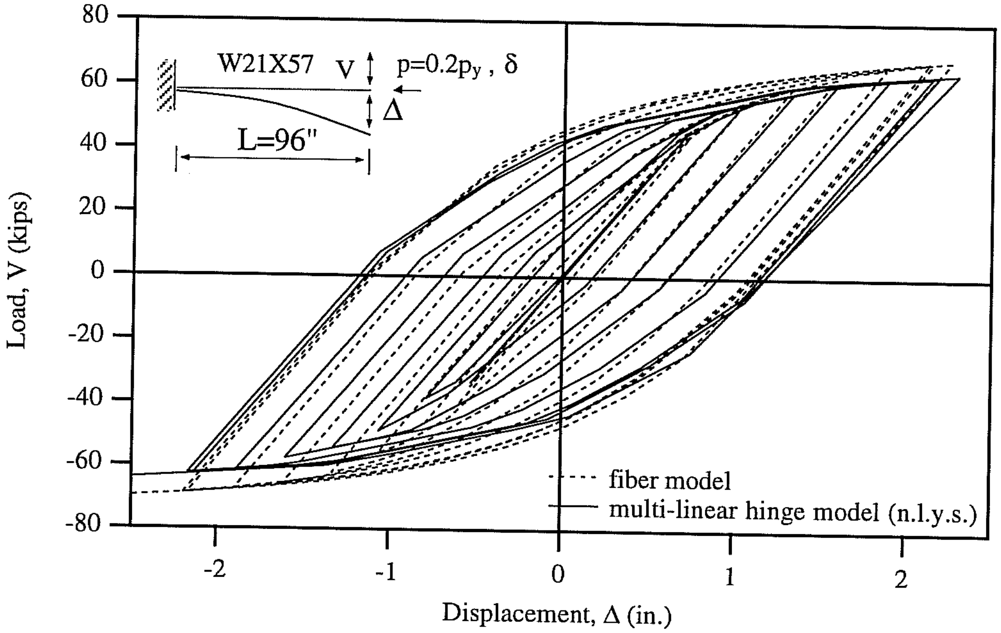

Fig. 4.39c: Comparison of Predicted Results by Fiber Model and Multi-Linear Hinge Model With Nonlinear Yield Surface Under $P = 0.2P_y$

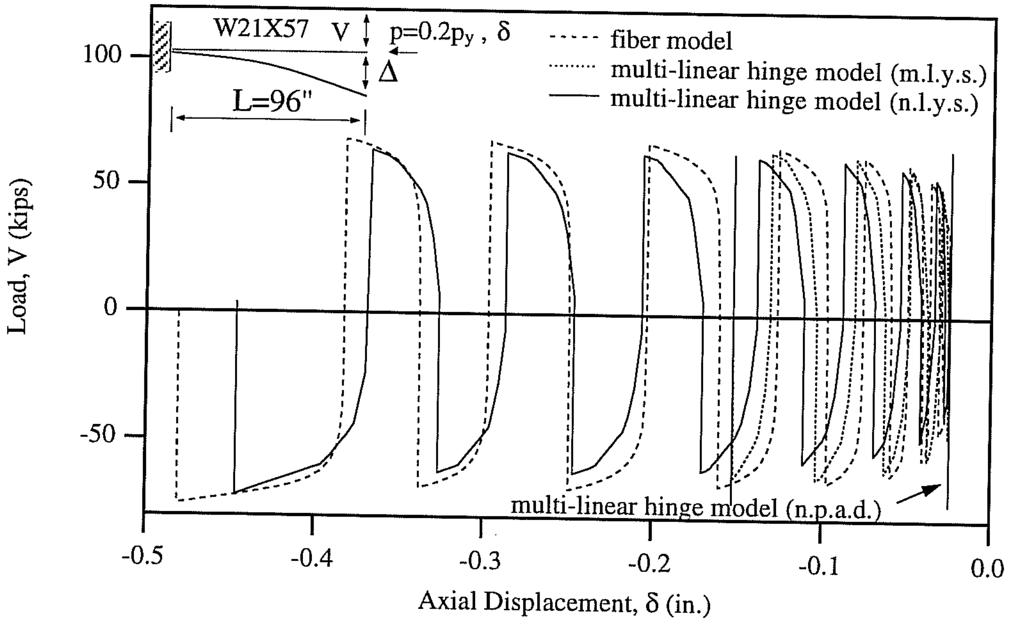

Fig. 4.39d: Transverse Load-Axial Deformation Relationships Obtained by the Multi-Linear Hinge and Fiber Models Under $P = 0.2P_y$.

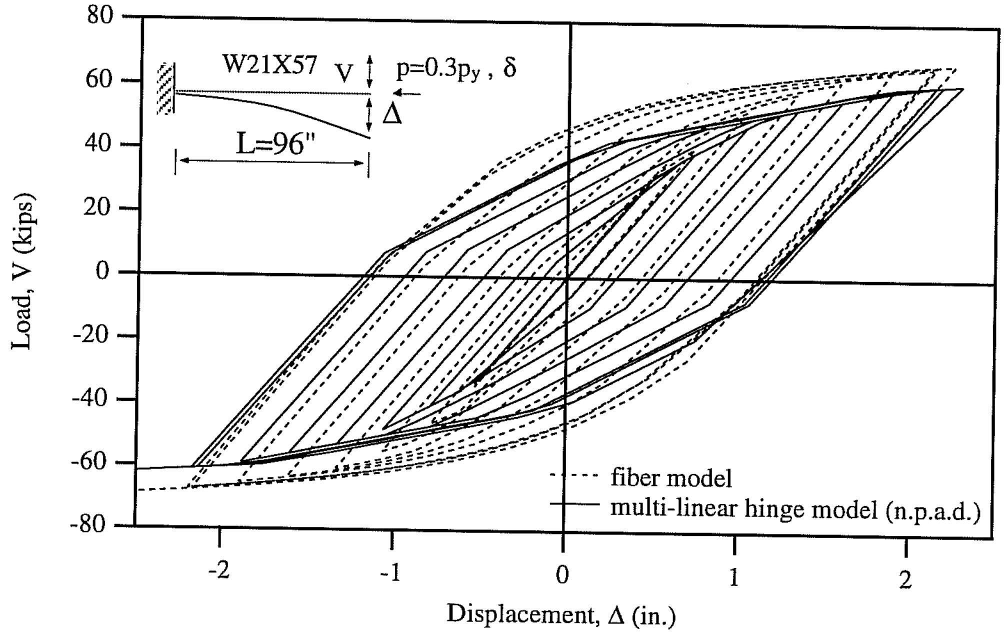

Fig. 4.40a: Comparison of Predicted Results by Fiber Model and Multi-Linear Hinge Model Neglecting Plastic Axial Deformation Under $P = 0.3P_y$.

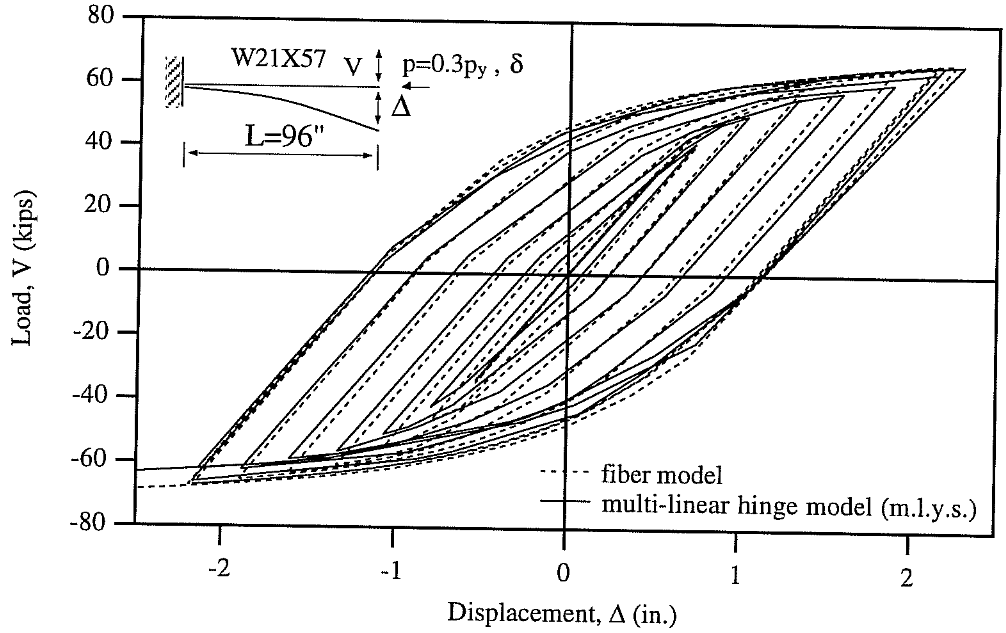

Fig. 4.40b: Comparison of Predicted Results by Fiber Model and Multi-Linear Hinge Model With Multi-linear Yield Surface Under $P = 0.3P_y$.

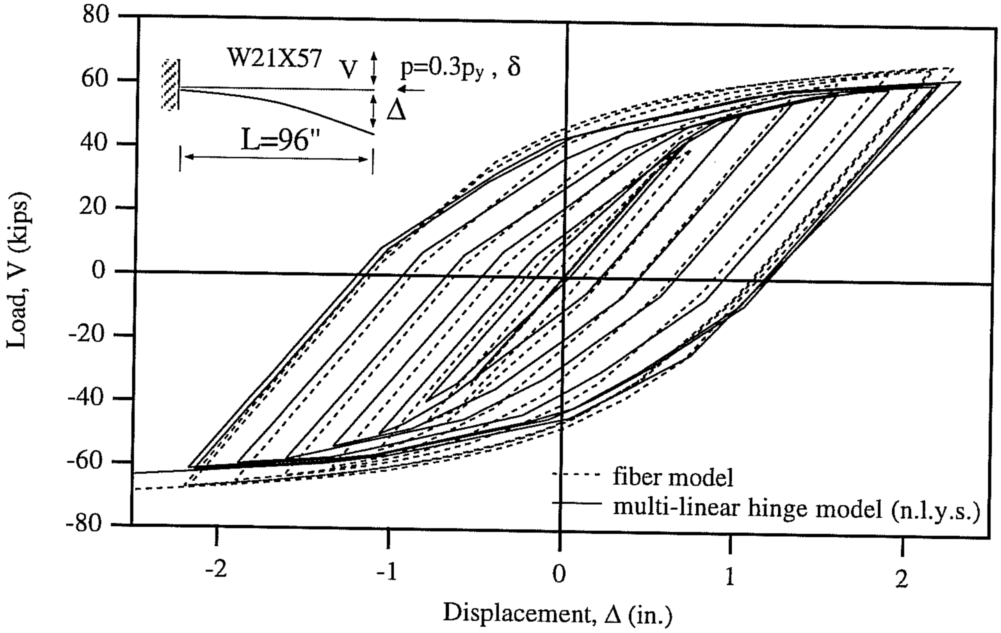

Fig. 4.40c: Comparison of Predicted Results by Fiber Model and Multi-Linear Hinge Model With Nonlinear Yield Surface Under $P = 0.3P_y$.

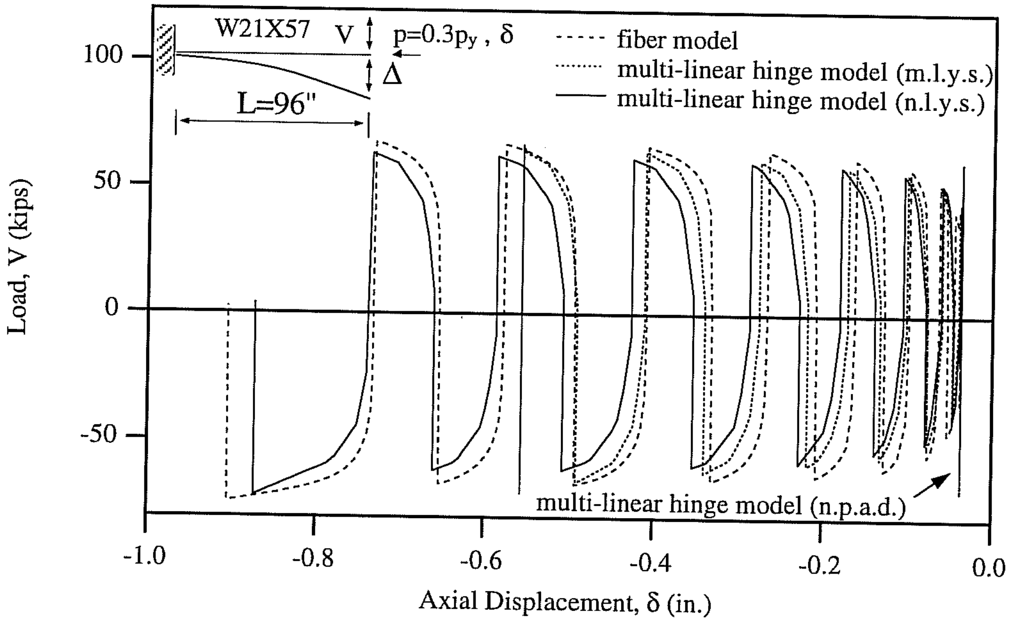

Fig. 4.40d: Transverse Load-Axial Deformation Relationships Obtained by the Multi-Linear Hinge and Fiber Models Under $P = 0.3P_y$.

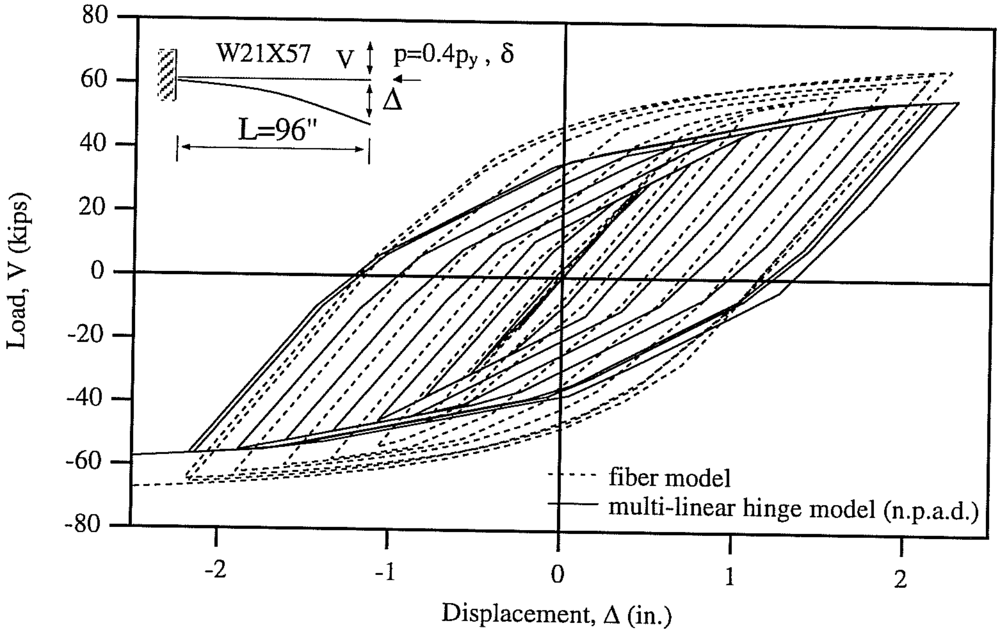

Fig. 4.41a: Comparison of Predicted Results by Fiber Model and Multi-Linear Hinge Model Neglecting Plastic Axial Deformation Under $P = 0.4P_y$.

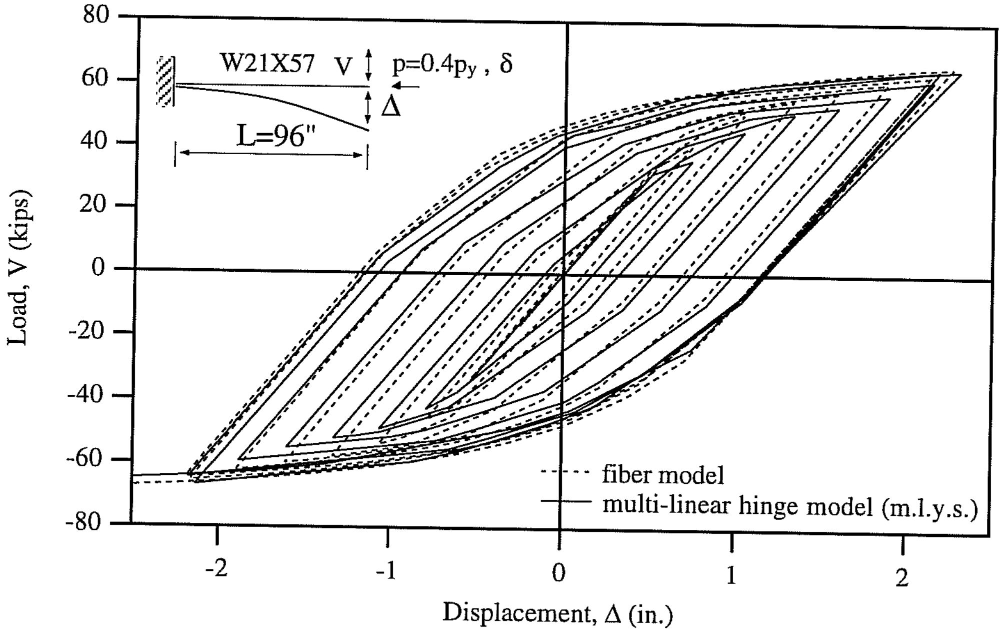

Fig. 4.41b: Comparison of Predicted Results by Fiber Model and Multi-Linear Hinge Model With Multi-linear Yield Surface Under $P = 0.4P_y$.

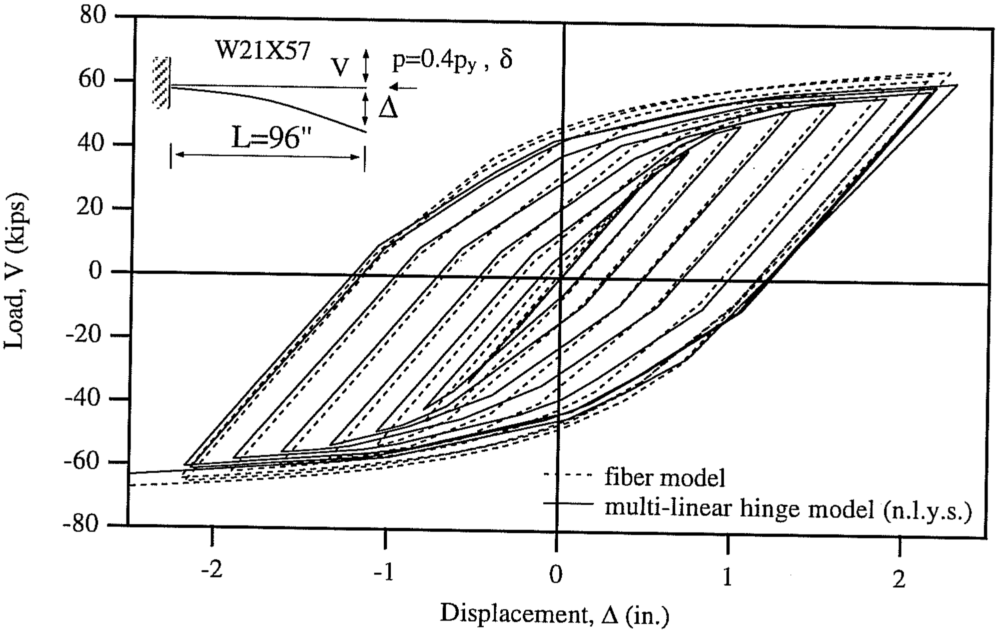

Fig. 4.41c: Comparison of Predicted Results by Fiber Model and Multi-Linear Hinge Model With Nonlinear Yield Surface Under $P = 0.4P_y$.

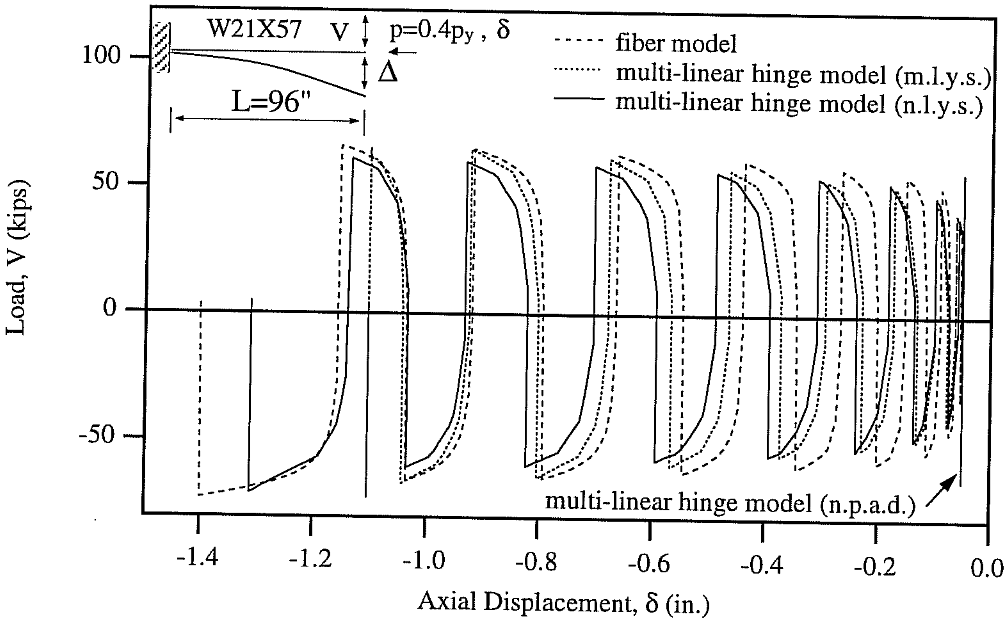

Fig. 4.41d: Transverse Load-Axial Deformation Relationships Obtained by the Multi-Linear Hinge and Fiber Models Under $P = 0.4P_y$.

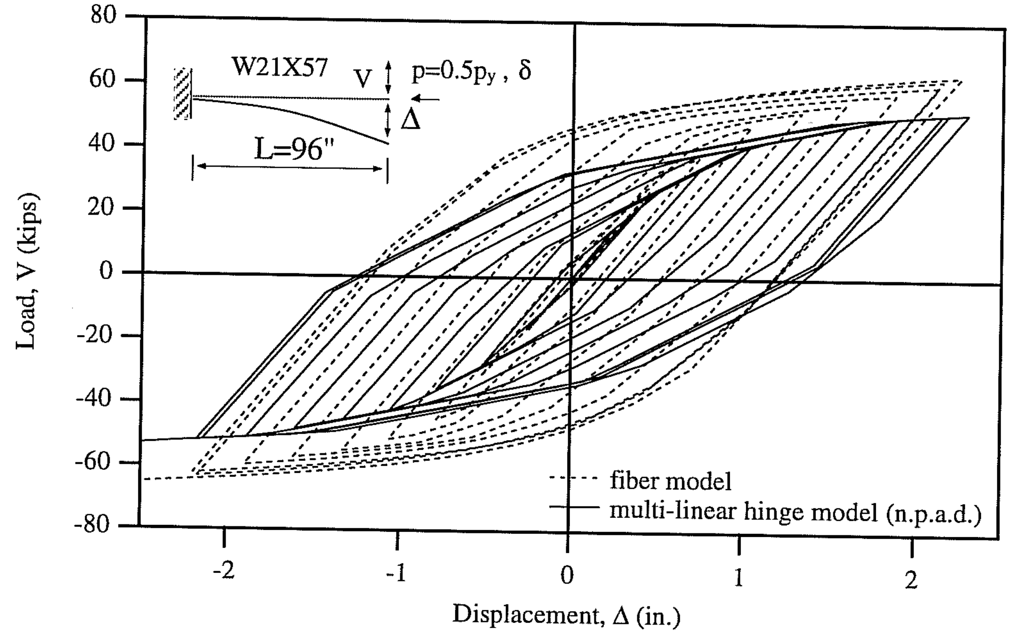

Fig. 4.42a: Comparison of Predicted Results by Fiber Model and Multi-Linear Hinge Model Neglecting Plastic Axial Deformation Under $P = 0.5P_y$.

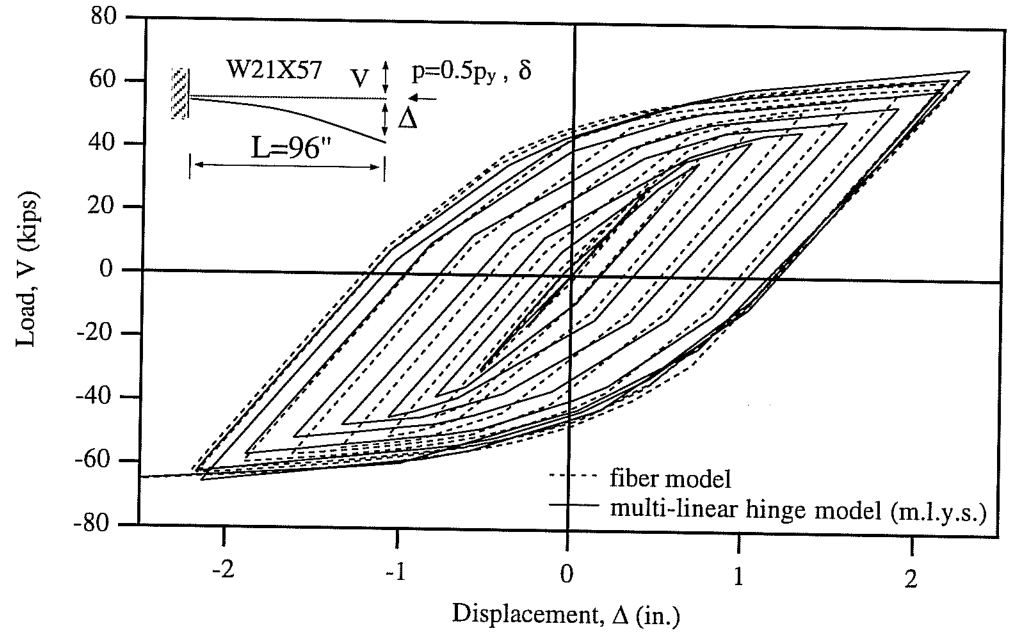

Fig. 4.42b: Comparison of Predicted Results by Fiber Model and Multi-Linear Hinge Model With Multi-linear Yield Surface Under $P = 0.5P_y$.

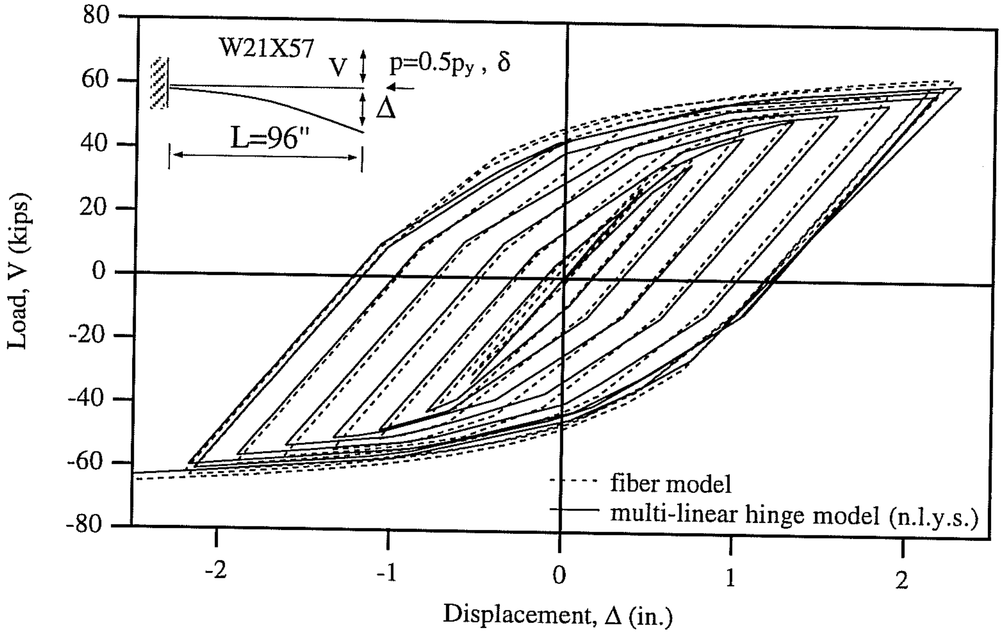

Fig. 4.42c: Comparison of Predicted Results by Fiber Model and Multi-Linear Hinge Model With Nonlinear Yield Surface Under $P = 0.5P_y$.

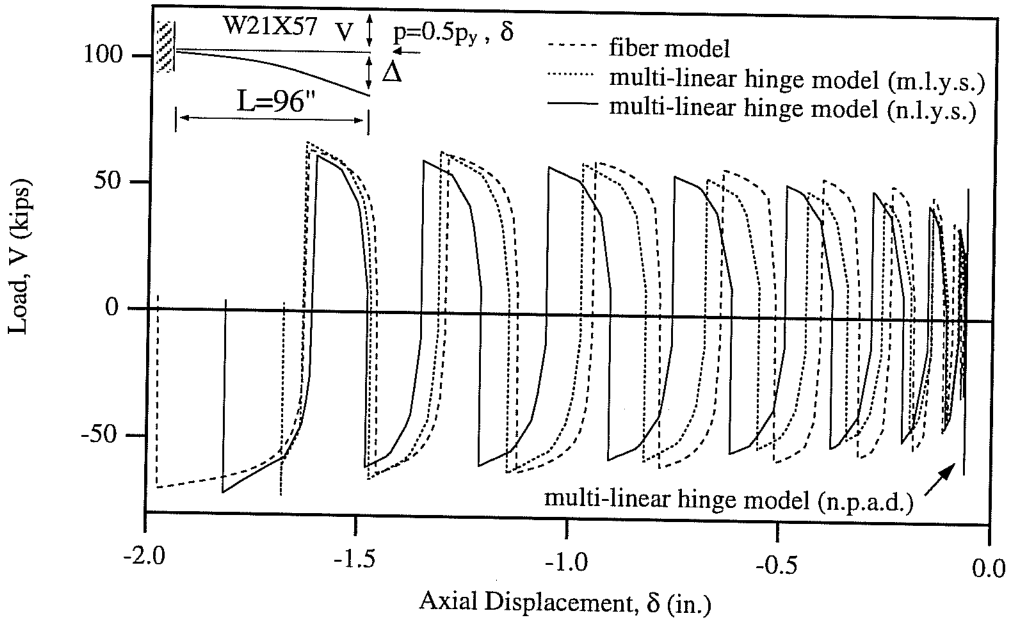

Fig. 4.42d: Transverse Load-Axial Deformation Relationships Obtained by the Multi-Linear Hinge and Fiber Models Under $P = 0.5P_y$.

4.4.4 Second Order Analyses

The transverse load-displacement and transverse load-axial deformation relationships obtained by second order analyses are shown in Figs. 4.43 to 4.49. In the results predicted by the fiber model, the member $\mathbf{P}-\delta$ (Eq. 2.95b) and system $\mathbf{P}-\Delta$ (Eq. 2.95c) effects are included. In the multi-linear hinge model, the system $\mathbf{P}-\Delta$ effects only are included. In Figs. 4.43 to 4.45, the analytical results for Engelhardt Specimen 8 subjected to various axial loads are presented. The predicted results for Popov Specimen 2 with various axial forces are presented in Figs. 4.46 to 4.49. To obtain the prediction made by the fiber model for Popov Specimen 2, the cyclic stress-strain parameters employed for the fiber model were first calibrated to the experimental results for the specimen subjected to no axial force. It was found that the parameters were the same as those listed in Table 3.1 except that the cyclic steady curve parameter n_c is 0.15 and the shape factor is 20. The prediction made by the fiber model is compared with the experimental data in Fig. 4.46

From Figs. 4.43 to 4.49, it can be seend that as far as the transverse load-displacement relationships are concerned, the multi-linear hinge model shows the same trends as in the first order analyses. As the level of axial force increases, the developed model neglecting plastic axial deformations exhibits more flexible behavior than the other models considering plastic axial deformations. When plastic axial deformations are considered in the multi-linear hinge model with the multi-linear yield surface, better performance is achieved as the level of axial force increases. The model with the nonlinear yield surface shows good agreement with the fiber model for Engelhardt Specimen 8, and produces somewhat smaller strength than the fiber model for Popov Specimen 2. In general, when plastic axial deformations are considered in the multi-linear hinge model, the model shows reasonable performance.

As far as the transverse load-axial deformation relationships are concerned, the multi-linear hinge model exhibits somewhat erratic behavior. For Popov Specimen 2, the developed hinge model produces similar results to those obtained by first order analyses. However, for Engelhardt Specimen 8, the model with the nonlinear yield surface produces much smaller axial deformations regardless of the level of axial force than the fiber model, and the model with the multi-linear yield surface shows better performance as the level of axial force increases. This can be attributed to the following. To account for the reduction of axial stiffness due to yielding on a finite region caused by bending moment, the length of the equivalent cantilever beam is determined from the empirical formulas (Eqs. 4.4 and 4.5), which are calibrated to predicted results by the first order analyses of the fiber model. The member $\mathbf{P}-\delta$ effects are included in the second order analyses of the fiber model, but are not included in the multi-linear hinge model.

Thus, when second order effects are considered, somwhat inaccurate axial force-plastic axial deformation predictions may result from the multi-linear hinge model. Nonetheless, the predictions are still considerably improved over conventional hinge models that totally neglect plastic axial deformations. More importantly however, the transverse load-displacement relationships are predicted quite well by the developed multi-linear hinge model. Consideration of plastic axial deformations in the model formulation results in significantly better predictions of flexural yielding behavior. The ability to better predict the transverse load-displacement response of steel columns should permit more accurate predictions of steel moment frame response under earthquake excitations.

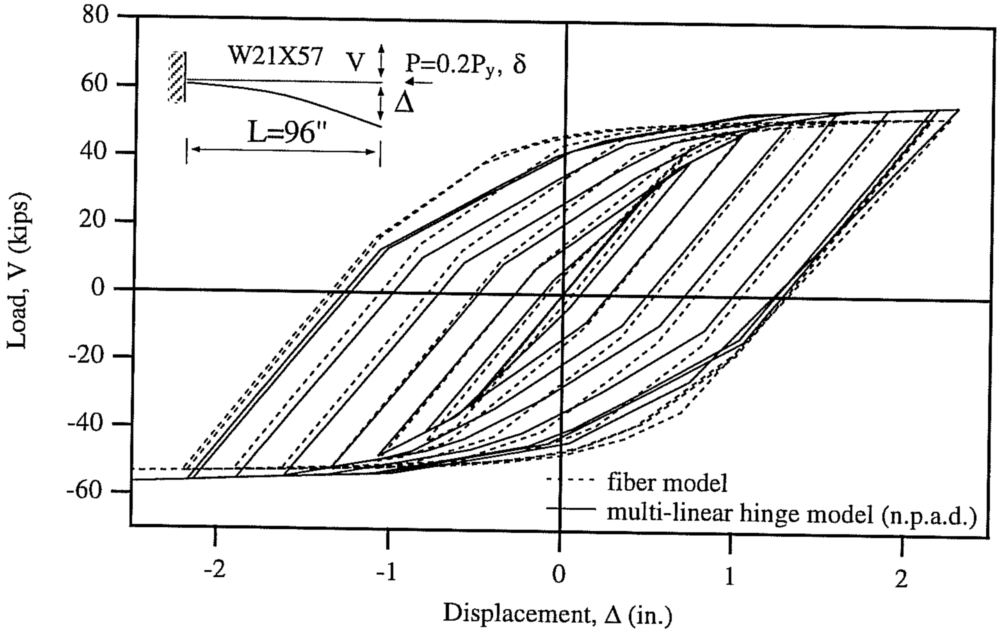

Fig. 4.43a: Comparison of Predicted Results by Fiber Model and Multi-Linear Hinge Model Neglecting Plastic Axial Deformation for $P = 0.2P_y$

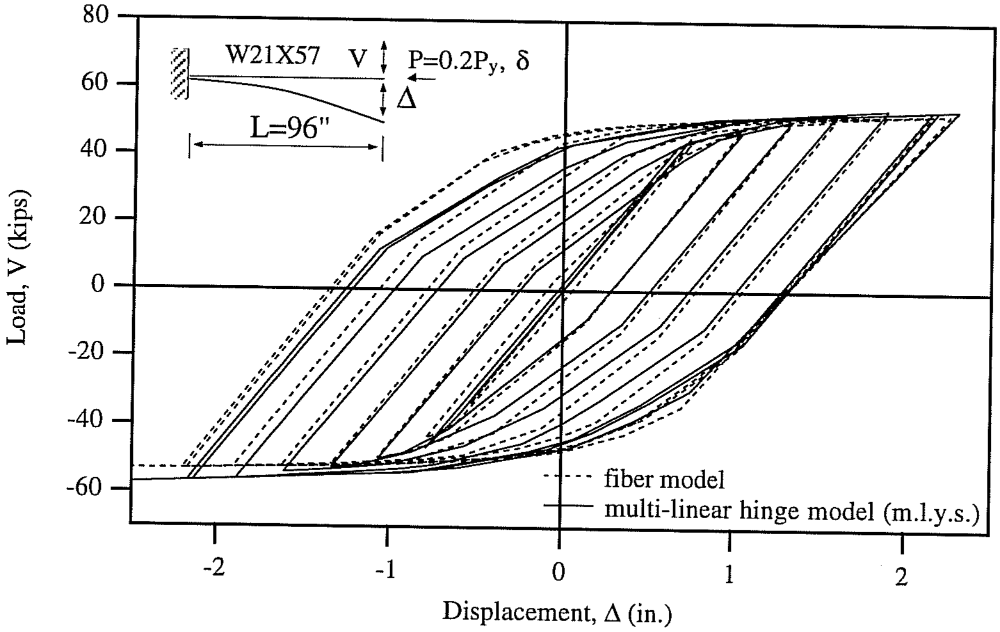

Fig. 4.43b: Comparison of Predicted Results by Fiber Model and Multi-Linear Hinge Model With Multi-linear Yield Surface for $P = 0.2P_y$

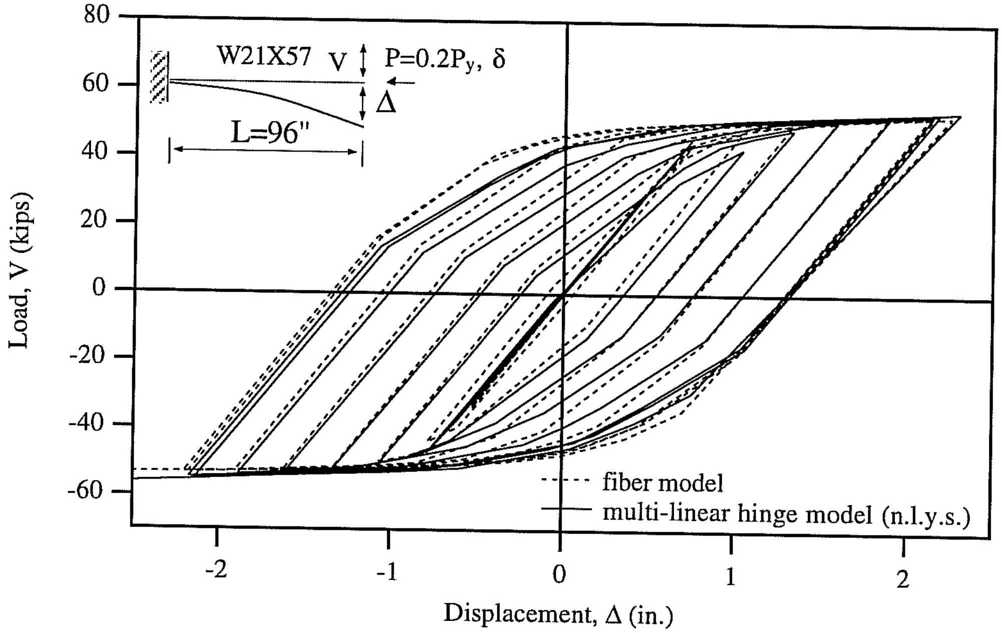

Fig. 4.43c: Comparison of Predicted Results by Fiber Model and Multi-Linear Hinge Model With Nonlinear Yield Surface for $P = 0.2P_y$

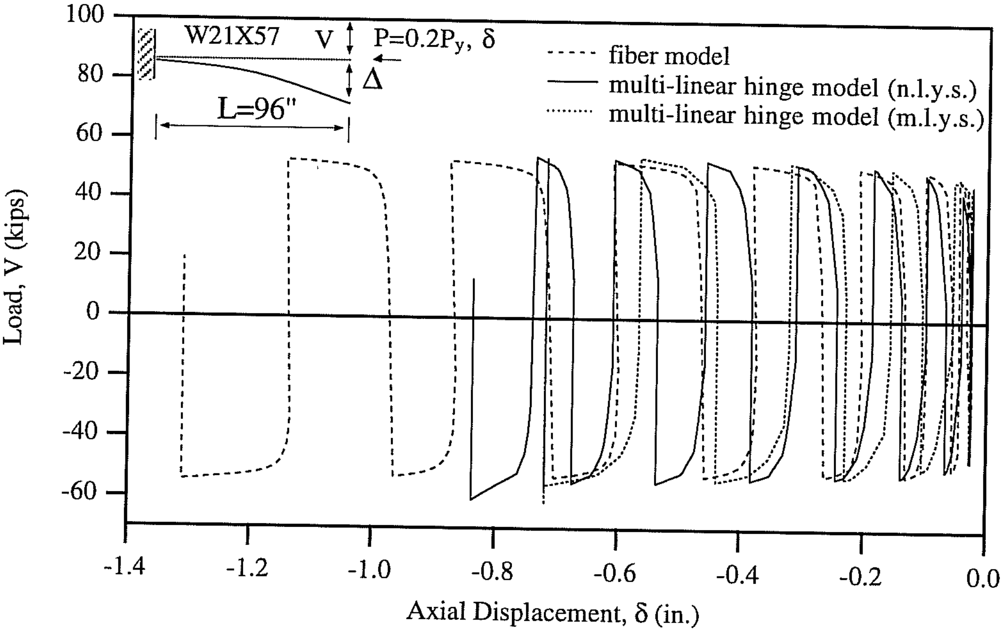

Fig. 4.43d: Comparison of Transverse Load-Axial Deformation Relationships Obtained by the Multi-Linear Hinge and Fiber Models for $P = 0.2P_y$.

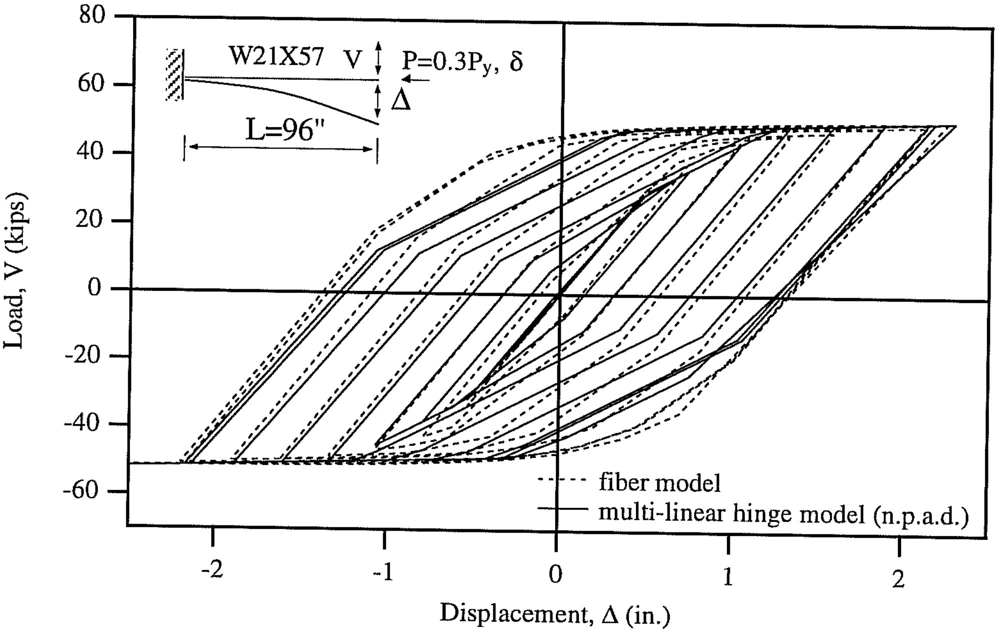

Fig. 4.44a: Comparison of Predicted Results by Fiber Model and Multi-Linear Hinge Model Neglectiing Plastic Axial Deformations for $P = 0.3P_y$

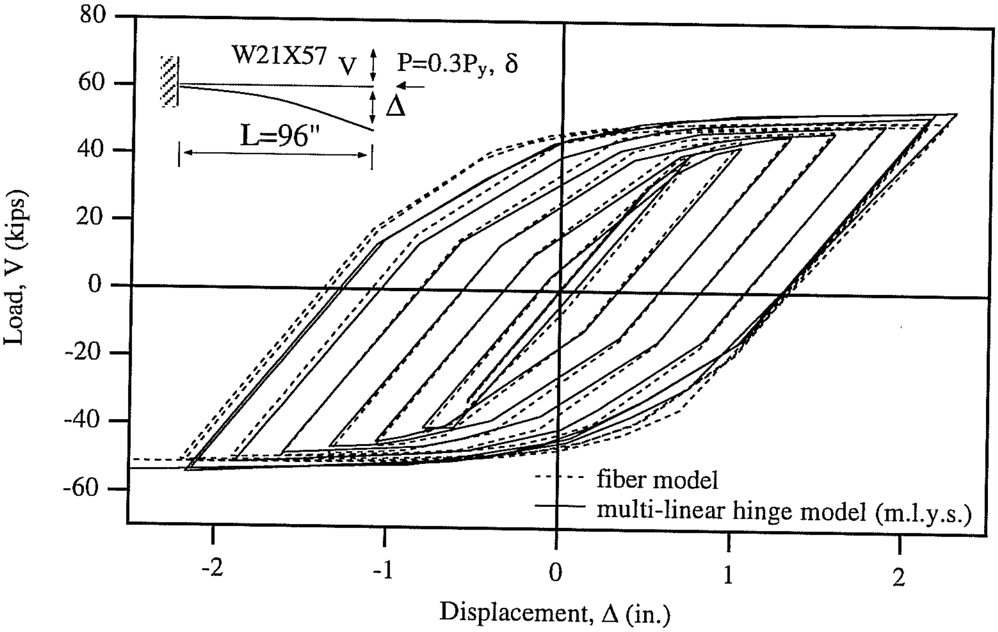

Fig. 4.44b: Comparison of Predicted Results by Fiber Model and Multi-Linear Hinge Model With Multi-linear Yield Surface for $P = 0.3P_y$

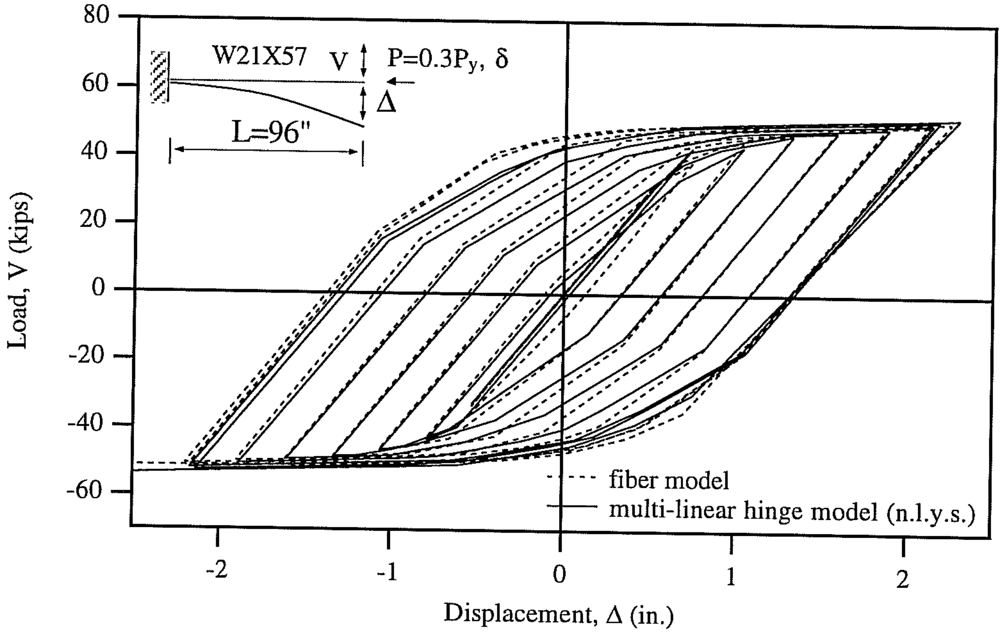

Fig. 4.44c: Comparison of Predicted Results by Fiber Model and Multi-Linear Hinge Model With Nonlinear Yield Surface for $P = 0.3P_y$

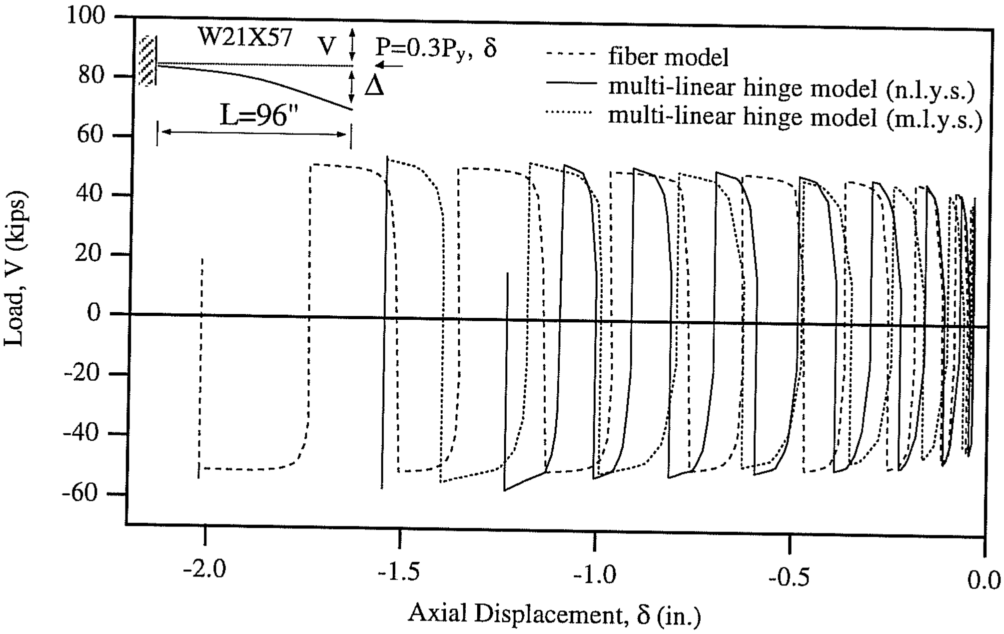

Fig. 4.44d: Comparison of Transverse Load-Axial Deformation Relationships Obtained by the Multi-Linear Hinge and Fiber Models for $P = 0.3P_y$.

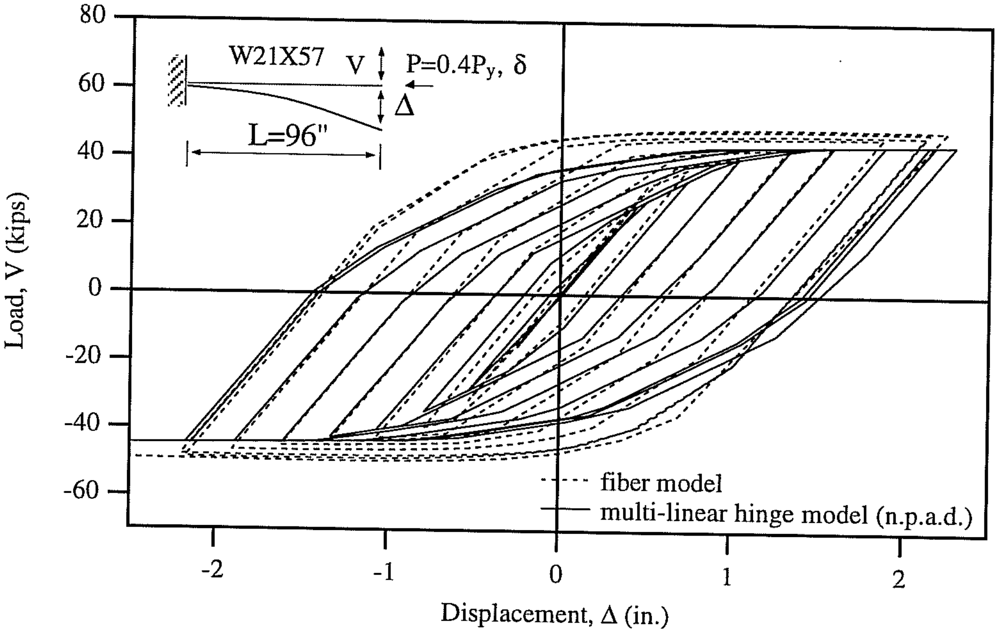

Fig. 4.45a: Comparison of Predicted Results by Fiber Model and Multi-Linear Hinge Model Neglectiing Plastic Axial Deformations for $P = 0.4P_y$.

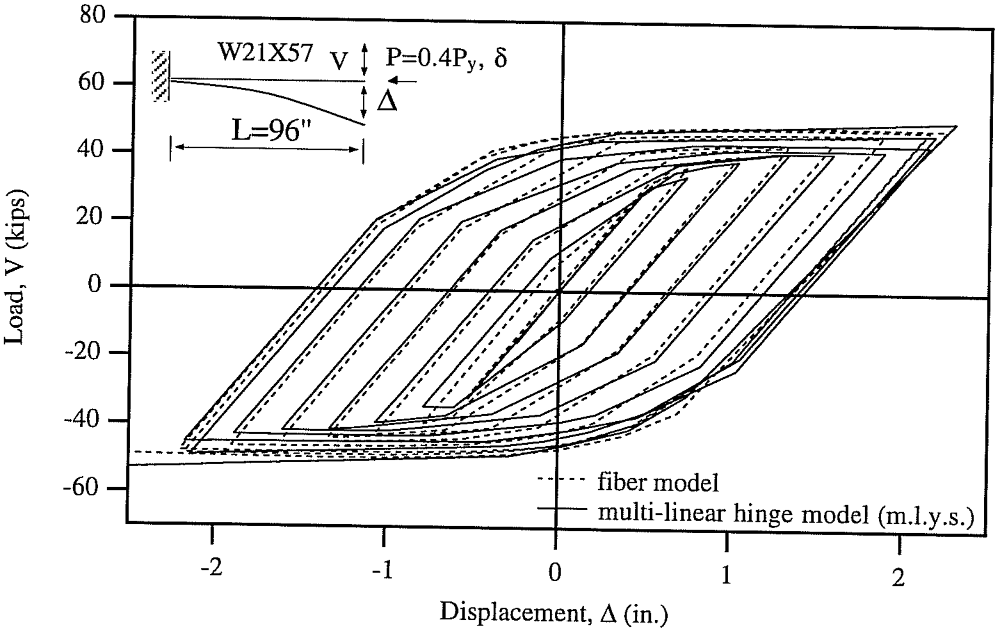

Fig. 4.45b: Comparison of Predicted Results by Fiber Model and Multi-Linear Hinge Model With Multi-linear Yield Surface for $P = 0.4P_y$.

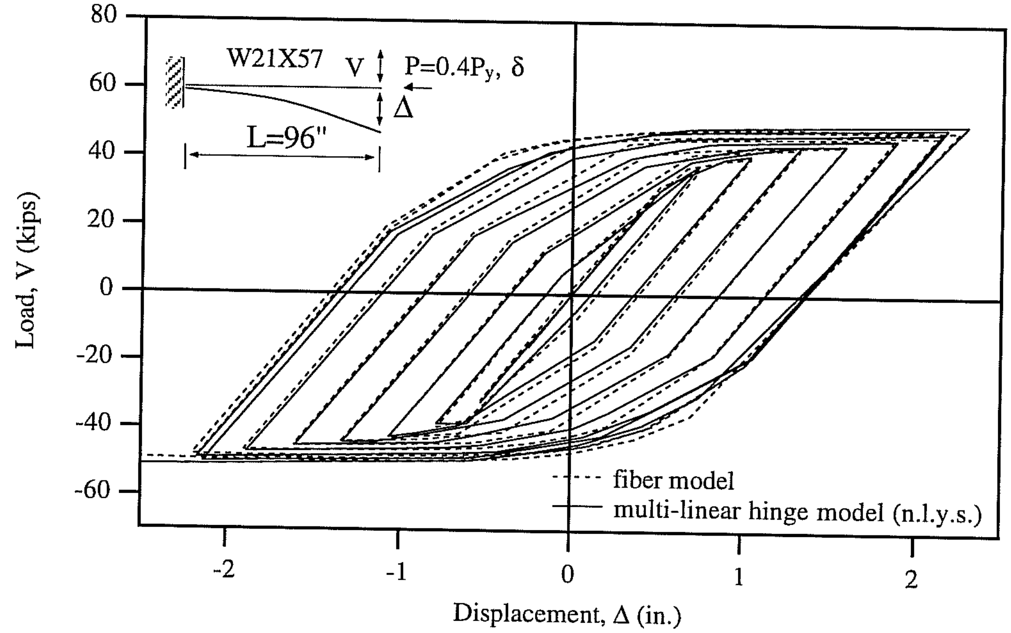

Fig. 4.45c: Comparison of Predicted Results by Fiber Model and Multi-Linear Hinge Model With Nonlinear Yield Surface for $P = 0.4P_y$.

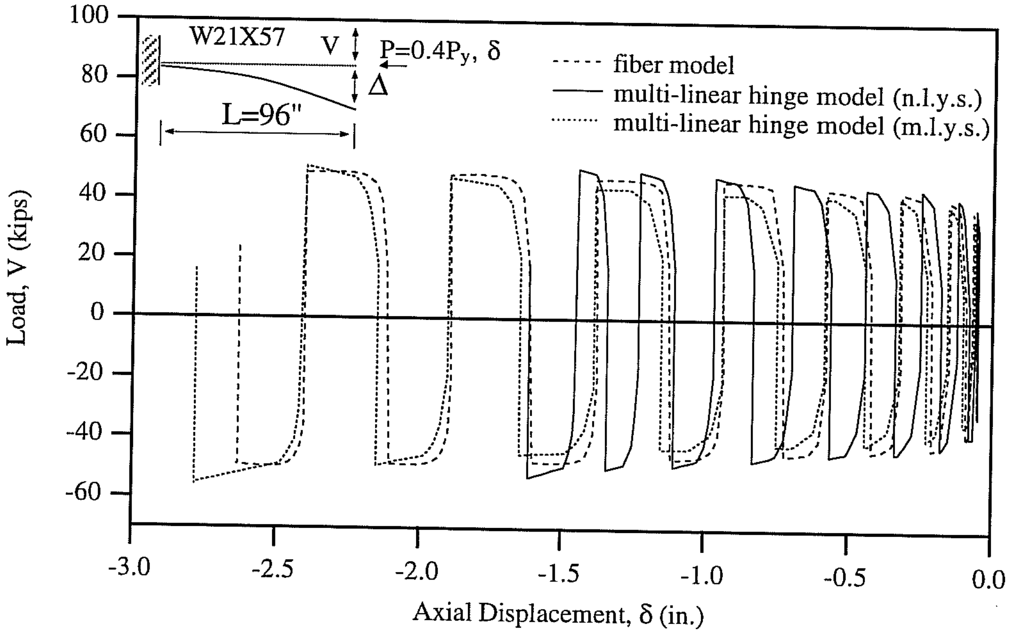

Fig. 4.45d: Comparison of Transverse Load-Axial Deformation Relationships Obtained by the Multi-Linear Hinge and Fiber Models for $P = 0.4P_y$.

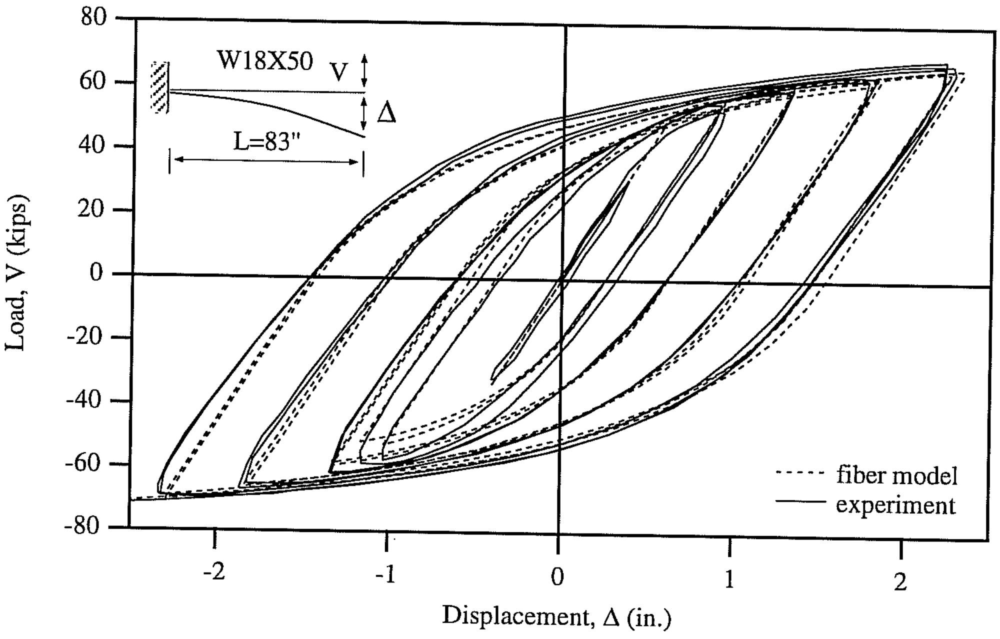

Fig. 4.46: Comparison of Experimental Results and Predictions Made by the Fiber Model for Popov Specimen 2.

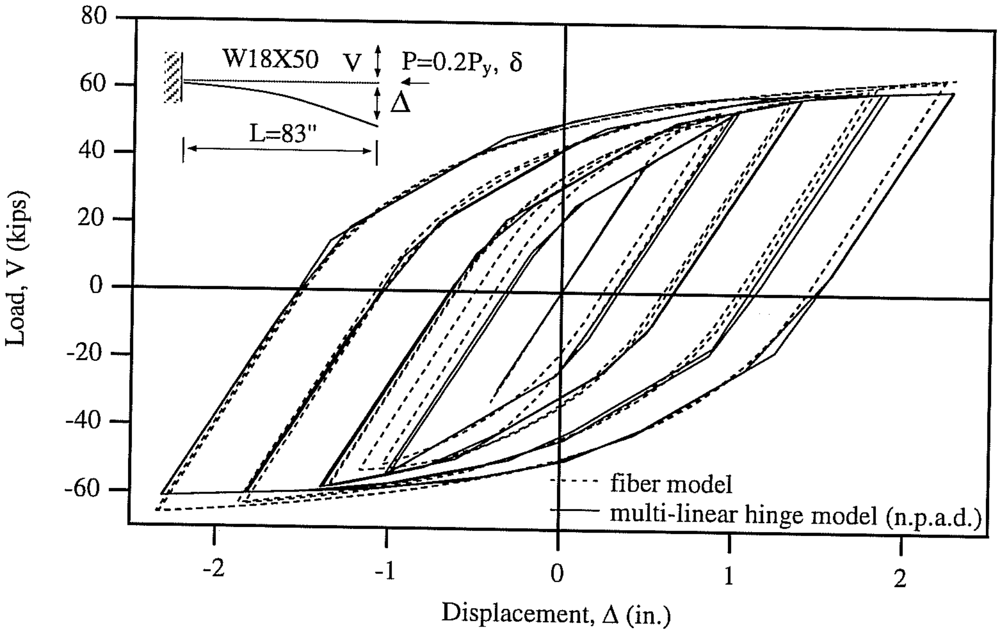

Fig. 4.47a: Comparison of Predicted Results by Fiber Model and Multi-Linear Hinge Model Neglecting Plastic Axial Deformation for $P = 0.2P_y$

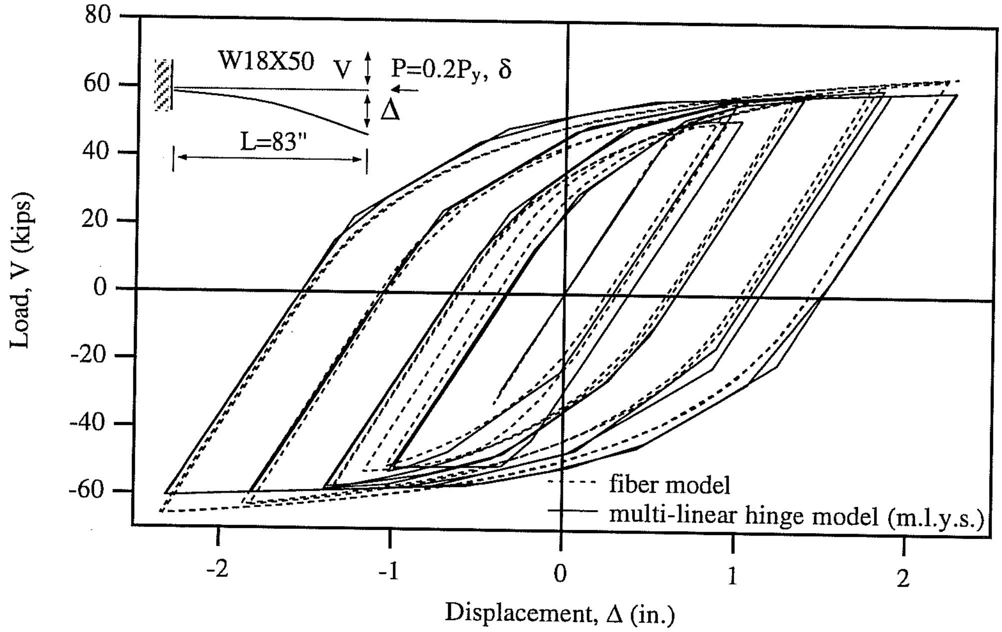

Fig. 4.47b: Comparison of Predicted Results by Fiber Model and Multi-Linear Hinge Model With Multi-linear Yield Surface for $P = 0.2P_y$

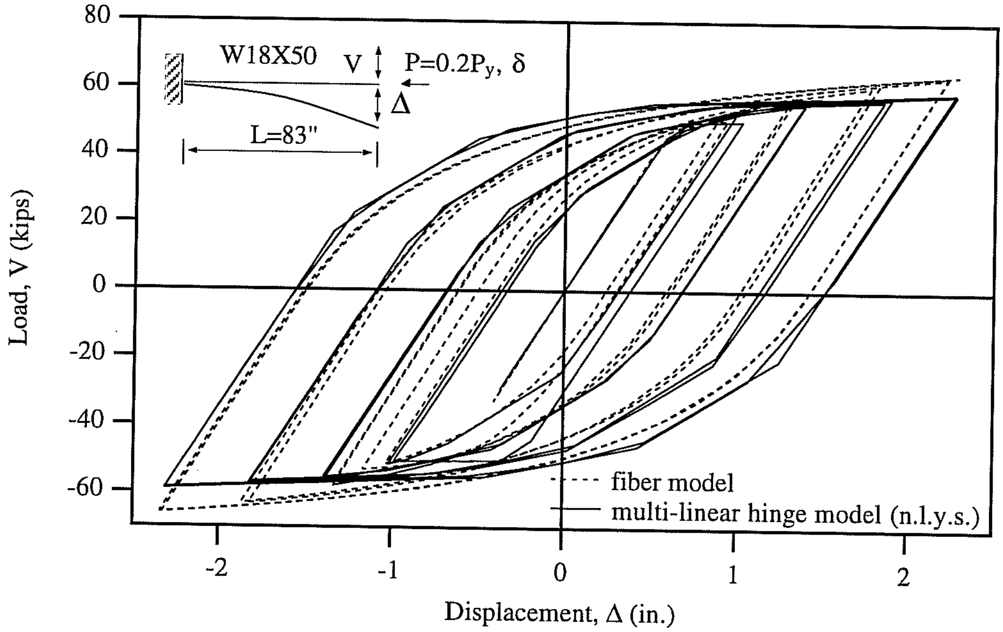

Fig. 4.47c: Comparison of Predicted Results by Fiber Model and Multi-Linear Hinge Model With Nonlinear Yield Surface for $P = 0.2P_y$

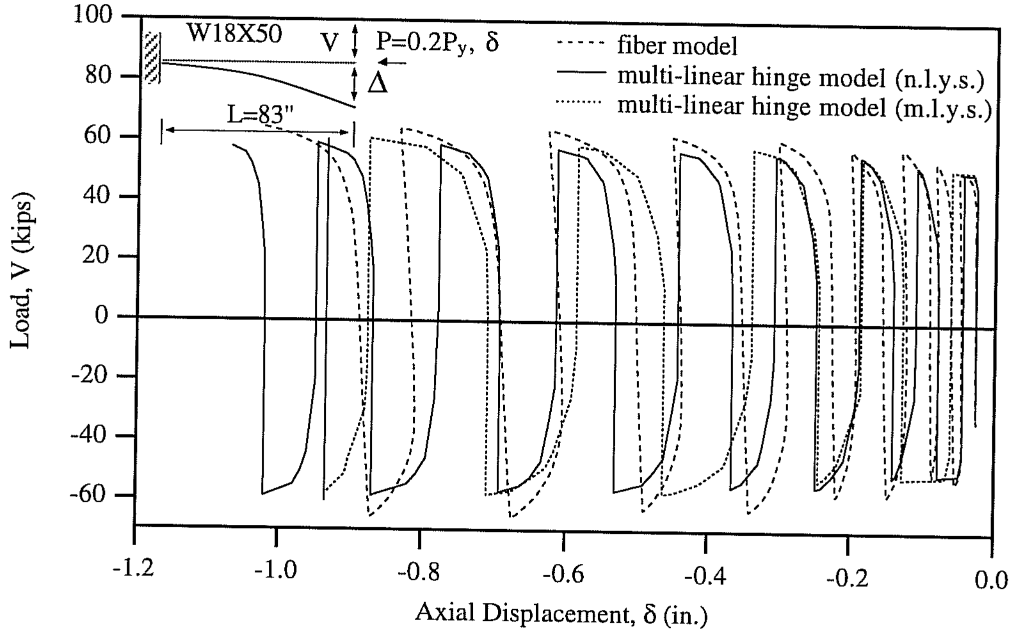

Fig. 4.47d: Comparison of Transverse Load-Axial Deformation Relationships Obtained by the Multi-Linear Hinge and Fiber Models for $P = 0.2P_y$.

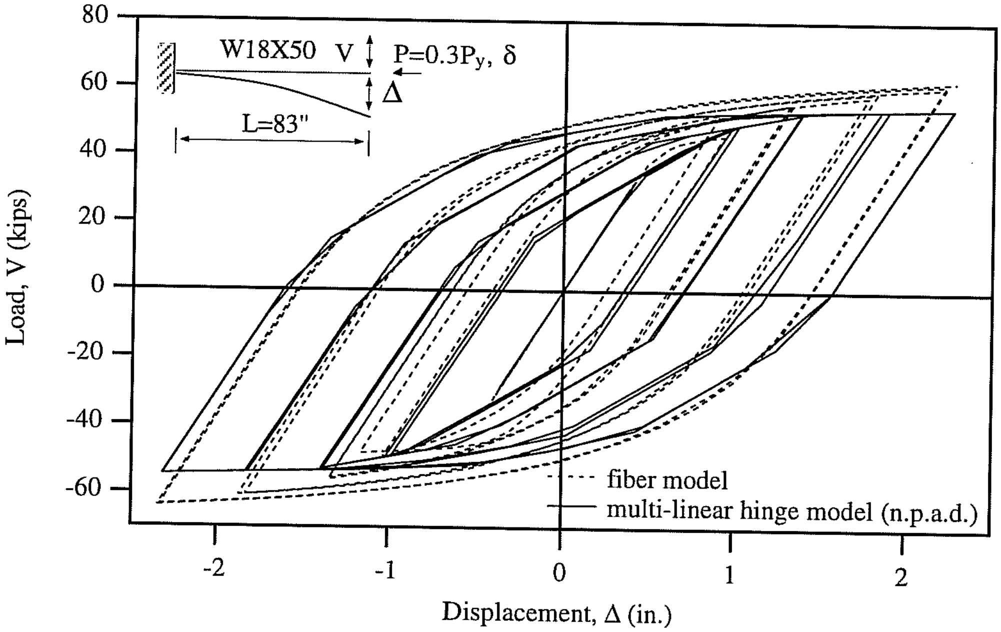

Fig. 4.48a: Comparison of Predicted Results by Fiber Model and Multi-Linear Hinge Model Neglectiing Plastic Axial Deformations for $P = 0.3P_y$

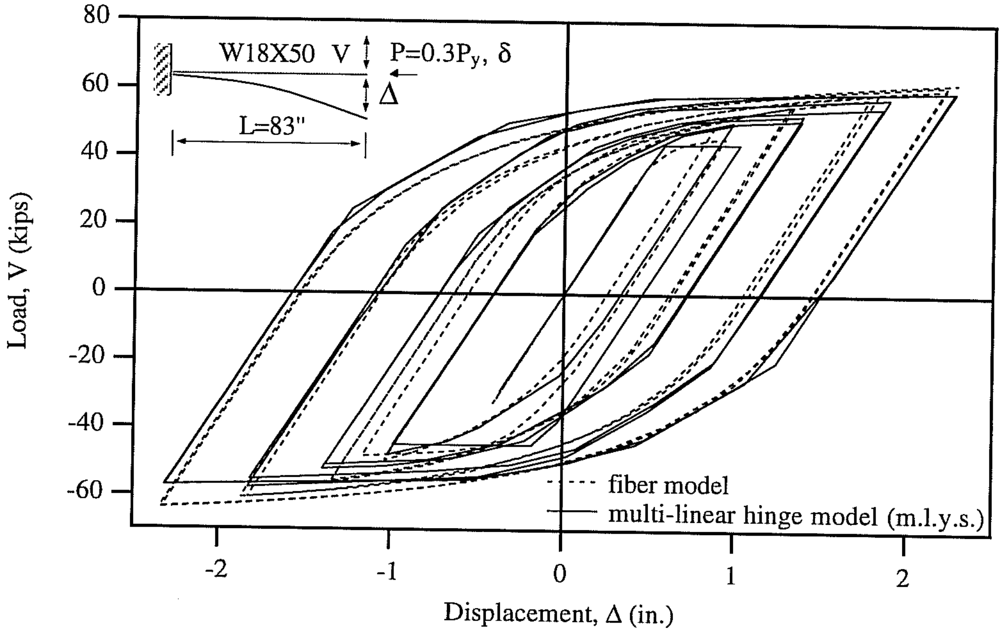

Fig. 4.48b: Comparison of Predicted Results by Fiber Model and Multi-Linear Hinge Model With Multi-linear Yield Surface for $P = 0.3P_y$

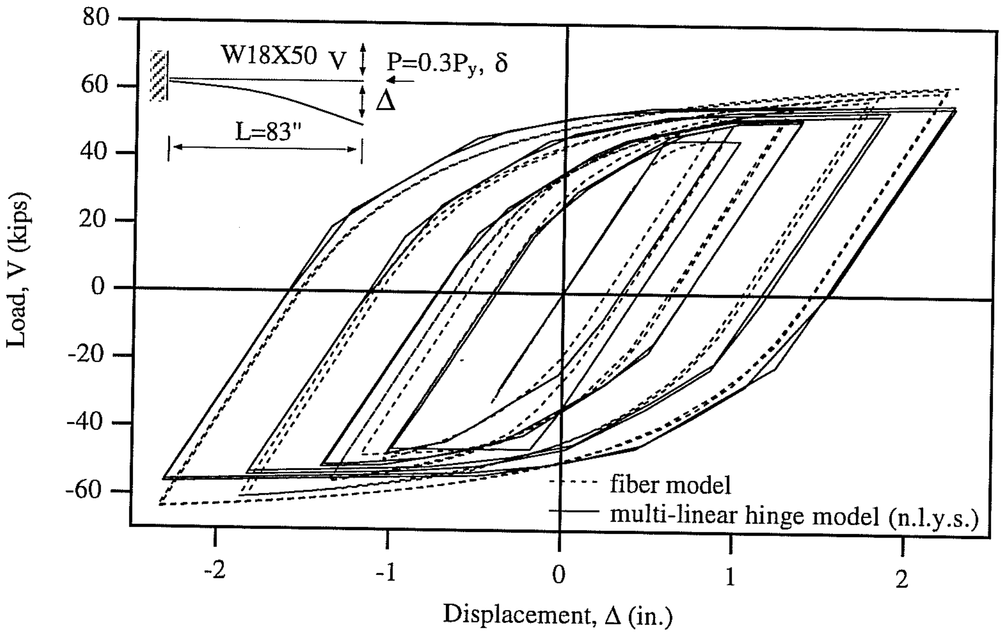

Fig. 4.48c: Comparison of Predicted Results by Fiber Model and Multi-Linear Hinge Model With Nonlinear Yield Surface for $P = 0.3P_y$

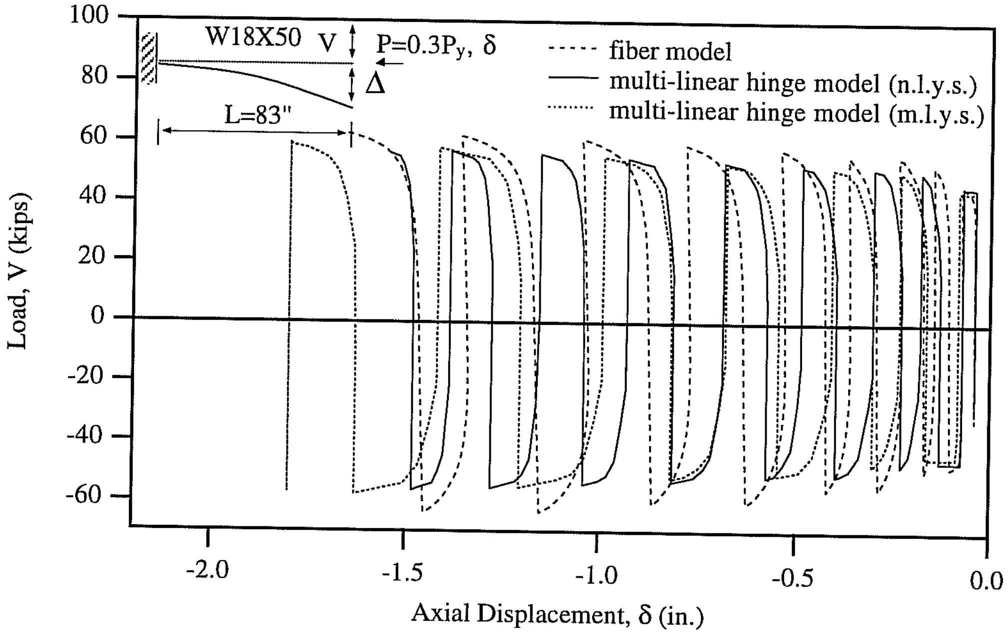

Fig. 4.48d: Comparison of Transverse Load-Axial Deformation Relationships Obtained by the Multi-Linear Hinge and Fiber Models for $P = 0.3P_y$.

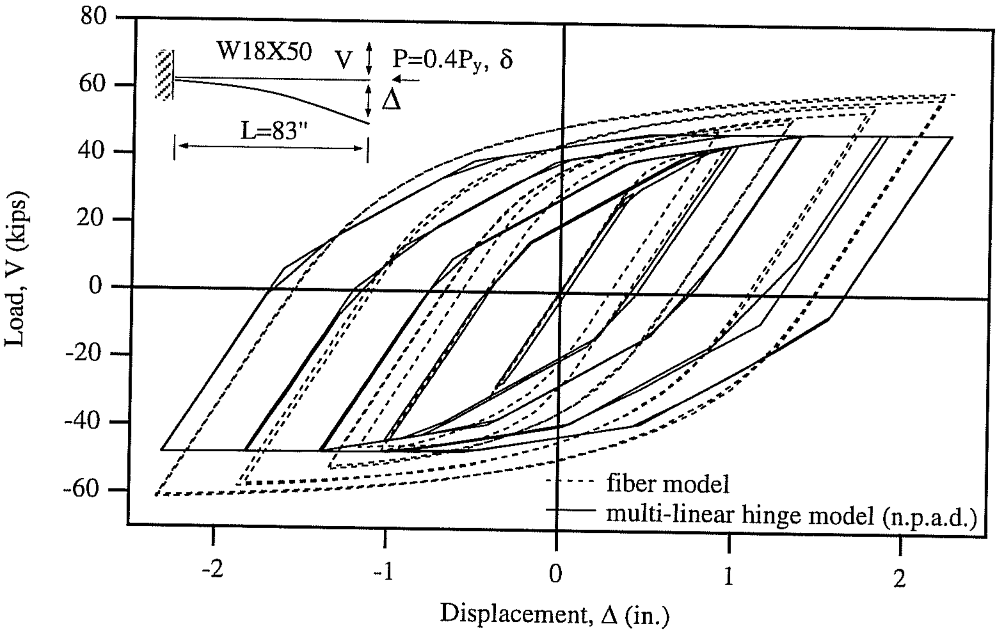

Fig. 4.49a: Comparison of Predicted Results by Fiber Model and Multi-Linear Hinge Model Neglectiing Plastic Axial Deformations for $P = 0.4P_y$.

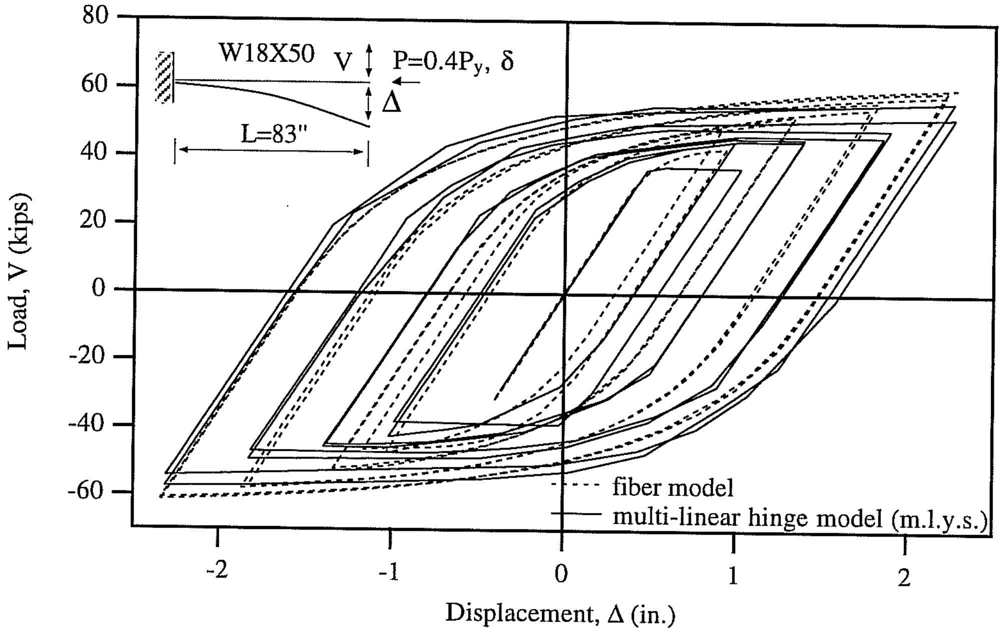

Fig. 4.49b: Comparison of Predicted Results by Fiber Model and Multi-Linear Hinge Model With Multi-linear Yield Surface for $P = 0.4P_y$.

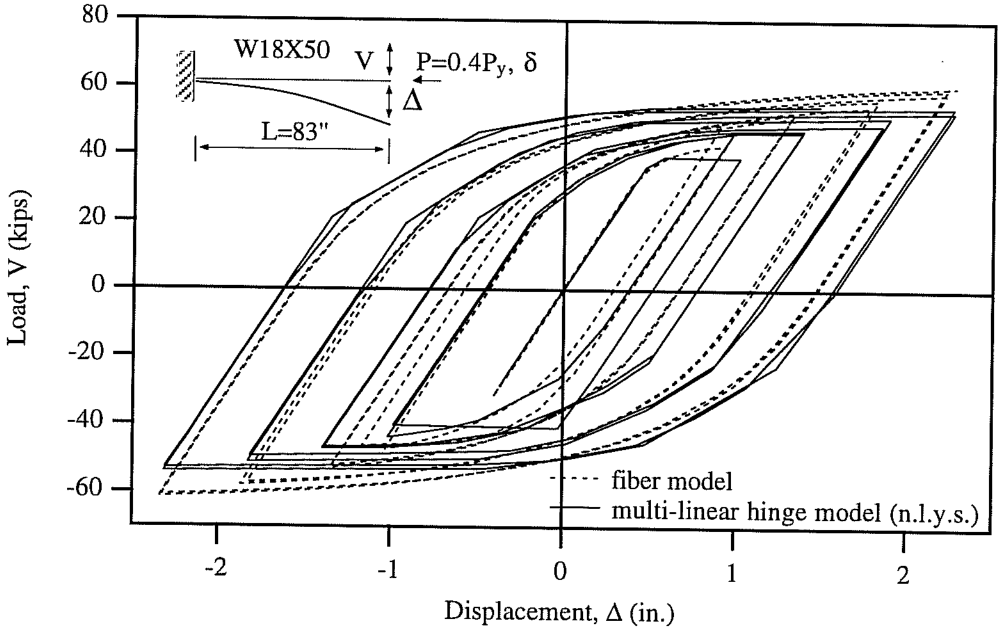

Fig. 4.49c: Comparison of Predicted Results by Fiber Model and Multi-Linear Hinge Model With Nonlinear Yield Surface for $P = 0.4P_y$.

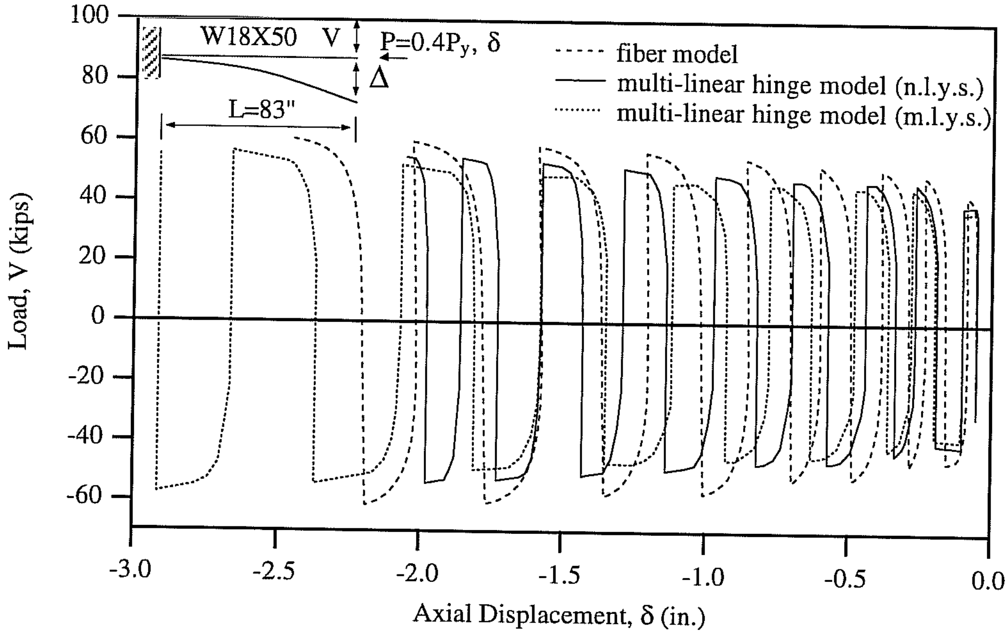

Fig. 4.49d: Comparison of Transverse Load-Axial Deformation Relationships Obtained by the Multi-Linear Hinge and Fiber Models for $P = 0.4P_y$.

4.5 Summary

In this chapter, the calibration and verification of the multi-linear hinge model have been presented. First, the beam behavior of the model was investigated. For all welded connections, the predicted results by the model were compared with experimental data for five test specimens. The agreement was reasonable. The model was also applied to eight test specimens with welded flange-bolted web connections. The correlation between the predicted results and experimental data was acceptable. To account for the transition from the virgin state to the saturated state, a weighting factor was determined through calibration to experimental data and to predictions made by the fiber model. The predictions made by the model employing the weighting factor matched well with the analytical results obtained by the fiber model. Second, the column behavior of the model was investigated. The multi-linear hinge model considering plastic axial deformations exhibited reasonable performance in the first and second order analyses. In general, the multi-linear hinge model showed significantly better performance than the bilinear hinge model and could properly model the beam-column behavior of bare steel members in moment resisting frames.

Chapter 5: PANEL ZONE ELEMENT

5.1 Introduction

In this chapter, an element is developed for modeling the cyclic load-deformation response of the panel zone region at the beam-column joint of a steel moment frame. The panel zone is the portion of the column contained within the beam-column joint. When a moment frame is subjected to lateral loads, high shear forces develop within the panel zone. The resulting deformations of the panel zone can have an important effect on the response of the frame in both the elastic and inelastic ranges of frame behavior (Tsai 1988).

Numerous tests have been performed in the past two decades to investigate the load-deformation behavior of the joint panel using connection subassemblies. Some significant observations from these tests are:

i)Joint panel zones often develop a maximum strength that is significantly greater than the strength at first yield. However, large inelastic panel zone deformations are typically required in order to develop maximum panel zone strength.

ii) Panel zone deformations can add significantly to the overall deformation of a subassembly, for both elastic and inelastic behavior of the panel zone.

iii) Panel zone stiffness and strength can be increased by the attachment of web doubler plates to the column within the joint region. The effectiveness of doubler plates is affected by the method used to connect them to the column.

iv) In the inelastic range, panel zones can exhibit very ductile behavior, both for monotonic and cyclic loading. Experimentally observed hysteresis loops are typically very stable, even at large inelastic deformations.

The Uniform Building Code, since its 1988 Edition, permits the formation of plastic hinges in the panel zones of steel moment frames under earthquake loading. Thus, rather than forming flexural hinges in the beams or columns, the primary source of energy dissipation in a steel moment frame can be the formation of plastic shear hinges in the panel zones. Consequently, an analytical model is needed to predict the cyclic inelastic response of a panel zone.

To include panel zone deformation in frame analysis, the traditional center-to-center line representation of the frame must be modified. Figure 5.1 shows a comparison of experimental results and analytical results for Krawinkler Specimen A-1 (Krawinkler 1971). The analytical results are obtained by using center-to-center line dimensions of the specimen. From the figure it can be seen that the analysis using the center-to-center line dimension may produce misleading results.

To model the behavior of panel zones in frame analysis, Lui (1985) developed a joint model based on the finite element method. The model consists of seven elements for interior beam-to-column joints: one web element, two flange elements (beam elements), and four connection elements. Although capable of representing a variety of deformation modes of panel zones, this model employed a simple isotropic hardening rule and therefore cannot realistically model cyclic behavior. Another disadvantage of this model is its high computational cost. Other finite element models using more sophisticated hardening rules could be developed for the analysis of column panel zones. However, in this study it was decided to use nonlinear rotational springs as the basis for modeling the panel zone in the nonlinear dynamic analysis of MRFs because of its simplicity and computational efficiency.

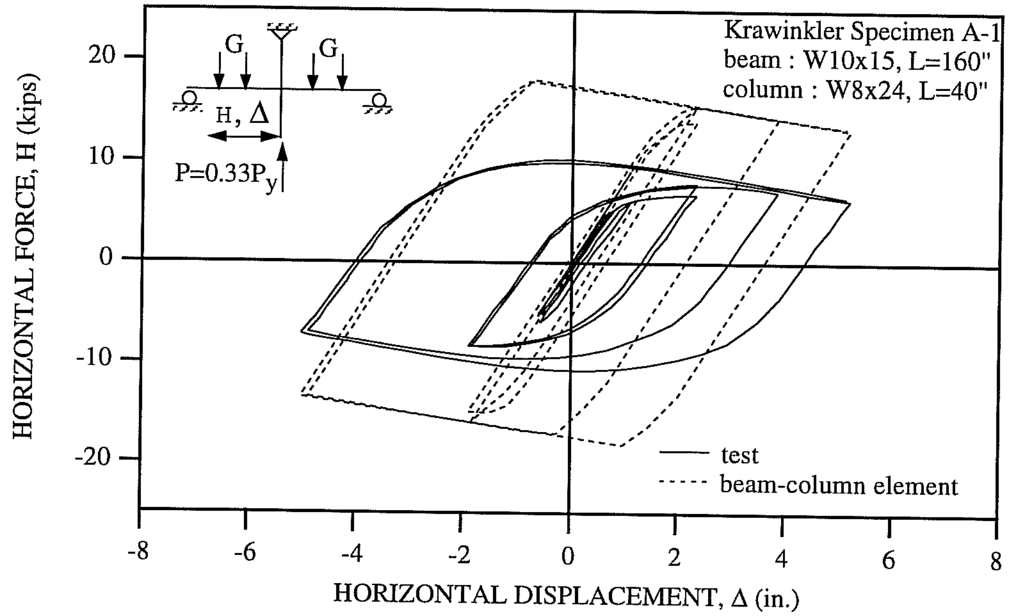

Fig. 5.1: Comparison of Test Results and Analytical Results Obtained by Using Center-to-Center Line Dimension Modeling

5.2 General Characteristics of Panel Zone Element

The panel zone element is essentially a rotational spring element, which transfers moment between the columns and beams framing into a joint (Kanaan and Powell 1973). The panel element has no dimension and connects two nodes with the same coordinates. One of these nodes is attached to the element(s) modeling the columns framing into the joint, as shown in Fig. 5.2, while the other node is attached to the element(s) modeling the beams. Therefore, the moment transferred by the panel element is related to relative rotation between the columns and beams framing into a joint. The vertical and horizontal translations of the two nodes are constrained to be identical so that the column and beam ends move together. Therefore, one vertical, one horizontal, and two rotational degrees of freedom exist at each joint.

The relative rotation between the connected nodes is related to the node rotations as follows:

$$d\Phi = \{1 \;\; -1\} \begin{Bmatrix} d\theta_I \\ d\theta_J \end{Bmatrix} \qquad (5.1)$$

or

$$d\Phi = [a]\,\{dr\} \qquad (5.2)$$

where $d\Phi$ is the increment of relative rotation (panel element deformation), and $d\theta_I$ and $d\theta_J$ are the increments of rotation of the connected nodes. The symbol γ is frequently used in the literature to represent panel zone deformation. This symbol reflects the shear deformation. The value of γ is the same as the value of Φ as defined above.

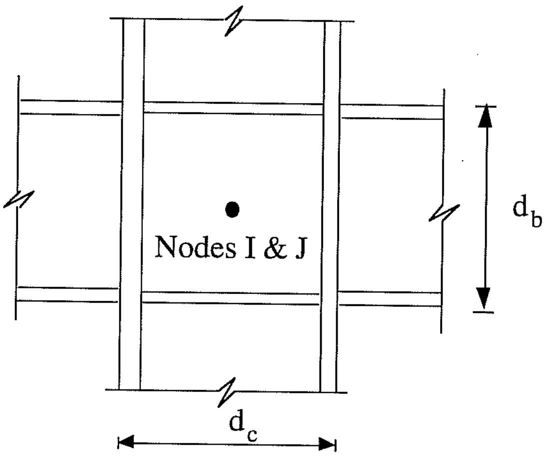

a) Interior Joint

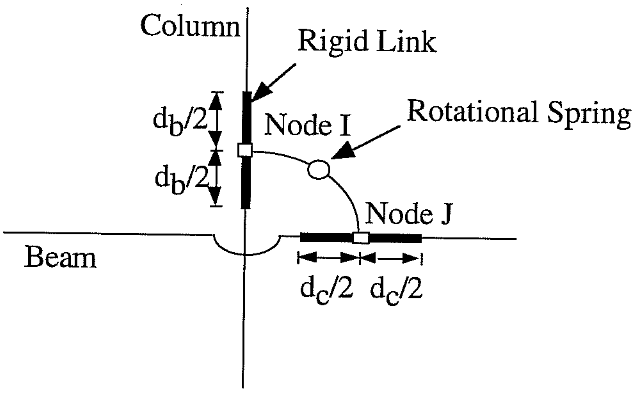

* Nodes I and J have identical coordinates

* Nodes I and J have identical translational displacments

b) Idealization of Interior Joint

Fig. 5.2: Idealization of Beam-to-Column Joint

Then the tangent stiffness relationship is

$$dM^{pa} = K_t \, d\Phi \tag{5.3}$$

where dM^{pa} is the increment of moment applied on a joint and K_t is the tangent stiffness of the joint. In terms of nodal rotations, the stiffness, $[K_T]$, is given by

$$[K_T] = [a]^T K_t [a] \tag{5.4}$$

The definable properties of a panel element are the rotational stiffnesses and yield moments. In the following sections, existing panel zone models for monotonic loading are reviewed, and an improved model is proposed. This is followed by the development of hysteretic rules for a cyclic loading model.

5.3 Mathematical Models for Monotonic Behavior of Panel Zones

5.3.1 Review of the Existing Models

Three researchers (Fielding 1971; Krawinkler 1971; Wang 1988) have proposed their mathematical models to predict panel zone behavior under monotonic loading. They are briefly reviewed below.

The boundary forces on a joint panel shown in Fig.5.3 can be transformed into an approximate equivalent shear force from equilibrium as follows;

$$\begin{aligned} V_{eq} &= \frac{M_{bl} + M_{br}}{d_b - t_{bf}} - 0.5 \cdot \left(V_{ct} + V_{cb}\right) \\ &\approx \frac{M_{bl} + M_{br}}{d_b - t_{bf}} \cdot (1 - \rho) = \frac{M^{pa}}{d_b - t_{bf}} \cdot (1 - \rho) \end{aligned} \tag{5.5a}$$

or

$$M^{pa} = \frac{V_{eq}}{(1 - \rho)} \cdot \left(d_b - t_{bf}\right) \tag{5.5b}$$

where $\rho = \dfrac{d_b - t_{bf}}{H_c}$

$M^{pa} = M_{bl} + M_{br}$ = panel zone moment

M_{bl} = moment in beam on left side of panel zone

M_{br} = moment in beam on right side of panel zone

V_{ct} = shear in column on top side of panel zone

V_{cb} = shear in column on bottom side of panel zone

d_b = depth of beam cross-section

t_{bf} = thickness of beam flange

H_c = column height

M_{ct} = moment in column at top of panel zone (Fig. 5.3)

M_{cb} = moment in column at bottom of panel zone (Fig. 5.3).

A key simplification in this analysis is that the beam moments are replaced by an equivalent couple, with the forces acting at mid-depth of the beam flanges. These forces produce a large shear in the panel zone. The shear in the column segments outside of the panel zone are then subtracted to obtain the net shear force, V_{eq}, acting on the panel zone. In obtaining the shear forces in the column segments outside of the panel zone, it is assumed that points of inflection in the column occur at a distance $H_c/2$ above and below the panel zone.

The three researchers proposed panel zone moment M^{pa}-panel zone deformation γ relations for monotonic loading, which are based on the equivalent shear force V_{eq}. Fielding proposed a bilinear relationship, as shown in Fig. 5.4a. Krawinkler and Wang each proposed different trilinear panel zone moment-panel zone deformation relations, as shown in Fig. 5.4b. In the following paragraphs, the formulations of these panel zone moment-panel zone deformation relations are presented in detail.

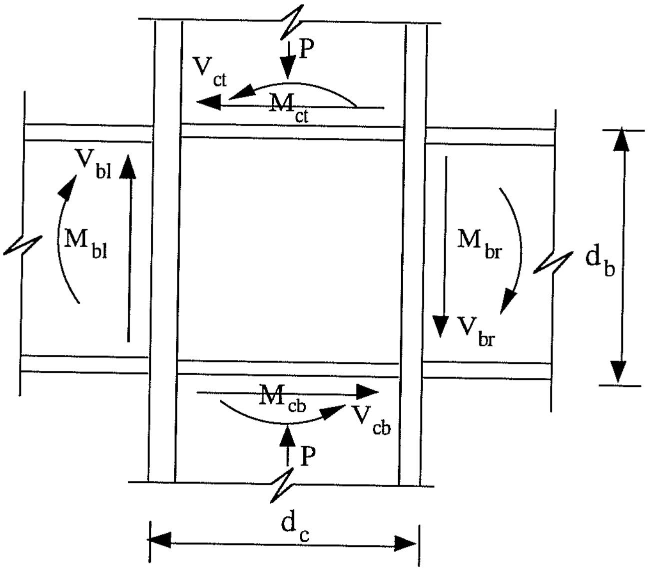

a) Panel Boundary Forces

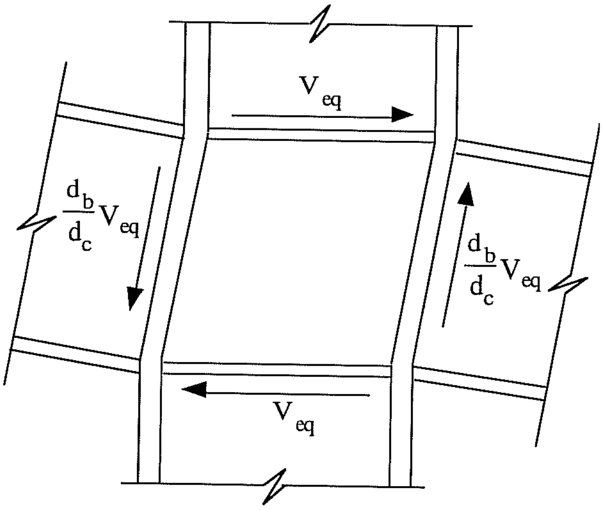

b) Equivalent Panel Shear Forces

Fig. 5.3: Boundary Forces and Equivalent Shear Forces on Panel Zone

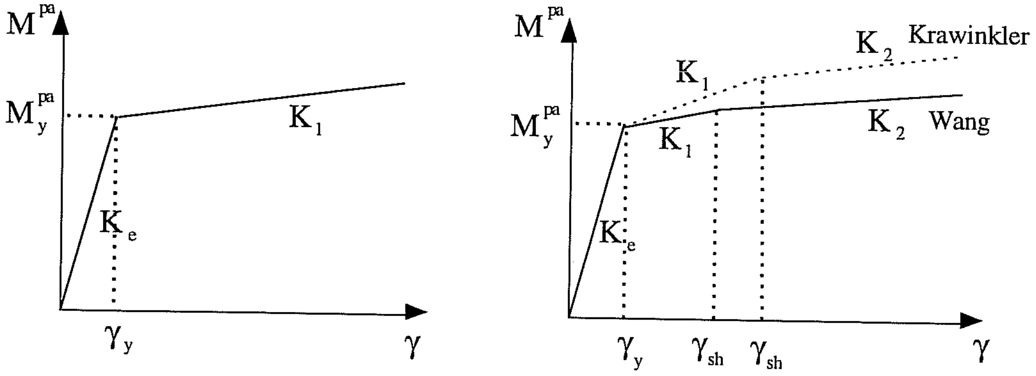

a) Fielding's Bilinear Model b) Krawinkler and Wang's Trilinear Models

Fig. 5.4: Existing Panel Zone Moment-Panel Zone Deformation Models

In the elastic range, these three researchers all assumed that the in-plane stiffness of the beams framing into the column is sufficiently large to justify the assumption of rigid boundaries around the panel zone. Therefore, the shearing stress is uniformly distributed throughout the panel, and the elastic stiffness of the panel zone is determined by considering the area of the panel zone web. Fielding and Krawinkler considered the effective shear area of $(d_c - t_{cf}) \cdot t_{cw}$, where the subscripts ‘c’, ‘f’, and ‘w’ stand for column, flange, and web, respectively. They suggested the yield moment and elastic stiffness of panel zones as follows:

$$M_y^{pa} = \frac{\bar{\tau}_y \cdot (d_c - t_{cf}) \cdot t_{cw} \cdot d_b}{(1-\rho)} \tag{5.6a}$$

$$K_e = \frac{M_y^{pa}}{\gamma_y} = \frac{G \cdot (d_c - t_{cf}) \cdot t_{cw} \cdot d_b}{(1 - \rho)} \tag{5.6b}$$

Neglecting the contribution of column flanges in resisting panel zone shear in the elastic range and considering an effective shear area of $(d_c - 2t_{cf}) \cdot t_{cw}$, Wang suggested the following yield moment and elastic stiffness

$$M_y^{pa} = \frac{\bar{\tau}_y \cdot (d_c - 2t_{cf}) \cdot t_{cw} \cdot (d_b - t_{bf})}{(1-\rho)} \tag{5.7a}$$

$$K_e = \frac{M_y^{pa}}{\gamma_y} = \frac{G \cdot (d_c - 2t_{cf}) \cdot t_{cw} \cdot (d_b - t_{bf})}{(1 - \rho)} \tag{5.7b}$$

where $\bar{\tau}_y$ is the Von Mises yield shear stress of the column web, based on shear and axial force interaction. The Von Mises yield shear stress $\bar{\tau}_y$ is taken as:

$$\bar{\tau}_y = \frac{\sigma_y}{\sqrt{3}} \cdot \sqrt{1 - (P/P_y)^2} \tag{5.7c}$$

where P and P_y are axial force and axial yield force on the column, respectively, and σ_y is the yield stress of the column web.

For the inelastic range, different formulas were presented in the models. Fielding considered the elastic bending stiffness of the column flange for the post yield stiffness as shown in Fig.5.5b and proposed a bilinear model, with:

$$K_1 = \frac{5.2 \cdot G \cdot b_{cf} \cdot t_{cf}^3}{d_b \cdot (1 - \rho)} \qquad (5.8)$$

The other researchers, Krawinkler and Wang, each proposed different empirical formulas for the post-elastic stiffness. Krawinkler's model is shown in Fig. 5.5c. It consists of an elastic-perfectly plastic shear panel surrounded by rigid boundaries with springs at the four corners. Krawinkler assumed that these springs simulate the resistance of the elements surrounding the panel zone, in particular the bending resistance of the column flanges and that the spring stiffness can be approximated by

$$K_s = \frac{E \cdot b_{cf} \cdot t_{cf}^2}{10} \quad K_1 \qquad (5.9a)$$

From the work equation and Eq.5.9a the post elastic stiffness K_1 is obtained

$$K_1 = \frac{\Delta M^{pa}}{\Delta \gamma} = \frac{1.04 \cdot G \cdot b_{cf} \cdot t_{cf}^2}{(1 - \rho)} \qquad (5.9b)$$

where $\Delta M^{pa} = \Delta V_{eq} \cdot (0.95 d_b)/(1 - \rho)$. Wang assumed that when strain hardening started($\gamma_{sh} = 3.5\gamma_y$), plastic hinges formed at the four corners of the column flanges shown in Fig. 5.5d. From this assumption the post elastic stiffness K_1 is

$$K_1 = \frac{\Delta M_{sh}^{pa}}{\Delta \gamma_{sh}} = 0.7 \cdot G \cdot b_{cf} \cdot t_{cf}^2 \qquad (5.10)$$

where $\Delta M_{sh}^{pa} = 4M_{pcf}$, $\Delta \gamma_{sh} = 2.5\, \gamma_y$, and M_{pcf} is the plastic moment of column flange. Note that the three researchers all considered the contribution only of column flanges in the post elastic stiffness K_1.

Krawinkler and Wang assumed that strain hardening begins at $\gamma_{sh} = 4\gamma_y$ and $3.5\gamma_y$, respectively. Both researchers considered strain-hardening effects of the panel zone and proposed a tri-linear model. The strain-hardening branch stiffness K_2 was suggested as follows:

$$K_2 = \frac{G_{st} \cdot A_{eff} \cdot d_b}{(1 - \rho)} \qquad (5.11)$$

where the effective shear A_{eff} is $(d_c - t_{cf})t_{cw}$ and $(d_c - 2t_{cf})t_{cw}$ for Krawinkler and Wang, respectively.

The existing models have been applied to four specimens tested by Krawinkler (1971), Fielding (1971), and Slutter (1981), as shown in Figs. 5.6a to 5.6d. Material properties and the type of connection for these specimens are presented in Table 5.1. Figures 5.7 to 5.10 show test results compared with the three existing models discussed above. Additional comparisons are shown in Figs. 5.11 to 5.16. In these figures, finite element analysis predictions are provided for Slutter's Specimen 1. This specimen was analyzed a number of times, varying the column flange thickness. These analyses were reported by Wang (1988). The finite element analyses provide an indication of the expected response of panel zones in columns with thick flanges. Only limited experimental data is available for cases with thick column flanges. In Figs. 5.11 to 5.16, the finite element predictions are compared with the predictions of the simplified models.

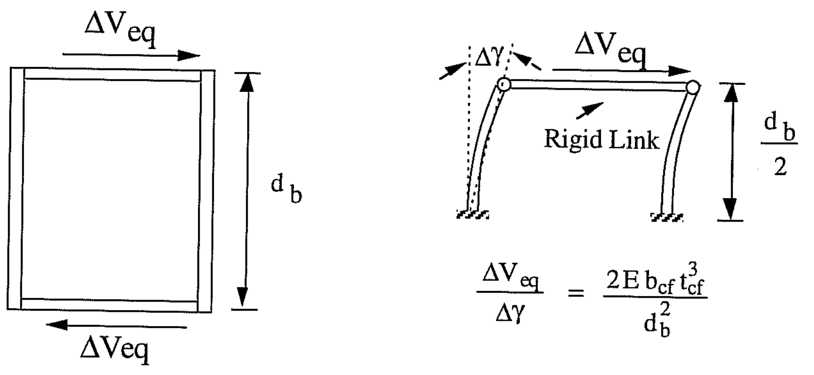

$$\frac{\Delta V_{eq}}{\Delta\gamma} = \frac{2E\, b_{cf}\, t_{cf}^3}{d_b^2}$$

a) Panel Zone

b) Fielding's Model

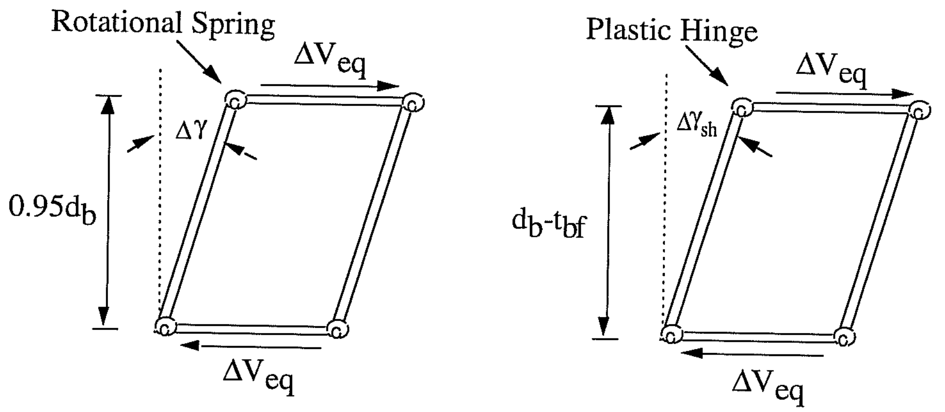

$$K_s = \frac{M_s}{\Delta\gamma} = \frac{E \cdot b_{cf} \cdot t_{cf}{}^2}{10}$$

$$\frac{\Delta V_{eq}}{\Delta\gamma} = \frac{4M_s}{0.95 d_b \Delta\gamma} = \frac{4K_s}{0.95 d_b}$$

$$M_{pcf} = \sigma_y \cdot b_{cf} \cdot t_{cf}^2/4$$

$$\Delta\gamma_{sh} = 2.5\,\gamma_y$$

$$\frac{\Delta V_{eq}}{\Delta\gamma_{sh}} = \frac{4M_{pcf}(1-\rho)}{2.5\gamma_y(d_b - t_{bf})}$$

c). Krawinkler's Model

d). Wang's Model

Fig. 5.5 Post Elastic Stiffness Models

Test Specimen	Yield Stress (ksi)				Connection Type	Doubler Plate	Continuity Plate
	Beam		Column				
	Web	Flg.	Web	Flg.			
Krawinkler A	52	41.5	41	40.5	fully welded	no	yes
Krawinkler B	46.5	38.5	47	42.5	fully welded	no	no
Fielding	31.4	29.35	33.3	29.55	fully welded	no	yes
Slutter 1	41.8	41.8	42.2	37.7	bolted web-welded flg.	no	yes

Table 5.1 Material Properties and Connection Types

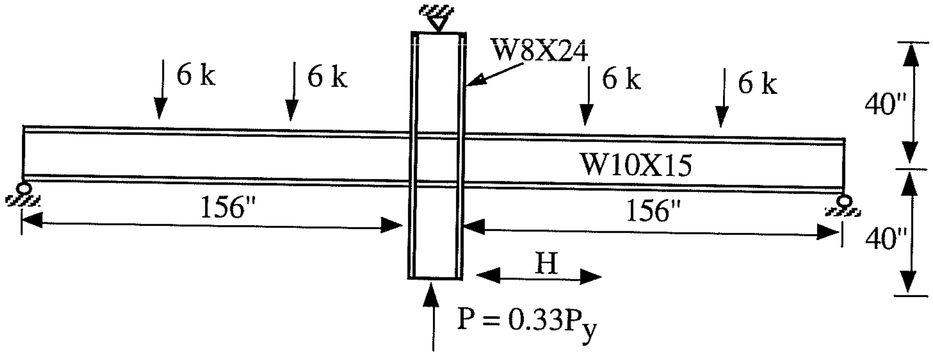

Fig. 5.6a): Krawinkler's Specimen A

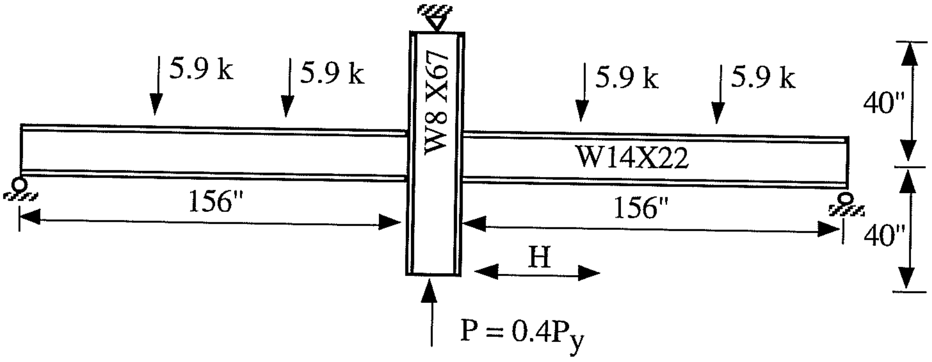

Fig. 5.6b): Krawinkler's Specimen B

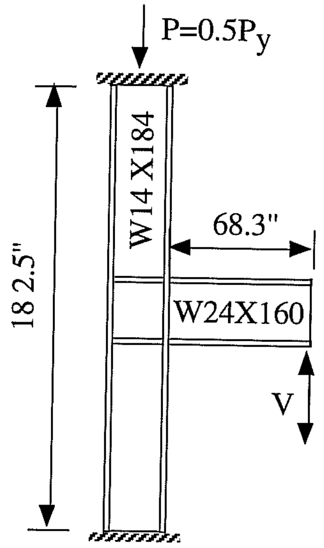

Fig. 5.6c): Fielding's Specimen

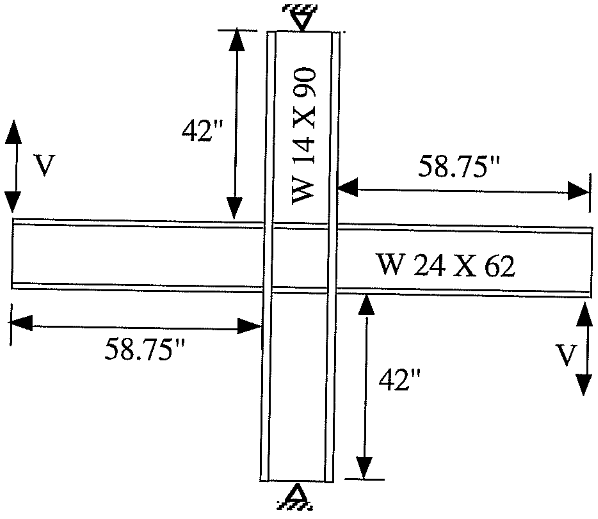

Fig. 5.6d): Slutter's Specimen 1

Fielding's bilinear model shows the poorest performance at large rotations regardless of column flange thickness because this model neglects strain-hardening. The performance of Krawinkler's model appears acceptable for panel zone joints with column flange thickness less than about one inch. However, for thicker column flanges, this model significantly overestimates panel zone strength. It appears that Krawinkler's model significantly overestimates the contribution of the column flanges. Wang's model generally underestimates panel zone strength regardless of column flange thickness apparently because in this model, the effective shear area of the panel zones is calculated as $(d_c - 2t_{cf})\cdot t_{cw}$ instead of the other models' effective shear area $(d_c - t_{cf})\cdot t_{cw}$.

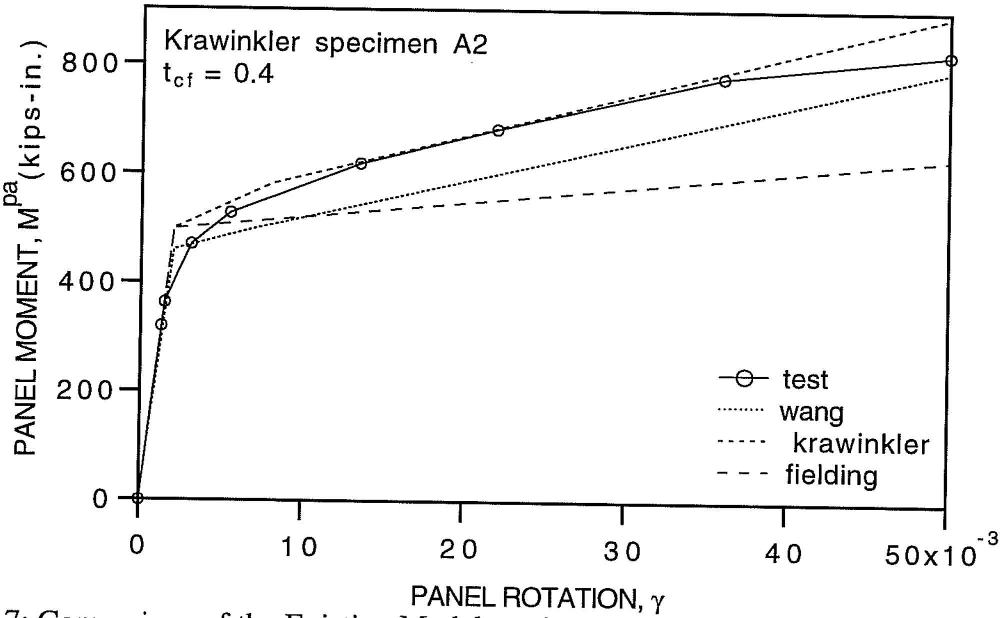

Fig. 5.7: Comparison of the Existing Models and Test Data for Krawinkler Specimen A2

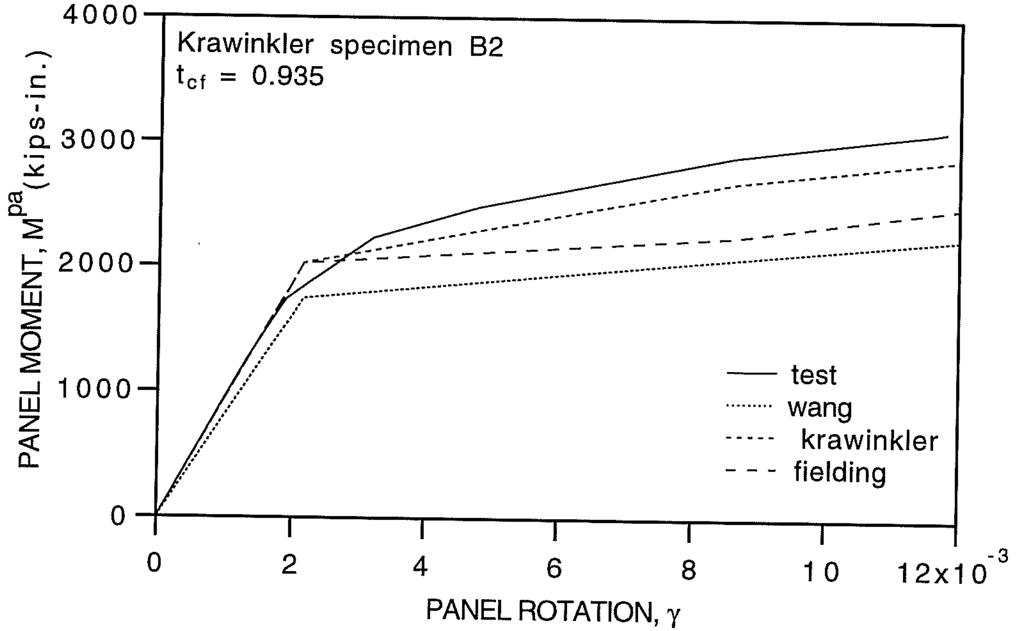

Fig. 5.8: Comparison of the Existing Models and Test Data for Krawinkler Specimen B2

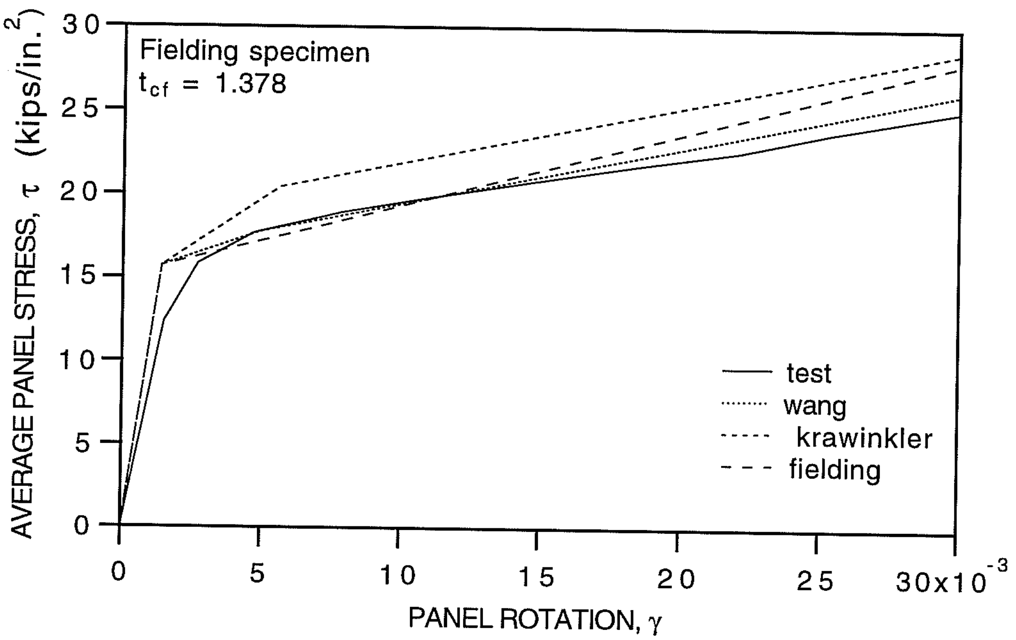

Fig. 5.9: Comparison of the Existing Models and Test Data for Fielding Specimen

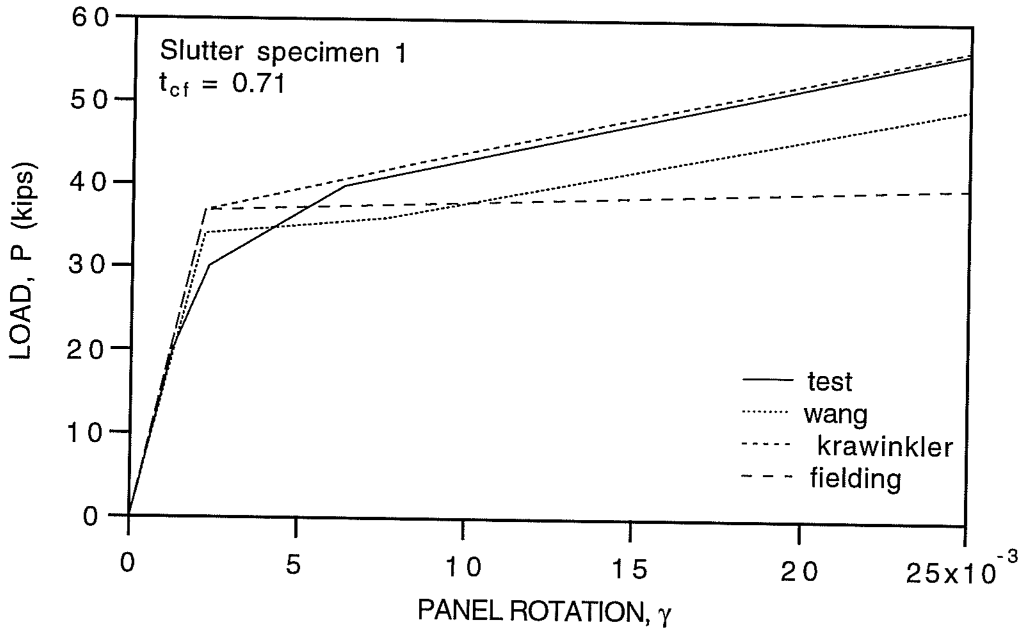

Fig. 5.10: Comparison of the Existing Models and Test Data for Slutter Specimen 1

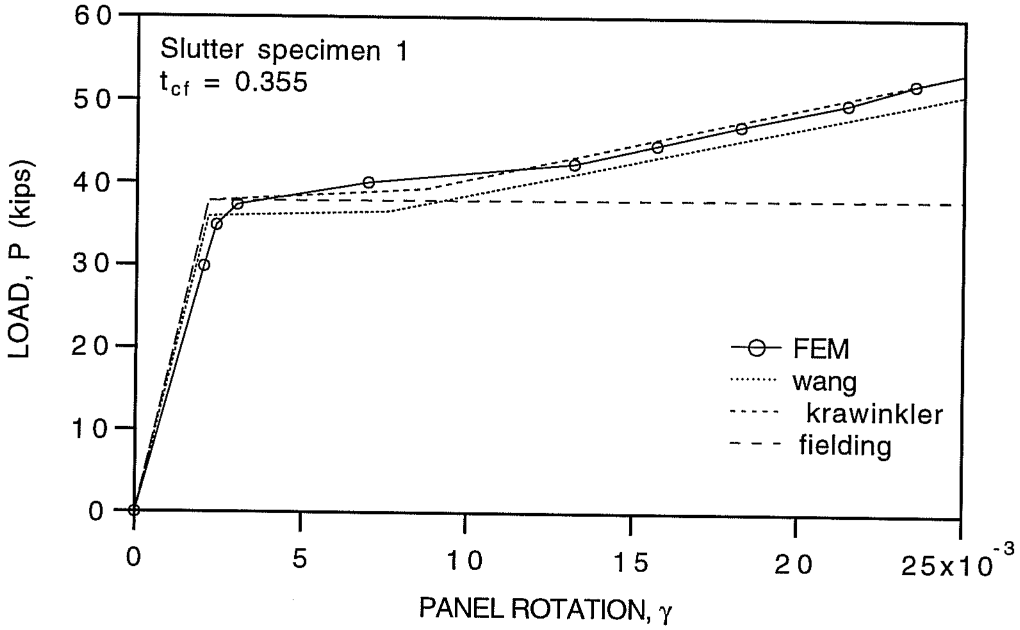

Fig. 5.11: Comparison of the Existing Models and FEM Result for Slutter Specimen 1 with t_{cf} = 0.355"

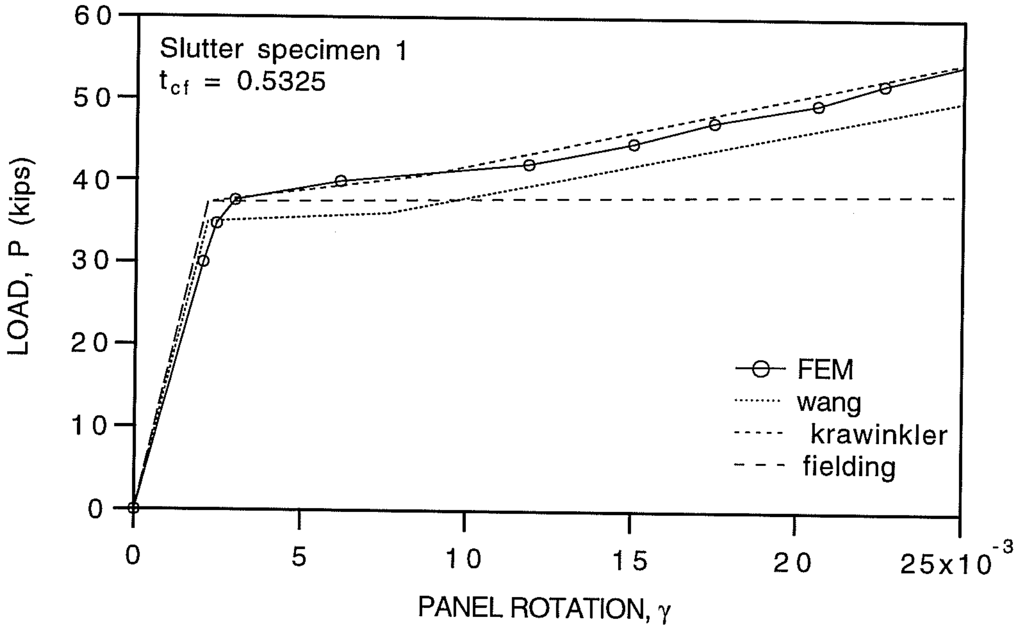

Fig. 5.12: Comparison of the Existing Models and FEM Result for Slutter Specimen 1 with t_{cf} = 0.5325"

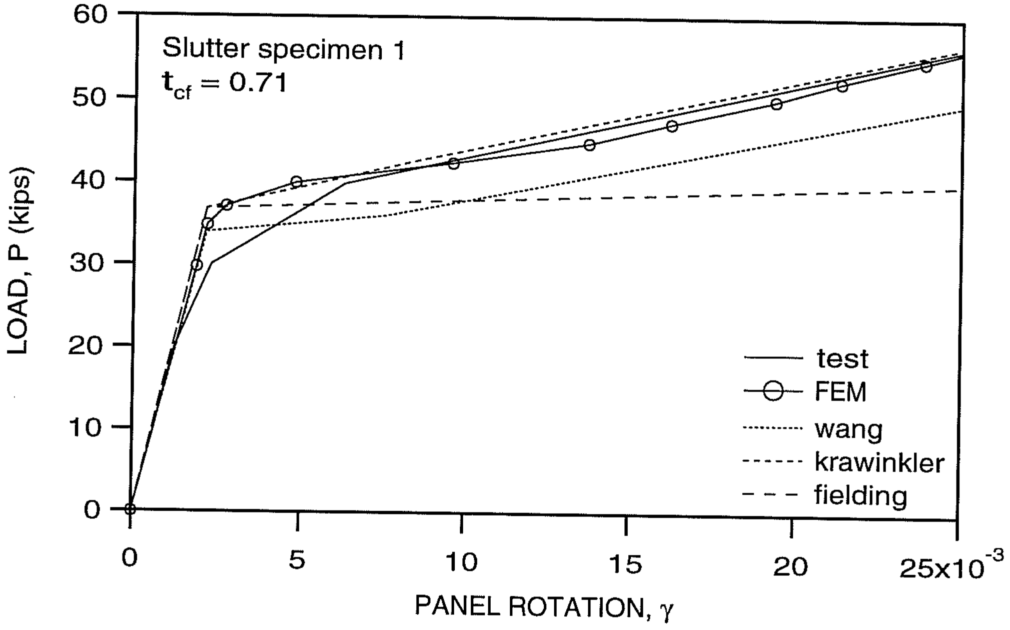

Fig. 5.13: Comparison of the Existing Models and FEM Result for Slutter Specimen 1 with t_{cf} = 0.71"

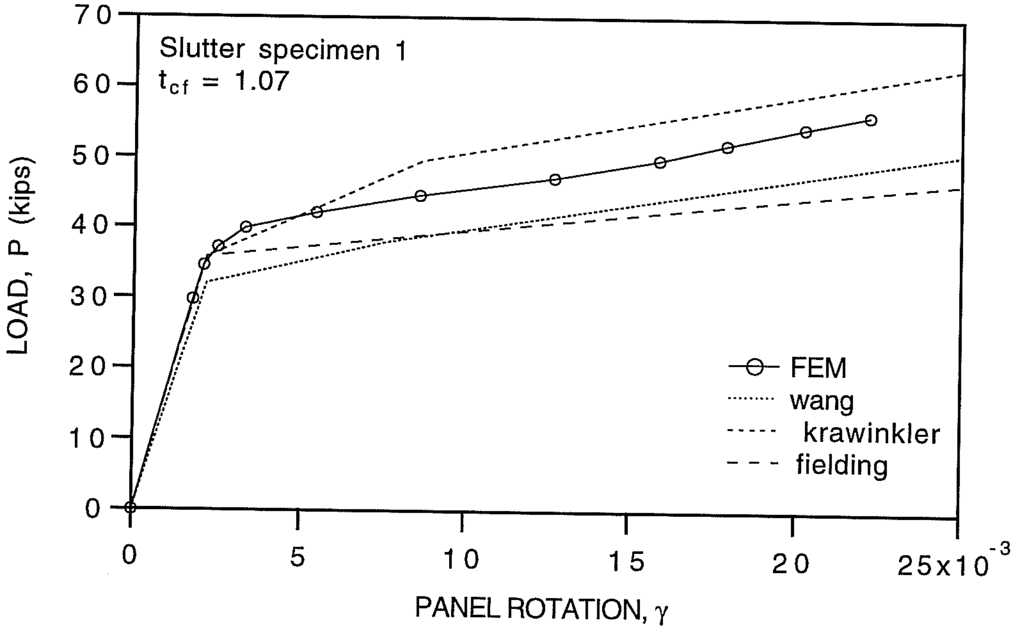

Fig. 5.14: Comparison of the Existing Models and FEM Result for Slutter Specimen 1 with t_{cf} = 1.07"

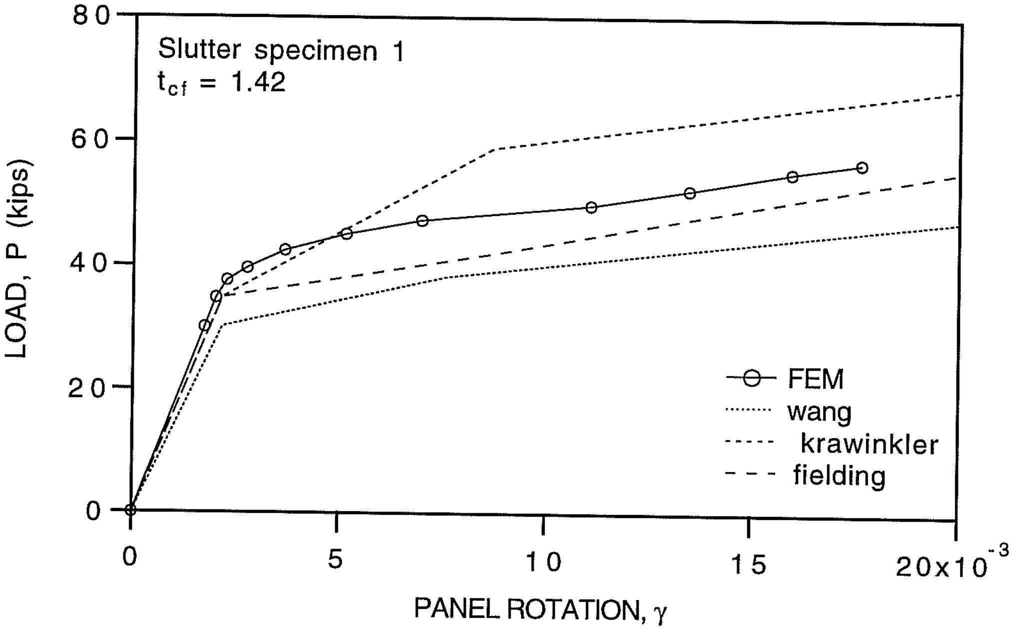

Fig. 5.15: Comparison of the Existing Models and FEM Result for Slutter Specimen 1 with t_{cf} = 1.42"

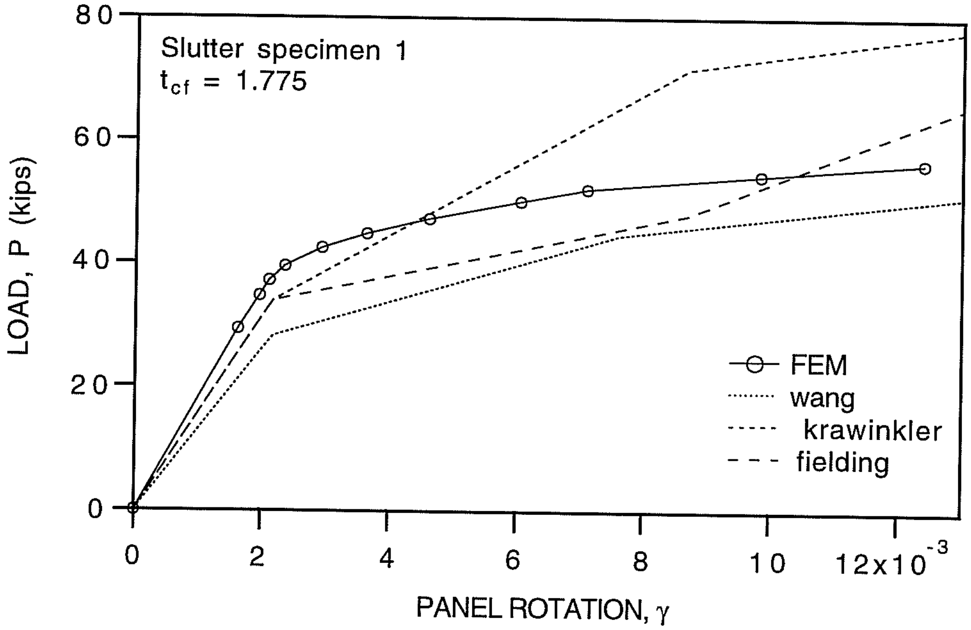

Fig. 5.16: Comparison of the Existing Models and FEM Result for Slutter Specimen 1 with t_{cf} = 1.775"

5.3.2 Modification of the Existing Models

In this study, simple modifications will be applied to Fielding's model and to Wang's model to provide better correlation with test and FEM results. Modifications to both models are accomplished as follows. i) The effective shear area is calculated as $d_c \cdot t_{cw}$ for both models because, as the ratio of column flange thickness to column depth increases, the influence of column flange thickness on panel yield moments and elastic stiffness increases. ii) For Fielding's bilinear model, assuming that strain-hardening starts at $4 \cdot \gamma_y$, strain-hardening effects are added to account for the fact that this model performs well except at large panel rotations.

The modified panel moment-rotation relationships are described as follows. For both models the elastic stiffness K_e and yield moment M_y^{pa} are

$$K_e = \frac{M_y^{pa}}{\gamma_y} = \frac{G \cdot d_c \cdot t_{cw} \cdot (d_b - t_{bf})}{(1 - \rho)} \tag{5.12a}$$

$$M_y^{pa} = \frac{\overline{\tau}_y \cdot d_c \cdot t_{cw} \cdot (d_b - t_{bf})}{(1 - \rho)} \tag{5.12b}$$

For the modified Fielding model, the post elastic stiffness K_1 and the second yield moment M_{sh}^{pa}, at which the strain hardening starts, are

$$K_1 = \frac{5.2 \cdot G \cdot b_{cf} \cdot t_{cf}^3}{d_b \cdot (1 - \rho)} \tag{5.13a}$$

$$M_{sh}^{pa} = M_y^{pa} + \frac{15.6 \cdot \overline{\tau}_y \cdot b_{cf} \cdot t_{cf}^3}{d_b \cdot (1 - \rho)} \tag{5.13b}$$

For the modified Wang model, the post elastic stiffness K_1 and the second yield moment M_{sh}^{pa} are

$$K_1 = \frac{\Delta M_{sh}^{pa}}{\Delta \gamma_{sh}} = 0.7 \cdot G \cdot b_{cf} \cdot t_{cf}^2 \tag{5.14a}$$

$$M_{sh}^{pa} = M_y^{pa} + \Delta M_{sh}^{pa} = M_y^{pa} + \overline{\sigma}_y \cdot b_{cf} \cdot t_{cf}^2 \tag{5.14b}$$

For both models the strain hardening stiffness K_2 is

$$K_2 = \frac{G_{st} \cdot d_c \cdot t_{cw} \cdot (d_b - t_{bf})}{(1 - \rho)} \tag{5.15}$$

5.3.3 Comparison with Test and FEM Results

Figures 5.17 to 5.26 show comparison of the modified models with test results and FEM results for various column flange thicknesses. From these figures it can be seen that these simple modifications have improved the performance of the two models (Fielding and Wang) except for Krawinkler Specimen B2. The modified models underestimate the panel zone strength of Krawinkler Specimen B2 by about 13 %. This can be attributed to the fact that the modified models cannot properly model unusual premature strain hardening effects due to a very short yield plateau ($\varepsilon_s = 4.4\varepsilon_y$) of the stress-strain relations of the column web. In this comparison the thickest column flange was t_{cf} = 1.775". In actual design practice, even thicker column flanges may be used, perhaps on the order of 3 to 5 inches. Additional test or FEM predictions for such column sections are needed to further verify these simple models. No such data was found in the literature.

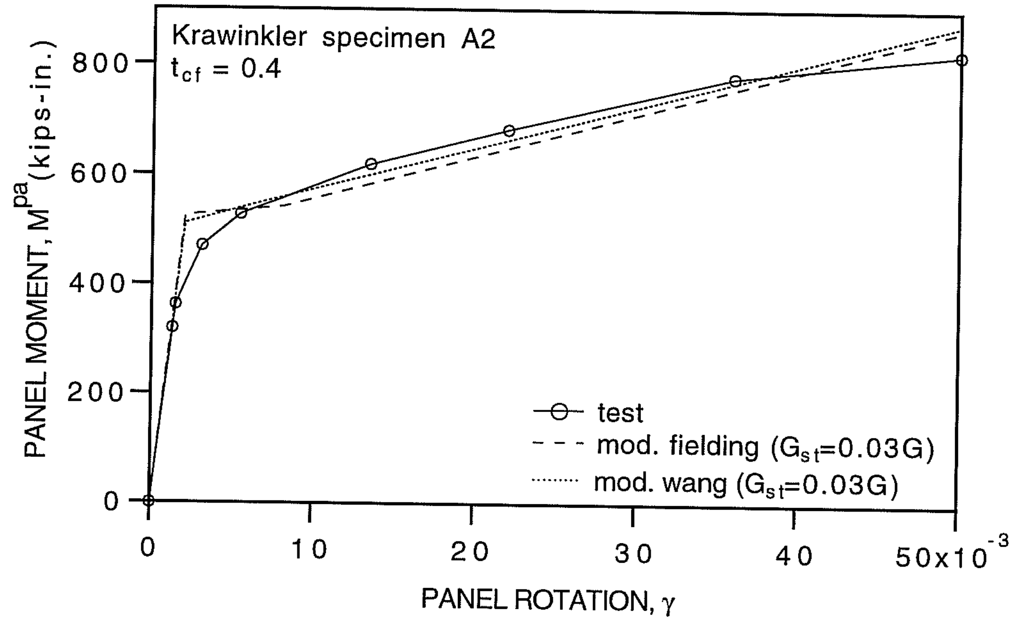

Fig. 5.17: Comparison of the Modified Models and Test Data for Krawinkler Specimen A2

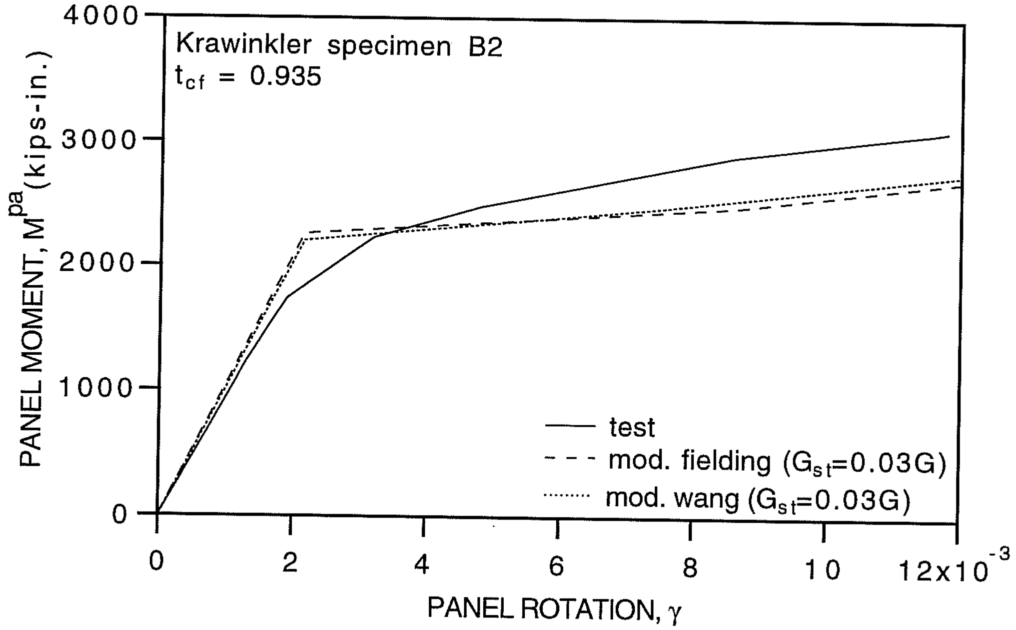

Fig. 5.18: Comparison of the Modified Models and Test Data for Krawinkler Specimen B2

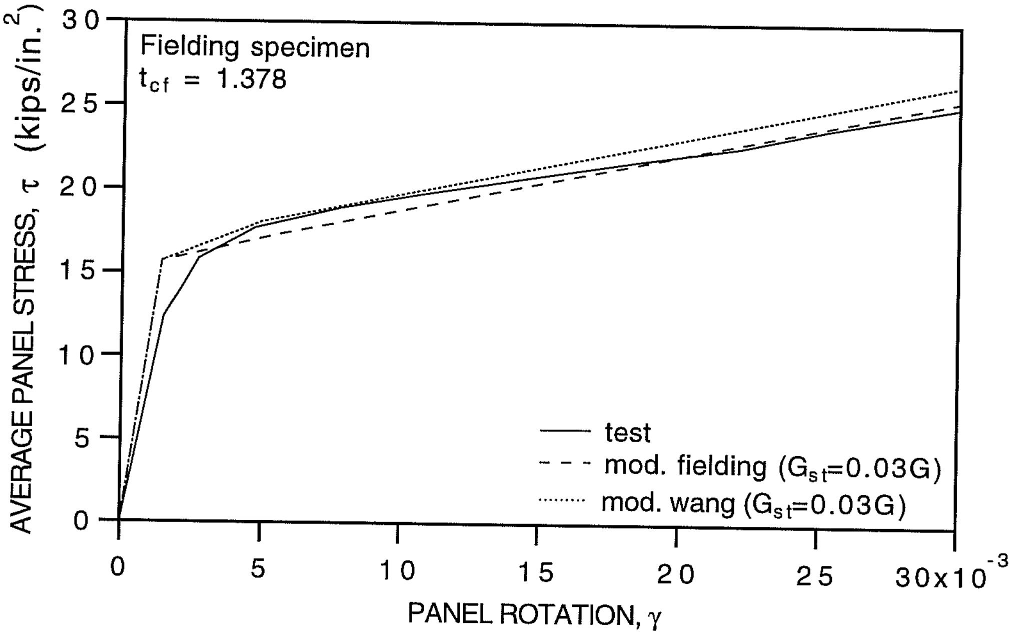

Fig. 5.19: Comparison of the Modified Models and Test Data for Fielding Specimen

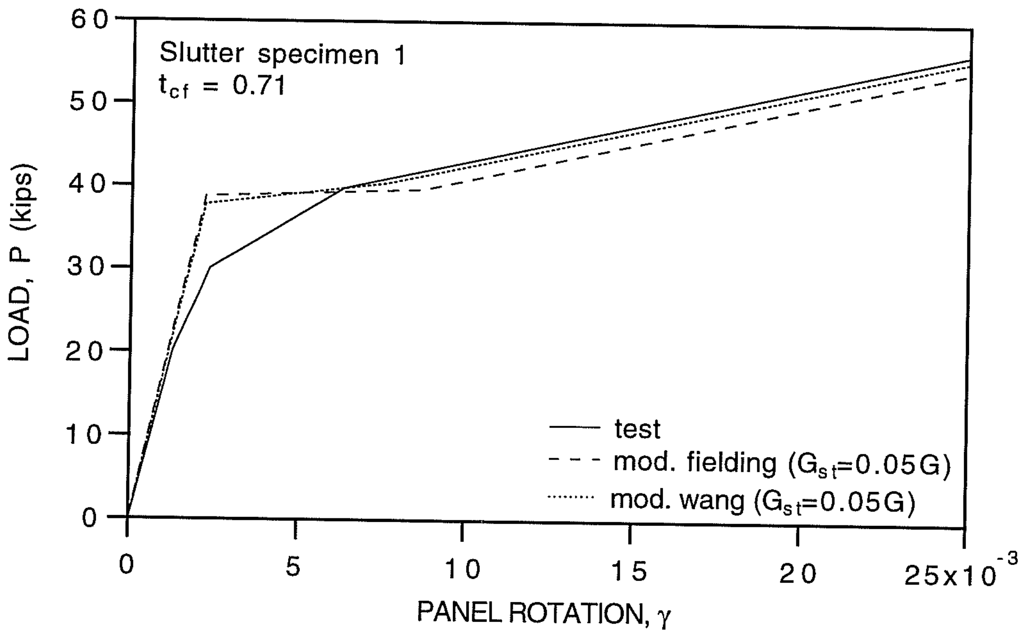

Fig. 5.20: Comparison of the Modified Models and Test Data for Slutter Specimen 1

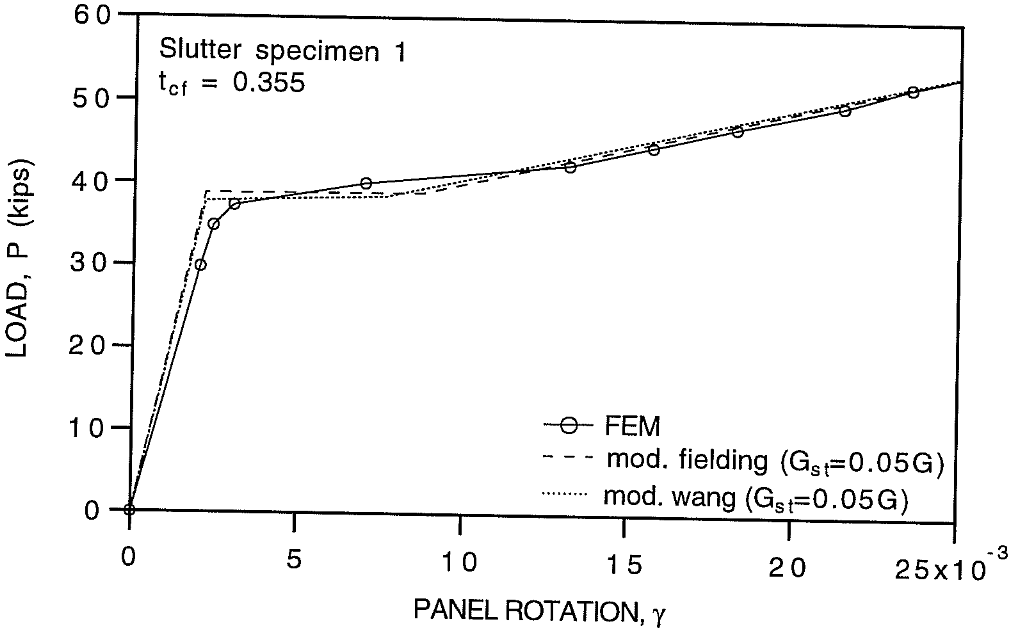

Fig. 5.21: Comparison of the Modified Models and FEM Result for Slutter Specimen 1 with t_{cf} = 0.355"

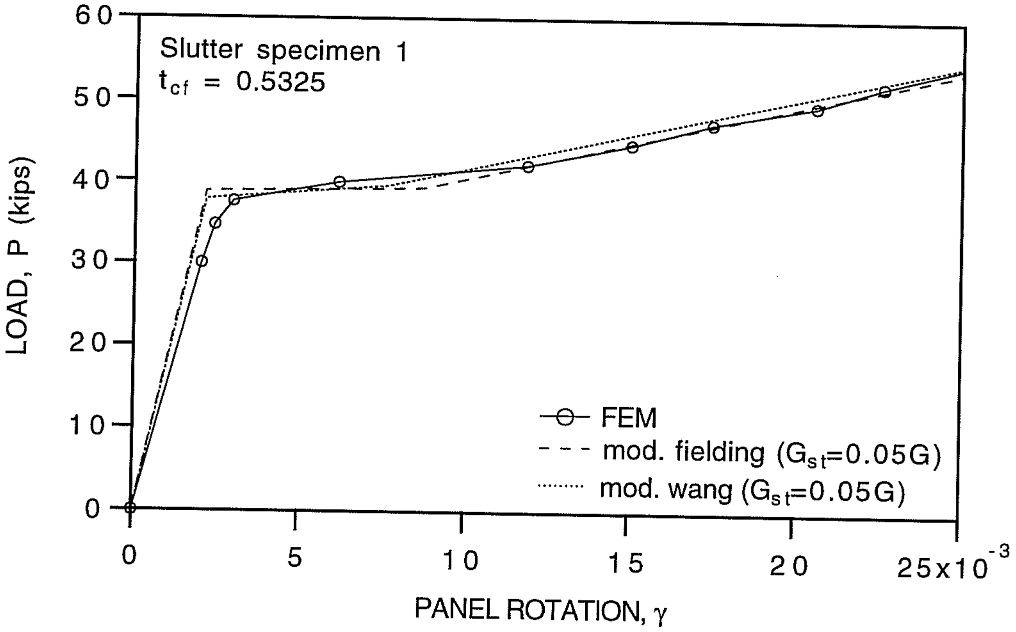

Fig. 5.22: Comparison of the Modified Models and FEM Result for Slutter Specimen 1 with t_{cf} = 0.5325"

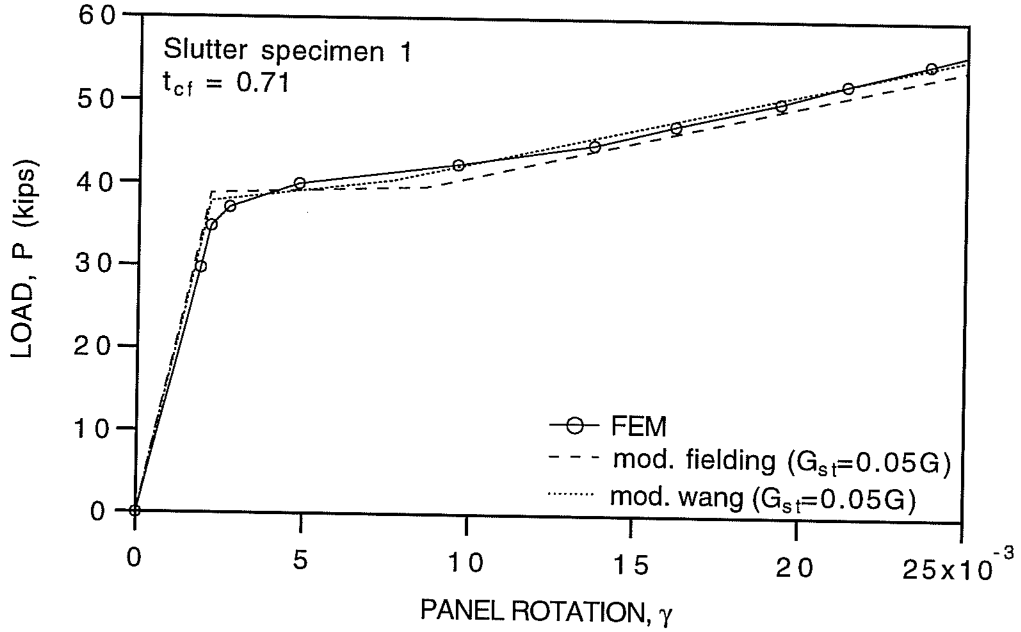

Fig. 5.23: Comparison of the Modified Models and FEM Result for Slutter Specimen 1 with t_{cf} = 0.71"

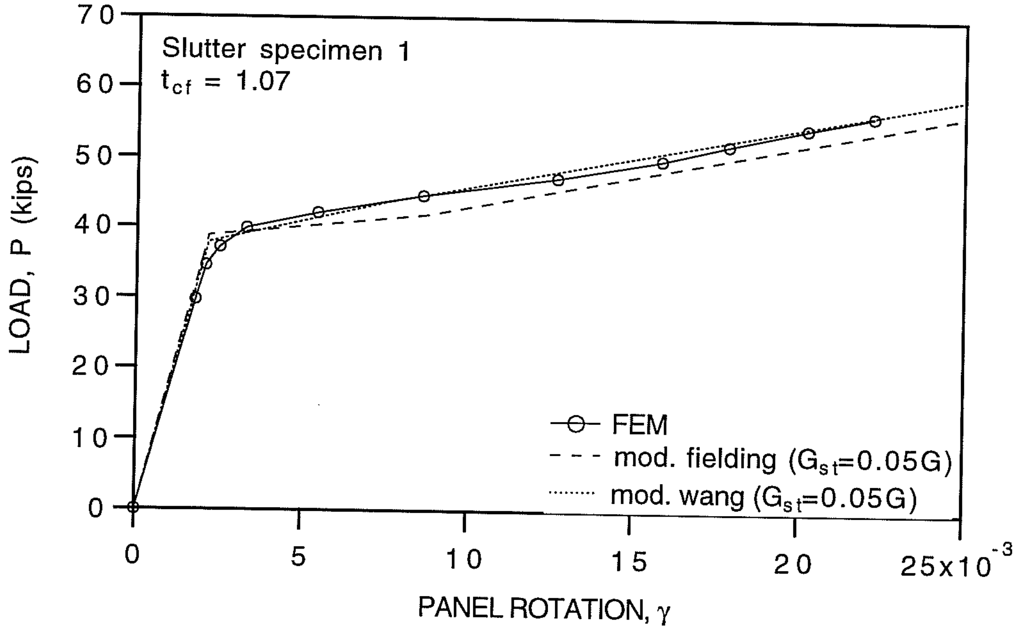

Fig. 5.24: Comparison of the Modified Models and FEM Result for Slutter Specimen 1 with t_{cf} = 1.07"

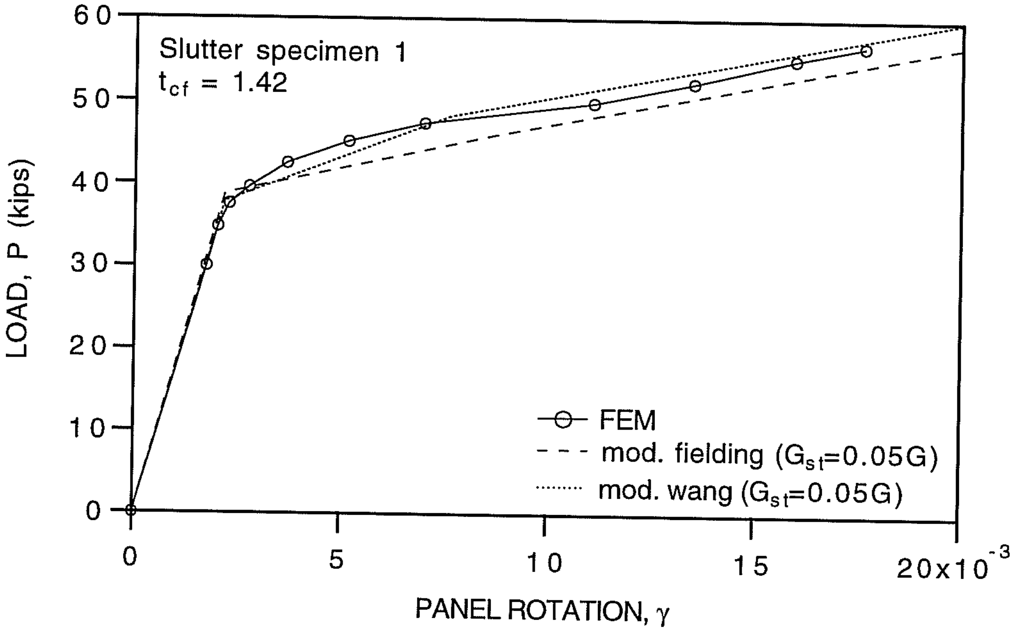

Fig. 5.25: Comparison of the Modified Models and FEM Result for Slutter Specimen 1 with t_{cf} = 1.42"

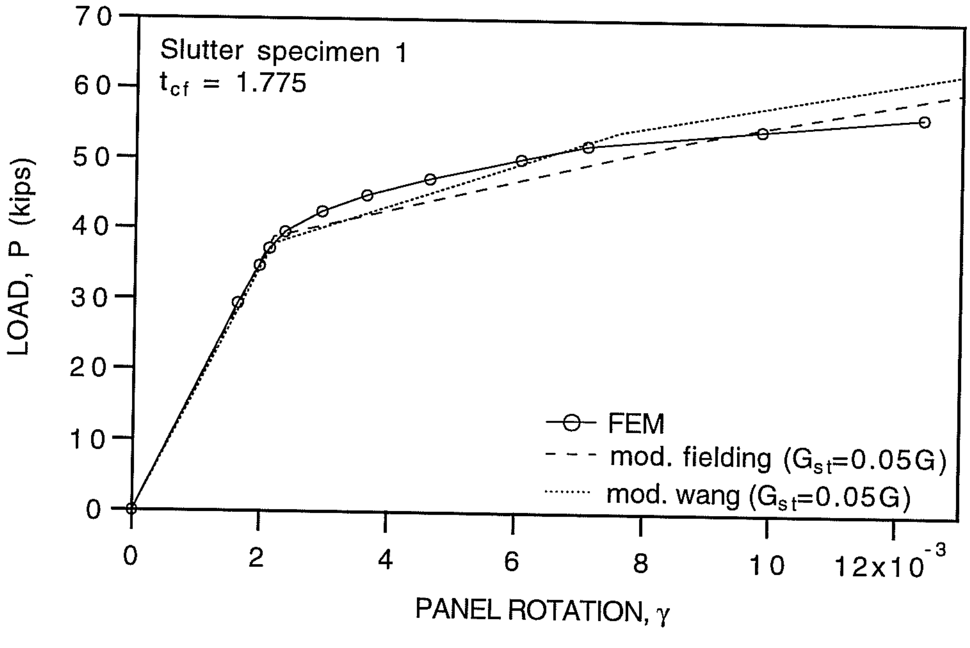

Fig. 5.26: Comparison of the Modified Models and FEM Result for Slutter Specimen 1 with t_{cf} = 1.775"

5.4 Hysteretic Rules for Cyclic Behavior of Panel Zones

5.4.1 Review of Existing Models

A couple of hysteretic models have been developed to describe the cyclic behavior of panel zones. The first model is based on bilinear kinematic hardening, and has been mostly used in the dynamic analysis of MRFs. The second model, which was developed by Wang (1988), is based on a multi-linear hardening rule. This model shows better correlation with test data than the bilinear model.

Figure 5.27 shows a comparison of the bilinear model and test data for the panel zone of Krawinkler specimen A1. The existing bilinear panel model shows poor performance. The model underestimates the strength by about 80 percent. The overall subassemblage displacement obtained by the bilinear panel zone model with the beam-column element developed in Chapter 2 are compared with the experimental response in Fig. 5.28. The figure shows that the analytical results underestimate the strength of the test subassemblage as in Fig. 5.27. From this discussion it can be concluded that the behavior of the panel zone can play an important role in the overall responses of moment resisting frames and a realistic model for the panel zone is needed.

5.4.2 Description of the Proposed Model

In this study, hysteretic rules for the panel zone are developed based on Dafalias's bounding theory. This model also uses Cofie's rules for the movement of the bound line, as discussed in Chapter 3. Based on observations from experimental and FEM analyses of panel zones, it has been found that for large plastic rotations, the shear strain in the panel zone are distributed nearly uniformly within the panel, and the value of joint rotation is close to the value of the average shear strain in the panel (Wang 1988). Therefore, it is assumed that the panel zone moment-rotation relationships can be determined from the material properties of the panel zone using Cofie's rules. These rules for the movement of the bound line, which were developed for stress-strain relationships, will be adopted for the panel zone moment-rotation relationships.

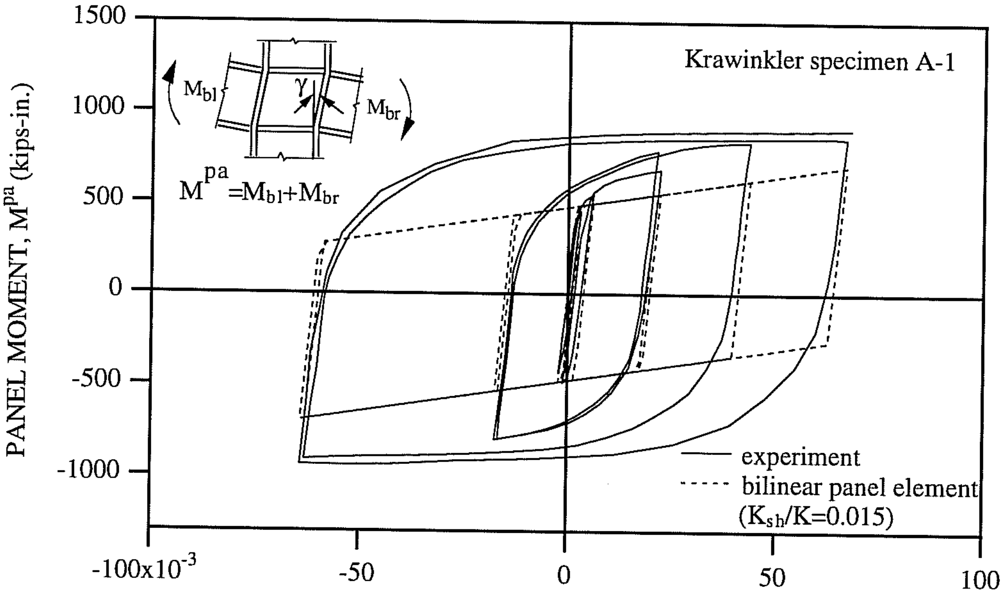

Fig. 5.27: Comparison of Test Results and the Existing Bilinear Panel Model for the Panel Zone

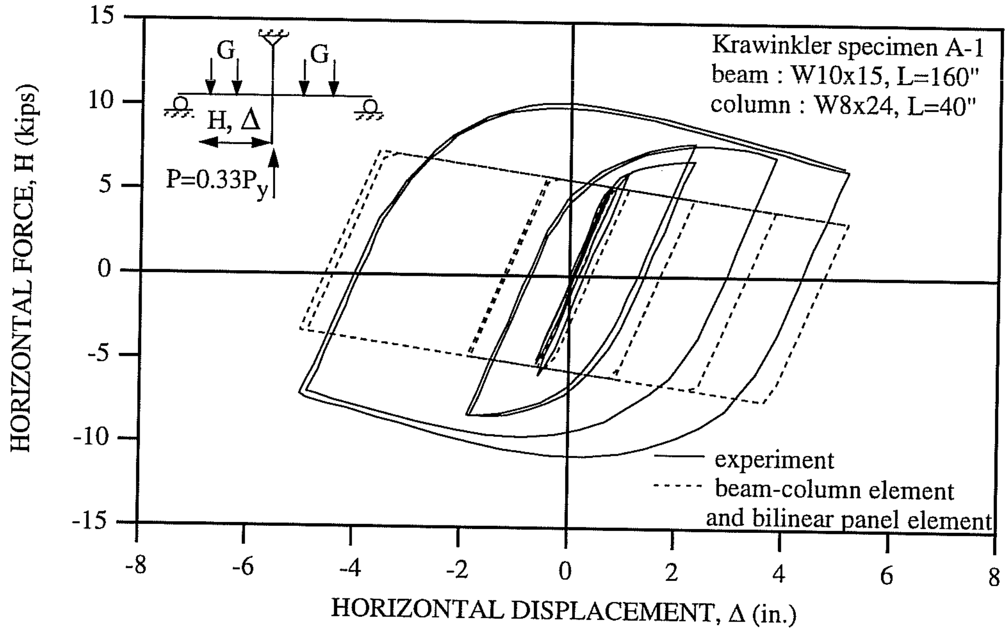

Fig. 5.28: Comparison of Test and the Analysis Using the Bilinear Panel Model for Overall Response

The main feature of Cofie's model is that the cyclic steady state curve is used to describe the movement of bounding line (see Chapter 3). In this study, the same kind of cyclic steady state curve is developed to describe the movement of the bounding line for the cyclic behavior of panel zones, as follows:

$$\frac{\gamma}{\gamma_n} = \frac{M^{pa}}{M^{pa}_n} + \left(\frac{M^{pa}}{0.85 \cdot M^{pa}_n}\right)^c \qquad (5.16)$$

where M^{pa}_n and γ_n are the normalizing panel moment and corresponding elastic rotation, respectively. By comparison with available cyclic test data, it has been empirically found that the constant C of the cyclic steady state curve is 4.2 to 4.4.

Experimental and FEM results suggest that column flanges do not significantly influence panel zone stiffness during cyclic loading, but do have a significant effect on panel zone strength. From FEM results for joints with the same dimensions except column flange thickness, it has been found that the effect of column flange thickness on the strength of the joint during cyclic loading can be normalized by M^{pa}_n (Wang 1988).

$$M^{pa}_n = M^{pa}_y + 2M_{pcf} \qquad (5.17)$$

where M_{pcf} is the plastic moment of column flange. The elastic rotation corresponding to the normalizing moment M^{pa}_n is

$$\gamma_n = M^{pa}_n / K_e \qquad (5.18)$$

To describe the inelastic behavior of the joint during cyclic loading the shape factor is employed, which was first used for cyclic stress-strain relationships by Dafalias (1975). The procedure for obtaining the shape factor $\hat{h}$ is as follows:

i) Choose the point A such that $\frac{1}{10} \leq \frac{\delta_A}{\delta_{in}} \leq \frac{1}{2}$, as shown in Fig. 5.29.

ii) Calculate the shape factor from $h = \frac{\delta_A}{\gamma_p^A} + \frac{\delta_{in}}{\gamma_p^A} \cdot \left[\ln\left(\frac{\delta_{in}}{\delta_A}\right) - 1 \right]$

iii) Normalize the shape factor by the plastic stiffness of the bound line $\hat{h} = \frac{h}{K_p^{bl}}$

It has been determined that a shape factor $\hat{h}$ of 20 for the inelastic curves of panel zones, as shown in Figs. 5.30a, provides a good correlation with experimental data. It has been also found that an elastic limit factor α of 1.4 and a plastic stiffness of the bound line of $K_p^{bl} = 0.008K_e$ provide good correlation with experimental data. The position of the initial bound line is determined by drawing the line with the slope of the bound line at the point with the corresponding slope on the cyclic steady state curve and making the resulting line intersect the moment axis. The plastic stiffness K_p^A at the point A as shown in Fig. 5.29 is calculated by using the shape factor $\hat{h}$ and the plastic stiffness of the bound line K_p^{bl}, as follows:

$$K_p^A = K_p^{bl}\left[1 + \hat{h}\frac{\delta_A}{\delta_{in} - \delta_A}\right] \tag{5.19}$$

The corresponding tangent stiffness K_t^A is determined by using the elastic stiffness K_e and the plastic stiffness K_p^A.

$$K_t^A = \frac{K_e \cdot K_p^A}{K_e + K_p^A} \tag{5.20}$$

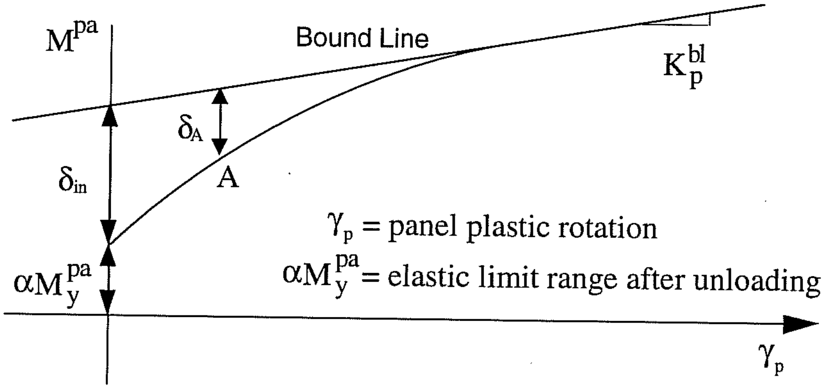

Fig. 5.29: Shape Factor for Inelastic Behavior

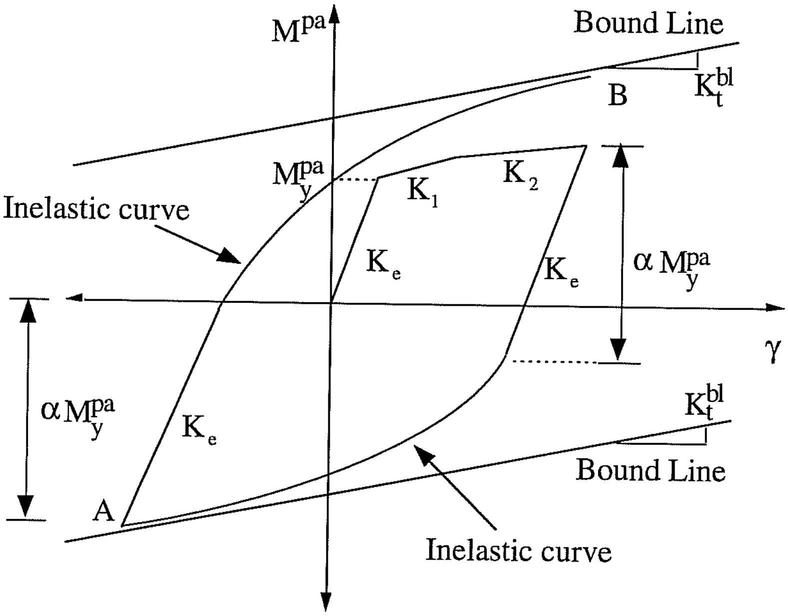

Fig. 5.30a): Elastic Limit Range After Unloading

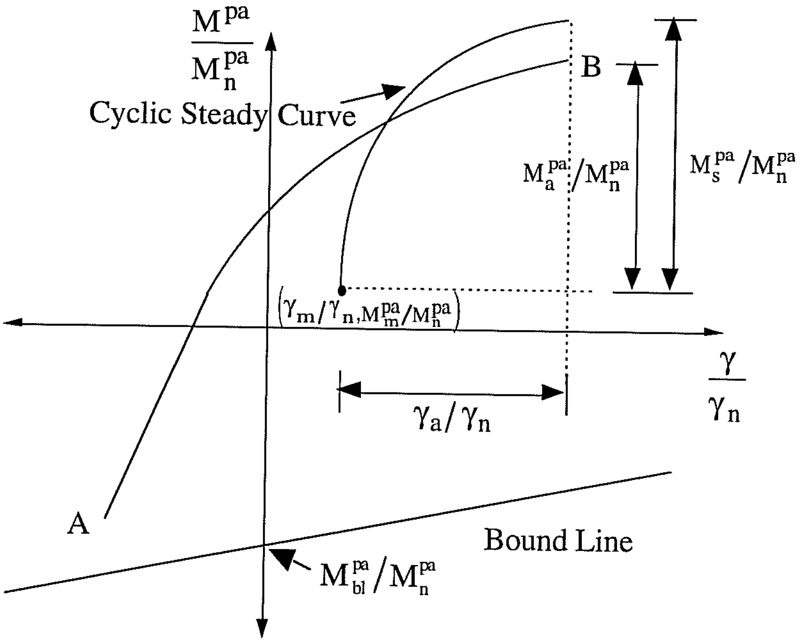

Fig. 5.30b): Movement of Bound Line

Fig. 5.30 : Hysteretic Rules for Panel Zones

The bounding line is updated whenever load reversals occur. The procedure for shifting the bounding line is presented below.

i) Whenever unloading occurs, the mean values and the amplitude for the last half cycle of loading history, as shown in Fig.5.30b, are calculated.

$$M_m^{pa} = 0.5\left(M_A^{pa} + M_B^{pa}\right) \tag{5.21a}$$

$$\gamma_m^{pa} = 0.5\left(\gamma_A^{pa} + \gamma_B^{pa}\right) \tag{5.21b}$$

$$M_a^{pa} = 0.5\left|M_A^{pa} - M_B^{pa}\right| \tag{5.22a}$$

$$\gamma_a^{pa} = 0.5\left|\gamma_A^{pa} - \gamma_B^{pa}\right| \tag{5.22b}$$

where the subscripts 'm' and 'a' stand for a mean value and an amplitude, respectively.

ii) Calculate the difference between the moment amplitude M_a^{pa} and the moment M_s^{pa} on the cyclic steady curve corresponding to the rotation amplitude, γ_a^{pa}

$$\Delta M^{pa} = M_s^{pa} - M_a^{pa} \tag{5.23}$$

iii) If $\Delta M^{pa} > 0$, cyclic hardening is predicted to take place in the next excursion. Update the bound by moving it outward by an amount equal to $2F_H\left(\Delta M^{pa}/M_n^{pa}\right)$, where F_H is the hardening factor.

$$\left(M_{bl}^{pa}/M_n^{pa}\right)_{new} = \left(M_{bl}^{pa}/M_n^{pa}\right)_{old} - 2F_H\left(\Delta M^{pa}/M_n^{pa}\right) \tag{5.24}$$

iv) If $\Delta M^{pa} < 0$, cyclic softening is predicted to take place in the next excursion. Update the bound by moving it inward by an amount equal to $2F_S\left(\Delta M^{pa}/M_n^{pa}\right)$, where F_S is the softening factor.

$$\left(M_{bl}^{pa}/M_n^{pa}\right)_{new} = \left(M_{bl}^{pa}/M_n^{pa}\right)_{old} - 2F_S\left(\Delta M^{pa}/M_n^{pa}\right) \tag{5.25}$$

v) Further move the bound by an amount equal to $F_R M_m^{pa}$, where F_R is the mean value relaxation factor.

$$\left(M_{bl}^{pa}/M_n^{pa}\right)_{new} = \left(M_{bl}^{pa}/M_n^{pa}\right)_{new} - F_R M_m^{pa} \tag{5.26}$$

5.4.3 Comparison with Experimental Results

The developed panel zone hysteretic rules are compared with test results for the specimens shown in Figs. 5.6a to 5.6d and in Figs. 5.31a to 5.31d. Material properties and panel zone details for the specimens in Figs. 5.31a to 5.31d are presented in Table 5.2.

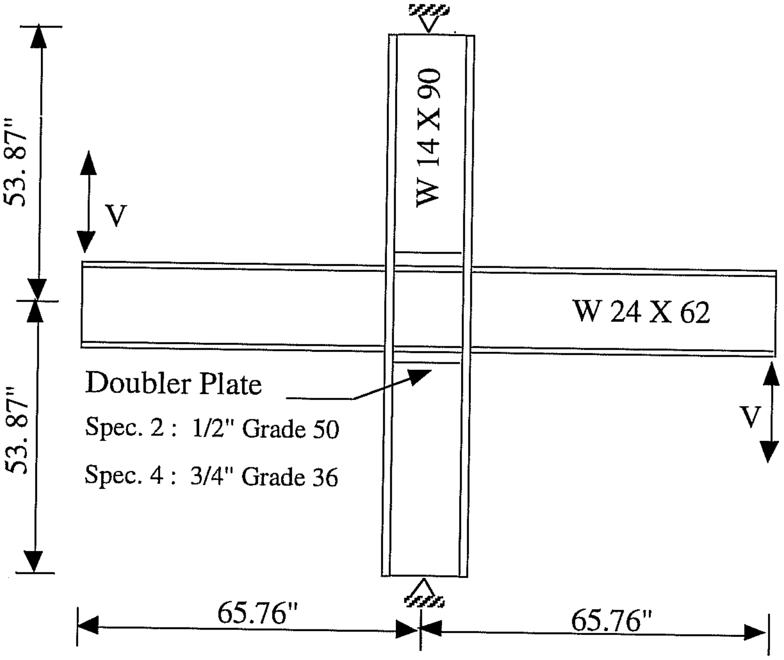

Fig. 5.31a): Slutter Specimens 2 and 4 (Slutter 1980)

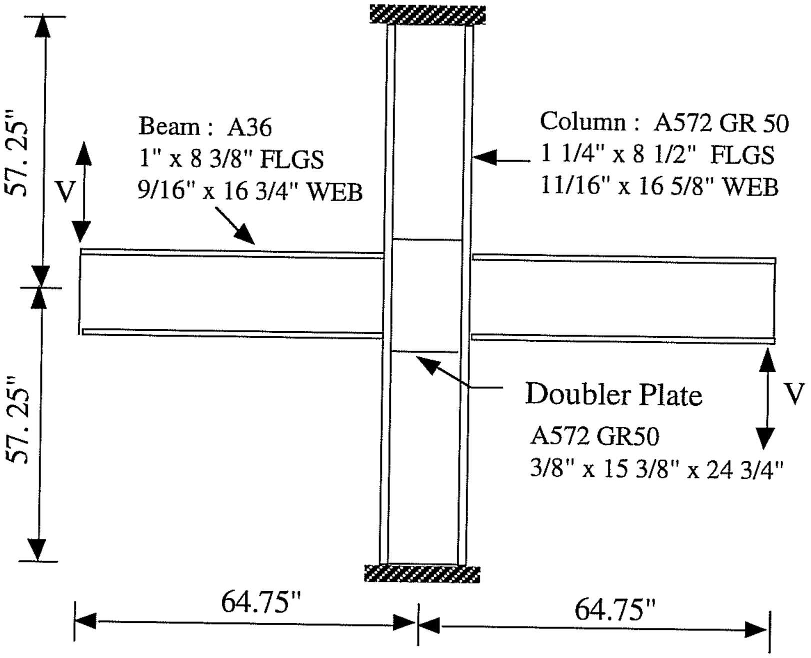

Fig. 5.31b): Popov Specimen 3 (Popov 1985)

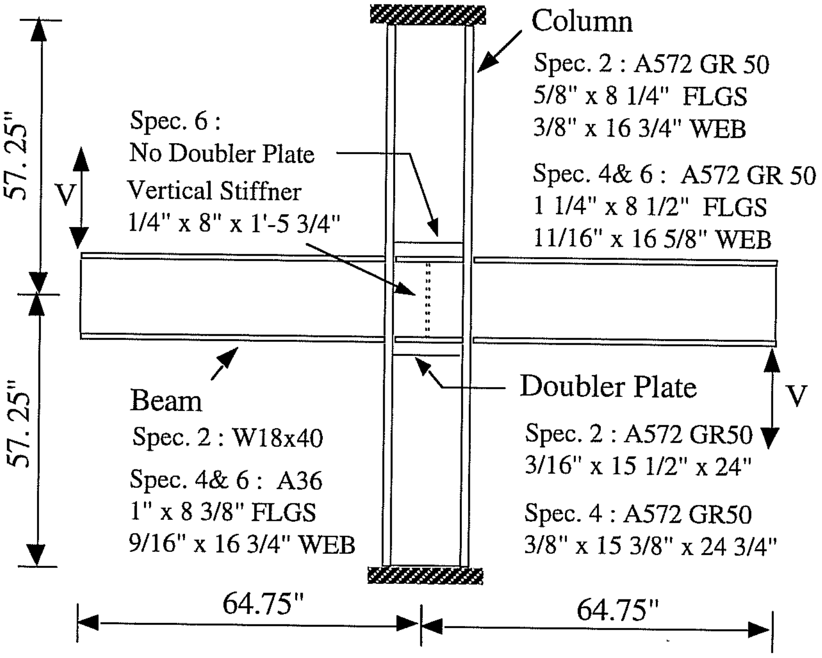

Fig. 5.31c): Popov Specimens 2, 4, and 6 (Popov 1985)

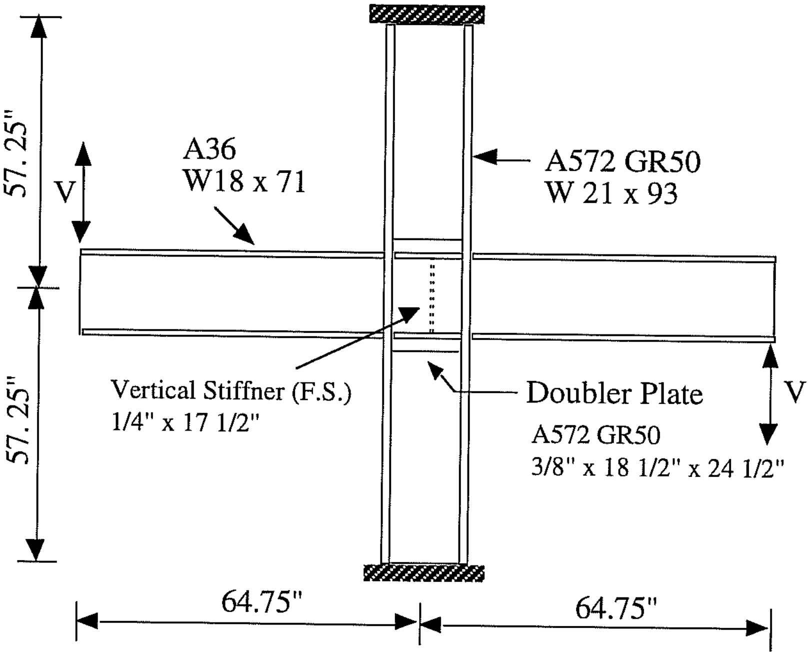

Fig. 5.31d): Popov Specimen 8 (Popov 1985)

Test Specimen	Yield Stress (ksi)					Connection Type	Continuity Plate	Vertical Plate
	Beam		Column		Doubler Plate			
	Web	Flg.	Web	Flg.				
Slutter 2	41.8	41.8	42.2	37.7	63.5	bolted web-welded flg.	yes	no
Slutter 4	47.4	41	42.3	39.1	43.5	bolted web-welded flg.	yes	no
Popov 2	46.4	46.4	49	49	49	bolted web-welded flg.	yes	no
Popov 3	38	38	49	49	49	bolted web-welded flg.	no	no
Popov 4	38	38	49	49	49	bolted web-welded flg.	yes	no
Popov 6	38	38	49	49	no	bolted web-welded flg.	yes	yes
Popov 8	43.5	43.5	60	60	49	bolted web-welded flg.	yes	yes

Table 5.2: Material Properties and Joint Details for Test Specimens

A vertical stiffener plate is attached approximately at mid-width of the panel zone in Popov's specimens 6 and 8. This is intended to represent a connection plate for a floor beam framing in from the perpendicular direction. In the analyses of Popov's specimens 6 and 8, the vertical stiffeners are not considered under the assumption that the resistance of these stiffeners to the panel zone shear forces is negligible.

Continuity plates are used to transfer beam flange forces to the column web in the specimens, except in Krawinkler's specimen B and Popov's specimen 3. If no continuity plates are required, the flange forces are assumed to be directly transferred to the column web. This detail can be used only if the column flanges are sufficiently thick. From comparison of test results for specimens with and without continuity plates, it has been reported by Popov (1985) that as far as the stiffness and strength of the panel zone were concerned, the test results showed little difference. Even though the monotonic and cyclic response rules for the panel zone are calibrated to test specimens with continuity plates, no modification is attempted to account for the behavior of panel zones without continuity plates under the above observation and the assumption that the validity of the panel zone tests is not dependent on the use of continuity plates.

For some specimens a doubler plate is used to increase the capacity of the panel zone. Test results (Becker 1971) showed that for every load level, except maximum load, the strain in the doubler plate was significantly less than that in the column web. Thus, the doubler plates were not fully effective. To include the contribution of a doubler plate in resisting panel zone shear, the panel yield moment, the elastic stiffness, and the strain hardening stiffness are modified as follows. By considering the limited participation of a doubler plate in resisting panel shear, the elastic stiffness K_e and the strain hardening stiffness K_2 are obtained

$$K_e = \frac{G \cdot \left(d_c \cdot t_{cw} + R_f \cdot t_{dp} \cdot w_{dp}\right) \cdot \left(d_b - t_{bf}\right)}{(1 - \rho)} \tag{5.27}$$

$$K_2 = \frac{G_{st} \cdot \left(d_c \cdot t_{cw} + R_f \cdot t_{dp} \cdot W_{dp}\right) \cdot \left(d_b - t_{bf}\right)}{\left(1 - \rho\right)} \tag{5.28}$$

where t_{dp} and w_{dp} are the thickness of a doubler plate and the width of a doubler plate between column flanges, respectively, and R_f is the reduction factor to account for the strain incompatibility between a doubler plate and column web. The panel yield moment M_y^{pa} is

$$M_y^{pa} = \frac{\bar{\tau}_y \cdot \left(d_c \cdot t_{cw} + R_f \cdot t_{dp} \cdot W_{dp}\right) \cdot \left(d_b - t_{bf}\right)}{\left(1 - \rho\right)} \tag{5.29}$$

When the yield stress of the doubler plate is different from that of the column web, two panel elements are employed in parallel instead of using Eqns. 5.27 to 5.29.

Figures 5.32 to 5.37 show the comparison of the analytical response obtained by the hysteretic rules and test results for the panel zones with no doubler plate. In Fig. 5.32, the test results for Krawinkler's specimen A1 are plotted against the predictions made by the developed model. The match is good for the cycles in which large deformations are imposed. For the first few cycles in which small deformations are imposed, the predictions are not as good.

Figure 5.33 shows results for Krawinkler specimen A2. The model works better in this case than for specimen A1. The difference between the prediction and test results is very small in any cycle. Specimens A1 and A2 are identical except that these specimens are tested with two different loading programs. For specimen A2, a large strain amplitude is applied for the first half cycle, causing large plastic deformation (far beyond the onset of strain hardening) in the panel zone. The model seems to work better for a large strain amplitude for which strain hardening effects are fully developed than for a small strain amplitude.

The analytical results for Krawinkler specimen B1 are plotted against the experimental response in Fig. 5.34. The match is good on the negative moment side, but the model somewhat underestimates the strength on the positive side. The experiment shows different strengths for positive and negative moment. The reason for this unsymmetrical experimental response is unclear.

Figures 5.35 to 5.37 provide additional comparisons between analytical and test results. These figures show a good correlation between test and analyses.

The developed model has been applied to six specimens with no doubler plate. In spite of the simplicity of the model, reasonable agreement has been established between model predictions and test results. In the following paragraphs, the model will be applied to the specimens with a doubler plate and compared with the test results.

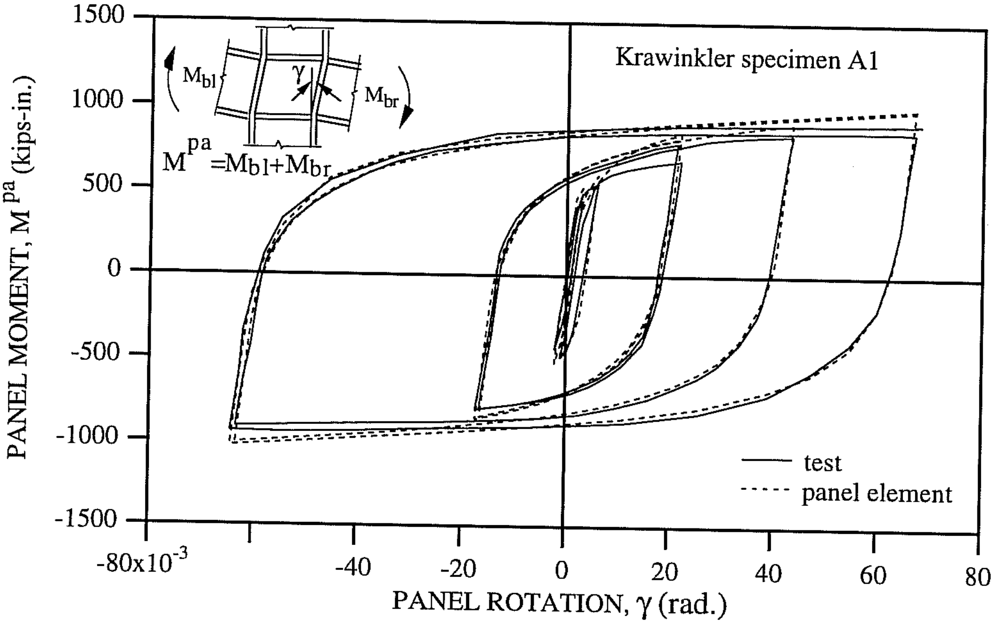

Fig. 5.32: Comparison of the Developed Hysteretic Rules and Test Data for Krawinkler Specimen A1

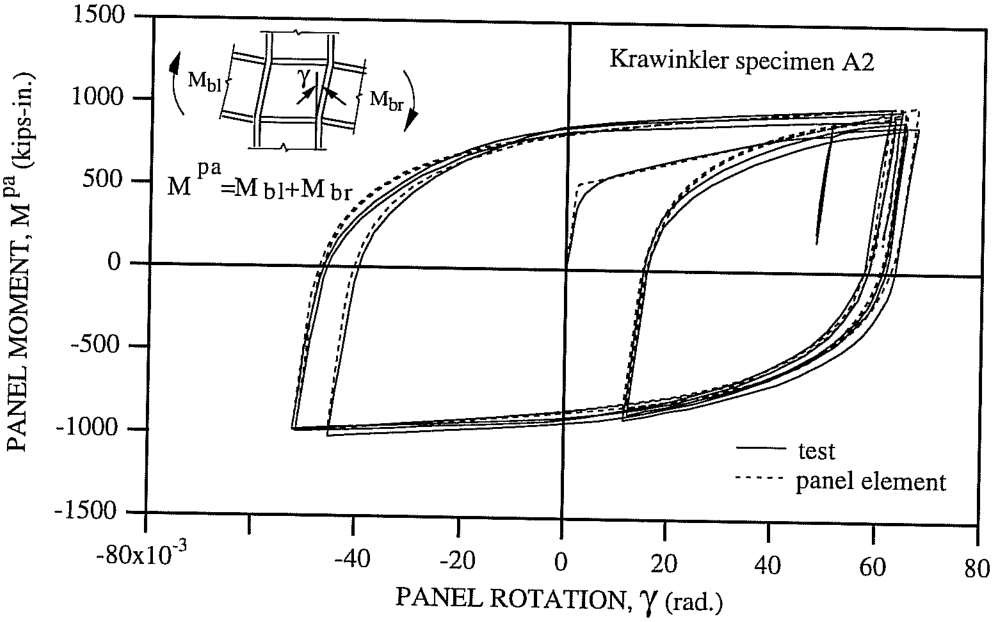

Fig. 5.33: Comparison of the Developed Hysteretic Rules and Test Data for Krawinkler Specimen A2

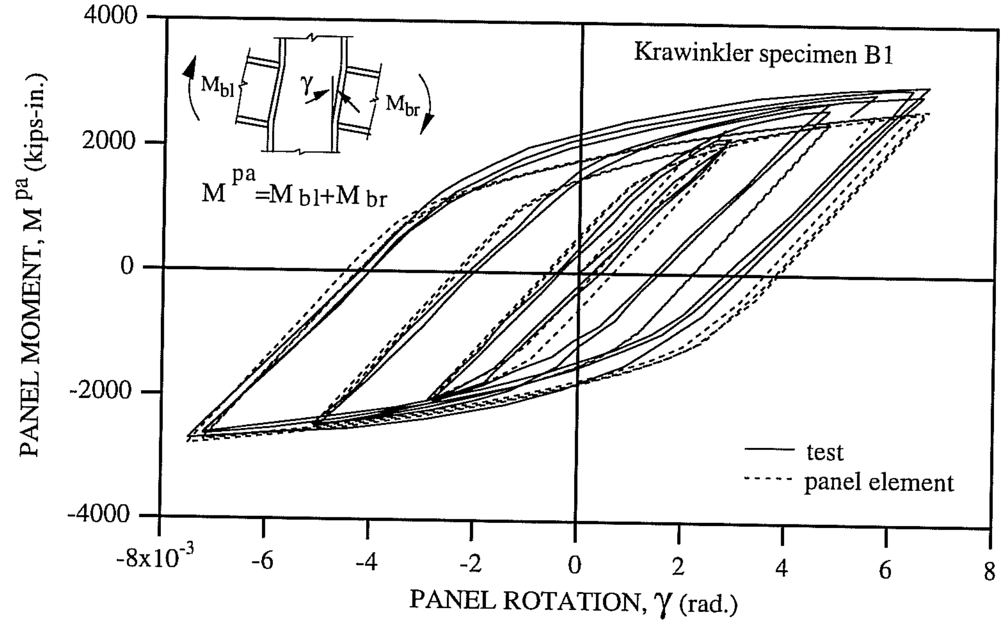

Fig. 5.34: Comparison of the Developed Hysteretic Rules and Test Data for Krawinkler Specimen B1

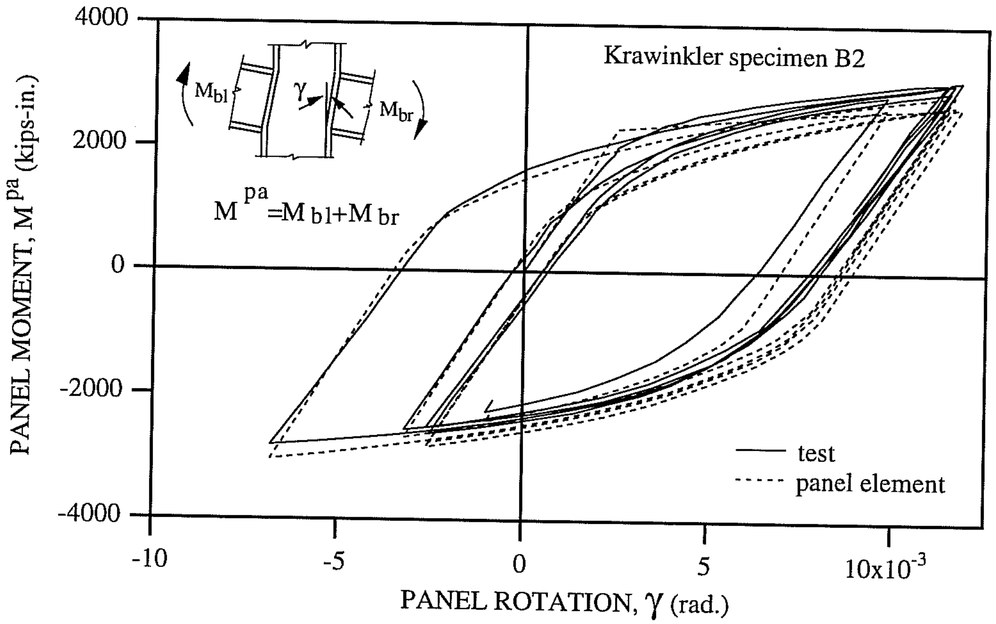

Fig. 5.35: Comparison of the Developed Hysteretic Rules and Test Data for Krawinkler Specimen B2

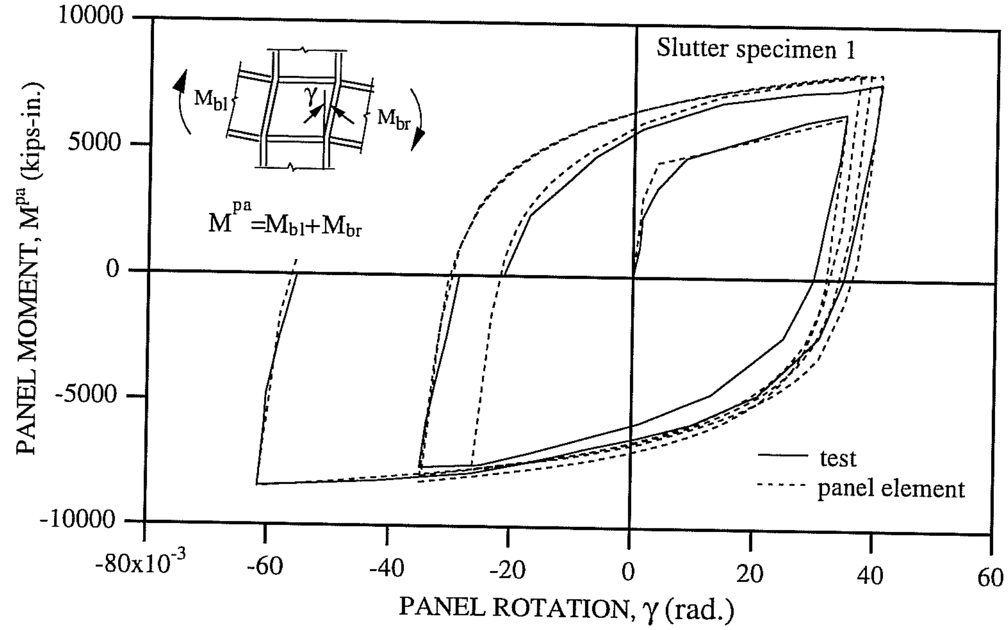

Fig. 5.36: Comparison of the Developed Hysteretic Rules and Test Data for Slutter Specimen 1

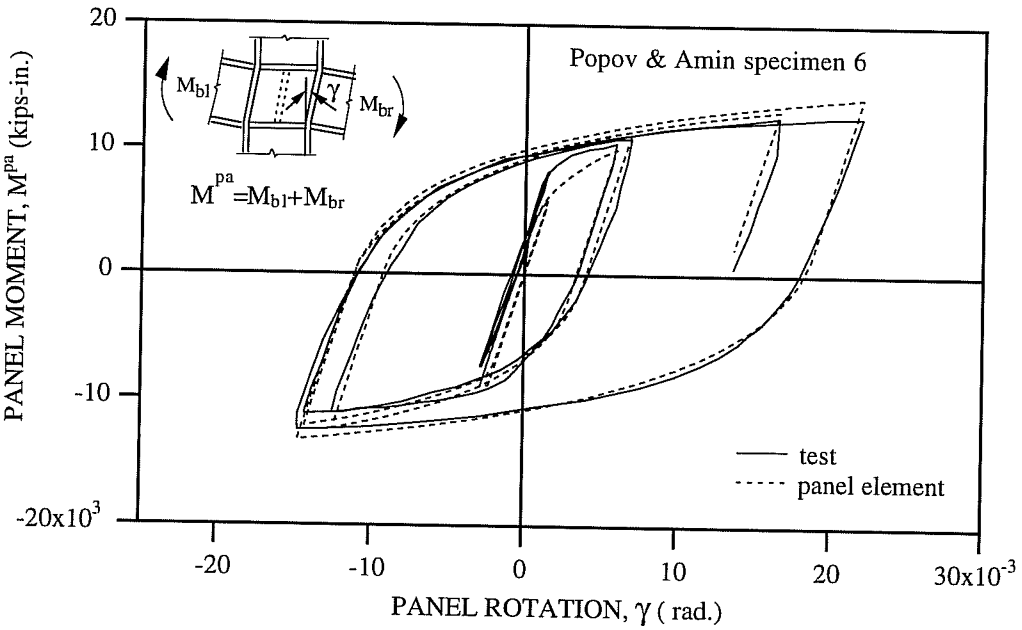

Fig. 5.37: Comparison of the Developed Hysteretic Rules and Test Data for Popov Specimen 6.

In Figs. 5.38 to 5.41, the analytical results are compared with test results for specimens with doubler plates. In these specimens, the yield stress of the doubler plates is approximately the same as that of the column web. In the analyses, the reduction factor of R_f=0.4 was applied to account for strain incompatibility between the column web and the doubler plate. For the small strain amplitude cycles, the difference between the model predictions and experimental responses can be explained by the same reason as in the discussions for the specimens with no doubler plate. From Fig. 5.41, it can be seen that even though less than half of the doubler plate area is included in the model, the stiffness of the analytical model is larger than that of test results. The doubler plate apparently provides little increase in panel zone stiffness at low loads. In general, the analytical results obtained by using the reduction factor of R_f=0.4 show fair agreement with test results in spite of the complexity of the problem.

Figures 5.42 and 5.43 show the comparison of the analytical and experimental results for specimens with a doubler plate, for which the yield stress of the doubler plate is different from the column web. Since the yield stress of the doubler plates is much different from that of the column webs, two panel elements are employed in parallel to obtain the analytical results. For Slutter specimen 2, in which the yield stress (σ_y=63.5 ksi) of the doubler plate was larger than that (σ_y=42.2 ksi) of the column web by about 50 %, the reduction factor of R_f=0.6 was applied to take into account the limited participation of the doubler plate in resisting the panel shear. For Popov specimen 8, in which the yield stress (σ_y=49 ksi) of the doubler plate was smaller than that (σ_y=60 ksi) of the column web by about 18 %, the reduction factor of R_f=0.1 was used . From the above discussion, it can be seen that reliable model predictions are difficult to obtain for cases where doubler plates have a yield stress significantly different from the column web.

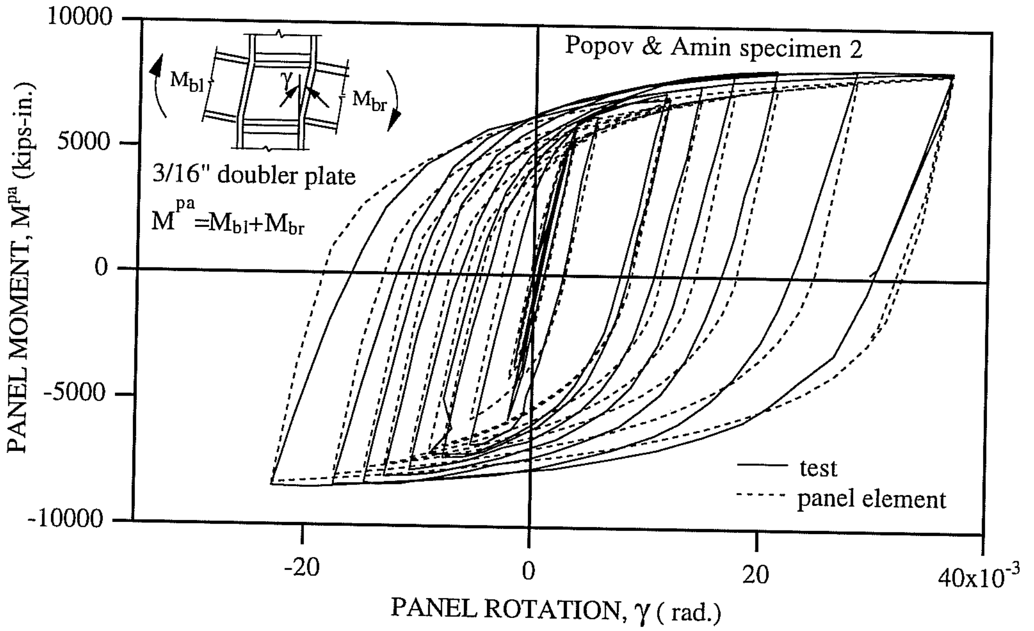

Fig. 5.38: Comparison of the Developed Hysteretic Rules and Test Data for Popov Specimen 2

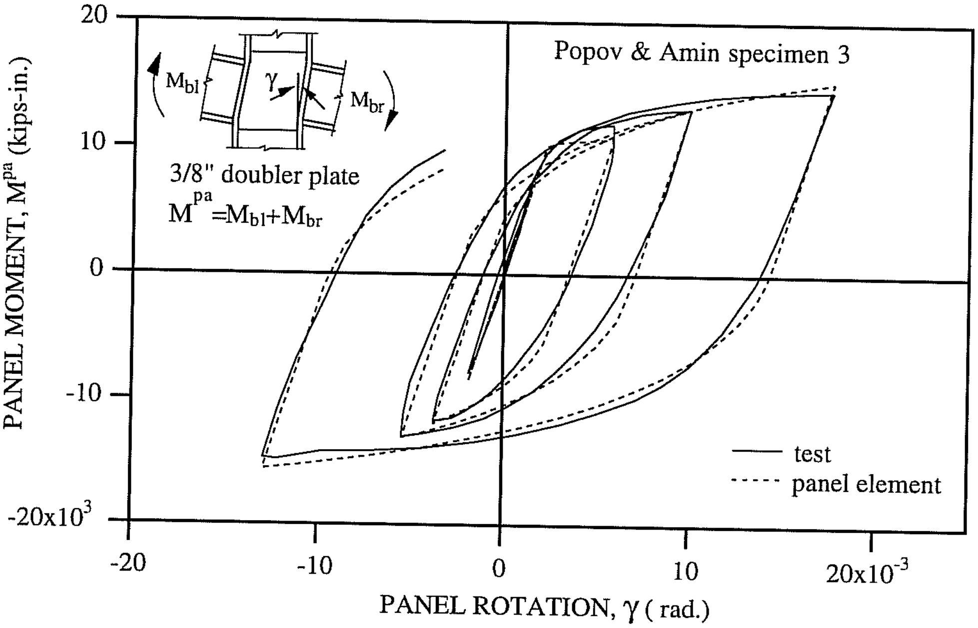

Fig. 5.39: Comparison of the Developed Hysteretic Rules and Test Data for Popov Specimen 3

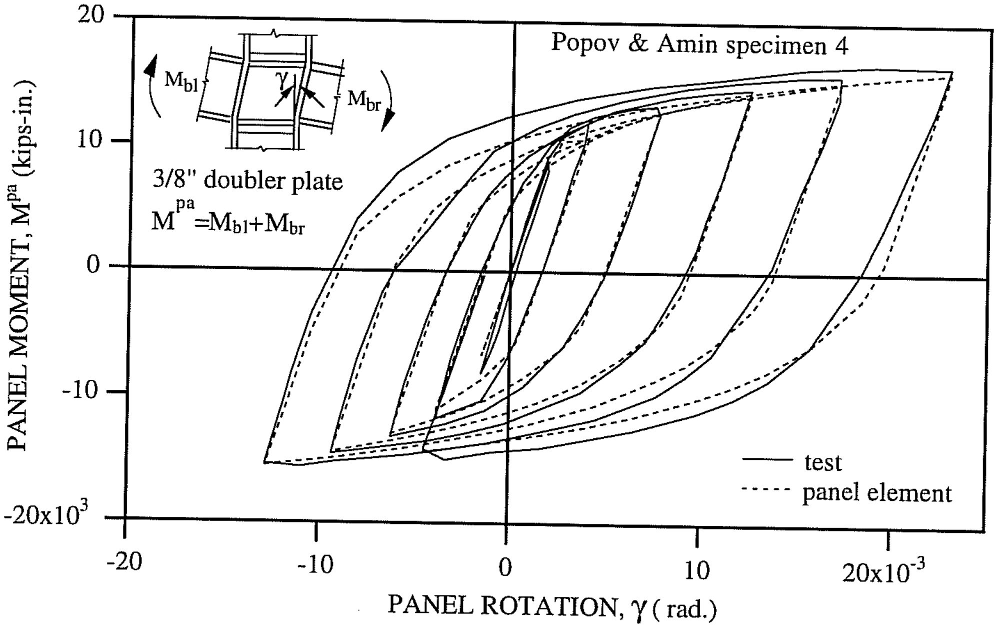

Fig. 5.40: Comparison of the Developed Hysteretic Rules and Test Data for Popov Specimen 4

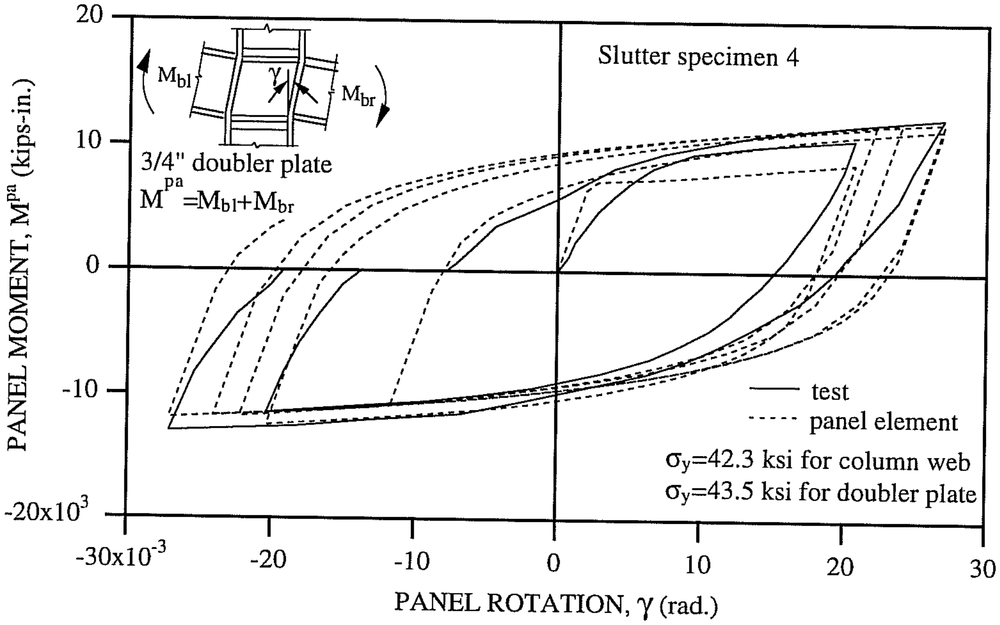

Fig. 5.41: Comparison of the Developed Hysteretic Rules and Test Data for Slutter Specimen 4

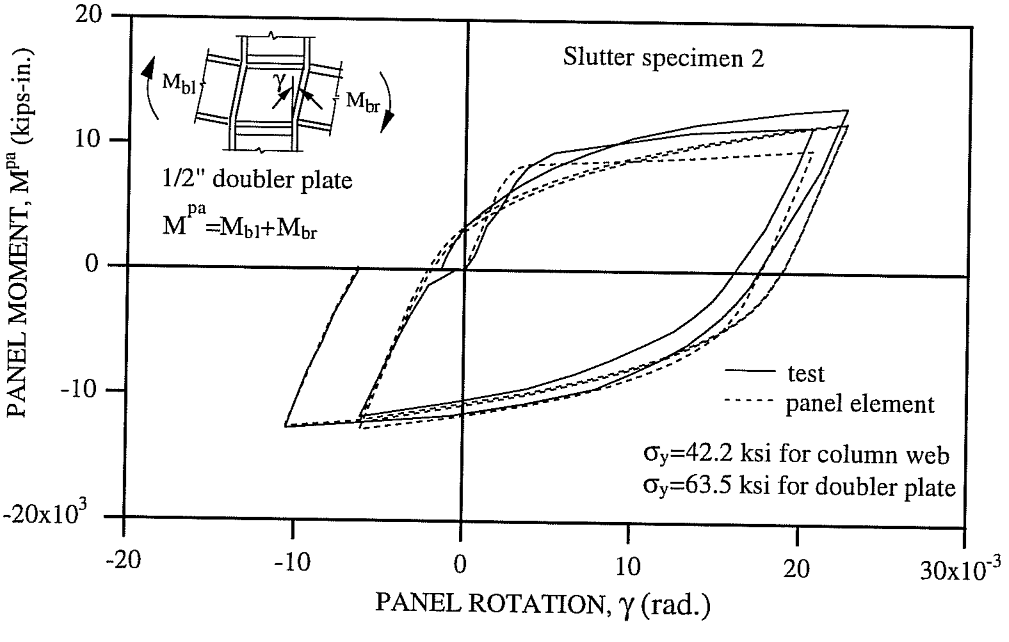

Fig. 5.42: Comparison of the Developed Hysteretic Rules and Test Data for Slutter Specimen 2

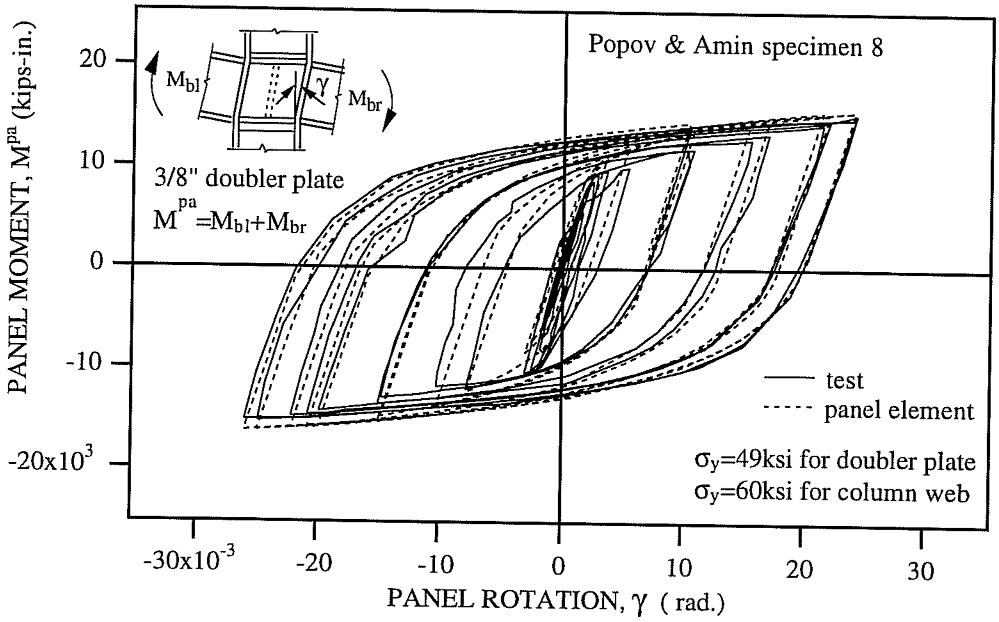

Fig. 5.43: Comparison of the Developed Hysteretic Rules and Test Data for Popov Specimen 8

5.5 Summary

The objective of the study in this chapter was to develop a model to describe cyclic panel zone behavior. First, the existing models for monotonic loading were reviewed and improved to obtain better correlation with experimental results. Second, hysteretic rules for cyclic loading were developed and the parameters needed for the developed hysteretic rules were determined through calibration with available experimental data. From the comparison of the analytical results with test results for the specimens with a doubler plate, it was found that doubler plates were only partially effective in resisting the panel zone shear. In spite of the simplicity of the model, reasonable agreement was established between model predictions and test results for panel zones with no doubler plates. For panel zones with doubler plates, the predictions of the simple model are not as reliable.

Chapter 6: COMPOSITE BEAM ELEMENT

6.1 General

To investigate the effect of a composite concrete floor slab on the seismic behavior of moment resisting frames under earthquake loading, an analytical model for composite beams is needed. A composite beam shows complex behavior due to slip between the concrete slab and the steel beam, and the variation of longitudinal stress across the width of the slab, which is dependent of the joint details and the loading pattern. To ideally model the behavior of composite beams during earthquake loading, these factors should be considered. Although a three-dimensional finite element analysis can most accurately model the behavior of composite beams, some researchers (Lee 1987; Tagawa et al 1989) have developed two-dimensional discrete member models as a compromise between simplicity and accuracy. In these models, it is assumed that the influence of slip and the variation of longitudinal membrane stress on the behavior of composite beams can be implicitly included in the moment-rotation relationships.

In this chapter, previous research on composite beams is first reviewed, and Lee's composite beam model (1987) is then outlined. By modifying Lee's model, a new model is proposed and verified by comparing with available experimental results.

6.2 Previous Research

This section summarizes previous research on composite beams subjected to reverse curvature bending, resulting in positive bending moment at one end of the beam and negative bending at the other end. Earlier and more extensive research addressed the behavior of simple span composite beams with positive moment at the midspan. In the early 1970's, research began to investigate the behavior of composite beams with positive moment at the beam end.

The strength and stiffness characteristics of composite beams have been studied both analytically and experimentally by Daniels et al (1970) and duPlessis et al (1972; 1973). The emphasis of the studies was on the interaction between the column flange and the concrete slab which was designed to act compositely with the steel beam. The study showed that the ultimate strength of the composite beam depends on the slab area which is in contact with the column flange. This study also indicated that, as a lower bound, the concrete compressive strength can be increased to $1.3 f'_c$ in computing the ultimate strength at the connection, because of confinement of the slab near the column.

Tagawa et al. (1986) investigated the elastic-plastic behavior of composite beams under positive moments. He found that the ultimate bearing stress at the column face was about $1.8\, f'_c$, where f'_c is the compressive strength of concrete by a standard cylinder test. He proposed that the contribution of the concrete slab to the ultimate moment could be determined by using the column width b_{cf} and the ultimate bearing stress $1.8\, f'_c$.

Two one-story, two-bay assemblages with composite beams were tested under monotonic gravity and lateral loadings by Wenk, et al.(1977). Cyclic test results are reported by Lu, et al. (1980).

Few studies have been done on the effective width of the composite slab in structures subjected to lateral load or earthquake induced forces. Ansourian (1975) applied the finite element method to study the contribution of the composite slabs to lateral load resistance of frames.

Uang (1985) and Wallace (1989) tested small scale models of composite beams. Comparing the model test results with the prototype test results (Lee 1987), Wallace showed that small scale models can be used to predict global elastic and inelastic behavior of structures very well.

Recently, Lee(1987) and Tagawa et al (1989) performed experimental and analytical research, and developed hysteresis models relating end moment to member rotation for cantilever composite beams. Both models were developed from subassemblages of steel columns and composite beams. Both models take into account pinching behavior and stiffness degradation, and employ multi-linear moment-rotation relationships.

6.3 Summary of Lee's Composite Beam Model

Modeling of the force-deformation relationship of composite beams as a structural element for a two-dimensional analysis is a difficult task. The longitudinal membrane stress is not uniform across the width of the concrete slab. The effective width, which accounts for the non-uniform longitudinal stress pattern, varies along the beam, and changes as the moments in the beam change during loading history. Since the non-uniform effective width variation of slab along the beam changes during the loading history, the use of a method that starts from the stress-strain relation or moment-curvature relation is not warranted in a two-dimensional analysis of composite beams. Also, the behavior of shear connectors is not fully understood, especially under cyclic loading, even though many researchers (Slutter et al. 1965; Ollgaard et al. 1971; Grant et al. 1977) have studied the behavior of shear studs under monotonic loading.

However, from the observation of experimental and analytical results, Lee (1987) suggested that it may be possible to use two bilinear skeleton models (Fig. 6.1) for the moment-rotation relationships of composite beams. One bilinear skeleton model was modeled for positive moment and another for negative moment, together with a hysteresis law (Fig. 6.2) based on a trilinear model, and including the effect of pinching of the loops. To describe the bilinear skeleton models presented in Fig. 6.1, elastic and post-elastic stiffnesses, and yield moments are required for positive and negative moments.

6.3.1 Effective Width of Concrete Slab

To define the positive elastic stiffness K_e^+, the effective width of the concrete slab is required. Assuming fully composite action, Lee (1987) conducted three-dimensional elastic finite element analyses to investigate the effects of several parameters influencing the effective width of composite beams. The parameters considered were aspect ratio (B/L), column flange width (b_{cf}), and torsional stiffness of the transverse beam (K_{tr}). B is the total slab width between the mid-distances of adjacent columns and L is the beam length from the column face to the end of the beam (zero moment). The values of the effective width for various aspect ratios were suggested by Lee and are reproduced by curve fitting in this study. When the resulting equation is combined with the increase of the effective width due to the other parameters, noted above, the effective width can be defined by Eq. 6.1.

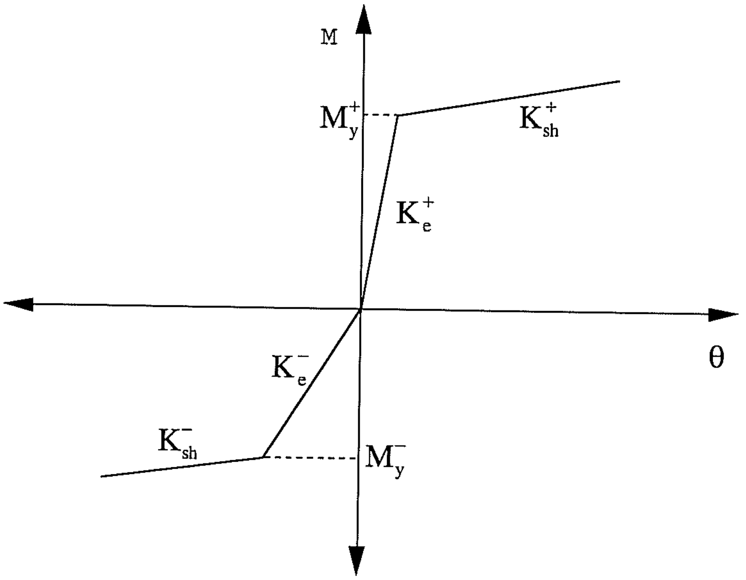

Fig. 6.1: Moment-Rotation Skeleton Model of Composite Beam (Lee 1987)

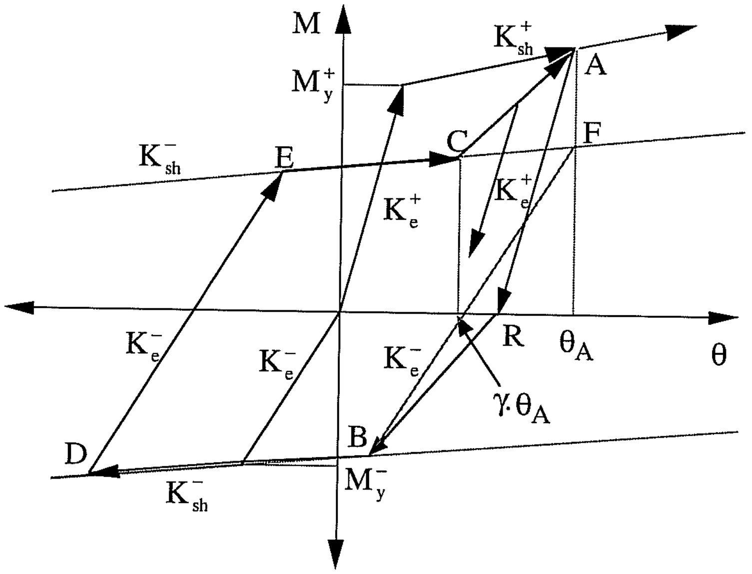

Fig. 6.2: Moment-Rotation Hysteresis Model of Composite Beam (Lee 1987)

$$b_{eff} = 0.19 \cdot \left(1 - e^{-6.6(B/L)}\right)L + b_{cf} + \frac{4GJ}{t_c d_t^2 E_c} \tag{6.1}$$

where G = the shear modulus of elasticity of steel,
J = the torsional constant of transverse beam,
E_c = the modulus of elasticity of concrete,
t_c = a slab thickness,
d_t = the depth of the transverse beam, measured from the midheight of the concrete slab.

For practical purpose, b_{eff} can be taken as $0.19L+b_{cf}$ in Lee's model.

Using the partial interaction theory (Newmark 1951; Robinson 1969) and experimental results, Uang (1985) and Lee (1987) investigated the influence of a slip on the effective width of composite beams. The following was found. When the partial interaction theory employs the stiffness of a shear stud calibrated to the average value of experimental slip data over the beam length, the theory can properly reflect the effect of slip on the positive elastic stiffness. However, for the partial interaction theory to be generally applied to obtain the positive elastic stiffness, more experimental data are required for the flexible behavior of a shear stud along the composite beam. The experimental positive elastic stiffness obtained at design load is smaller by about 15 % than that computed under the full interaction assumption. Later, Lee et al. (1989) used one quarter of the beam length (column face to the inflection point) as the effective width to account for the influence of a slip on the positive elastic stiffness of composite beams.

6.3.2 Ultimate Strength of Composite Beam at Connection

The positive yield moment M_y^+ of the skeleton model shown in Fig. 6.1 is assumed to be a fraction of the ultimate moment at the connection, which can be estimated based on the plastic stress distribution shown in Fig. 6.3. It has been reported that the ultimate strength of composite beams is dependent on the slab area which is contact with the column flange and, as a lower bound, the concrete compressive strength can be increased to $1.3f'_c$ due to the confinement of concrete near the column (duPlessis et al. 1973). In Lee's study, the contribution of the concrete slab to the ultimate strength is determined by using the column width b_{cf} and the concrete compressive stress of $1.4f'_c$. The plastic neutral axis is determined by solving the following equation for compressive steel area, A_{sc}:

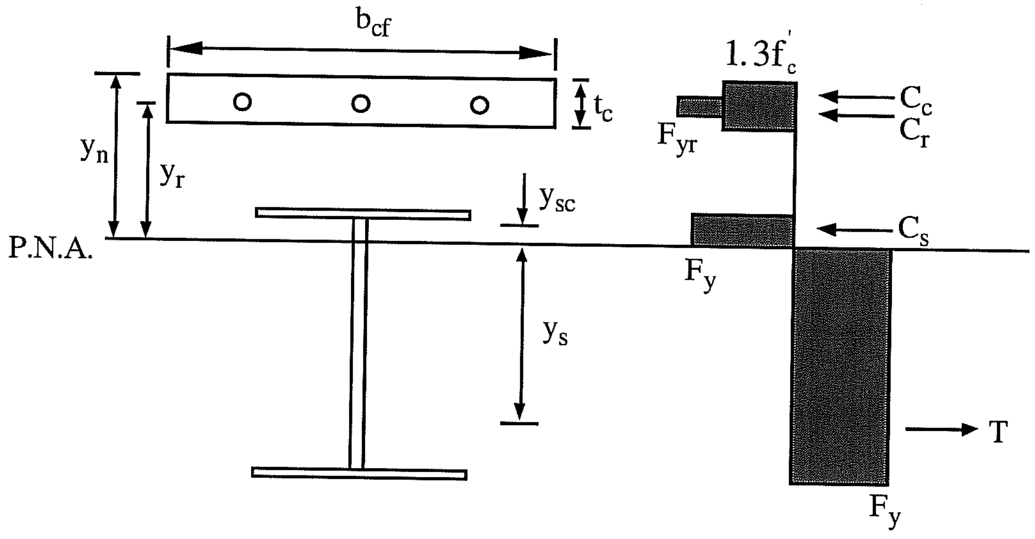

(a) Cross Section (b) Stress Distribution

Fig. 6.3: Plastic Stress Distribution of Composite Beam.

$$2A_{sc}F_y = A_sF_y - 1.4f'_c b_{cf} t_c - A_r F_{yr} \tag{6.2a}$$

The ultimate moment at the connection is defined by

$$M^+_{max} = 1.4f'_c b_{cf} t_c y_n \left(1 - \frac{t_c}{2y_n}\right) + 2A_{sc}F_y y_{sc} + A_s F_y y_s + A_r F_{yr} y_r \tag{6.2b}$$

where y_n = distance from the neutral axis to the top surface of the slab

y_{sc} = distance from the neutral axis to the compression resultant of steel

y_s = distance from the neutral axis to the tension resultant of steel

y_r = distance from the neutral axis to the compression resultant of reinforcing bars

b_{cf} = column flange width

t_c = concrete slab thickness from the top surface to the top of metal deck

A_s = total steel area

A_r = area of reinforcing bars

F_{yr} = yield stress of reinforcing bars.

6.3.3 Moment-Rotation Skeleton and Hysteresis Models

To describe the moment-rotation skeleton and hysteresis models shown in Figs. 6.1 and 6.2, the yield moment, elastic stiffness, and strain-hardening stiffness are required for each of positive and negative moments. From the experimental results, these parameters are empirically determined. The elastic stiffness of an equivalent cantilever composite beam with an effective slab width is

$$K^+_e = \frac{M^+}{\theta^+} = \frac{3EI^+}{L} \qquad \text{for positive moment} \tag{6.3a}$$

$$K^-_e = \frac{M^-}{\theta^-} = \frac{3EI^-}{L} \qquad \text{for negative moment} \tag{6.3b}$$

where I^+ is the moment of inertia of a composite section, I^- is the moment of inertia of a bare steel section, and L is the length of the equivalent cantilever beam. The positive yield moment M^+_y is taken equal to $0.9 \cdot M^+_{max}$. The negative yield moment M^-_y is the plastic moment of the bare steel section. The strain-hardening stiffnesses for positive and negative bending moments are expressed as fractions of the respective elastic stiffnesses as follows:

$$K^+_{sh} = 0.025 \cdot K^+_e \tag{6.4a}$$

$$K^-_{sh} = 0.05 \cdot K^-_e \tag{6.4b}$$

The hysteresis curve (Fig. 6.2), which is created to trace the inelastic behavior of the composite beam, is based on experimental results and finite element analysis results. The basic features are the bilinear hysteresis curve of the bare steel beam (loop B-D-E-F) and a modification for the effect of the concrete slab (line C-A). To model the closing of the crack at the reloading stage to the positive moment region, the crack closing point C is empirically chosen. When the crack starts to close (point C), the reloading path will follow the line C-A. The rotation at the crack closing point, $\gamma \cdot \theta_A$ is assumed to be one-half of the maximum rotation θ_A .

6.3.4 Stiffness of a Plastic Hinge

Lee's composite beam element is a one component series model in which each element is represented by an elastic beam with plastic hinges at its two ends. The inflection point is fixed at an arbitrary point (in the program, the user inputs the data), and the lengths L^+ and L^- are determined, where L^+ and L^- are the lengths of equivalent cantilever beams for positive and negative moments, respectively. The lengths L^+ and L^- are assumed by Lee to be 0.7L and 0.3L, respectively. It is then assumed that the stiffness of the elastic beam element is the elastic stiffness of the composite beam (EI^+), and the two plastic hinges represent inelastic flexural deformation within the lengths L^+ and L^-. The stiffness of a plastic hinge under positive and negative moments is defined as:

$$\frac{1}{K^+_{p.h}} = \frac{1}{K^+_t} - \frac{L^+}{3EI^+} \qquad \text{for positive moment} \qquad (6.5a)$$

$$\frac{1}{K^-_{p.h}} = \frac{1}{K^-_t} - \frac{L^-}{3EI^+} \qquad \text{for negative moment} \qquad (6.5b)$$

where K^+_t is the tangent stiffness of the moment-rotation skeleton and hysteresis models based on the flexural rigidity of the composite beam EI^+ and L^+, and K^-_t is the tangent stiffness based on the flexural rigidity of a bare steel beam EI^- and L^-. It is noted that the plastic hinge stiffness formulation accounts for the reduction of elastic stiffness under negative moment.

6.4 Improvement of Lee's Composite Beam Model

In this study, a new hysteretic moment-rotation model, which is a modification of Lee's hysteretic moment-rotation model, is developed. In the composite beam element, the capability to account for the influence of a moving inflection point on the element stiffness is added.

6.4.1 Hysteresis Behavior of Composite Beam

Lee's skeleton model (Fig. 6.1) is employed as the monotonic moment-rotation relation for a plastic hinge. The basic parameters to describe the monotonic relations are determined through calibration to available experimental data (Uang 1985; Lee 1987; Tagawa 1986, 1989). In Lee's approach, the effective width of L/4 is applied to calculate the positive elastic stiffness, where L is the beam length from the column face to the inflection point. In this work, however, the minimum of the following three criteria (LRFD Specification 1994) determines the effective width of the concrete slab on each side of the beam center-line for computing positive elastic stiffness:

$$b_{eff} \le \begin{cases} L/8 \\ b_o/2 \\ b_{es} \end{cases} \qquad (6.6)$$

where L is the beam span, center to center of supports, b_o is the distance from the beam center-line to the center-line of the adjacent beam, and b_{es} is the distance from the beam center-line to the edge of the slab. Using the effective concrete slab width, the moment of inertia of a composite section I_{tr} is calculated. To account for the influence of slip between the concrete slab and the steel beam on the positive elastic stiffness, the moment of inertia I^+ applied to the positive elastic stiffness is assumed to be a fraction of I_{tr}. From the available experimental results, it has been found that I^+ equal to $0.85 \cdot I_{tr}$ is reasonable. To obtain the moment of inertia I^- used for the negative elastic stiffness, the steel beam section and reinforcing steel bars within the effective slab width are considered. The negative yield moment M_y^- is the plastic moment of both the steel beam section and reinforcing steel bars within the effective width. The contribution of the concrete slab to the ultimate moment M_{max}^+ at the connection is determined by using the column width b_{cf} and the concrete compressive bearing stress of $1.3f_c^{'}$ (duPlessis et al. 1973). The plastic neutral axis is determined by solving the following equation for compressive steel area, A_{sc}:

$$2A_{sc}F_y = A_sF_y - 1.3f_c^{'}b_{cf}t_c - A_rF_{yr} \tag{6.7a}$$

From Fig. 6.3 and Eq. 6.7a, the ultimate moment at the connection is written as

$$M_{max}^+ = 1.3f_c^{'}b_{cf}t_cy_n\left(1 - \frac{t_c}{2y_n}\right) + A_{sc}F_yy_{sc} + (A_s - A_{sc})F_yy_s + A_rF_{yr}y_r \tag{6.7b}$$

where A_r is the area of reinforcing steel bars within the effective slab width. The positive yield moment M_y^+ is assumed to be a fraction of M_{max}^+. From the available experimental data, it has been found that the positive yield moment M_y^+ of $0.95M_{max}^+$ is reasonable. The strain-hardening stiffnesses for positive and negative bending moments are the same as those suggested by Lee (1987).

The proposed hysteretic moment-rotation model of a composite beam is shown in Fig. 6.4. The model is divided into positive and negative moment regions by an inclined neutral line, which has the slope K_{sh}^- and passes through the origin of the coordinate system. The envelope of the positive moment curve and the bound lines in the negative and positive moment regions are taken from the monotonic model.

The stiffness degradation in the negative moment region is illustrated in Fig. 6.4a. The factor α defines the ratio of the negative linear elastic range to the negative yield moment. The factor α is determined empirically by examining the available experimental results (Uang 1985; Lee 1987; Tagawa 1986, 1989), and is chosen to be:

$$\alpha = 0.5 \tag{6.8}$$

Figure 6.4b shows the stiffness degradation, pinching, and strength deterioration for the positive moment region. The stiffness degradation begins at the inclined neutral line. The effect of pinching and strength deterioration are represented, respectively, by the γ and β factors, which are determined empirically by examining available experimental data:

$$\gamma = 0.2 \tag{6.9}$$

$$\beta = 0.05 \tag{6.10}$$

It is noted that whenever the crack starts to close (point F) after the crack opens, the reloading path will follow the linear crack closing line F-A'.

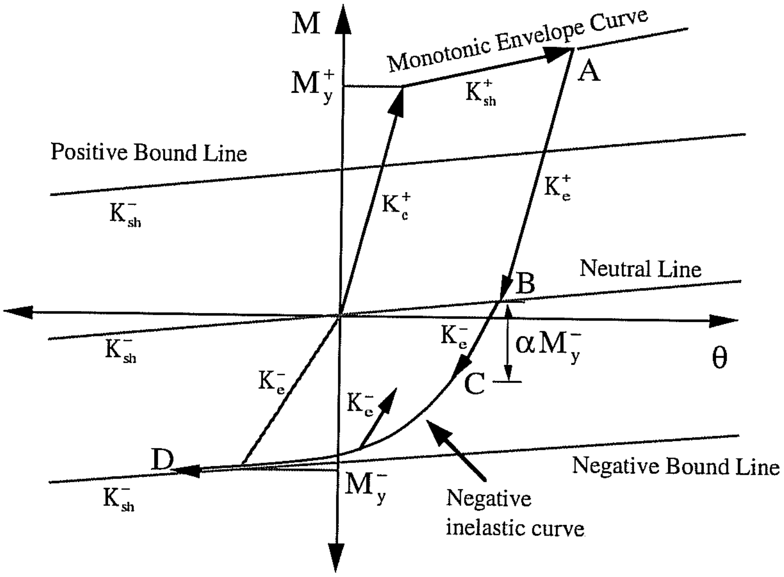

a) Stiffness Degradation for Negative Moment

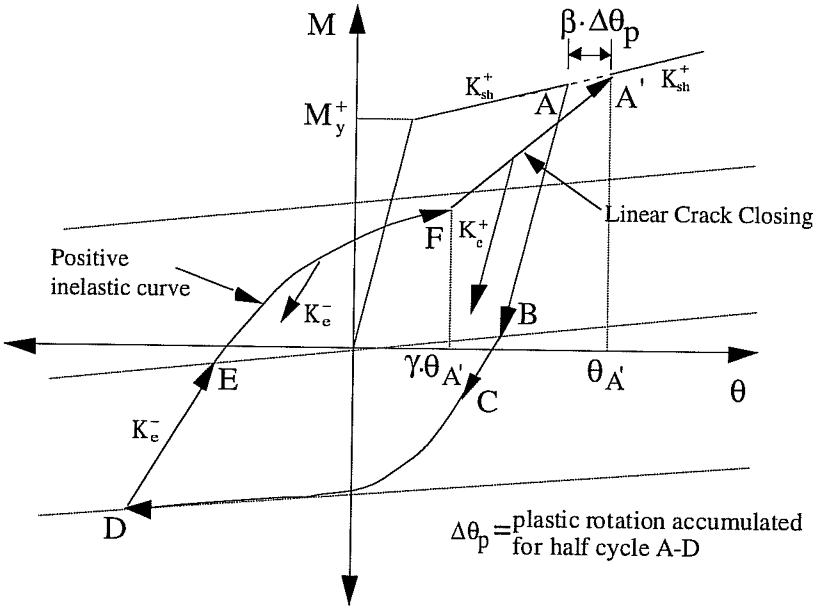

b) Stiffness Degradation and Pinching for Positive Moment

Fig. 6.4: Proposed Hysteretic Moment-Rotation Model of Composite Beam

The negative and positive inelastic curves (lines C-D and E-F) are described by the plastic stiffness obtained by using the shape factor $\hat{h}$ (Dafalias 1975). Figure 6.5 shows the plastic stiffness K_p^A at an arbitrary point A on the inelastic curve, which is a function of the shape factor $\hat{h}$. The plastic stiffness K_p^A is determined from the following equation:

$$K_p^A = K_{sh}^{-p}\left[1+\hat{h}\frac{\delta_A}{\delta_{in}-\delta_A}\right] \tag{6.11}$$

where δ_{in} is the initial distance between the starting point of the inelastic curve and the corresponding point on the bound line, and δ_A is the distance between an arbitrary point A on the inelastic curve and the corresponding point on the bound line.

The procedure to determine the shape factor $\hat{h}$ is presented as follows:

i) Choose an arbitrary point A such that $\frac{1}{10} \le \frac{\delta_A}{\delta_{in}} \le \frac{1}{2}$

ii) $h = \frac{\delta_A}{\theta_p^A} + \frac{\delta_{in}}{\theta_p^A}\cdot\left[\ln\left(\frac{\delta_{in}}{\delta_A}\right) - 1\right]$ (Dafalias 1975)

iii) $\hat{h} = \frac{h}{K_{sh}^{-p}}$

By applying the above procedure to the available experimental data, it has been determined that the shape factors, $\hat{h}_n$ and $\hat{h}_p$ were chosen as 10 and 6, respectively, for the negative and positive inelastic curves as shown Figs. 6.4a and 6.4b.

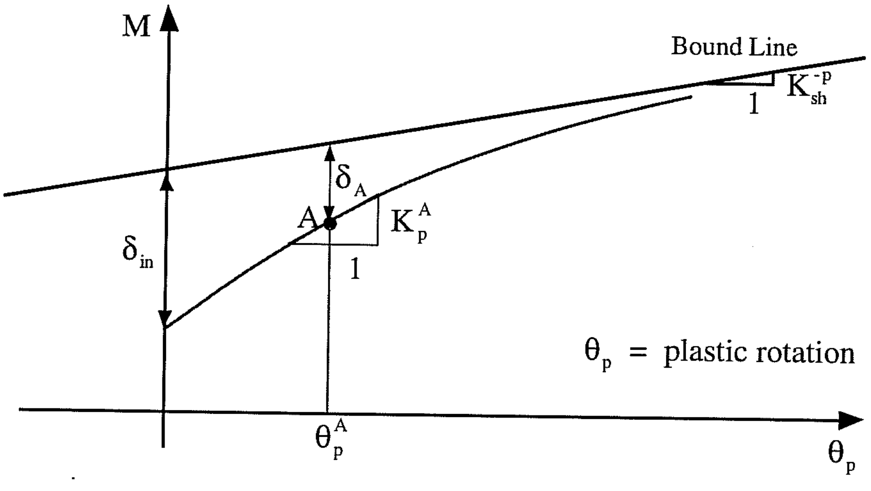

Fig. 6.5: Plastic Stiffness of Inelastic Moment-Rotation Curve

6.4.2 Element Stiffness Matrix

The proposed composite beam element is a one component series model in which each element is represented by an elastic beam with plastic hinges at its two ends. The element has the capability to account for the influence of a moving inflection point on the element stiffness. It is assumed that the inflection point does not change during a small load or time step and the inflection point obtained at the end of the previous load step can be applied to the next load step. At the end of a load step, the inflection point is determined from the linear moment distribution induced by earthquake motions alone, under the assumption that the moment distribution due to the gravity load is not significant when compared to that due to earthquake excitations.

According to the inflection point obtained at the end of the previous load step, the lengths L^I and L^J are determined, where L^I and L^J are the lengths of equivalent cantilever beams for positive and negative moments. It is then assumed that the stiffness of the elastic beam element is the elastic stiffness of the composite beam (EI^+), and the two plastic hinges at the member ends I and J represent inelastic flexural deformation within the lengths L^I and L^J. The stiffness of each of the two plastic hinges is defined as:

$$\frac{1}{K_{p.h}^{I}} = \frac{1}{K_t^I} - \frac{L^I}{3EI^+} \qquad \text{for plastic hinge of end I} \tag{6.12a}$$

$$\frac{1}{K_{p.h}^{J}} = \frac{1}{K_t^J} - \frac{L^J}{3EI^+} \qquad \text{for plastic hinge of end J} \tag{6.12b}$$

where K_t^I is the tangent stiffness of the hysteresis moment-rotation model based on the equivalent cantilever length L^I, and K_t^J is the tangent stiffness based on the length L^J.

In the local coordinate system, the element can be assumed as a simply supported beam after the rigid body motions are removed. The element deformations in the local coordinate system can be represented by three relative deformations shown in Fig. 6.6. The flexibility relation of a simply supported beam is formulated in a matrix form as

$$\begin{Bmatrix} d\delta \\ d\theta^I \\ d\theta^J \end{Bmatrix} = \begin{bmatrix} f_{11} & 0 & 0 \\ 0 & f_{22} & f_{23} \\ 0 & f_{32} & f_{33} \end{bmatrix} \cdot \begin{Bmatrix} dF \\ dM^I \\ dM^J \end{Bmatrix} \tag{6.13a}$$

or

$$\mathbf{dv} = \mathbf{F}_t \cdot \mathbf{ds} \tag{6.13b}$$

where

$$f_{11} = \frac{L}{EA}$$

$$f_{22} = \frac{L}{3EI^+} + \frac{1}{K_{p.h}^{I}} + \frac{1}{GA_sL}$$

$$f_{23} = f_{32} = -\frac{L}{6EI^+} + \frac{1}{GA_sL}$$

$$f_{33} = \frac{L}{3EI^+} + \frac{1}{K_{p.h}^{J}} + \frac{1}{GA_sL}$$

A_s = effective shear area of composite beam.

The element stiffness matrix is obtained by inverting the flexibility matrix which results in the form,

$$\mathbf{ds} = \mathbf{K}_t \cdot \mathbf{dv} \tag{6.14}$$

in which $\mathbf{K}_t = \mathbf{F}_t^{-1}$.

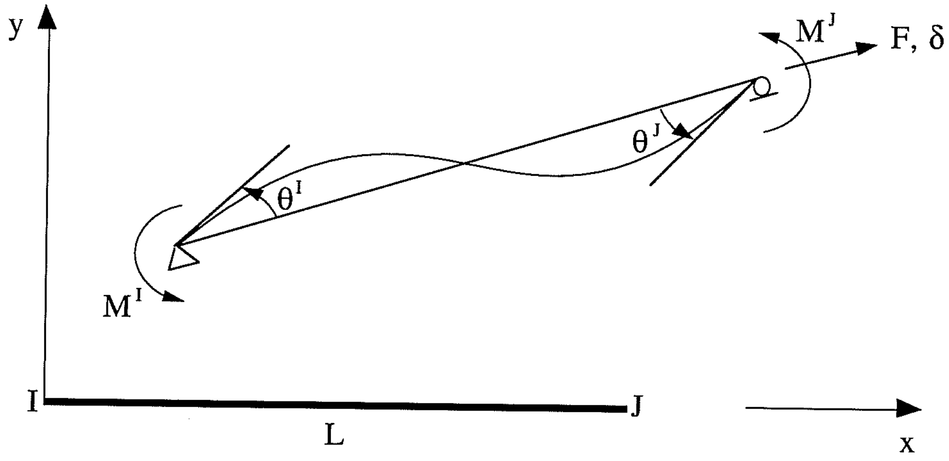

Fig. 6.6: Relative Deformations of Composite Beam Element

6.5 Comparison to Experimental Results

To investigate the behavior of the proposed model, comparison of analytical and experimental results for available composite beam test specimens is presented in this section. In the next chapter, the developed composite beam element, combined with the developed beam-column and panel zone elements will be applied to subassemblages and frames with a concrete slab.

The cross-sections of composite beams of two small-scale specimens CG3 and CG4 (Uang 1985) and full-scale specimens EJ-WC (Lee 1987), Tagawa 86 (Tagawa 1986), and Tagawa 89 (Tagawa 1989) are shown in Fig. 6.7. The other dimensions and material properties are listed in Table 6.1 and Figs. 6.8 to 6.13. The only difference between the specimens CG3 and CG4 is that the metal deck in specimen CG3 is sand-blasted before pouring the concrete, whereas in specimen CG4 it was not sand-blasted.

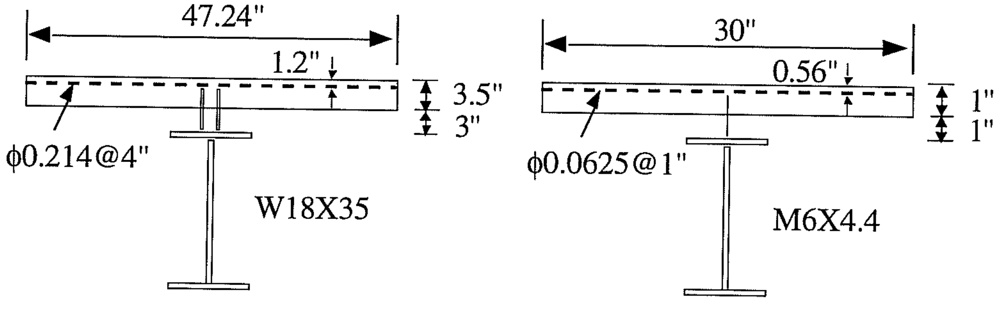

a) Specimen EJ-WC

b) Specimens CG3 and CG4

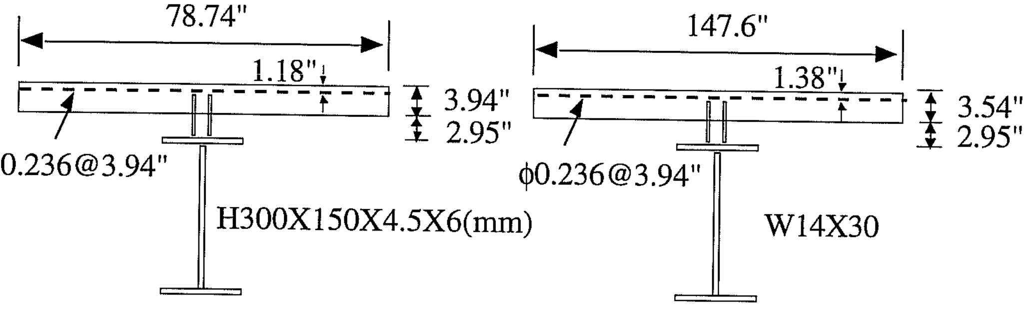

c) Specimen Tagawa 86

d) Specimens Tagawa 89

Fig. 6.7: Cross-Sections of Test Specimens (Lee 1987; Uang 1985; Tagawa 1986, 1989).

Test Specimen	Steel Yield Stress (ksi)				Reinforced Steel Strength (ksi)	Concrete Strength (ksi)
	Beam		Column			
	Web	Flange	Web	Flange		
Uang CG3	41.5	37.0	no	no	79	4.26
Uang CG4	41.5	37.0	no	no	79	4.26
Lee EJ-WC	37.8	36.65	39.2	36.4	60	5.1
Tagawa 86	43.8	40.61	no	no	no	3.96
Tagawa 89	47.86	41.19	54.68	41.48	51.63	3.55

Table 6.1: Material Properties of Test Specimens (Lee 1987, Uang 1985, and Tagawa 1986, 1989).

Figure 6.8 shows the comparison of experimental and analytical results of Lee's specimen EJ-WC. The specimen was an exterior joint assemblage, and its beam was connected to the column web by connecting plates. The comparison shows good agreement until the bottom flange of steel beam develops severe local buckling. The comparisons of experimental and analytical results of Uang's specimens CG3 and CG4 are presented in Figs. 6.9 and 6.10. The comparisons show reasonable agreement until local buckling occurs at the bottom flange.

The correlation of the experimental and analytical results for the specimen Tagawa 86 is shown in Figs. 6.11 and 6.12. The analytical and experimental results are the beam moment-rotation relations at point A of the subassemblage shown in Figs. 6.11 and 6.12. In the analytical results shown in Fig. 6.11, the effect of reinforcing bars was not considered because the yield stress of reinforcing bars was not available. The analytical model develops much smaller strengths for the negative and positive moments than the experiment, and shows more flexible behavior on the negative moment region than the experiment. In Fig. 6.12, the analytical results in which the effect of reinforcing bars is considered, are presented. The yield stress of reinforcing bars was assumed to be that of the steel beam. The correlation of the experimental and analytical results is greatly improved by accounting for the effect of the reinforcing bars.

The comparison of the experimental and analytical results for the specimen Tagawa 89 is presented in Fig. 6.13. The agreement between the experimental and analytical results is reasonable except that the analytical model overestimates the strength for small amplitudes of rotation.

From the comparisons, it has been shown that the developed composite beam element can reasonably model the strength, stiffness, pinching, and stiffness degradation of a composite beam until local buckling of the beam bottom flange occurs.

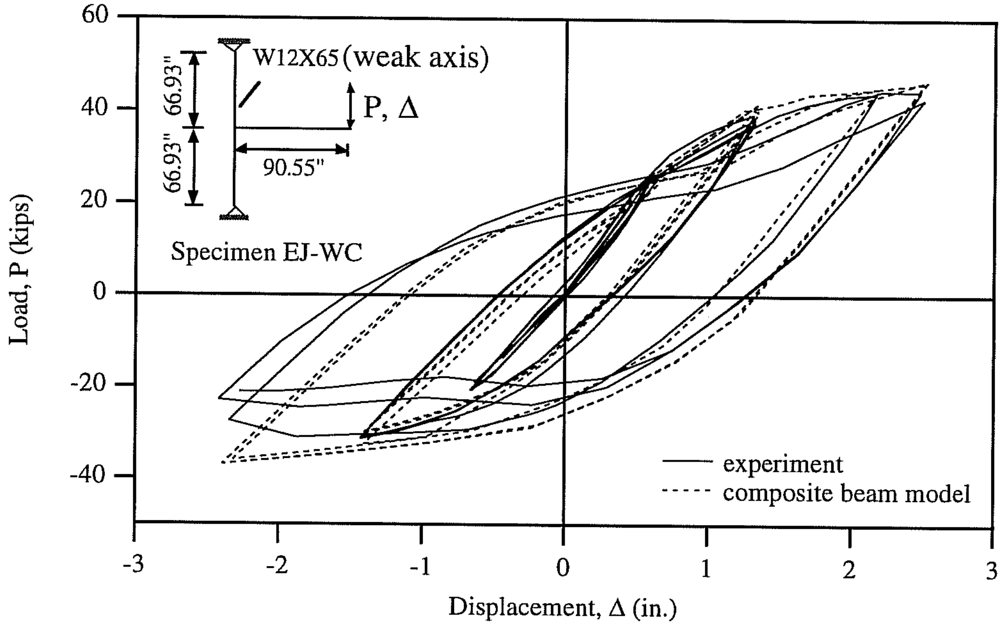

Fig. 6.8: Comparison of Experimental and Analytical Results of Specimen EJ-WC

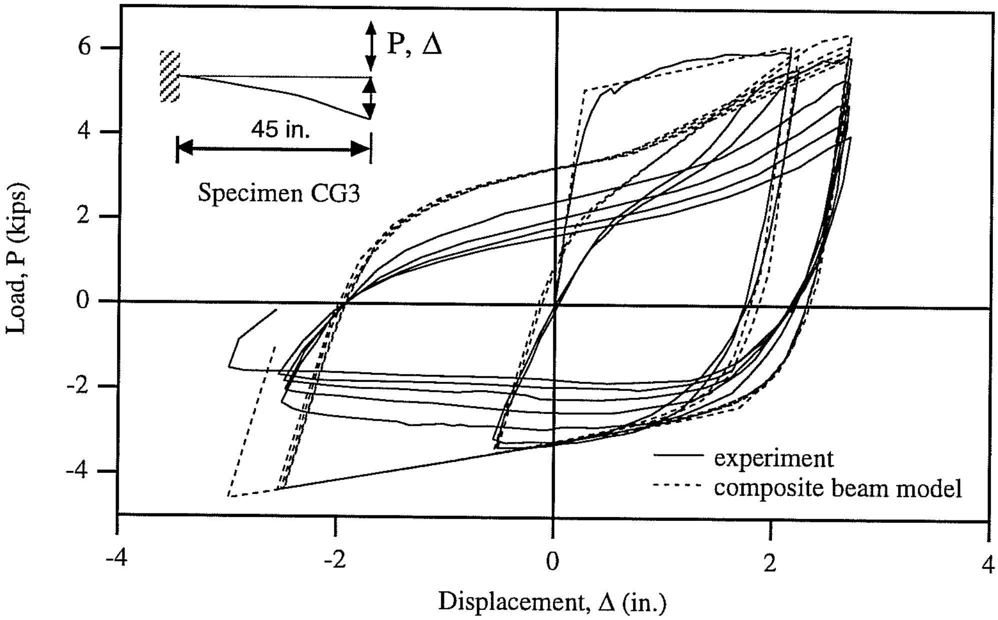

Fig. 6.9: Comparison of Experimental and Analytical Results of Specimen CG3

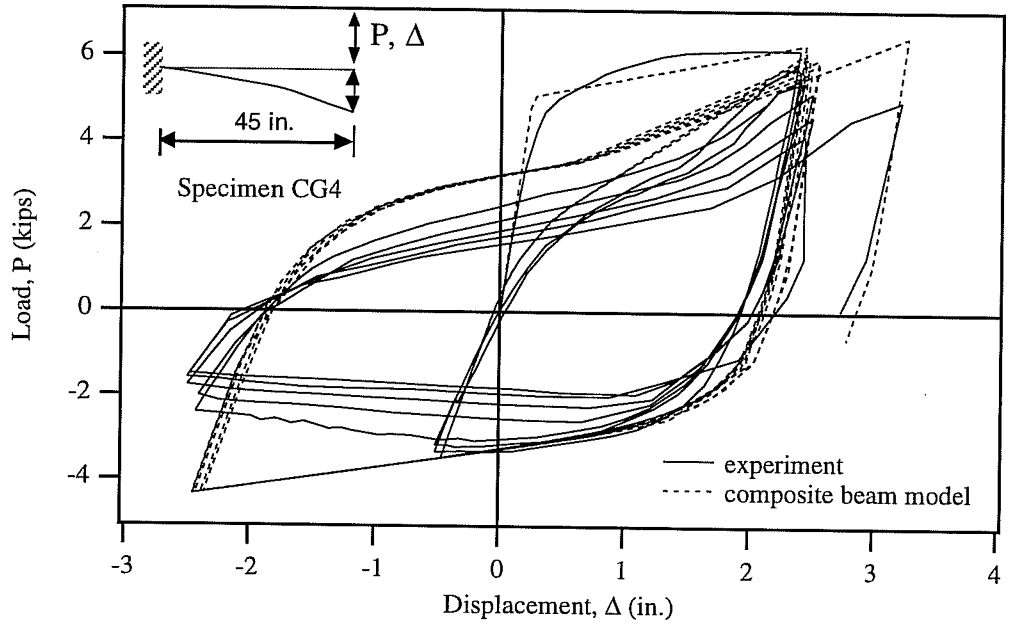

Fig. 6.10: Comparison of Experimental and Analytical Results of Specimen CG4

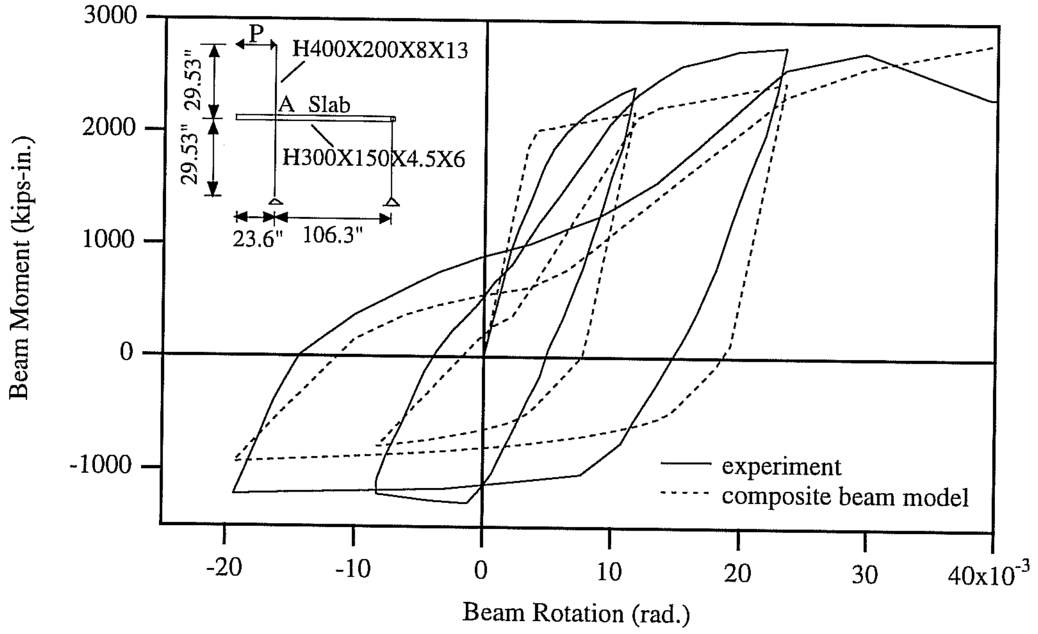

Fig. 6.11: Comparison of Experimental and Analytical Results of Specimen Tagawa 86

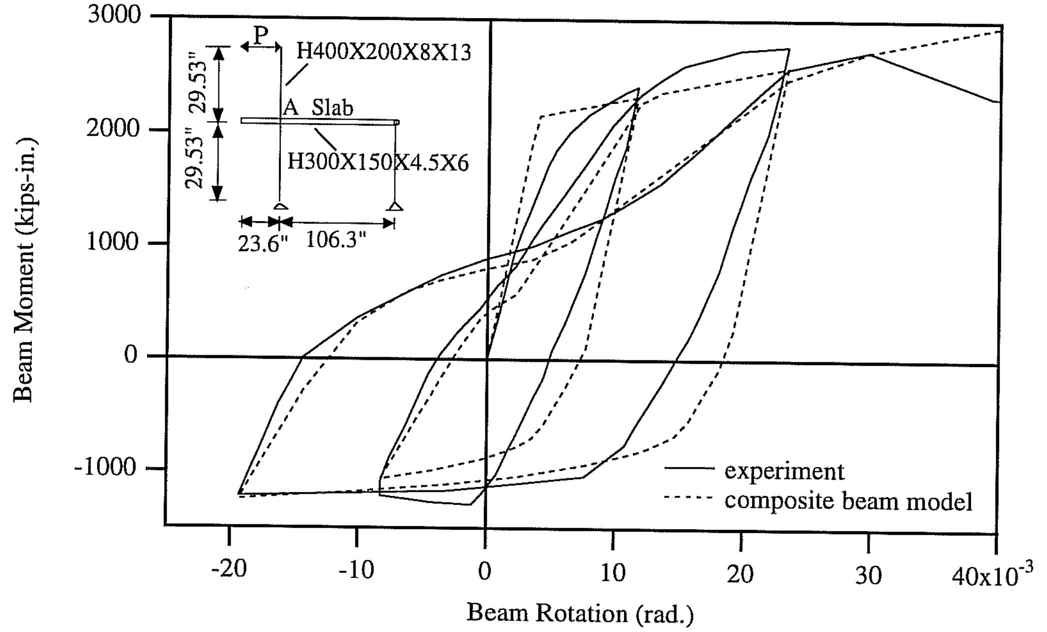

Fig. 6.12: Comparison of Experimental and Analytical Results of Specimen Tagawa 86

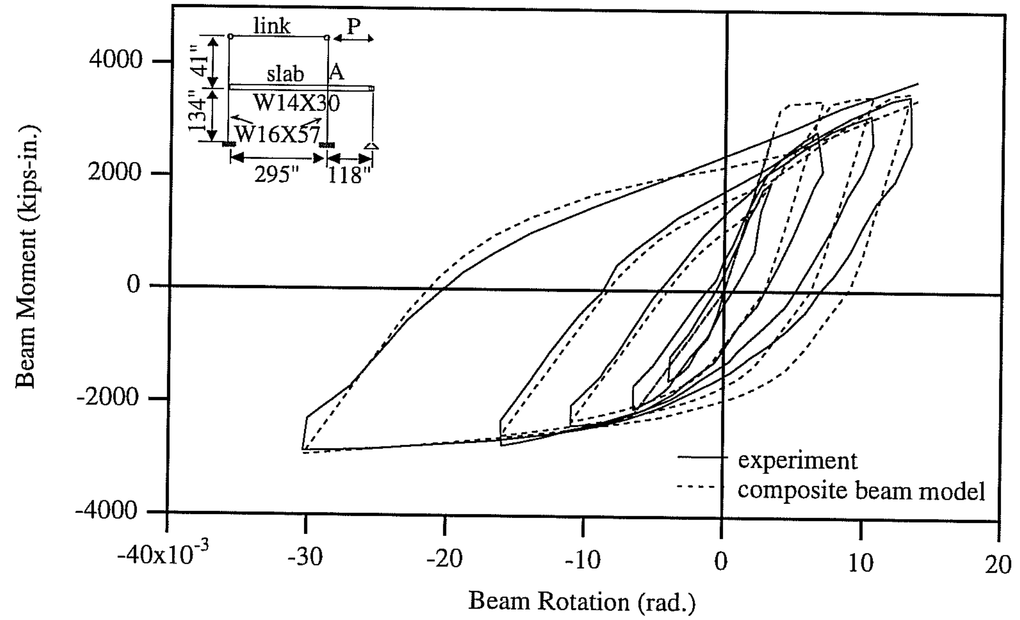

Fig. 6.13: Comparison of Experimental and Analytical Results of Specimen Tagawa 89

6.6 Summary

In this chapter, a composite beam element has been developed by modifying the model proposed by Lee. In the hysteretic model of the developed element, a smooth transition from the elastic stage to the inelastic stage and the strength deterioration at the linear crack closing stage were considered. The capability to account for a moving inflection point was added in the element. The predicted results by the developed element matched reasonably well with the experimental results before local buckling dominated the experimental response.

Chapter 7: APPLICATION OF MODELS TO SUBASSEMBLAGES AND FRAMES

7.1 Introduction

In the previous chapters, the multi-linear hinge element, nonlinear panel zone element, and composite beam element were developed for bare steel beams and columns, column panel zones, and composite beams. The performance of each element was investigated by comparison with experiments on isolated components. In this chapter, to investigate the interaction between these analytical elements for the various components of a structure, the elements are combined into steel subassemblages with and without a concrete slab and into steel frames with and without a concrete slab. Overall and local analytical responses are compared with experimental data and with the results predicted by the existing bilinear hinge element and the bilinear panel zone element.

To model bare steel subassemblages and frames, the multi-linear hinge elements with multi-linear yield surfaces are combined with nonlinear panel zone elements, unless the columns are oriented in the direction of the weak axis bending. The member end eccentricities as shown in Fig. 5.2 are considered to model the joints of structures instead of the center-to-center line representation of structures. To model steel subassemblages and frames with concrete slabs, the multi-linear hinge elements with multi-linear yield surfaces and composite beam elements are combined with nonlinear panel zone elements. The structural P-Δ effects are included in the analyses. For both the existing bilinear hinge element and bilinear panel zone element, the ratio of the strain hardening stiffness to the elastic stiffness of 0.03 is employed.

7.2 Bare Steel Subassemblages and Frames

In this section, bare steel subassemblages and frames are analyzed by the multi-linear hinge element and nonlinear panel zone element developed in the previous chapters. Material properties and panel zone details of the available test specimens (Krawinkler 1971; Popov 1975; Popov 1985; Engelhardt 1994; Wakabayashi 1974; Carpenter 1973) for bare steel subassemblages and frames are presented in Tables 5.1, 5.2, and 7.1.

The comparison between the experimental data and the analytical results obtained by the multi-linear hinge and nonlinear panel zone elements for Krawinkler Specimens A-1 and A-2 is shown in Figs 7.1a through 7.2d. The results predicted by the bilinear hinge and bilinear panel zone elements are also compared with the experimental data. To facilitate the discussion, the analysis by the multi-linear hinge and nonlinear panel zone elements will be referred to as "Analysis 1", and the analysis by the bilinear hinge and bilinear panel zone elements will be referred to as "Analysis 2". Specimens A-1 and A-2 are identical except that these specimens are tested with two different loading programs.

Figures 7.1a and 7.2a show the comparison of overall responses obtained by the test and Analysis 1. The agreement between the experimental and analytical results is good. Figures 7.1b and 7.2b show the comparison of overall responses obtained by the test and Analysis 2. The correlation of the experimental and analytical results is quite poor. In Figs 7.1c, 7.1d, 7.2c, and 7.2d, the comparisons of local responses obtained by displacement control (Ramm 1980) for the horizontal displacement Δ at the bottom of the column are presented. The horizontal force-beam rotation relations are presented in Figs.

7.1c and 7.2c. In Figs. 7.1d. and 7.2d the panel moment-rotation relations are shown. As far as the strength is concerned, Analysis 1 produces significantly better results than Analysis 2. However, as far as rotation is concerned, both analyses show some discrepancies.

Test Specimen	Yield Stress (ksi)					Connection Type	Doubler Plate Thickness
	Beam		Column		Doubler Plate		
	Web	Flg.	Web	Flg.			
Engelhardt 2B	44.2	41.4	58.6	56.9	no	fully welded	no
Popov C2	38	38	32.5	32.5	n/a	fully welded	0.25"
Wakabayashi FC0	37.7	37.7	37.7	37.7	n/a	n/a	n/a
Wakabayashi FC5	37.7	37.7	37.7	37.7	n/a	n/a	n/a
Carpenter Frame A	41.1	34.7	35.7	35.2	n/a	fully welded	0.1875"
Carpenter Frame B	41.6	34.7	42.5	37.7	n/a	fully welded	0.1875"

* n/a = not available.

Table 7.1: Material Properties of Test Specimens (Engelhardt 1994, Popov 1975, Wakabayashi 1974, and Carpenter 1973).

Figures 7.3a and 7.4a show the comparison of overall responses obtained by the test and Analysis 1 for Specimens B-1 and B-2, respectively. Specimens B-1 and B-2 are identical but are subjected to different cyclic loadings. The analytical results obtained by the multi-linear hinge and nonlinear panel zone elements (Analysis 1) match well with the experimental data. In Figs. 7.3b and 7.4b, the results predicted by Analysis 2 are plotted against the experimental data. The overall analytical results obtained by the bilinear hinge and bilinear panel zone elements (Analysis 2) are acceptable. The comparisons of local responses obtained by displacement control for the horizontal displacement Δ shown in Fig. 7.3a are presented in Figs 7.3c, 7.3d, 7.4c, and 7.4d. The horizontal force-beam rotation relations are presented in Figs. 7.3c and 7.4c. In Figs. 7.3d. and 7.4d the panel moment-rotation relations are shown. The positive and negative maximum beam rotations predicted by Analysis 2 are much smaller than those predicted by the test, and the corresponding panel rotations predicted by Analysis 2 are much larger than the experimental data. However, the beam rotations and panel rotations obtained by Analysis 1 are much closer to the experimental data than those predicted by Analysis 2.

Based on the experimental data, the panel zones of Specimens A-1 and A-2 are the weakest element when compared with the other elements (the yielding of the beams is very limited and the columns remain elastic). The difference between local deformations predicted by Analysis 1 and Analysis 2 for Specimens A-1 and A-2 is therefore not significant. However, the experimental data indicates that significant yielding occurs in both the beams and the panel zones for Specimens B-1 and B-2 (the yielding of the beams is more severe than that of the panel zones). Consequently, in the analysis it is necessary for the yielding to be properly distributed between the elements. For the yielding to be properly distributed between the elements during the analyses, the analytical elements for the structural components should be able to accurately model the mechanical behavior of the structural components. Since the multi-linear hinge and nonlinear panel zone elements have the capability to more accurately model the mechanical behavior of the structural components, as shown in chapters 4 and 5, the local deformations predicted by Analysis 1 are much better than those obtained by Analysis 2.

When the structure shown in Fig. 7.1a is analyzed by displacement control for the horizontal displacement Δ, the corresponding horizontal force H is obtained such that it is equilibrated with the member forces of the structure caused by a given displacement Δ. Therefore, the local responses obtained by displacement control for the horizontal displacement Δ are actually obtained by force control for the member forces in equilibrium with the horizontal force H. When the force-deformation relations obtained by force control are compared with the experimental data, the discrepancy between the displacements obtained by the experiment and the analysis for the same force may be large due to a small stiffness in the inelastic range. This is the reason that even though the multi-linear hinge and nonlinear panel zone elements can reasonably model the mechanical behavior of the structural components as shown in chapters 4 and 5, there are some discrepancies between the experimental data and the local responses predicted by Analysis 1. If the more refined analytical models for the structural components employ the specific parameters suitable to a given test specimen which are required to describe the material properties, the discrepancy between the local responses predicted by the test and the analysis for the given test specimen will decrease. However, when the more refined analytical elements employ the general parameters as employed to describe the material properties in this work, it is not guaranteed that they can always produce more exact local responses than the multi-linear hinge and nonlinear panel zone elements.

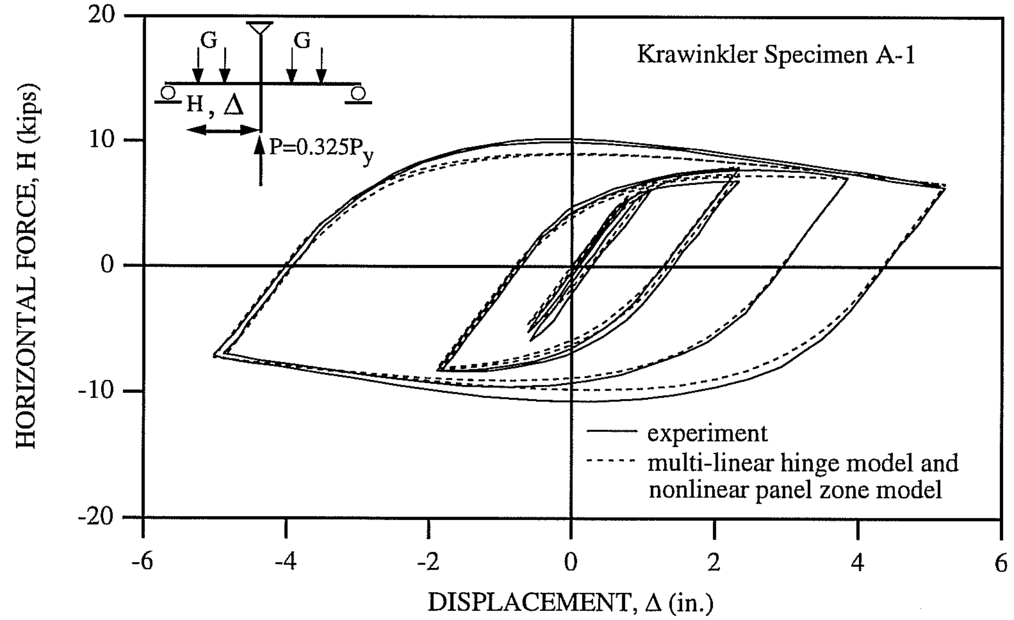

Fig. 7.1a: Comparison of Experimental and Analytical Results Obtained by Multi-linear Hinge Model and Nonlinear Panel Zone Model for Krawinkler Specimen A-1 (Krawinkler 1971).

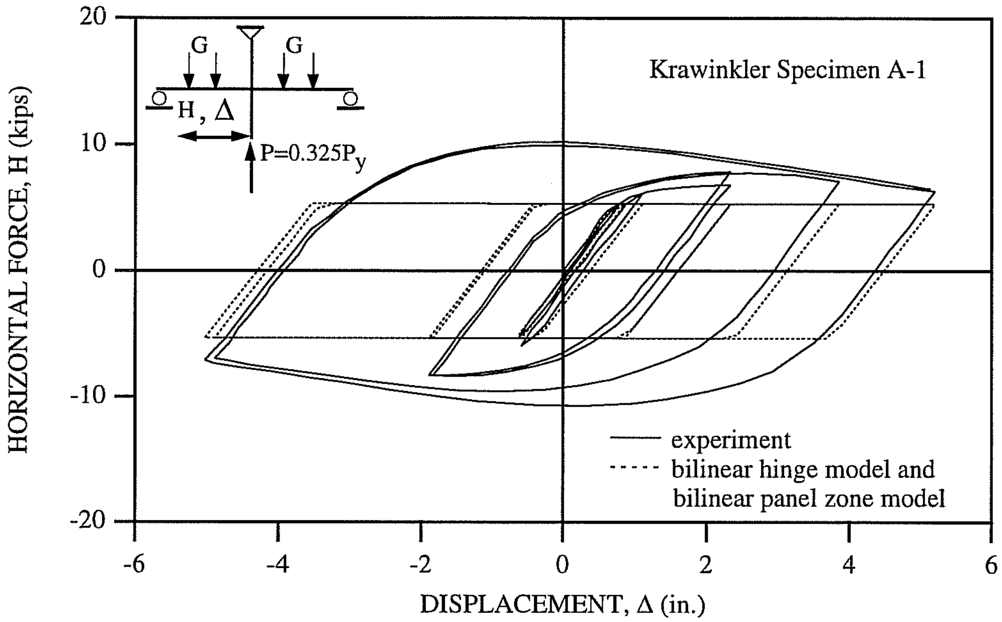

Fig. 7.1b: Comparison of Experimental and Analytical Results Obtained by Bilinear Hinge Model and Bilinear Panel Zone Model for Krawinkler Specimen A-1(Krawinkler 1971).

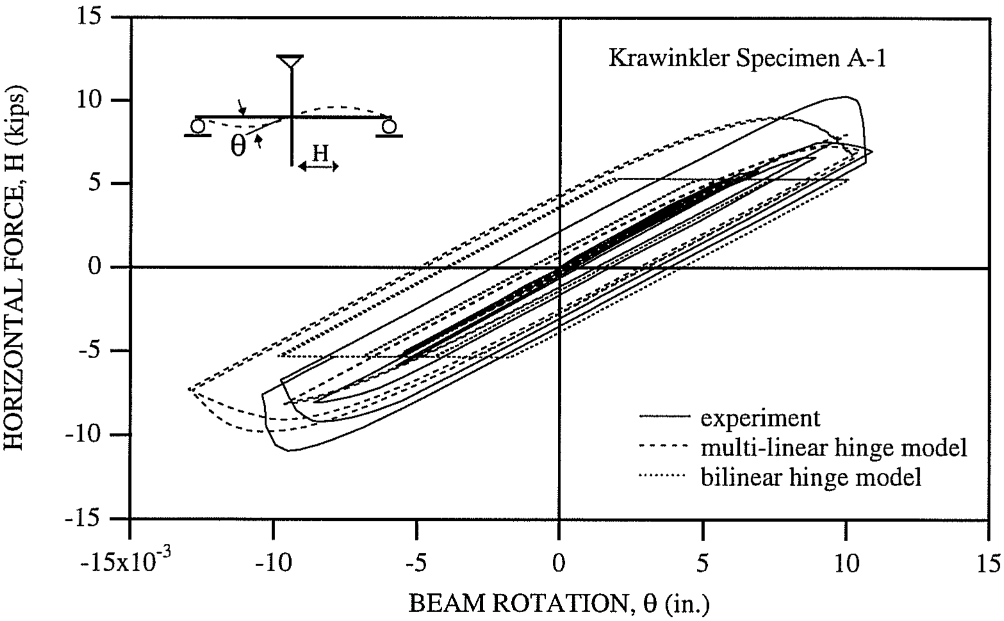

Fig. 7.1c: Comparison of Experimental and Analytical Horizontal Force-Beam Rotation Relations of Krawinkler Specimen A-1 (Krawinkler 1971).

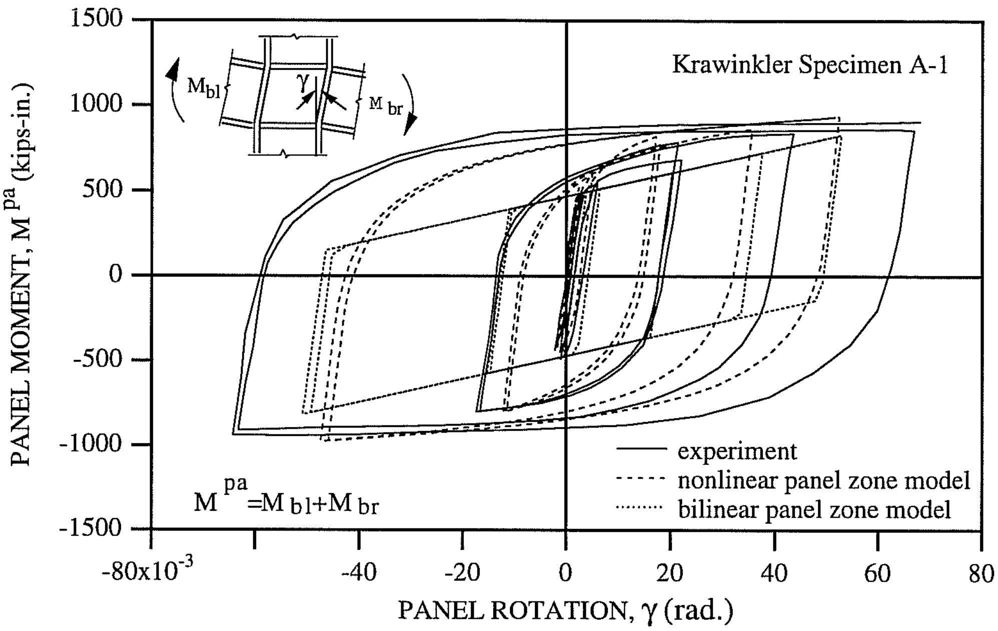

Fig. 7.1d: Comparison of Experimental and Analytical Panel Moment-Rotation Relations of Krawinkler Specimen A-1 (Krawinkler 1971).

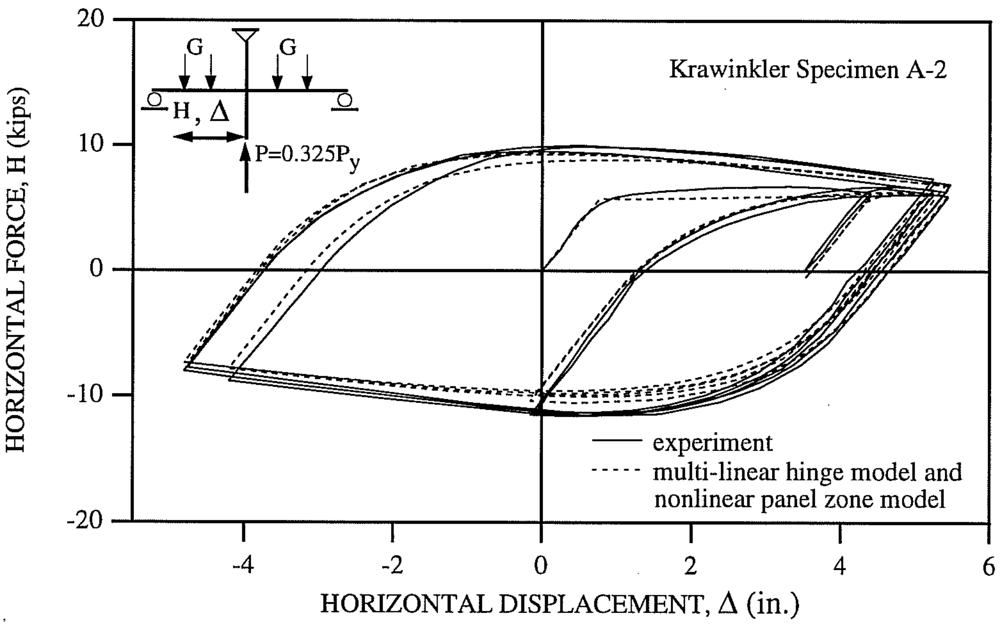

Fig. 7.2a: Comparison of Experimental and Analytical Results Obtained by Multi-linear Hinge Model and Nonlinear Panel Zone Model for Krawinkler Specimen A-2 (Krawinkler 1971).

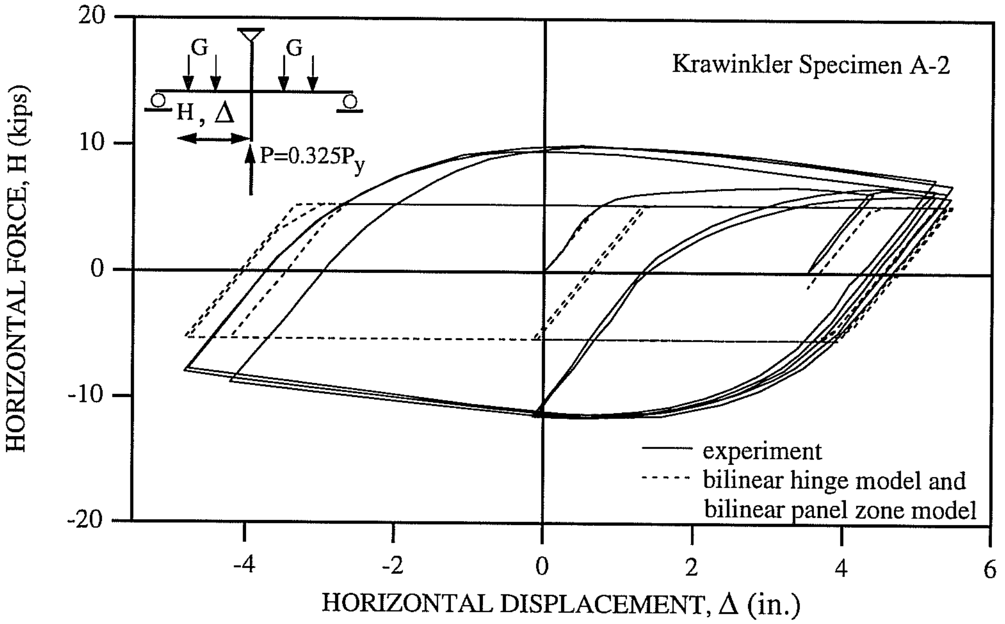

Fig. 7.2b: Comparison of Experimental and Analytical Results Obtained by Bilinear Hinge Model and Bilinear Panel Zone Model for Krawinkler Specimen A-2 (Krawinkler 1971).

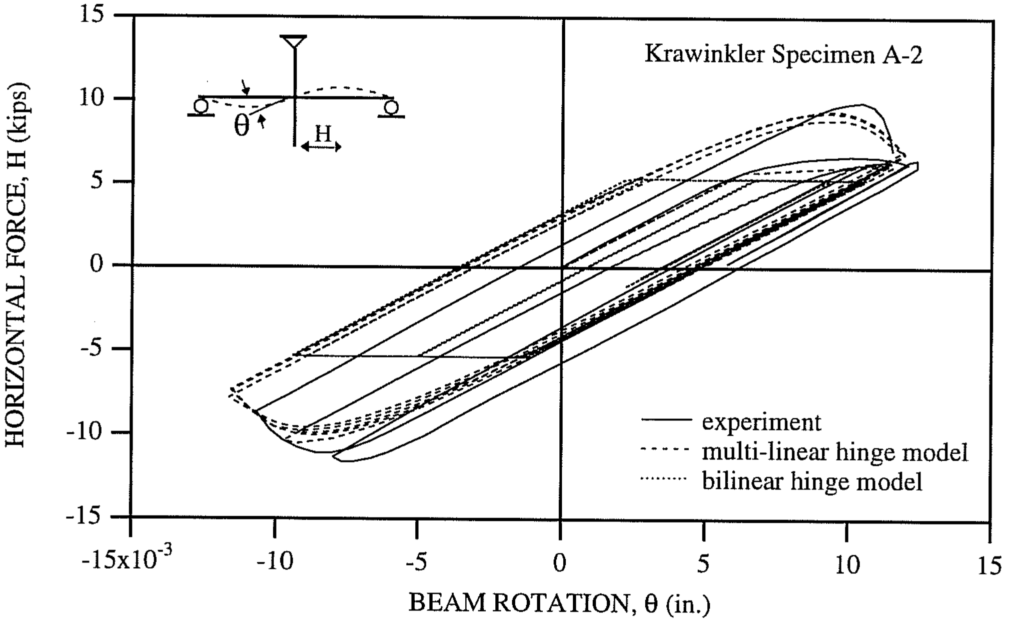

Fig. 7.2c: Comparison of Experimental and Analytical Horizontal Force-Beam Rotation Relations of Krawinkler Specimen A-2 (Krawinkler 1971).

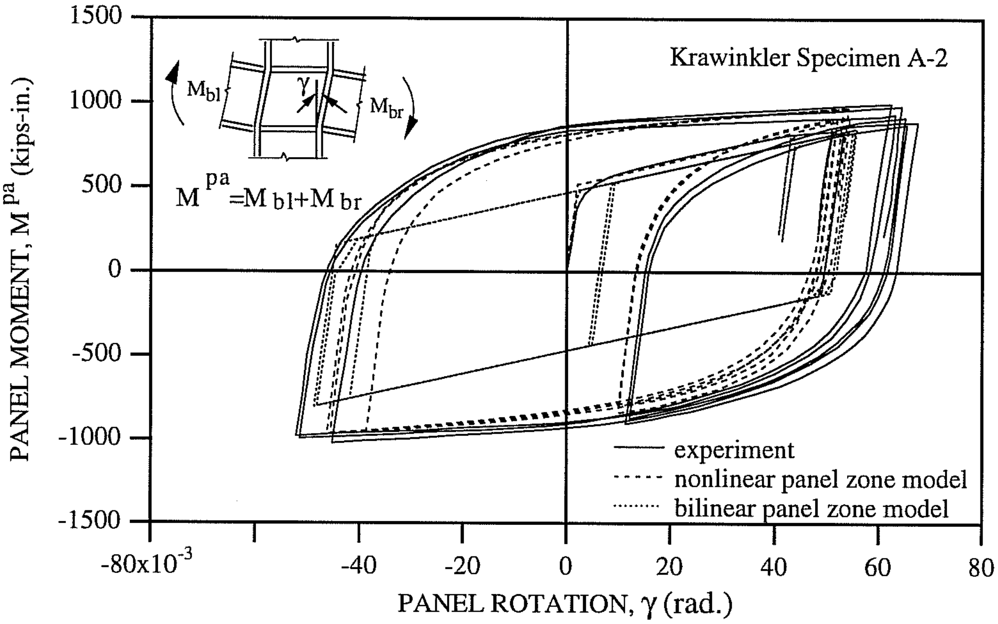

Fig. 7.2d: Comparison of Experimental and Analytical Panel Moment-Rotation Relations of Krawinkler Specimen A-2 (Krawinkler 1971).

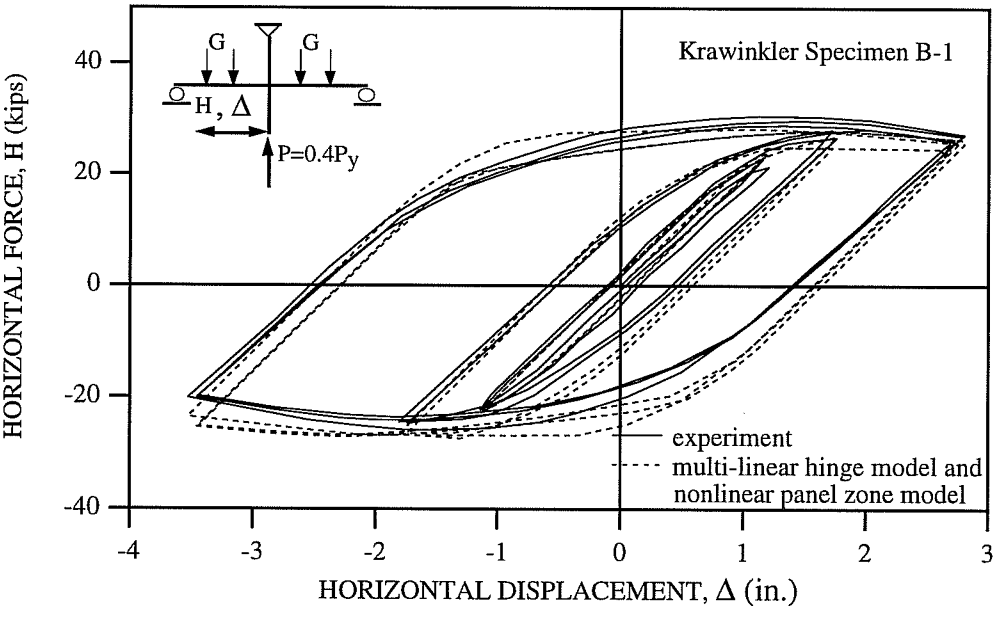

Fig. 7.3a: Comparison of Experimental and Analytical Results Obtained by Multi-linear Hinge Model and Nonlinear Panel Zone Model for Krawinkler Specimen B-1 (Krawinkler 1971).

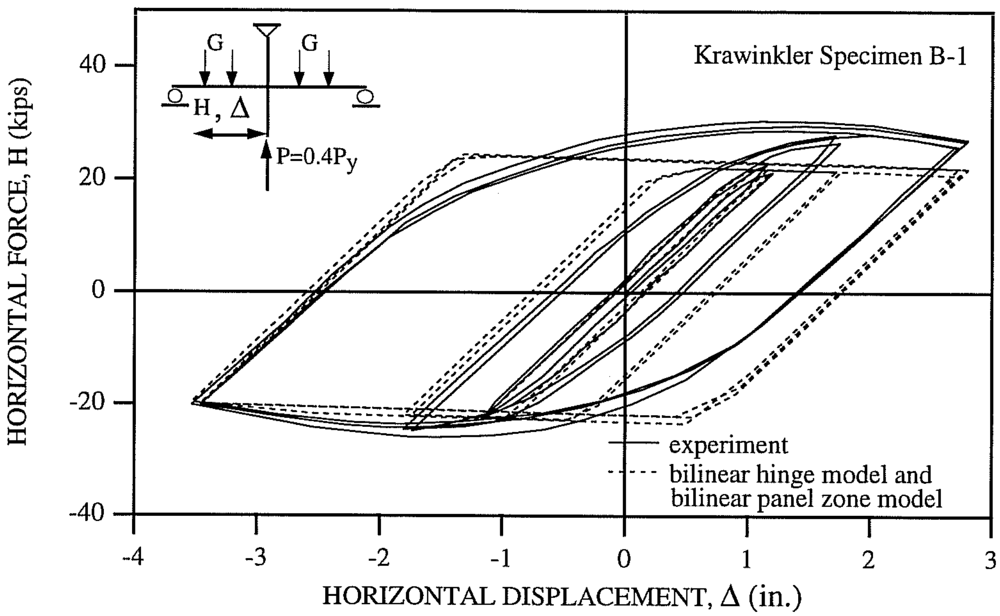

Fig. 7.3b: Comparison of Experimental and Analytical Results Obtained by Bilinear Hinge Model and Bilinear Panel Zone Model for Krawinkler Specimen B-1 (Krawinkler 1971).

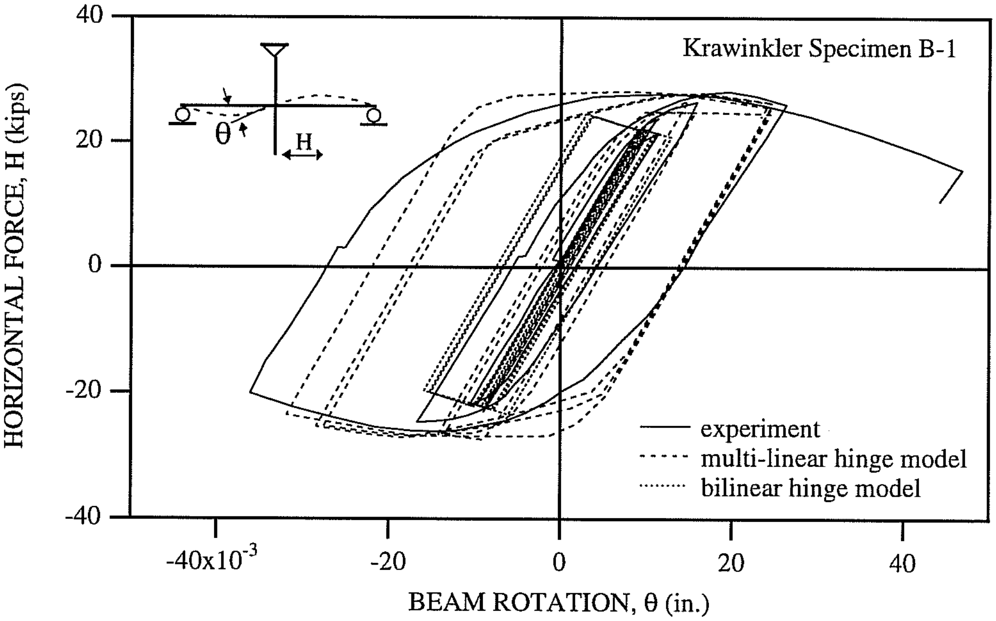

Fig. 7.3c: Comparison of Experimental and Analytical Horizontal Force-Beam Rotation Relations of Krawinkler Specimen B-1 (Krawinkler 1971).

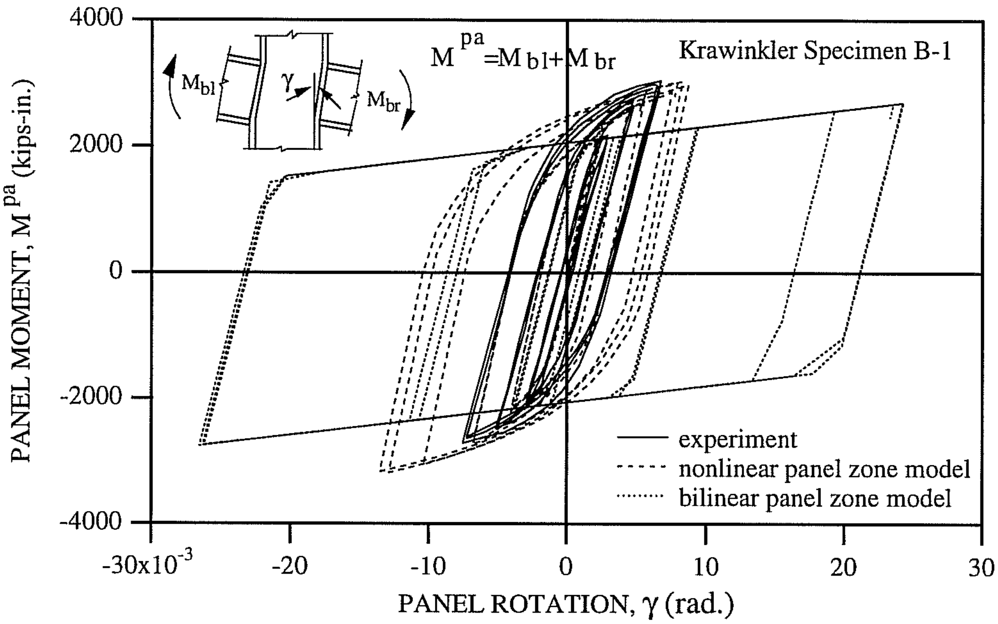

Fig. 7.3d: Comparison of Experimental and Analytical Panel Moment-Rotation Relations of Krawinkler Specimen B-1 (Krawinkler 1971).

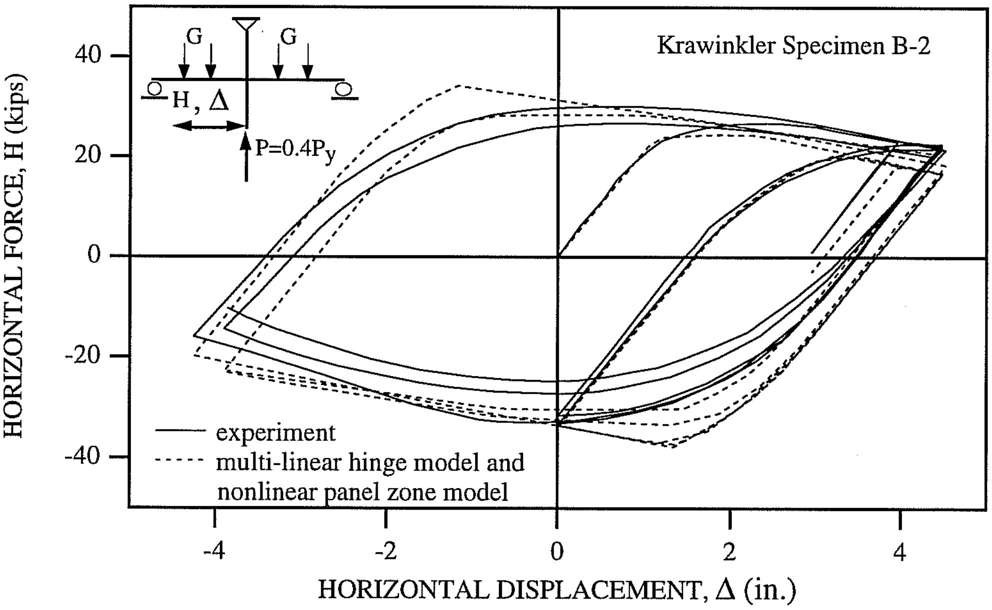

Fig. 7.4a: Comparison of Experimental and Analytical Results Obtained by Multi-linear Hinge Model and Nonlinear Panel Zone Model for Krawinkler Specimen B-2 (Krawinkler 1971).

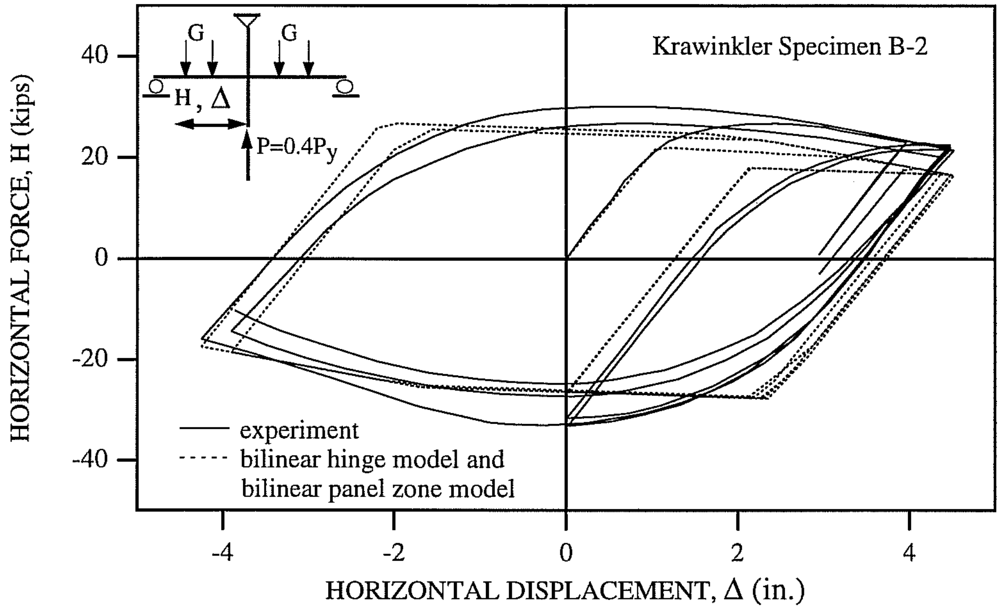

Fig. 7.4b: Comparison of Experimental and Analytical Results Obtained by Bilinear Hinge Model and Bilinear Panel Zone Model for Krawinkler Specimen B-2 (Krawinkler 1971).

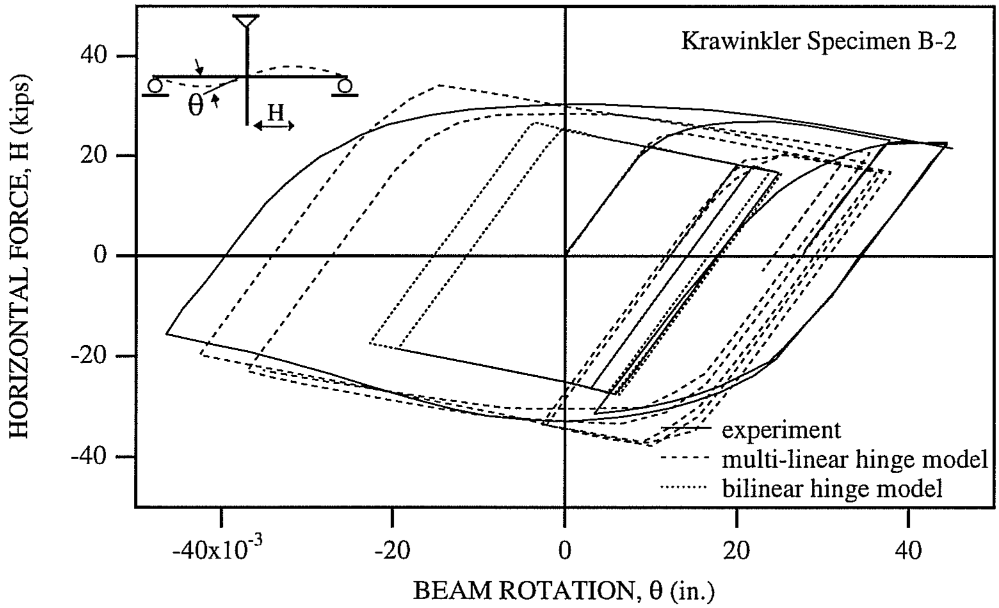

Fig. 7.4c: Comparison of Experimental and Analytical Horizontal Force-Beam Rotation Relations of Krawinkler Specimen B-2 (Krawinkler 1971).

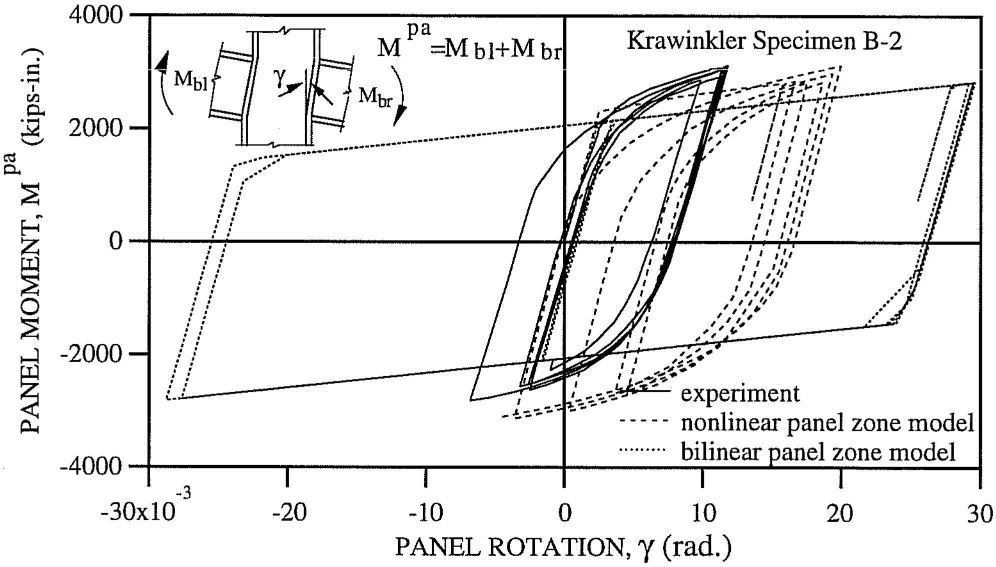

Fig. 7.4d: Comparison of Experimental and Analytical Panel Moment-Rotation Relations of Krawinkler Specimen B-2 (Krawinkler 1971).

Figures 7.5a through 7.9b show comparisons of the analytical and experimental results for the Popov specimens (Popov 1985). To account for strain incompatibility between the column web and the doubler plate, a doubler plate area of 40 %, as used for the study of panel zone behavior in the chapter 5, is used for the analyses of Popov Specimens 2, 3 and 4. For the analysis of Specimen 8, a doubler plate area of 10 % is used. Since the yield stress of the doubler plate is much different from that of the column web, two panel elements are employed in parallel to obtain the analytical results of Specimen 8. From both the tests and the analyses, it has been found that for these specimens the yielding is largely confined to the panel zones and is very limited in the beams.

As far as the overall response predicted by Analysis 1 for the Popov Specimens is concerned (see figures with the subscript "a"), the agreement between the experimental and analytical results is reasonable. The strength for the overall response obtained by Analysis 2 (see Figs. 7.5b and 7.6b) is underestimated by about 50 %. The strength for the local response obtained by Analysis 2 (see Figs. 7.5c and 7.6c) is also underestimated significantly. Since the yielding in these specimens is confined to the panel zones, the difference between local deformations predicted by Analysis 1 and Analysis 2 is not significant. The panel rotations predicted by Analysis 1 are also compared with the experimental data in Figs. 7.7b, 7.8b and 7.9b. The correlation of the local deformations predicted by the tests and the analyses is acceptable.

In Figs. 7.10a to 7.10c, the analytical and experimental results of Engelhardt Specimen 2B (Engelhardt 1994) are presented. This subassemblage involves a 36" deep beam member and a very heavy column member. These members are significantly larger than used in other cyclic loading experiments. From the test and the analysis, it has been found that the yielding is mainly concentrated in the beam. The overall responses obtained by Analysis 1 are compared with the experimental data in Fig.7.10a. The analytical results match well with the experimental data. However, the strength for the overall response predicted by Analysis 2 is underestimated by about 20 % (see Fig. 7.10b). In Fig. 7.10c, the beam moment-relative beam rotation relations are presented. Since the yielding is confined to the beam, the difference between the beam rotations predicted by Analysis 1 and Analysis 2 is not significant.

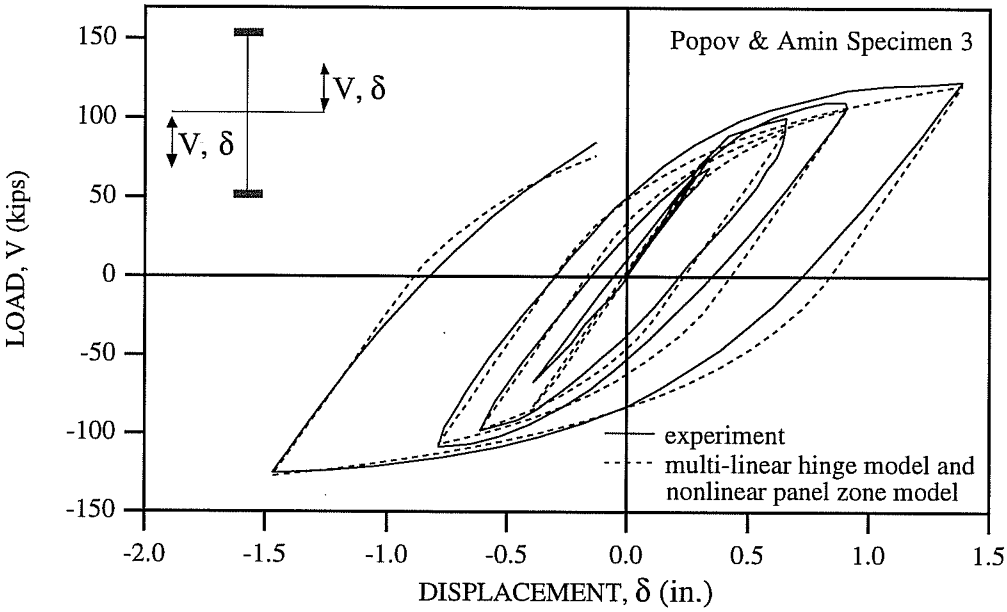

Fig. 7.5a: Comparison of Experimental and Analytical Results Obtained by Multi-linear Hinge Model and Nonlinear Panel Zone Model for Popov Specimen 3 (Popov 1985).

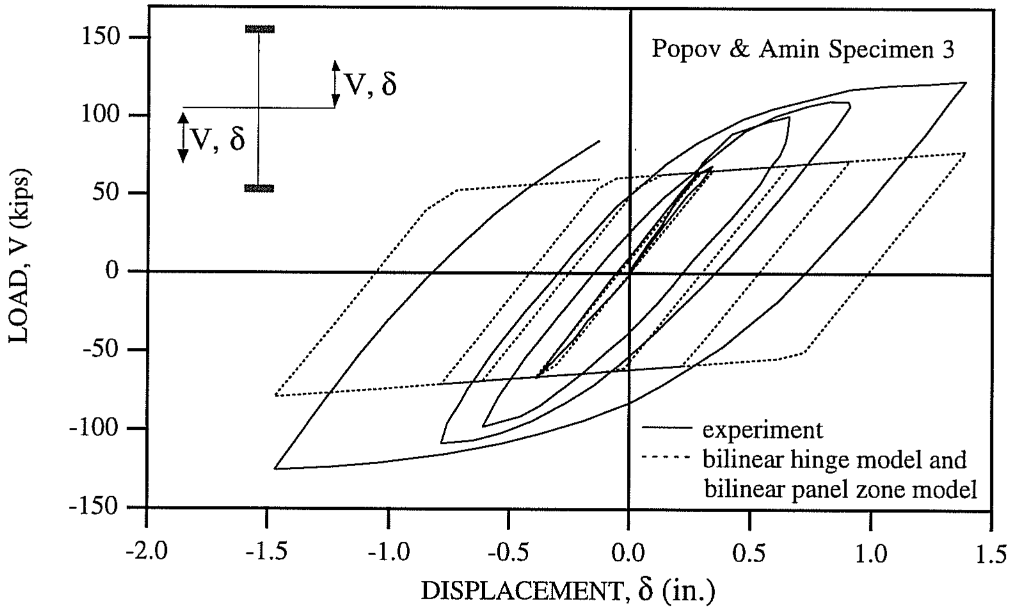

Fig. 7.5b: Comparison of Experimental and Analytical Results Obtained by Bilinear Hinge Model and Bilinear Panel Zone Model for Popov Specimen 3 (Popov 1985).

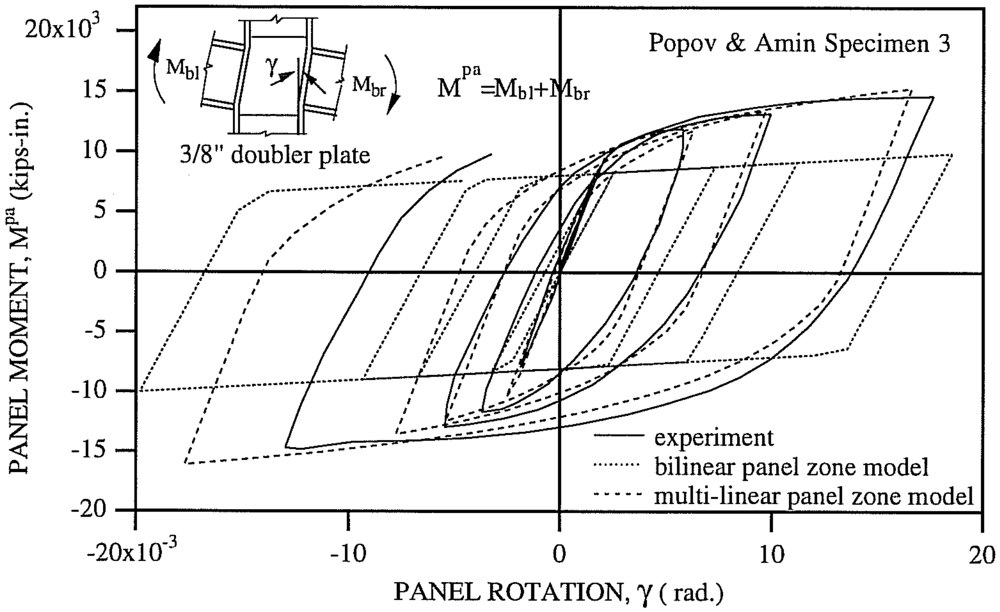

Fig. 7.5c: Comparison of Experimental and Analytical Panel Moment-Rotation Relations of Popov Specimen 3 (Popov 1985).

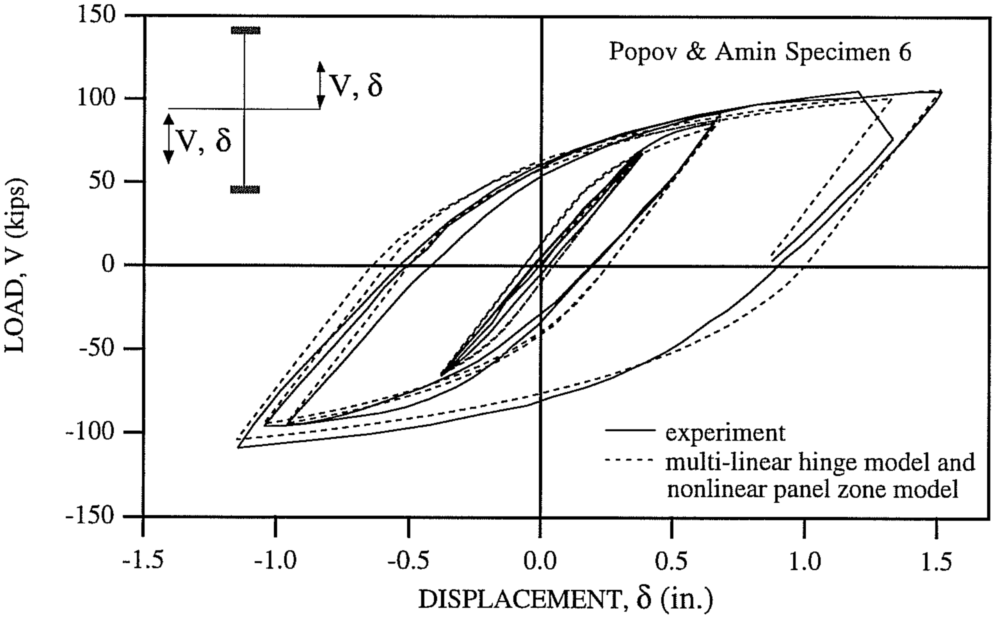

Fig. 7.6a: Comparison of Experimental and Analytical Results Obtained by Multi-linear Hinge Model and Nonlinear Panel Zone Model for Popov Specimen 6 (Popov 1985).

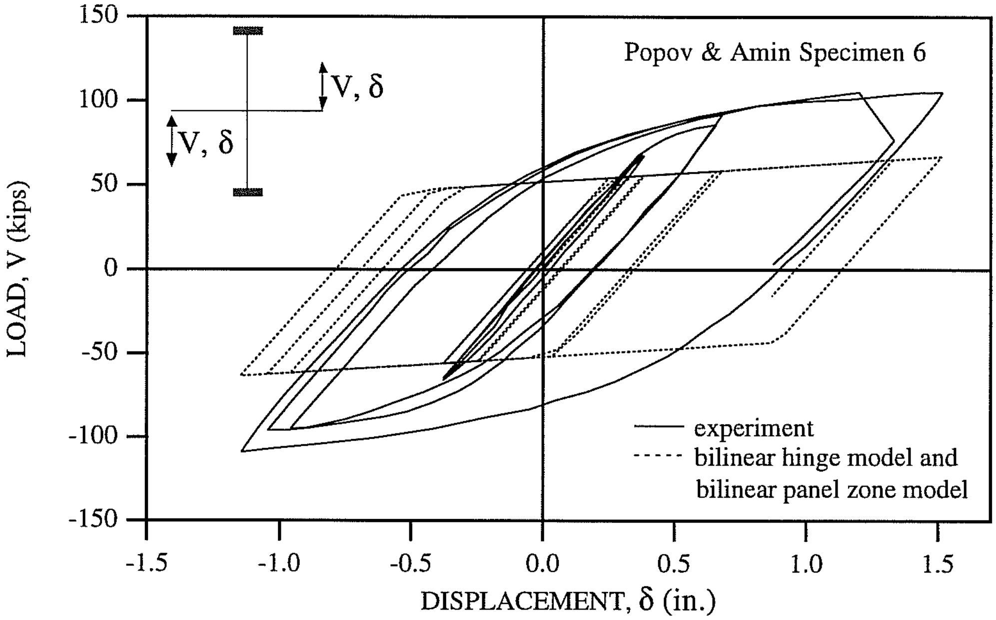

Fig. 7.6b: Comparison of Experimental and Analytical Results Obtained by Bilinear Hinge Model and Bilinear Panel Zone Model for Popov Specimen 6 (Popov 1985).

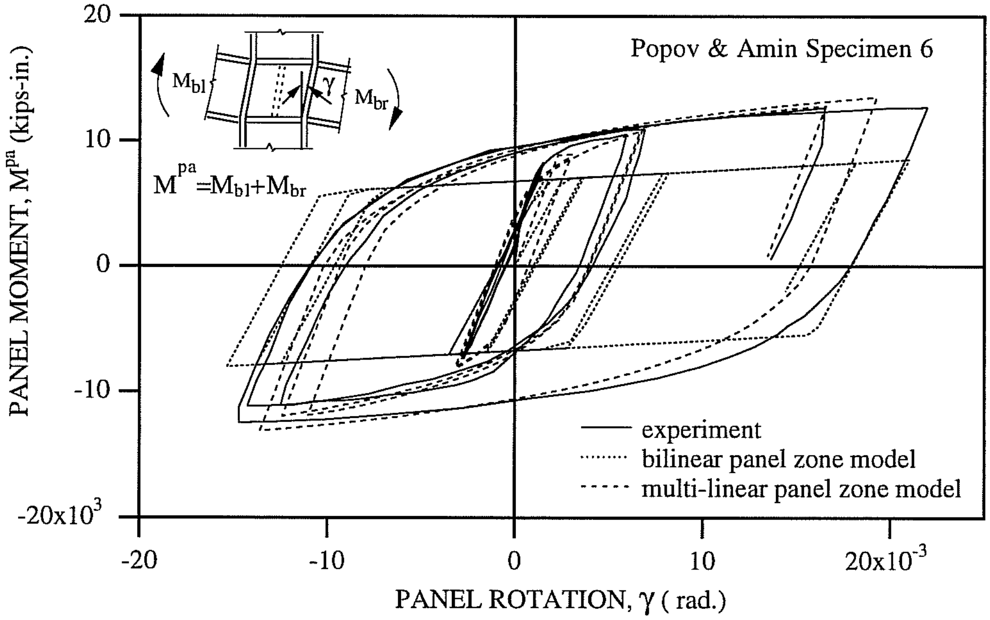

Fig. 7.6c: Comparison of Experimental and Analytical Panel Moment-Rotation Relations of Popov Specimen 6 (Popov 1985).

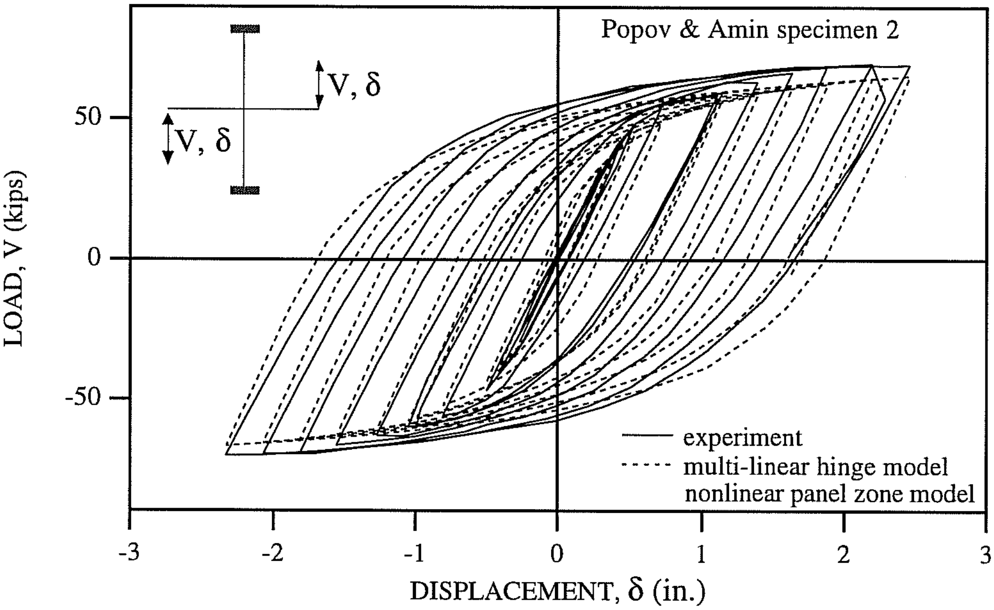

Fig. 7.7a: Comparison of Experimental and Analytical Results Obtained by Multi-linear Hinge Model and Nonlinear Panel Zone Model for Popov Specimen 2 (Popov 1985).

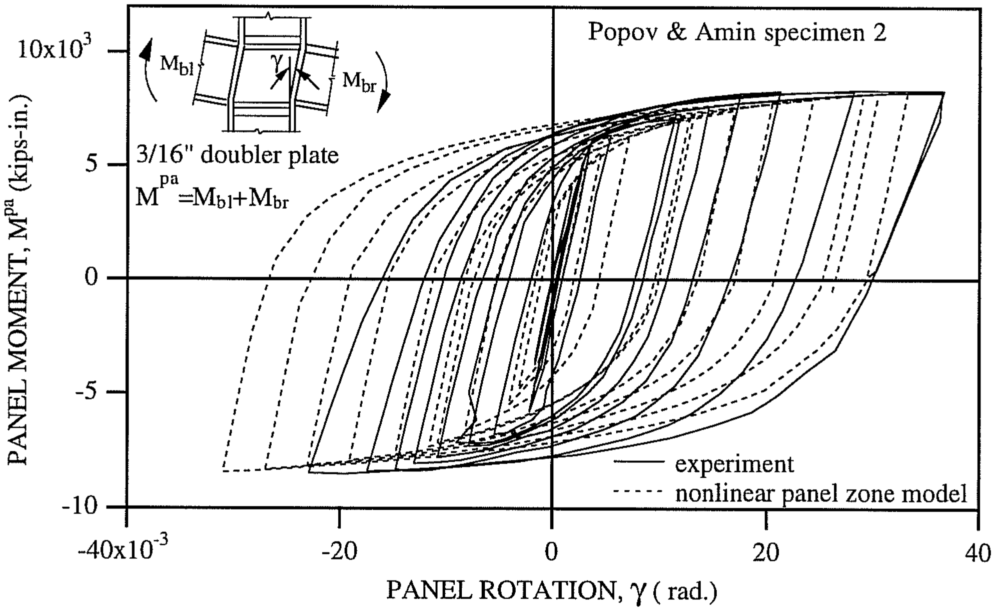

Fig. 7.7b: Comparison of Experimental and Analytical Panel Moment-Rotation Relations of Popov Specimen 2 (Popov 1985).

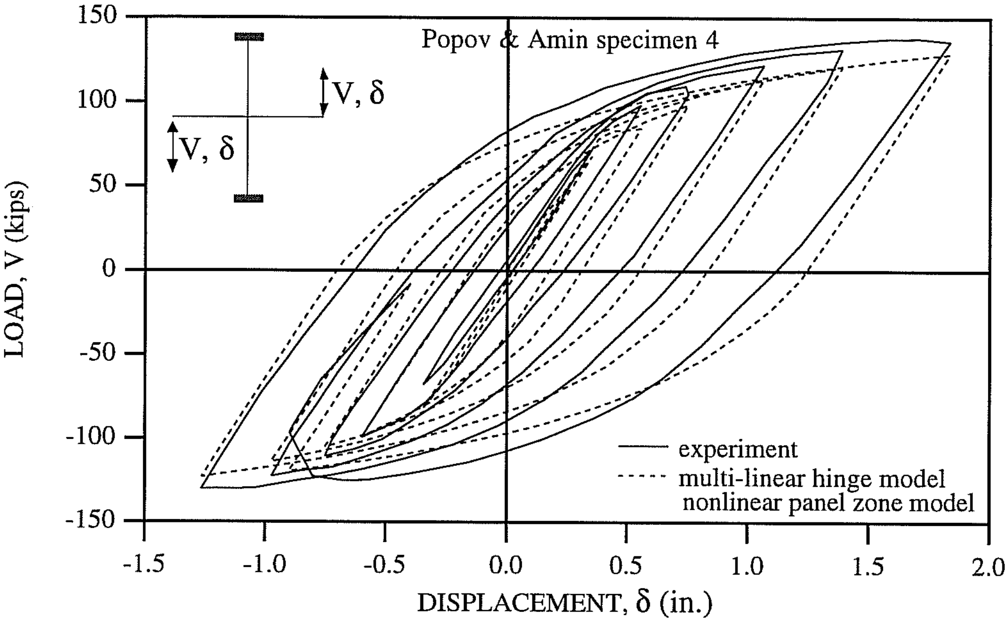

Fig. 7.8a: Comparison of Experimental and Analytical Results Obtained by Multi-linear Hinge Model and Nonlinear Panel Zone Model for Popov Specimen 4 (Popov 1985).

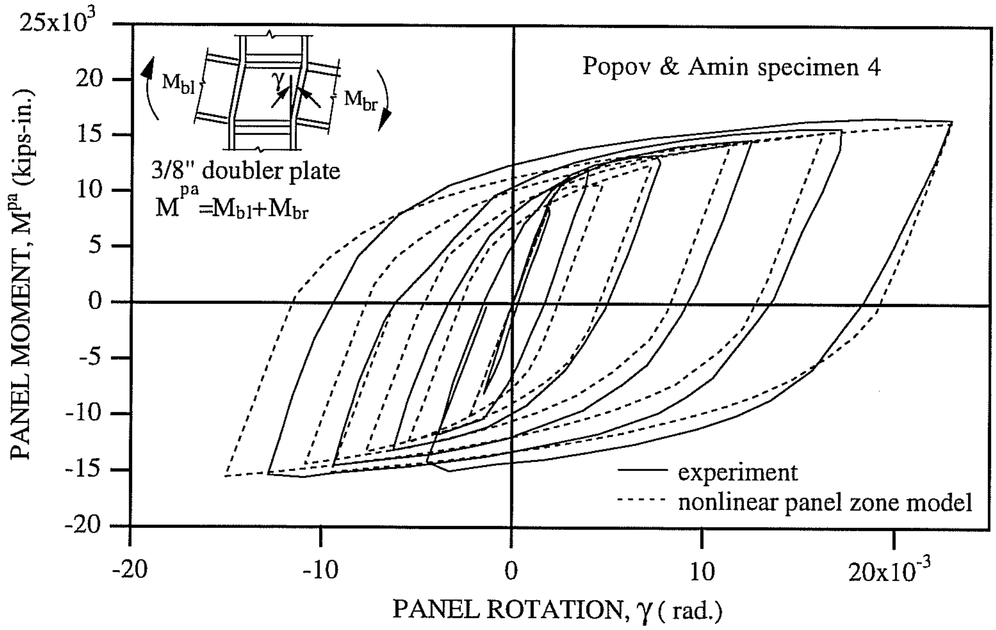

Fig. 7.8b: Comparison of Experimental and Analytical Panel Moment-Rotation Relations of Popov Specimen 4 (Popov 1985).

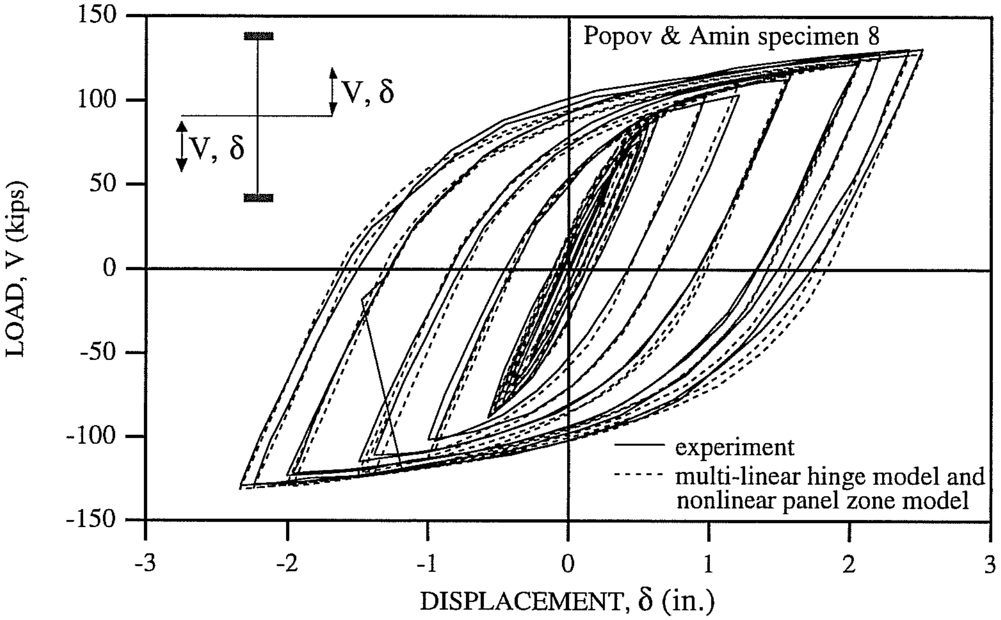

Fig. 7.9a: Comparison of Experimental and Analytical Results Obtained by Multi-linear Hinge Model and Nonlinear Panel Zone Model for Popov Specimen 8 (Popov 1985).

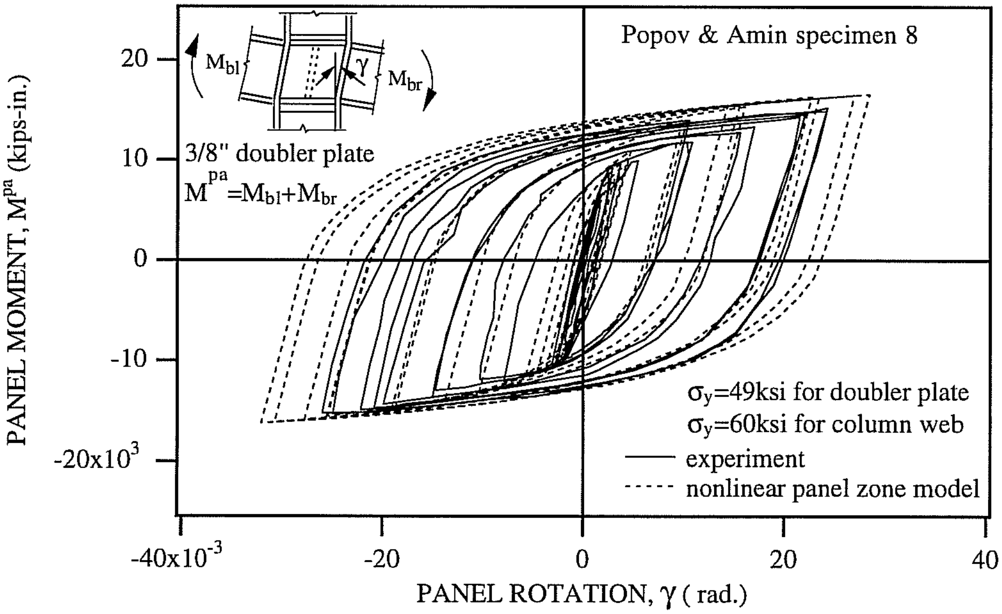

Fig. 7.9b: Comparison of Experimental and Analytical Panel Moment-Rotation Relations of Popov Specimen 8 (Popov 1985).

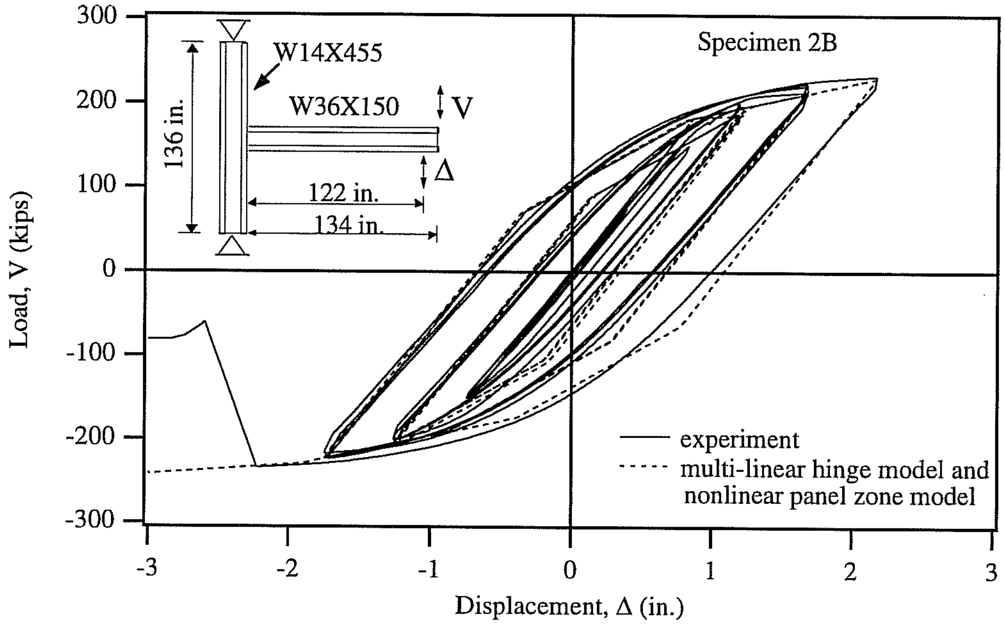

Fig. 7.10a: Comparison of Experimental and Analytical Results Obtained by Multi-linear Hinge Model and Nonlinear Panel Zone Model for Engelhardt Specimen 2B (Engelhardt 1994).

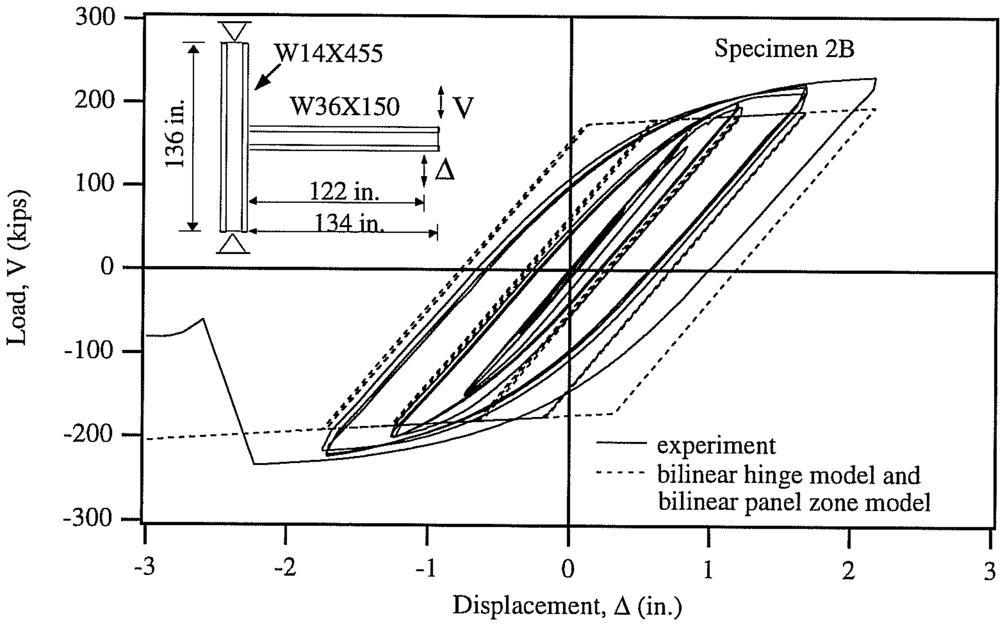

Fig. 7.10b: Comparison of Experimental and Analytical Results Obtained by Bilinear Hinge Model and Bilinear Panel Zone Model for Engelhardt Specimen 2B (Engelhardt 1994).

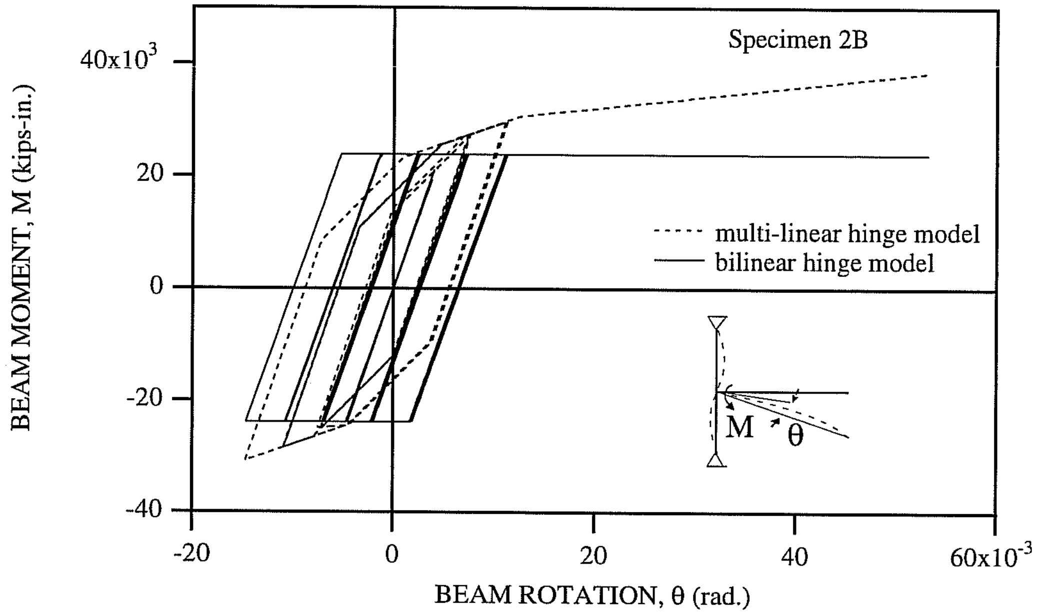

Fig. 7.10c: Comparison of Analytical Beam Moment-Rotation Relations of Engelhardt Specimen 2B (Engelhardt 1994).

Figures 7.11a to 7.11f show comparisons of experimental and analytical results for Popov Specimen C-2 (Popov 1975). This specimen is subjected to a large axial force of $0.6P_y$, in which P_y is the section yield force of the column. Since the yield stress of the doubler plate was not reported, it was adjusted for the analysis of the specimen such that the analytical panel response matches well with the experimental data. In Fig. 7.11a, the analytical panel response obtained by the nonlinear panel zone element is compared with the experimental data. For the analysis, the value of 42 ksi is used as the yield stress of the doubler plate and two panel elements are employed in parallel due to the difference between the yield stresses of the column web and the doubler plate.

For Popov Specimen C-2, two doubler plates are attached to both sides of the column panel zone. The entire area of two doubler plates is used for the analysis. From the comparison of the experimental and analytical elastic stiffnesses (Fig. 7.11a), it can be seen that the doubler plates participate well in resisting the panel shear, as compared to the case discussed in chapter 5, where a doubler plate is attached to only one side of the panel zone.

The overall response predicted by the multi-linear hinge element and the nonlinear panel zone element (Analysis 1) is plotted against the experimental data in Fig. 7.11b. The analytical results match well with the experimental data. However, the strength for the overall response predicted by the bilinear hinge element and the bilinear panel zone element (Analysis 2) is underestimated by about 30 % (see Fig. 7.11c). The beam moment-rotation relations and the column moment-rotation relations predicted by Analysis 1 and Analysis 2 are presented in Figs. 7.11d and 7.11e, respectively. In Fig. 7.11f, the analytical panel responses are compared with the experimental data. The maximum local deformations predicted by Analysis 2 are much smaller than those obtained by Analysis 1. The maximum positive and negative panel rotations predicted by Analysis 1 are more reasonable than those by Analysis 2 when compared to the experimental data. From the comparison of the column responses predicted by Analysis 1 and Analysis 2, it can be seen that the bilinear hinge element overestimates the reduction of the moment capacity due to the axial force.

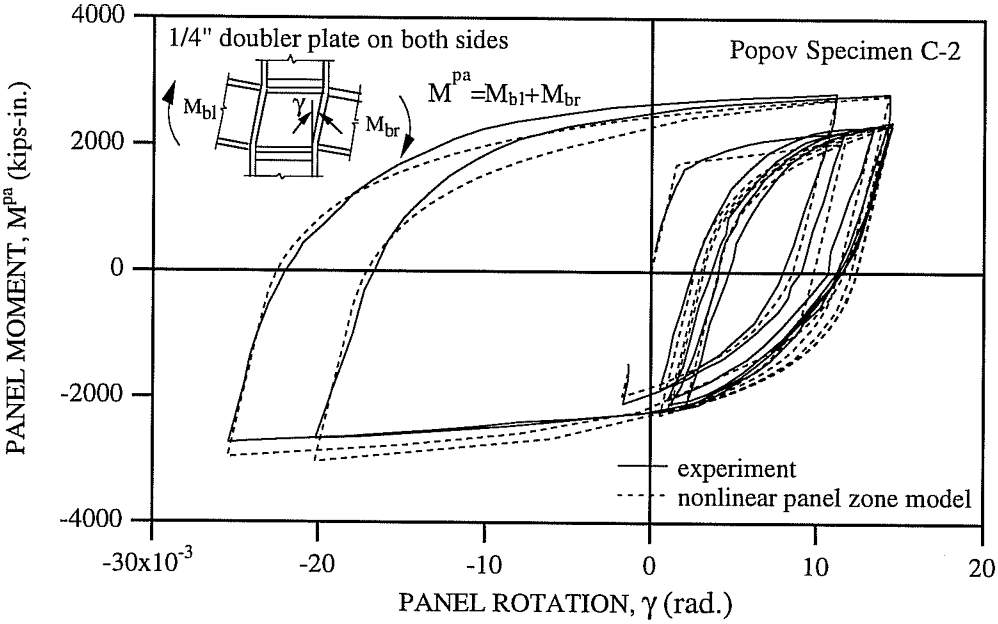

Fig. 7.11a: Comparison of Experimental Results and Analytical Panel Moment-Rotation Relations Obtained by Nonlinear Panel Zone Model for Popov Specimen C-2 (Popov 1975).

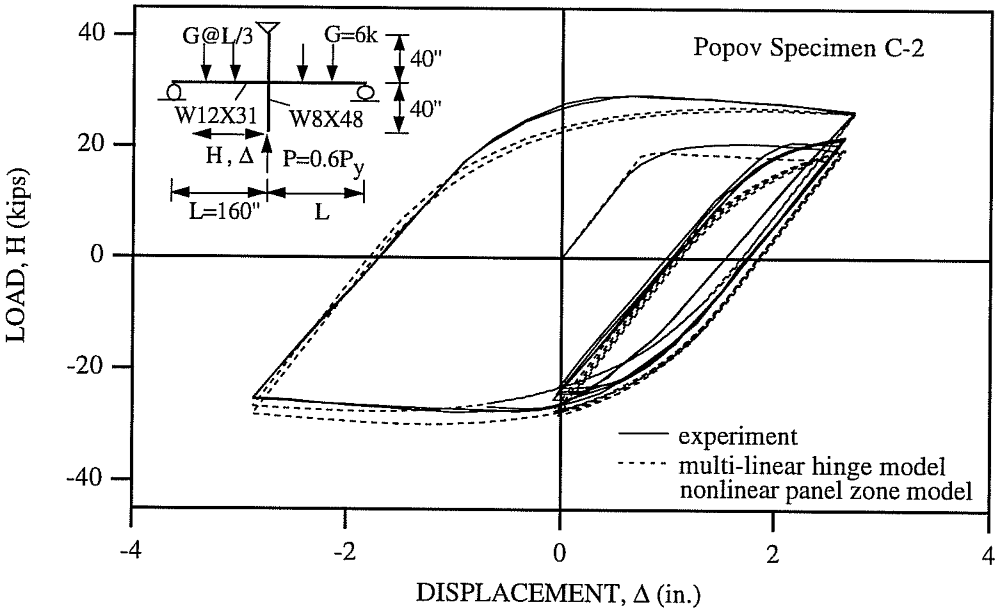

Fig. 7.11b: Comparison of Experimental and Analytical Results Obtained by Multi-linear Hinge Model and Nonlinear Panel Zone Model for Popov Specimen C-2 (Popov 1975).

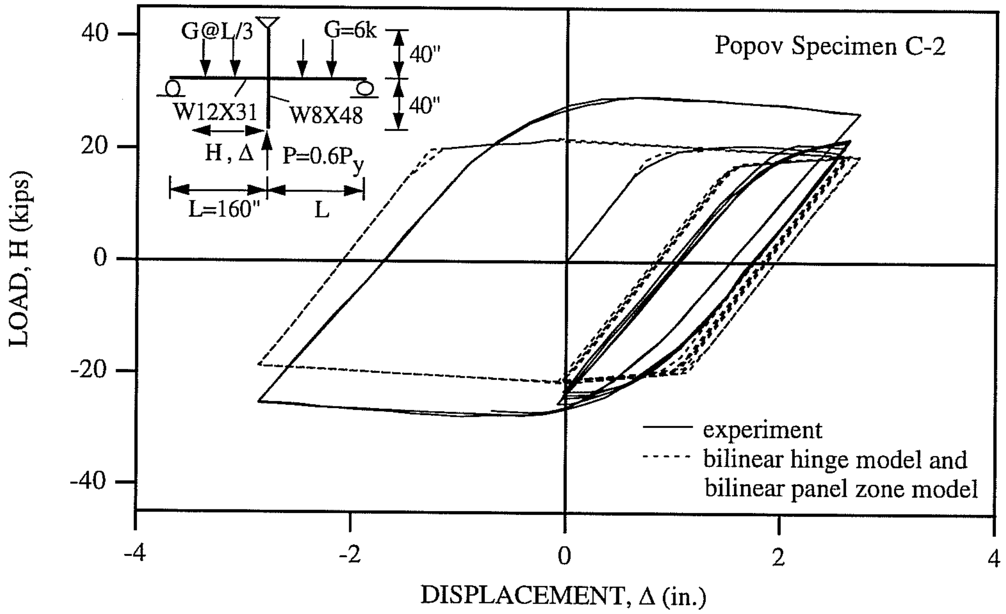

Fig. 7.11c: Comparison of Experimental and Analytical Results Obtained by Bilinear Hinge Model and Bilinear Panel Zone Model for Popov Specimen C-2 (Popov 1975).

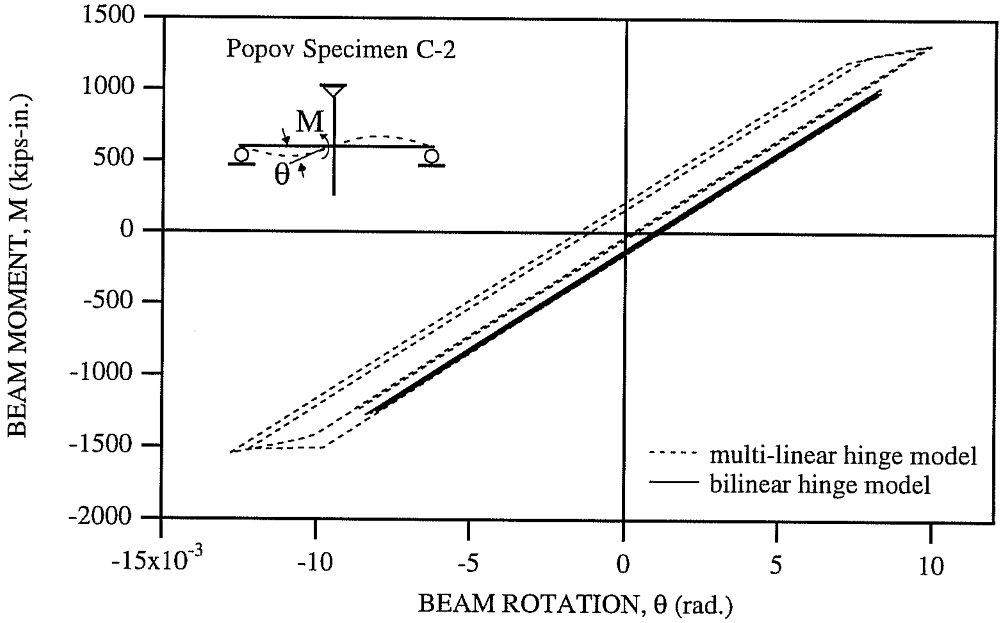

Fig. 7.11d: Comparison of Analytical Beam Moment-Rotation Relations of Popov Specimen C-2 (Popov 1975).

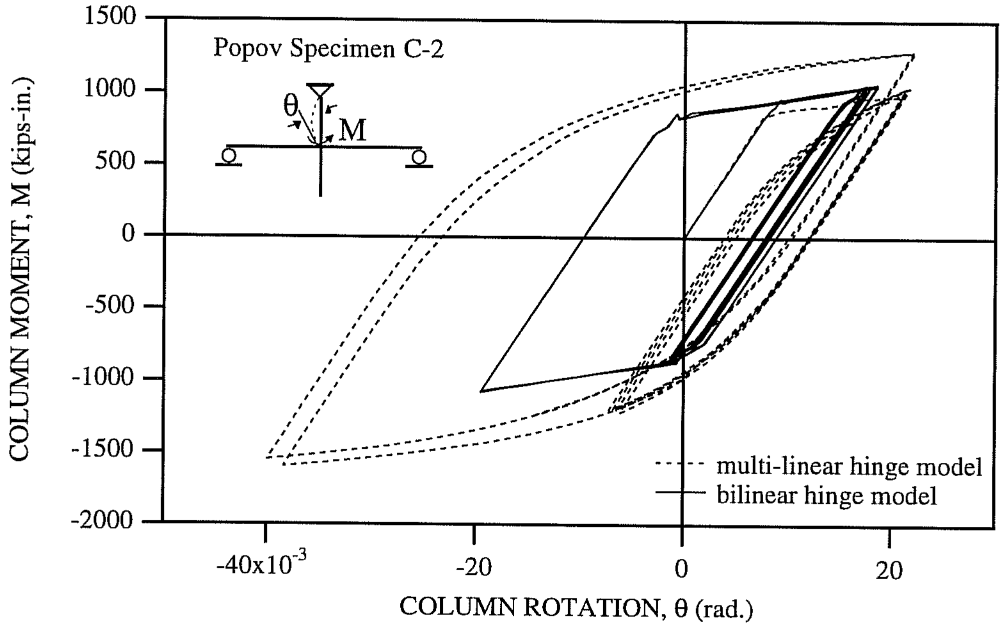

Fig. 7.11e: Comparison of Analytical Column Moment-Rotation Relations of Popov Specimen C-2 (Popov 1975).

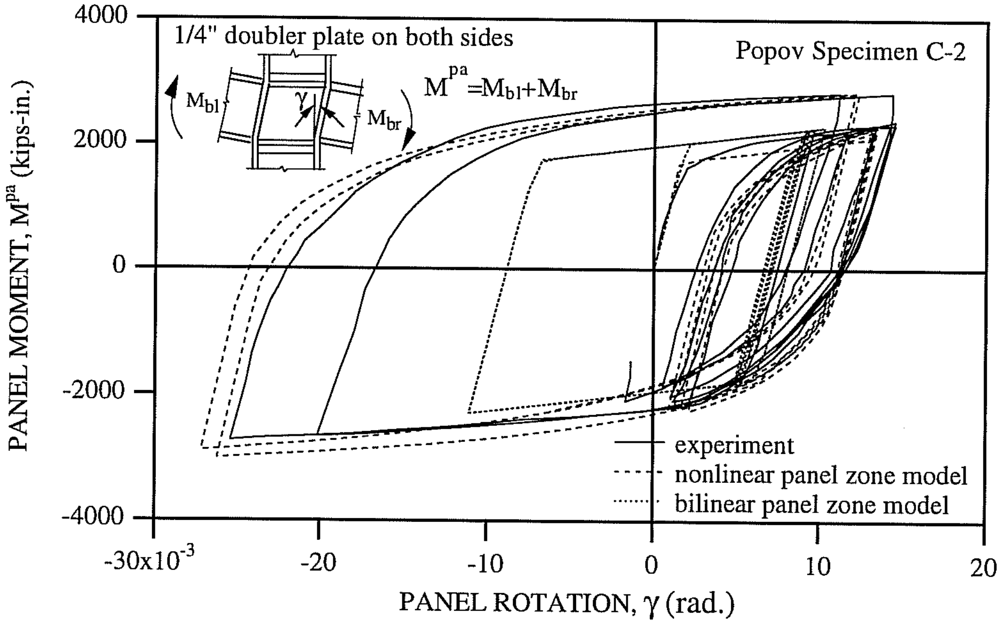

Fig. 7.11f: Comparison of Analytical Panel Moment-Rotation Relations of Popov Specimen C-2 (Popov 1975).

In Figs. 7.12a through 7.13d, analytical results predicted by the multi-linear hinge element for Wakabayashi Specimens FC5 and FC0 (Wakabayashi 1974) are compared with the experimental data and the predictions by the bilinear hinge element. Although the connection types of these specimens are not reported, the parameters required to define the moment-rotation relations for fully welded connections are used because the ratio of the plastic modulus of the flanges to the plastic modulus of the entire beam section (Z_f/Z=0.77) is greater than 0.75. Since the details of the column panel zones are not reported, it is assumed that the panel zones remain elastic during the analysis as assumed in Wakabayashi's analyses of the test frames.

Figure 7.12a shows the comparison of the overall response obtained by the test and Analysis 1 for Specimen FC5 subjected to the relatively large axial forces of 0.516P_y. The overall response predicted by Analysis 1 matches well with the experimental data except for the second to the last cycle. The stiffness of the experimental response in the negative displacement region of the second to the last cycle is about 10 % larger than the stiffnesses of the other cycles. The reason for this larger stiffness is unclear. While the strength at the maximum displacement predicted by Analysis 2 is underestimated by about 34 % (see Fig. 7.12b), the corresponding strength obtained by Analysis 1 is underestimated by about 8 %. In Figs. 7.12c and 7.12d, the analytical local responses are presented. From these figures, it can be seen that the yielding is largely confined to the columns. The bilinear hinge element overestimates the reduction of the moment capacity due to the axial force. The difference between the moments at the column base predicted by the multi-linear hinge element and the bilinear hinge element is about 34 percent.

Figure 7.13a shows the comparison of the overall response obtained by the test and Analysis 1 for Specimen FC0 subjected to no axial force. The overall response predicted by Analysis 1 matches well with the experimental data. While the strength at the maximum displacement predicted by Analysis 2 is underestimated by about 18 % (see Fig. 7.13b), the corresponding strength obtained by Analysis 1 is underestimated by about 7 %. In Fig. 7.13c, the analytical beam moment-rotation relations are shown. The beam response predicted by the bilinear hinge element remains elastic, but that obtained by the multi-linear hinge element shows inelastic behavior at the last cycle. From Fig. 7.13d, it can be seen that the difference between the moments at the column base predicted by the multi-linear hinge element and the bilinear hinge element is about 24 percent.

From comparison of the overall response obtained by the bilinear hinge element for the test frames with and without axial forces, it can be seen that the bilinear hinge element shows less accurate performance for the test frame subjected to the relatively large axial forces. However, the multi-linear hinge element exhibits consistent performance regardless of whether or not the structure is subjected to large axial forces.

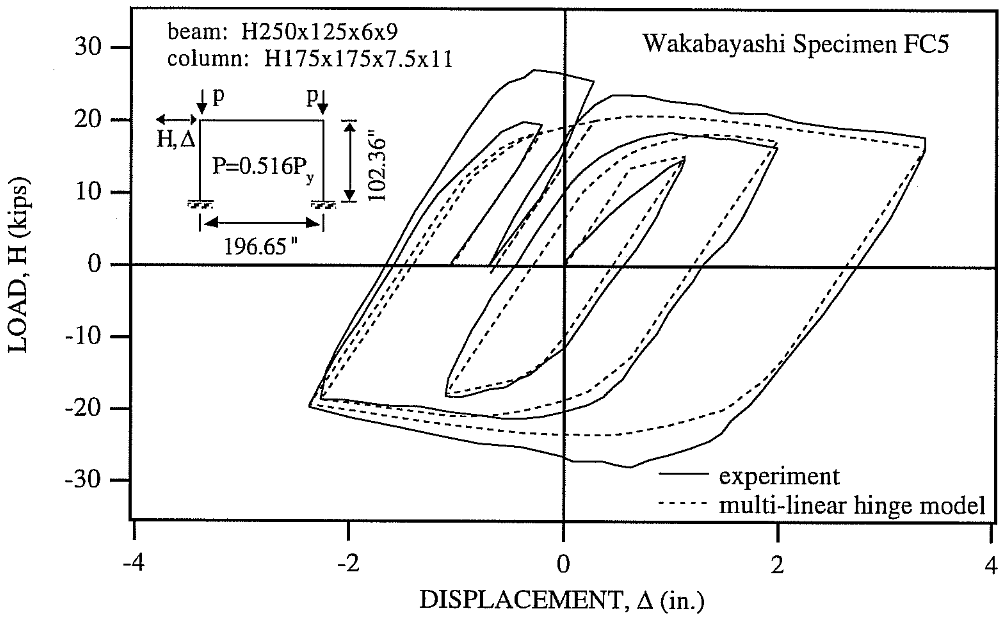

Fig. 7.12a: Comparison of Experimental Results and Analytical Prediction Made by Multi-linear Hinge Model for Wakabayashi Specimen FC5 (Wakabayashi 1974).

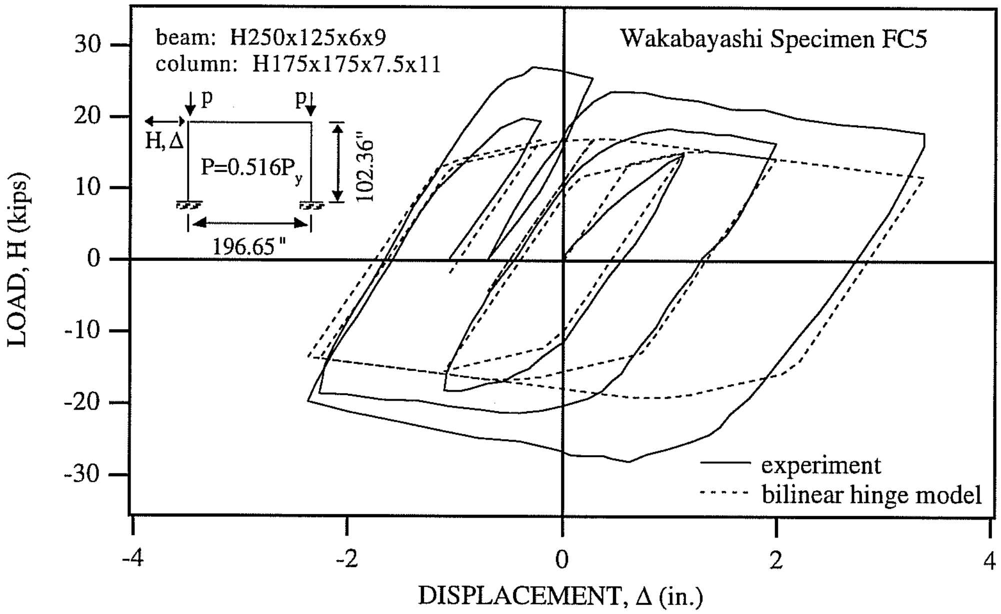

Fig. 7.12b: Comparison of Experimental Results and Analytical Prediction Made by Bilinear Hinge Model for Wakabayashi Specimen FC5 (Wakabayashi 1974).

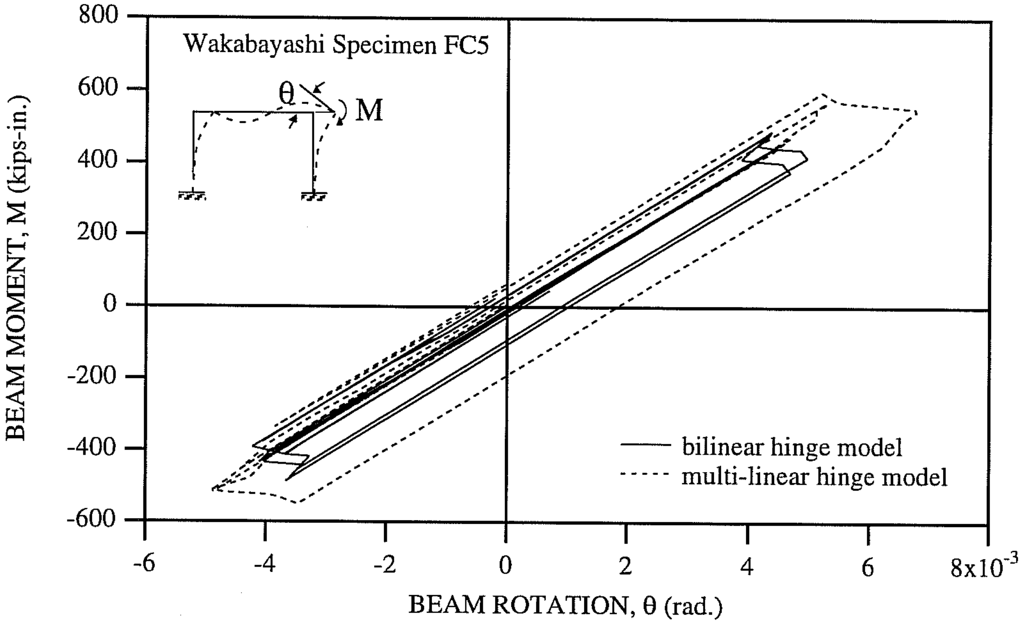

Fig. 7.12c: Comparison of Analytical Beam Moment-Rotation Relations of Wakabayashi Specimen FC5 (Wakabayashi 1974).

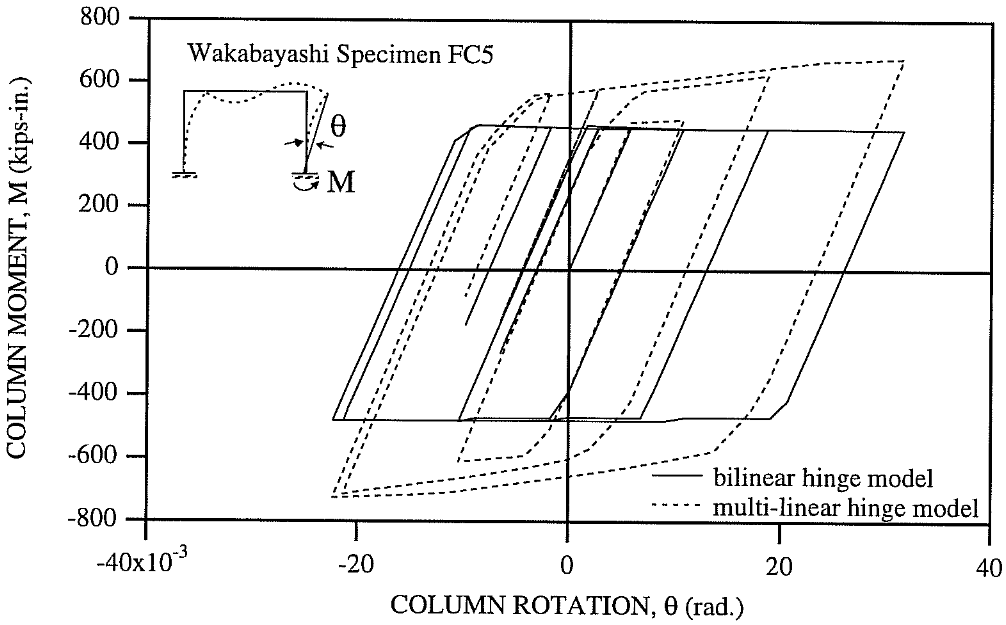

Fig. 7.12d: Comparison of Analytical Column Moment-Rotation Relations of Wakabayashi Specimen FC5 (Wakabayashi 1974).

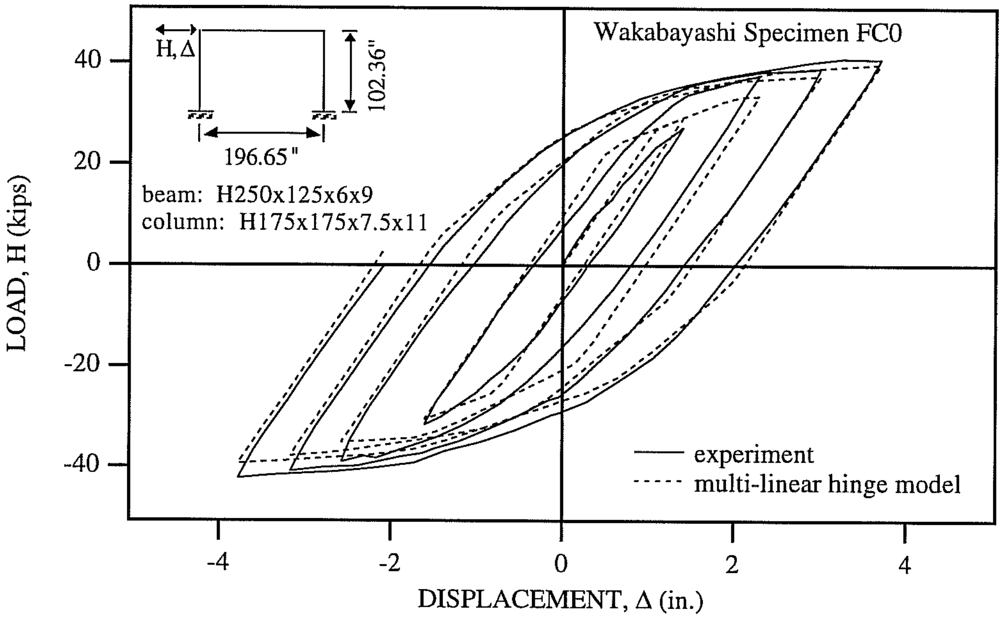

Fig. 7.13a: Comparison of Experimental Results and Analytical Prediction Made by Multi-linear Hinge Model for Wakabayashi Specimen FC0 (Wakabayashi 1974).

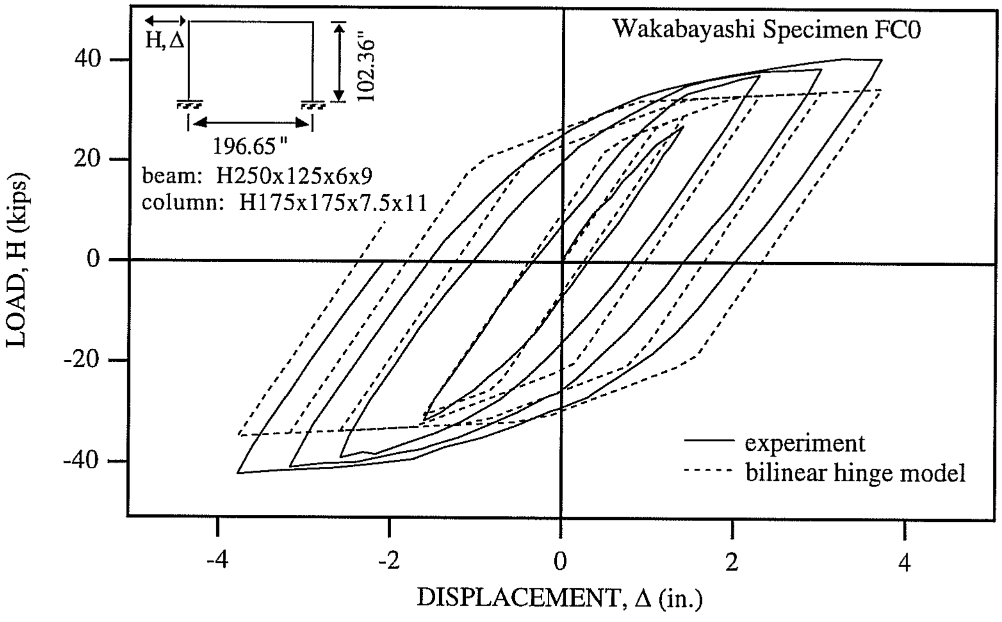

Fig. 7.13b: Comparison of Experimental Results and Analytical Prediction Made by Bilinear Hinge Model for Wakabayashi Specimen FC0 (Wakabayashi 1974).

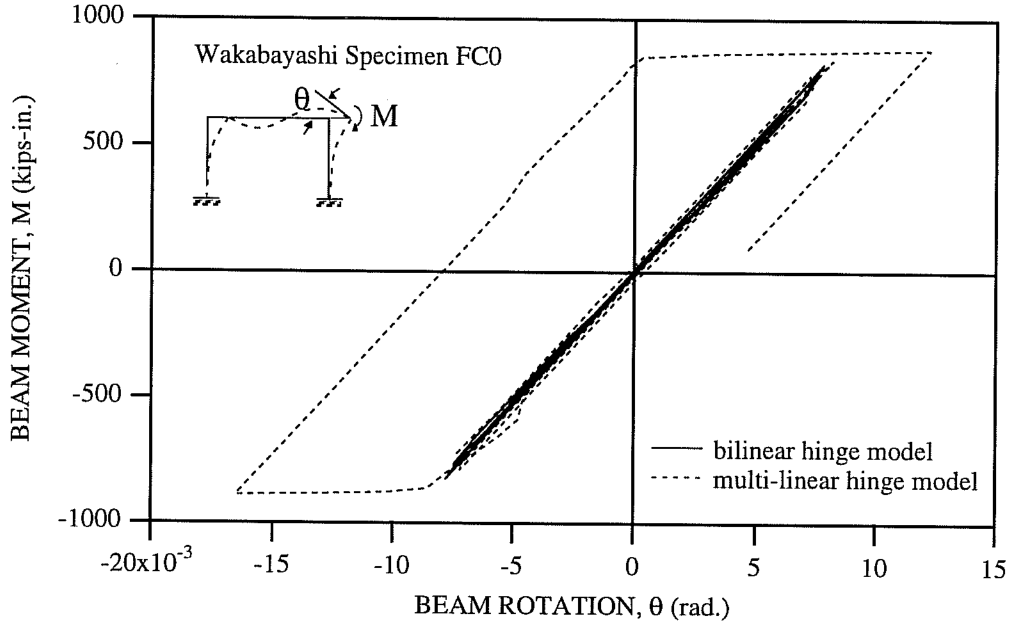

Fig. 7.13c: Comparison of Analytical Beam Moment-Rotation Relations of Wakabayashi Specimen FCO (Wakabayashi 1974).

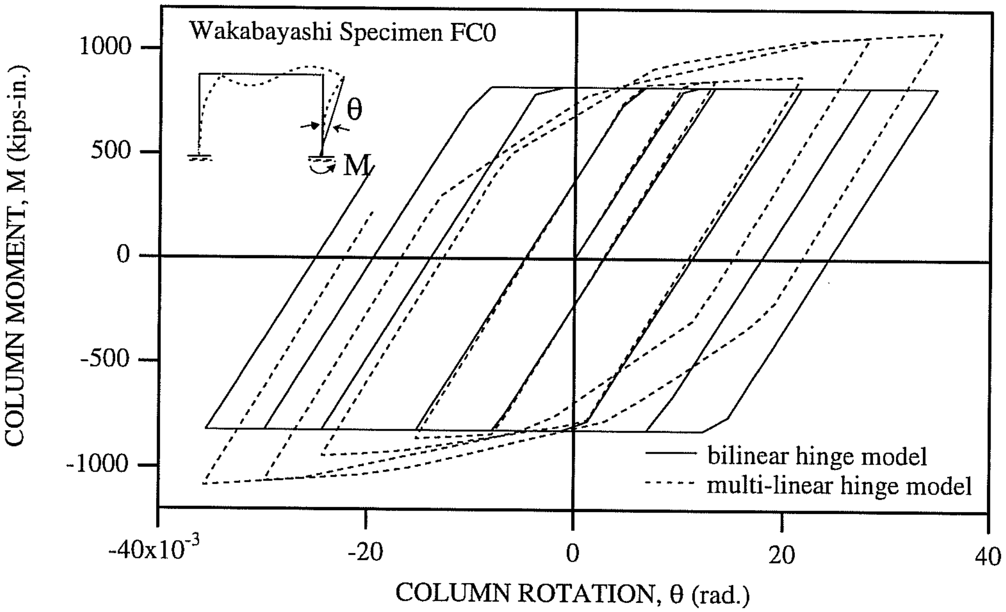

Fig. 7.13d: Comparison of Analytical Column Moment-Rotation Relations of Wakabayashi Specimen FCO (Wakabayashi 1974).

Figures 7.14a to 7.15c show comparisons of the experimental and analytical results for Carpenter Specimens Frame A and Frame B (Carpenter 1973). For these specimens, two doubler plates are attached to both sides of the column panel zone. The entire area of the two doubler plates is used for the analyses. Two panel elements are employed in parallel to account for the doubler plates. Since the yield stress of the doubler plates was not reported and the experimental panel response was not available, the effect of the yield stress of the doubler plates on the overall responses of the specimens was first investigated. In Figs. 7.14a, 7.14b, 7.15a, and 7.15b, the overall analytical response obtained by "Analysis A" and "Analysis B" are compared with the experimental data. Both Analysis A and Analysis B employ the multi-linear hinge elements and the nonlinear panel zone elements. While the doubler plates remain elastic in Analysis A, the yield stress of the doubler plates is the same as that of the column webs in Analysis B. From these figures, it can be seen that the yield stress of the doubler plates has little influence on the overall response of the test frames. Yielding of the doubler plates of the column panel zones appears to have little influence on the overall lateral stiffness of the frames.

Investigating the overall response obtained by assuming the yield stress of the column webs equal to that of the doubler plates, the performance of the multi-linear hinge elements and the nonlinear panel zone elements (Analysis B) is compared with that of the bilinear hinge elements and the bilinear panel zone elements (Analysis C). In Figs. 7.14c and 7.15c, the overall response predicted by Analysis C is compared with the experimental data. From the comparisons of Figs. 7.14b and 7.14c, and of Figs. 7.15b and 7.15c, it can be seen that the combination of the multi-linear hinge elements and the nonlinear panel zone elements produces more consistent response predictions than that of the bilinear hinge elements and the bilinear panel zone elements.

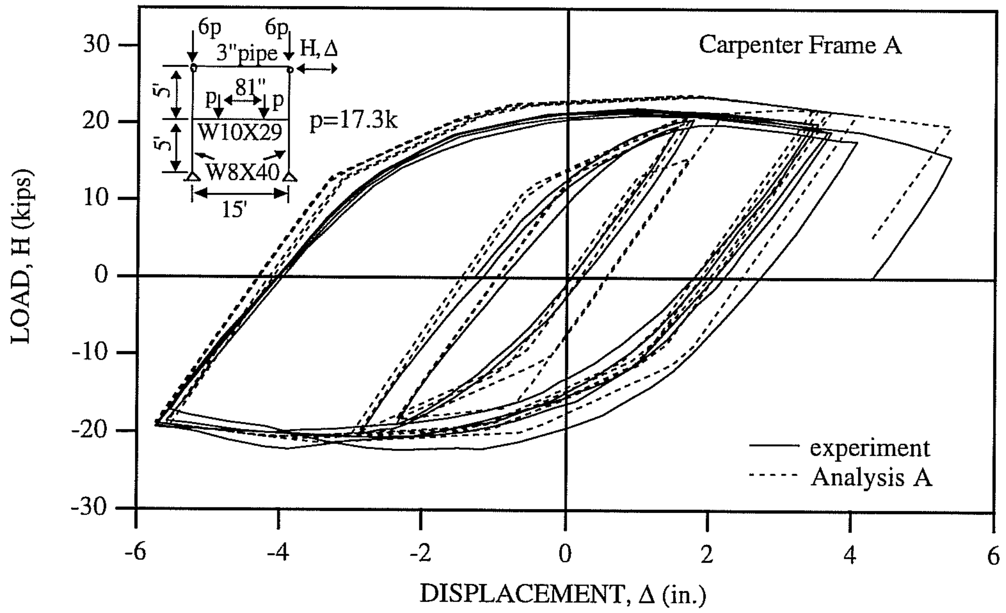

Fig. 7.14a: Comparison of Experimental Data and Analytical Results Obtained by Multi-linear Hinge Model and Nonlinear Panel Zone Model for Carpenter Specimen Frame A (Carpenter 1973).

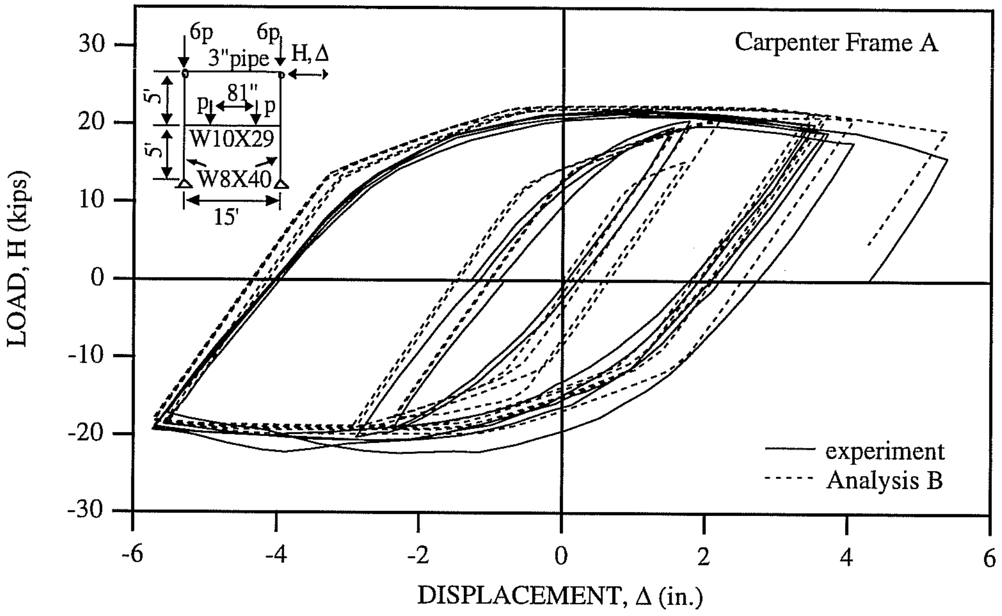

Fig. 7.14b: Comparison of Experimental Data and Analytical Results Obtained by Multi-linear Hinge Model and Nonlinear Panel Zone Model for Carpenter Specimen Frame A (Carpenter 1973).

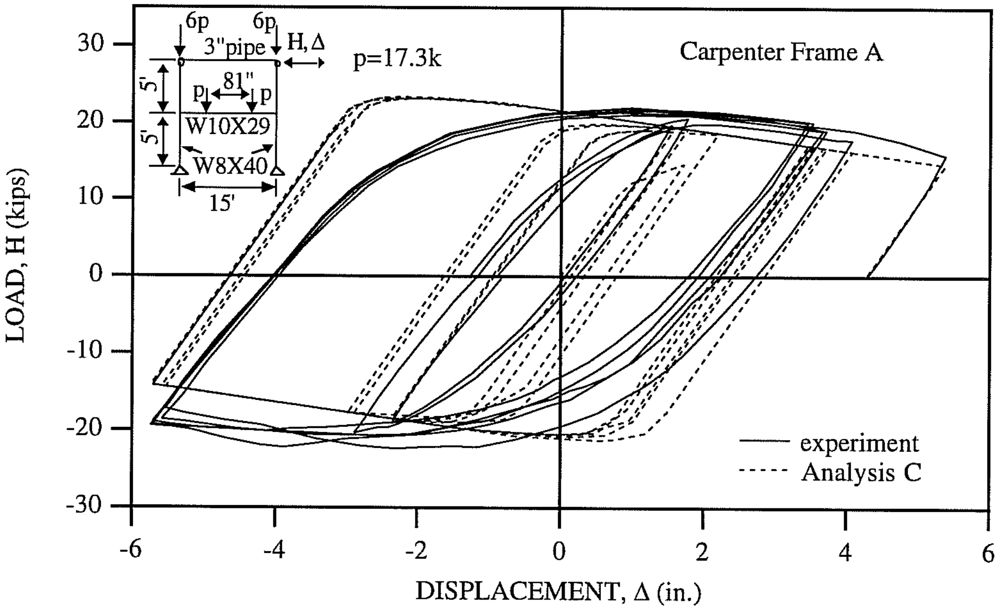

Fig. 7.14c: Comparison of Experimental Data and Analytical Results Obtained by Bilinear Hinge Model and Bilinear Panel Zone Model for Carpenter Specimen Frame A (Carpenter 1973).

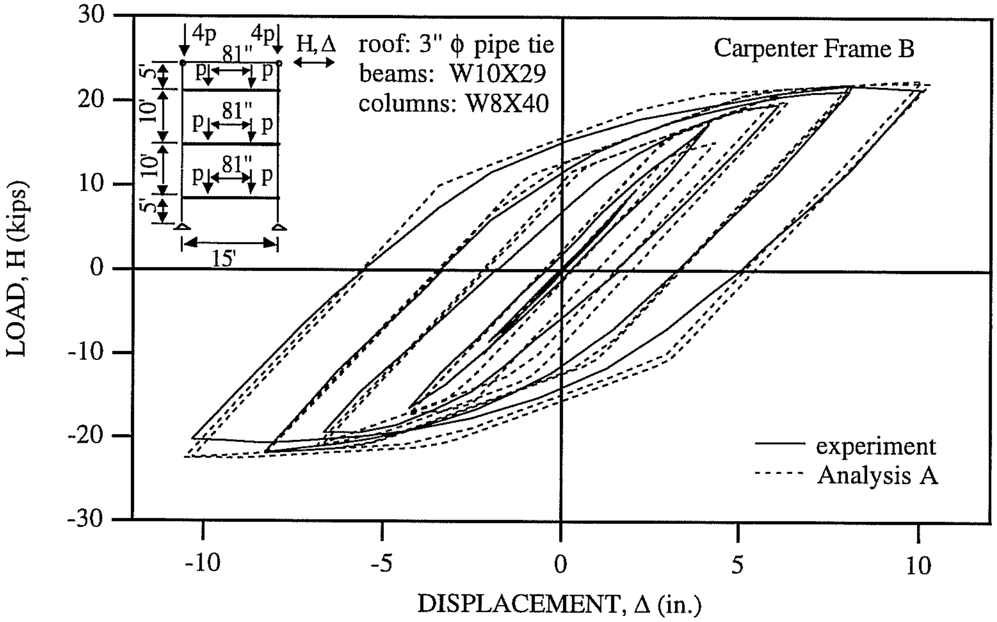

Fig. 7.15a: Comparison of Experimental Data and Analytical Results Obtained by Multilinear Hinge Model and Nonlinear Panel Zone Model for Carpenter Specimen Frame B (Carpenter 1973).

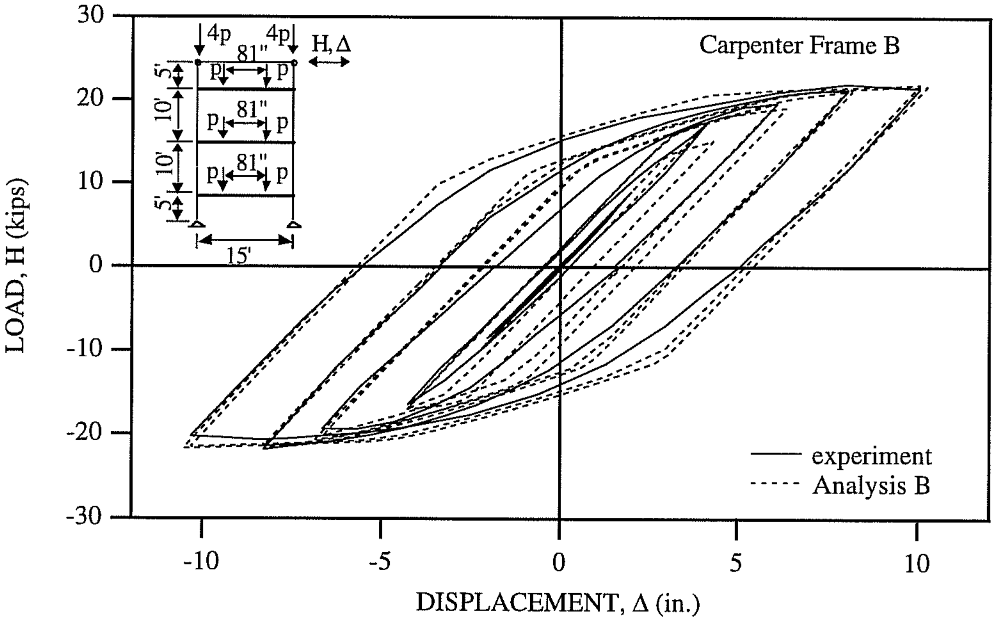

Fig. 7.15b: Comparison of Experimental Data and Analytical Results Obtained by Multilinear Hinge Model and Nonlinear Panel Zone Model for Carpenter Specimen Frame B (Carpenter 1973).

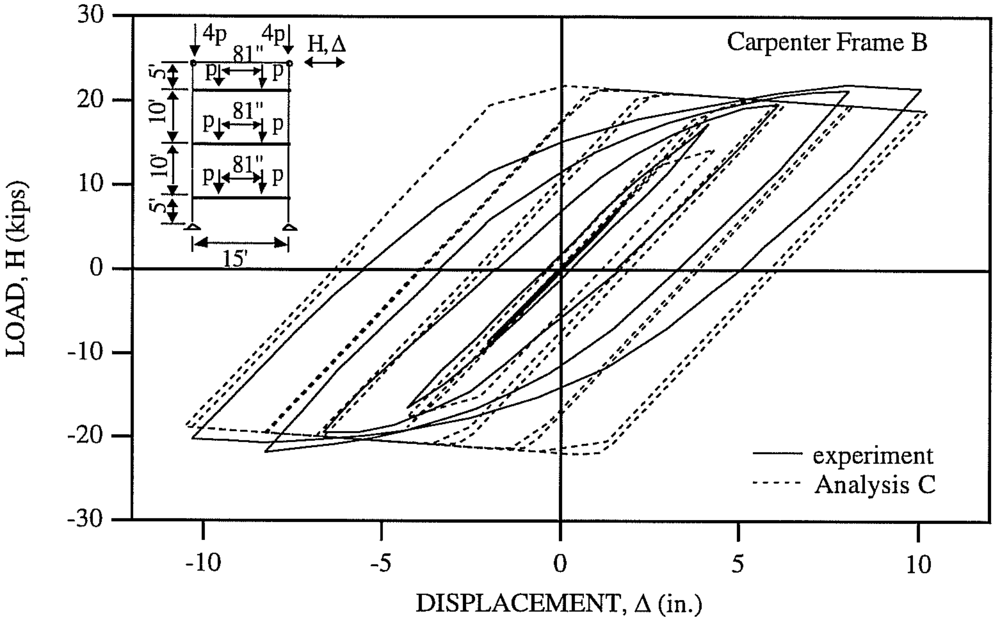

Fig. 7.15c: Comparison of Experimental Data and Analytical Results Obtained by Bilinear Hinge Model and Bilinear Panel Zone Model for Carpenter Specimen Frame B (Carpenter 1973).

7.3 Subassemblages and Frames with Concrete Slab

In this section, steel subassemblages and frames with concrete slabs are analyzed by the composite beam element developed in the previous chapter, combined with the multi-linear hinge element and the nonlinear panel zone element. Material properties of the available test specimens (Lee 1987; Wenk 1977) are presented in Table 7.2. The cross-section of composite beams of Lee Specimens EJ-FC and IJ-FC is the same as that of Lee Specimen EJ-WC shown in Fig. 6.7a.

Test Specimen	Steel Yield Stress (ksi)				Reinforcing Steel Strength (ksi)	Concrete Strength (ksi)
	Beam		Column			
	Web	Flange	Web	Flange		
Lee EJ-FC	37.8	36.65	35.4	34.3	60	5.1
Lee IJ-FC	37.8	36.65	37.96	35.1	60	5.1
Wenk CA-1	43.4	37	n/a	n/a	48.8	2.97

Table 7.2: Material Properties of Test Specimens with Concrete Slab (Lee 1987 and Wenk 1977).

Figures 7.16a and 7.17a show comparisons of panel zone responses of Lee Specimens EJ-FC and IJ-FC obtained by the test and Analysis A. In these figures, Analysis A represents the analysis using the nonlinear panel zone element for the panel zone of bare steel beam-to-column joints. For composite beam-to-column joints, the presence of the composite slab increases the stiffness and strength of the panel zone because it effectively increases the depth of the panel zone. However, the nonlinear panel zone element for bare steel beam-to-column joints does not account for the enlargement of the panel zone due to the presence of composite slabs. From Figs. 7.16a and 7.17a, it can be seen that Analysis A can not properly model the experimentally observed behavior due to the effect of composite slab after crack closure. The nonlinear panel zone element underestimates the panel zone strength by about 20 % for the exterior composite beam-to-column joint (Specimen EJ-FC), and by about 10 % for the interior composite beam-to-column joint (Specimen IJ-FC). In Figs. 7.16b and 7.17b, the overall response predicted by Analysis A is compared with the experimental data. The analysis using the nonlinear panel zone element for bare steel beam-to-column joints (Analysis A) underestimates the overall strength by about 26 % for Specimen EJ-FC, and by about 15 % for Specimen IJ-FC. When these discrepancies between the experimental and analytical strengths are compared to those between the experimental and analytical panel zone strengths, it can be seen that the error in the analysis largely comes from the underestimation of panel zone strength by the nonlinear panel zone element for bare steel beam-to-column joints.

Since there is little experimental data to model the panel zone behavior of composite beam-to-column joints, this study does not attempt to develop a panel zone element for composite beam-to-column joints. However, the parameters to define the hysteretic rules for the panel zone of bare steel beam-to-column joints, which are presented in chapter 5, will be adjusted such that analytical panel zone strengths match well with the experimental panel zone strengths for the limited number of test specimens with composite beams

The adjusted parameters are listed in Table 7.3. For the exterior composite beam-to-column joint (Specimen EJ-FC), two different shape factors $\hat{h}_{neg.}$ and $\hat{h}_{pos.}$ are used to describe the inelastic behavior for the negative and positive panel zone moments, respectively, because of the unsymmetrical behavior of the exterior joint. The cyclic factors F_H, F_S, and F_R are not considered because they are based on the symmetrical panel zone behavior of bare steel beam-to-column joints. For the panel zone of the interior joint, the variable d_b used to define the monotonic panel zone behavior (Eqs. 5.12 to 5.15) is the depth from the mid-height of composite slab to the steel bottom flange regardless of the sign of panel zone moment. However, for the panel zone of the exterior joint, the depth of steel cross-section is used as the value of d_b to describe the panel zone behavior for the negative panel zone moment.

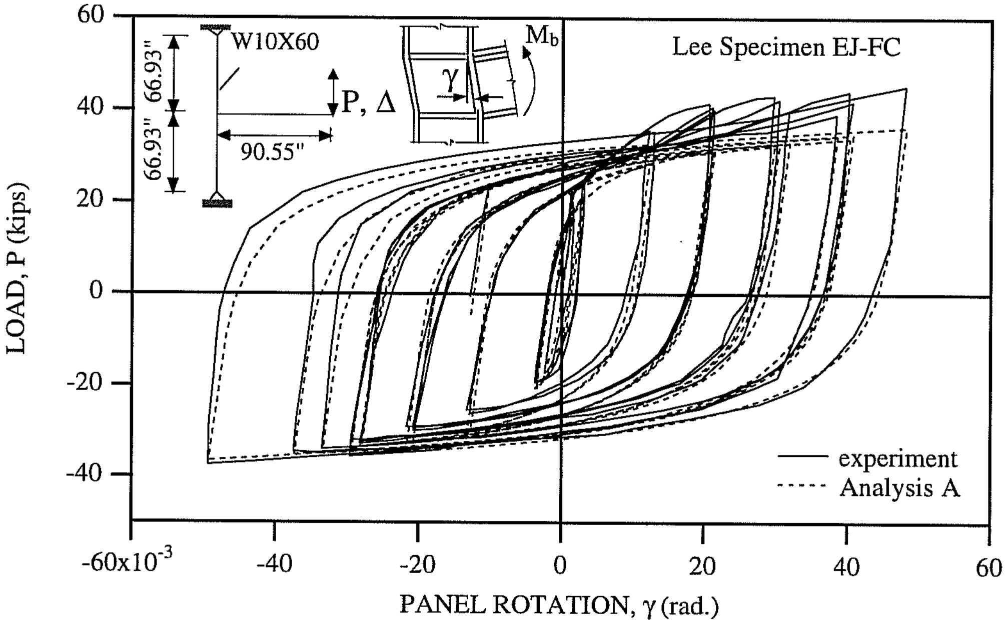

Fig. 7.16a: Comparison of Panel Zone Response Obtained by the Test and the Nonlinear Panel Zone Model Using the Material Parameters of Bare Steel Beam-to-Column Joint for Lee Specimen EJ-FC (Lee 1987).

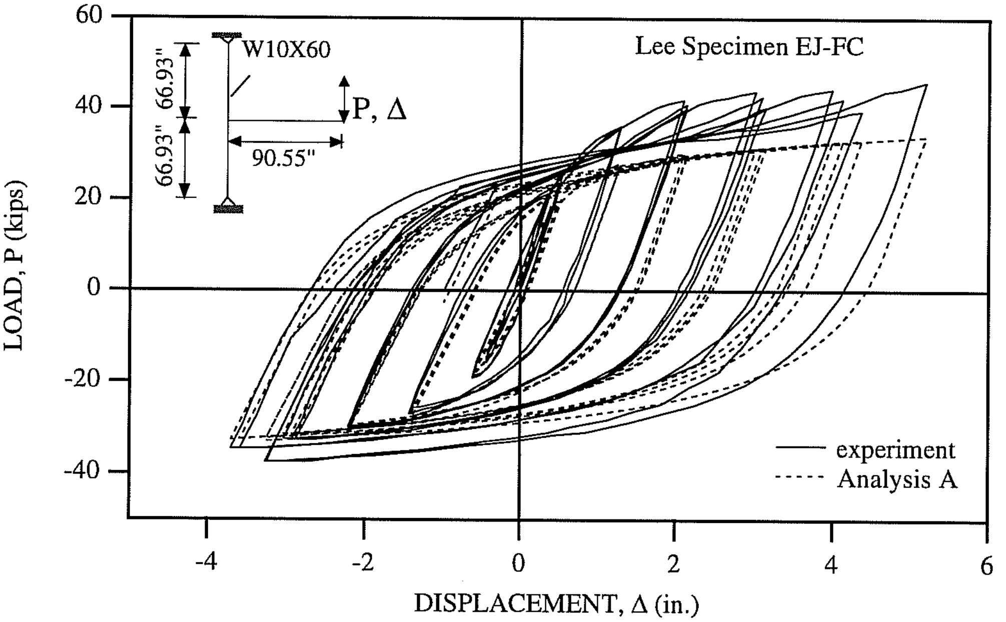

Fig. 7.16b: Comparison of Overall Response Obtained by the Test and the Analysis Using the Material Parameters of Bare Steel Beam-to-Column Joint for Lee Specimen EJ-FC (Lee 1987).

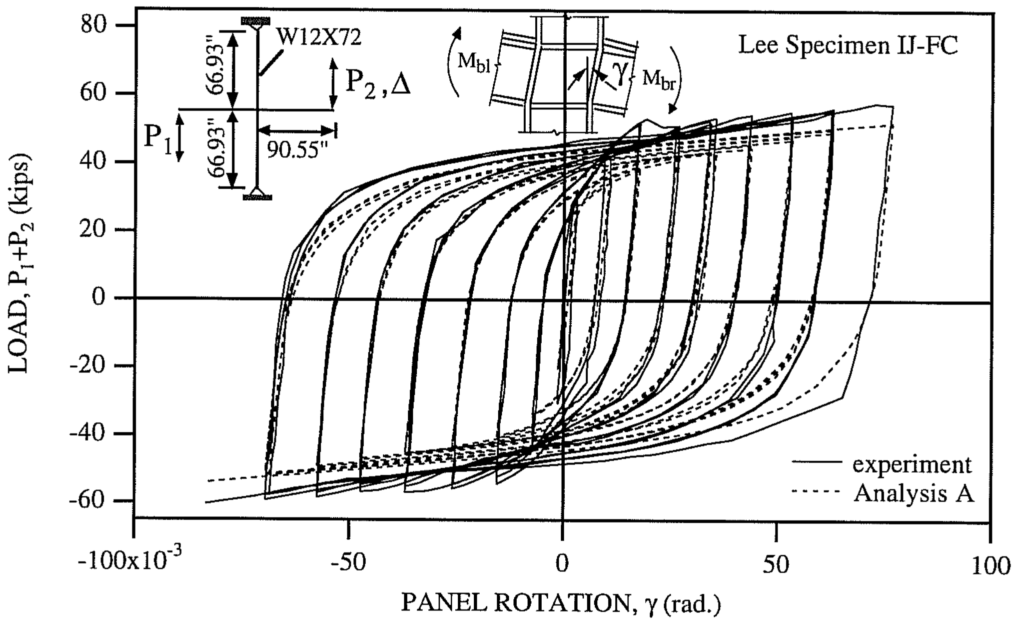

Fig. 7.17a: Comparison of Panel Zone Response Obtained by the Test and the Nonlinear Panel Zone Model Using the Material Parameters of Bare Steel Beam-to-Column Joint for Lee Specimen IJ-FC (Lee 1987).

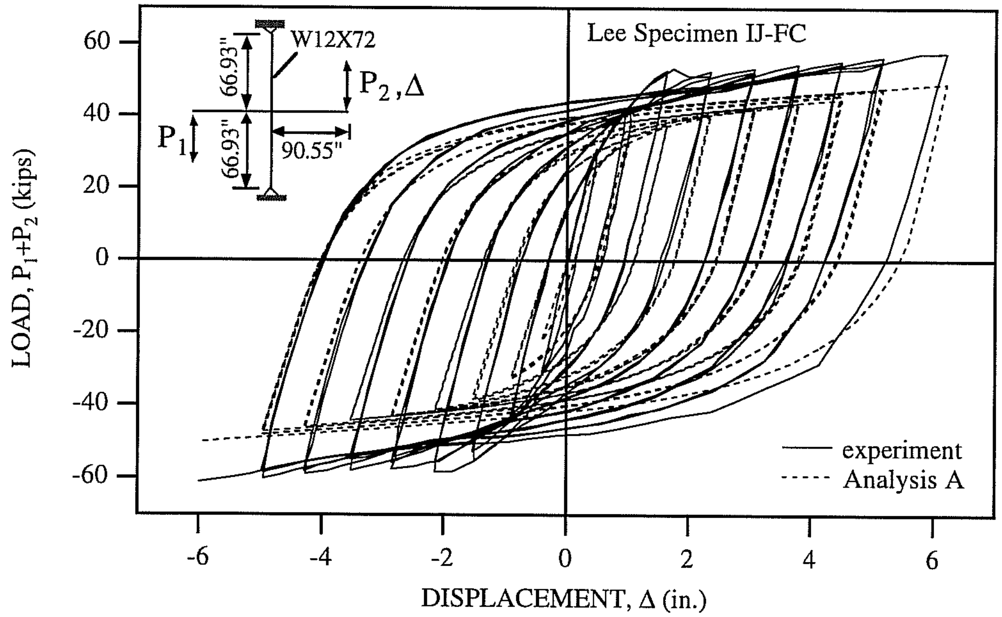

Fig. 7.17b: Comparison of Overall Response Obtained by the Test and the Analysis Using the Material Parameters of Bare Steel Beam-to-Column Joint for Lee Specimen IJ-FC (Lee 1987).

Specimen	α	K_p^{bl}	$\hat{h}_{neg.}$	$\hat{h}_{pos.}$	F_H	F_S	F_R
Lee EJ-FC	1.6	$0.005K_e$	15	30	0	0	0
Lee IJ-FC	1.6	$0.005K_e$	30	30	0	0	0

Table 7.3: Parameters to Define Hysteretic Rules for the Panel Zone of Composite Beam-to-Column Joints.

Figures 7.18a and 7.18b show comparisons of the experimental data and the analytical panel zone response obtained by the nonlinear panel zone element using the parameters shown in Table 7.3. In these figures, "Analysis B" represents the analysis using the parameters shown in Table 7.3 for the nonlinear panel zone element. In Figs. 7.19a and 7.20a, the overall response predicted by Analysis B is compared with the experimental data. The agreement between the experimental and analytical results is reasonable. In Figs. 7.19b and 7.19c, the local response obtained by Analysis B for Specimen EJ-FC is compared with the experimental data. While the maximum negative beam rotation predicted by Analysis B is larger by about 50 % than that predicted by the test, the maximum negative panel zone rotation predicted by Analysis B is much smaller than that obtained by the test. If the hysteretic rules for the panel zone of composite beam-to-column joints can properly model the effect of the composite slab after cracks close, the correlation between the local responses predicted by the test and the analysis will be improved. In Figs. 7.20b and 7.20c, the local response obtained by Analysis B for Specimen IJ-FC is compared with the experimental data. The analytical local response shows that yielding is confined to the panel zone, as in the test.

Wenk et al. (1977) tested a one-story, two-bay steel frame with composite slabs under combined gravity and lateral loading (Specimen CA-1). Since Specimen CA-1 was designed for the yielding to be confined to the composite beams, and the panel zones of the specimen were diagonally braced to remain elastic throughout the test, it is assumed that the columns and panel zones remain elastic during the analysis.

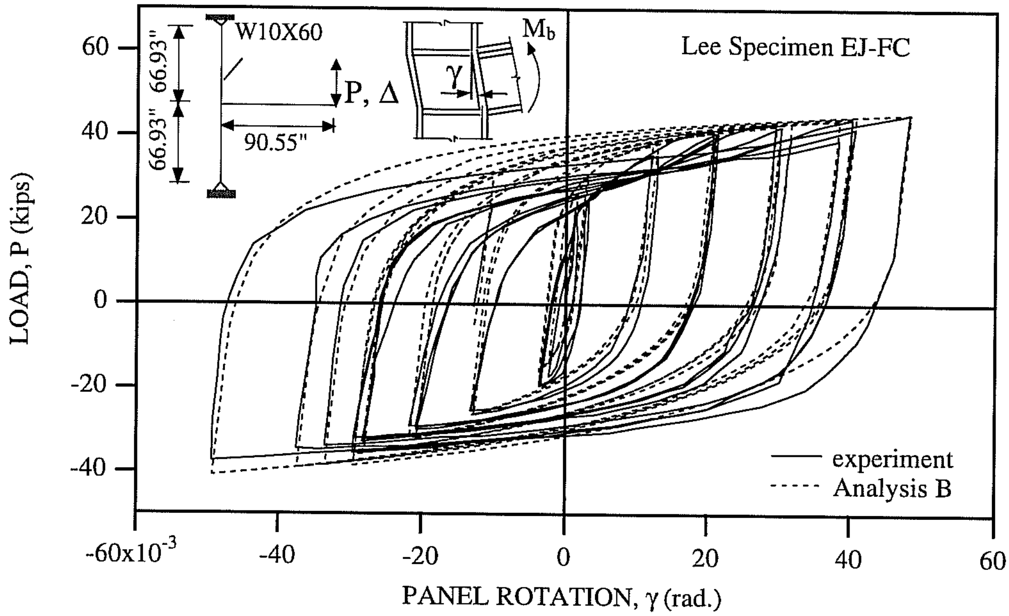

Fig. 7.18a: Comparison of Panel Zone Response Obtained by the Test and the Nonlinear Panel Zone Model Using the Parameters for the Panel Zone of the Exterior Composite Beam-to-Column Joints (Lee 1987).

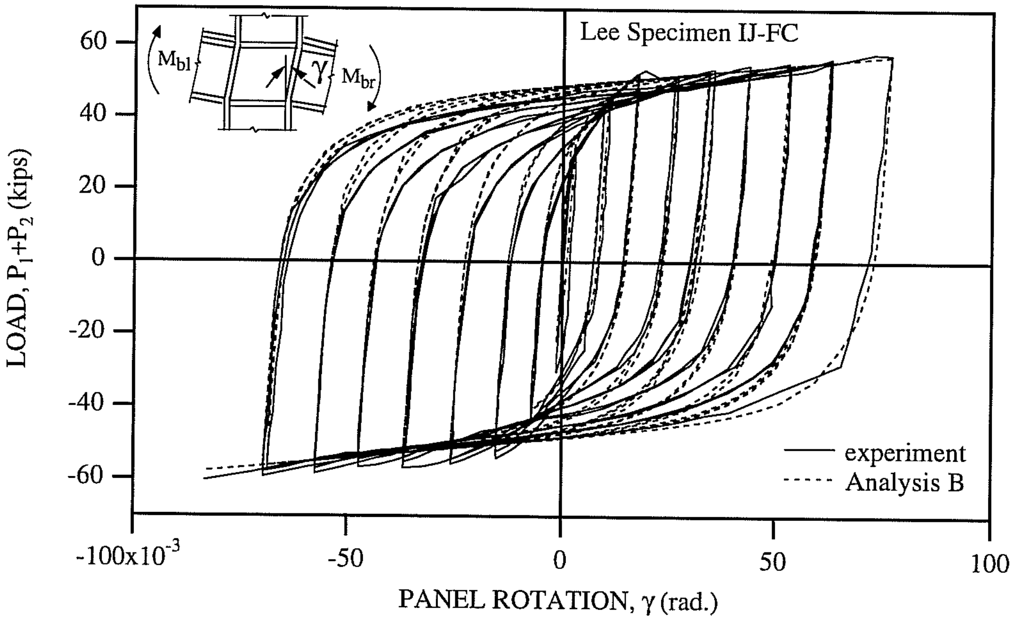

Fig. 7.18b: Comparison of Panel Zone Response Obtained by the Test and the Nonlinear Panel Zone Model Using the Parameters for the Panel Zone of the Interior Composite Beam-to-Column Joints (Lee 1987).

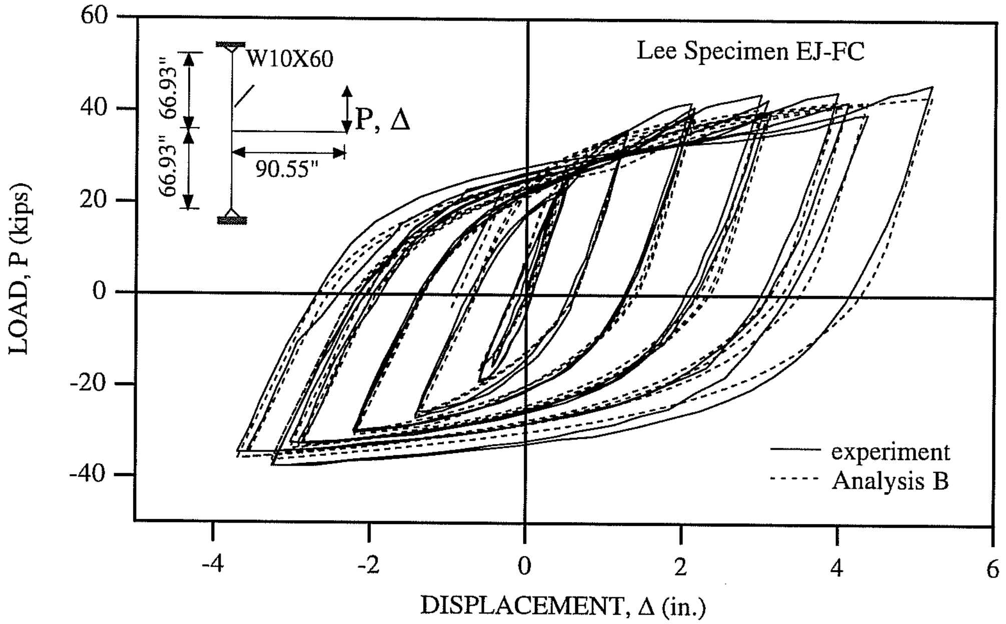

Fig. 7.19a: Comparison of Overall Response Obtained by the Test and the Analysis Using the Parameters for the Panel Zone of the Exterior Composite Beam-to-Column Joints (Lee 1987).

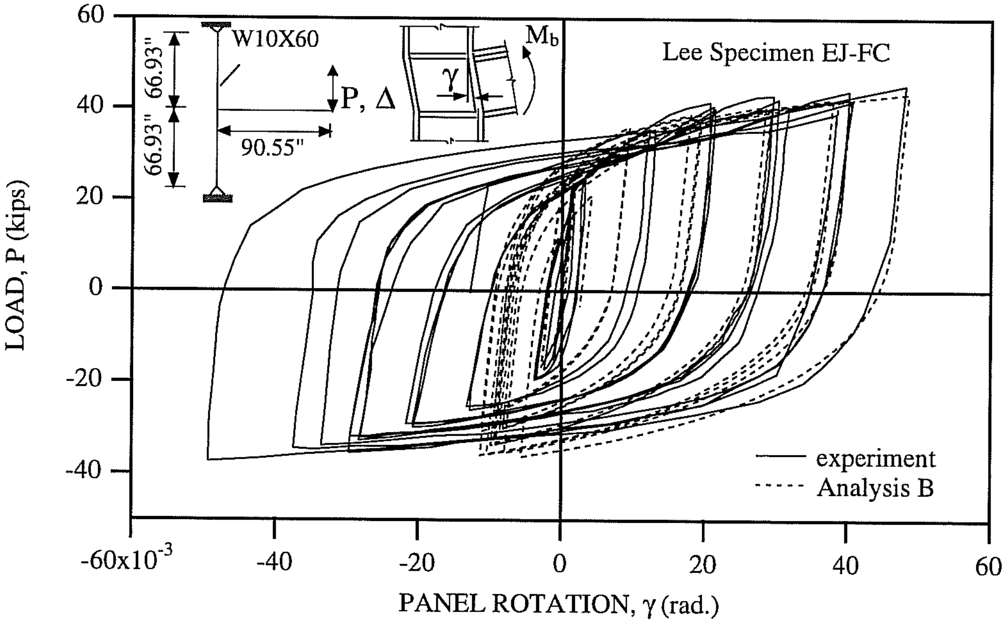

Fig. 7.19b: Comparison of Panel Zone Response Obtained by the Test and the Analysis Using the Parameters for the Panel Zone of the Exterior Composite Beam-to-Column Joints (Lee 1987).

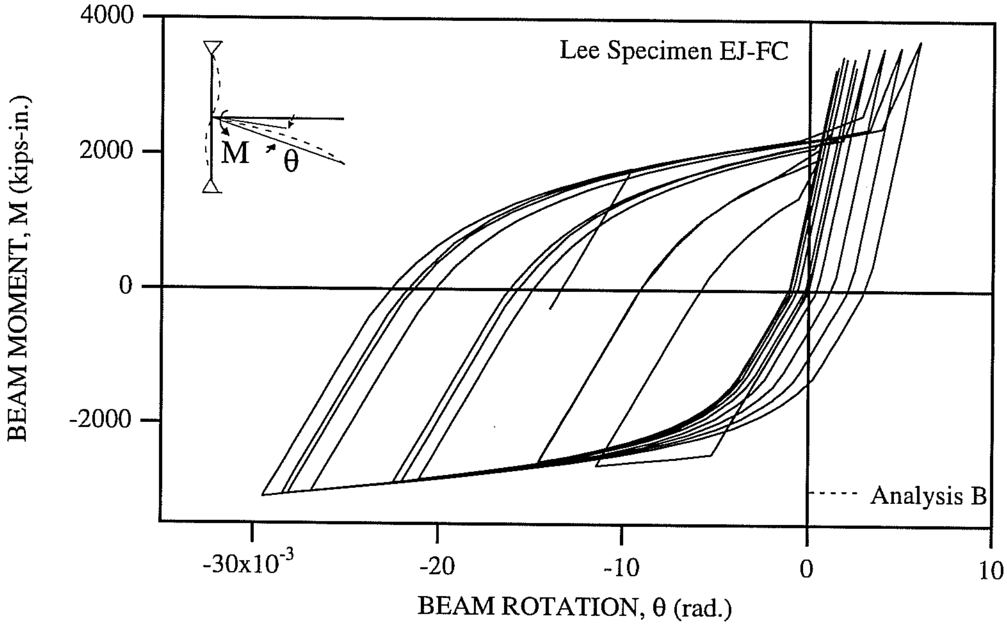

Fig. 7.19c: Beam Moment-Rotation Relation Obtained by the Analysis Using the Parameters for the Panel Zone of the Exterior Composite Beam-to-Column Joints (Lee 1987).

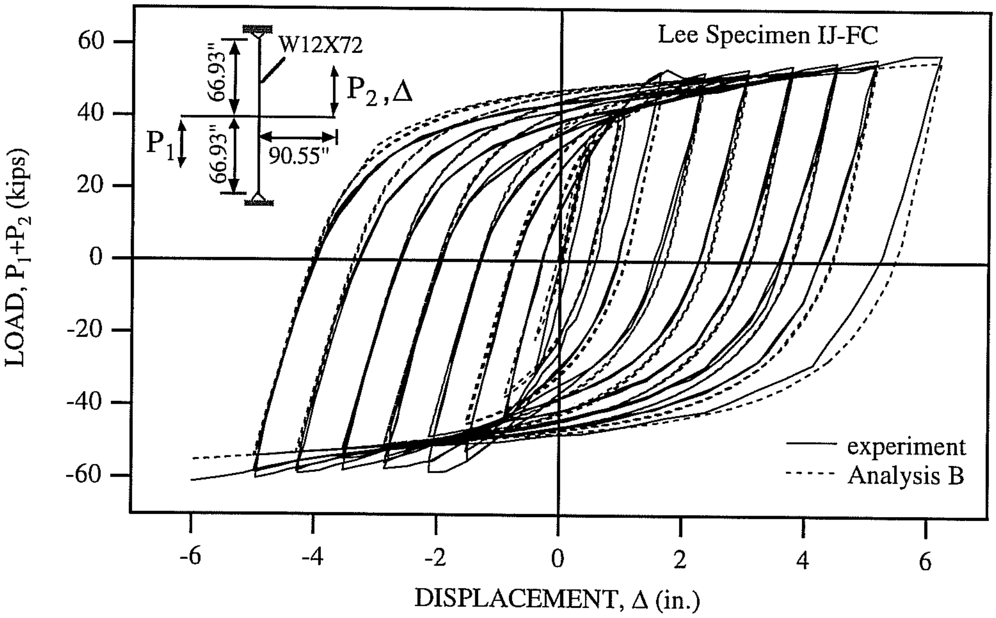

Fig. 7.20a: Comparison of Overall Response Obtained by the Test and the Analysis Using the Parameters for the Panel Zone of the Interior Composite Beam-to-Column Joints (Lee 1987).

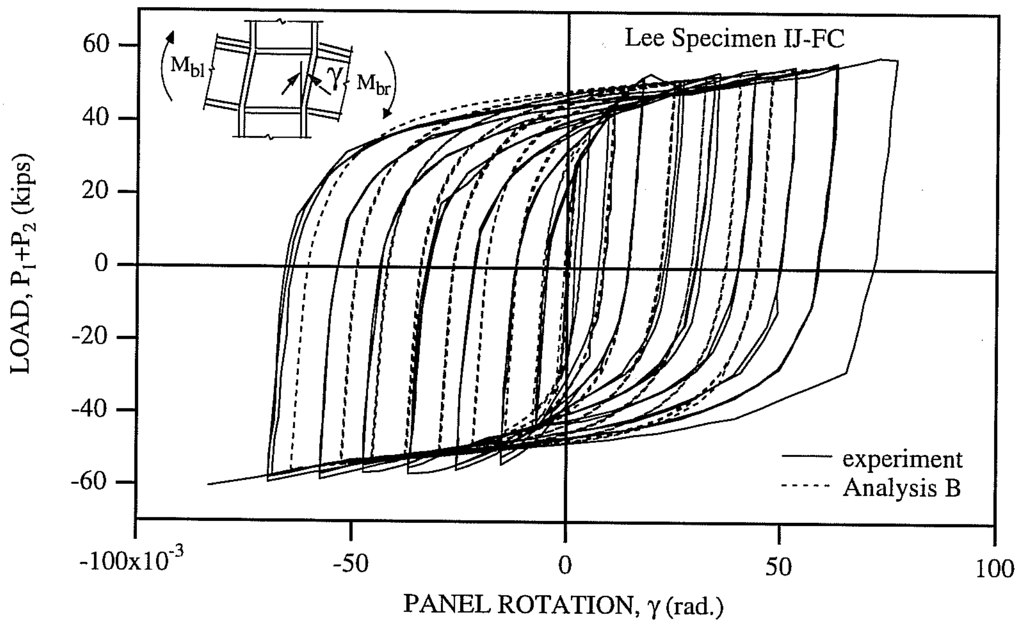

Fig. 7.20b: Comparison of Panel Zone Response Obtained by the Test and the Analysis Using the Parameters for the Panel Zone of the Interior Composite Beam-to-Column Joints (Lee 1987).

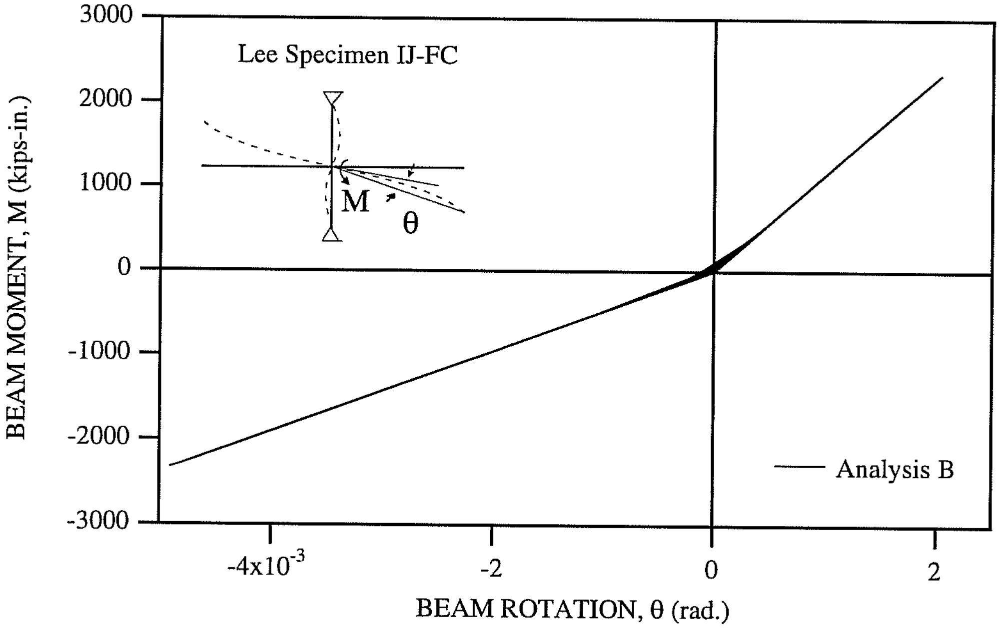

Fig. 7.20c: Beam Moment-Rotation Relation Obtained by the Analysis Using the Parameters for the Panel Zone of the Interior Composite Beam-to-Column Joints (Lee 1987).

In Fig. 7.21, the overall response predicted by an analysis modeling the composite beams using the multi-linear hinge elements for bare steel beams is compared with the experimental data. From this figure, it can be seen that by ignoring the effect of the composite slab, the overall stiffness and strength of the test frame are underestimated by about 40 % and 30 %, respectively.

Figures 7.22a and 7.22b compare the overall response predicted by the test and the analyses using the composite beam element. In the analysis of Fig. 7.22a, the ultimate moments M^+_{max} obtained by Eq. 6.7b, which is based on the compression yield of reinforcing bars, are used to determine the positve yield moments M^+_y at the exterior and interior connections. In the analysis of Fig. 7.22b, the ultimate moment M^+_{max} obtained by Eq. 6.7b is employed to calculate the positive yield moment M^+_y at the exterior connection, whereas to determine the positive yield moment M^+_y at the interior connection, the ultimate moment obtained by a method based on the tension yield of reinforcing bars is applied.

To determine the ultimate moment at the interior connection, Wenk (1977) suggested a method based on tension yield of reinforcing bars as follows. Figure 7.23a shows the maximum slab forces in the positive moment region of the interior joint. Between the column flange and the slab a maximum force of $1.3f'_c b_{cf} t_c$ acts as in Eq. 6.7b, where b_{cf}=column flange width and t_c=thickness of the slab. Unlike Eq. 6.7b, a tension force acts in the longitudinal slab reinforcement. The reinforcement is assumed to have yielded in tension. The maximum tension force is therefore equal to $A_r F_{yr}$, where A_r=area of reinforcing bars within the effective width defined by Eq. 6.6 and F_{yr}=yield strength of reinforcing bars. The stress distribution of the composite section in the positive moment region of the interior joint is shown in Fig. 7.23b. The resultant maximum slab force is equal to $1.3f'_c b_{cf} t_c - A_r F_{yr}$. The plastic neutral axis is determined by solving the following equation for compressive steel area, A_{sc}:

$$2A_{sc}F_y = A_s F_y - 1.3f'_c b_{cf} t_c + A_r F_{yr} \qquad (7.1a)$$

From Fig. 7.23b and Eq. 7.1a, the ultimate moment at the interior connection is written as

$$M^+_{max} = 1.3f'_c b_{cf} t_c y_n \left(1 - \frac{t_c}{2y_n}\right) + A_{sc} F_y y_{sc} + \left(A_s - A_{sc}\right) F_y y_s - A_r F_{yr} y_r \qquad (7.1b)$$

As far as the monotonic behavior is concerned, the analysis using Eq. 6.7b to determine the ultimate moment at the interior connection overestimates the strength by about 15 % (Fig. 7.22a), whereas the analysis using Eq. 7.1b overestimates the strength by about 6 % (Fig. 7.22b). The unloading elastic stiffnesses after the first half cycle of loading predicted by both analyses do not match well with that predicted by the test. However, for the rest of loading cycles the unloading elastic stiffnesses predicted by both analyses match well with that predicted by the test. While the analysis using Eq.6.7b shows reasonable performance except for the monotonic loading, the analysis using Eq. 7.1b exhibits reasonable performance as a whole. It seems to be more reasonable that for the analysis of a steel frame with composite slabs, the ultimate moments obtained by Eq. 6.7b and Eq. 7.1b, respectively, are applied to determine the positive yield moments at the exterior and interior connections.

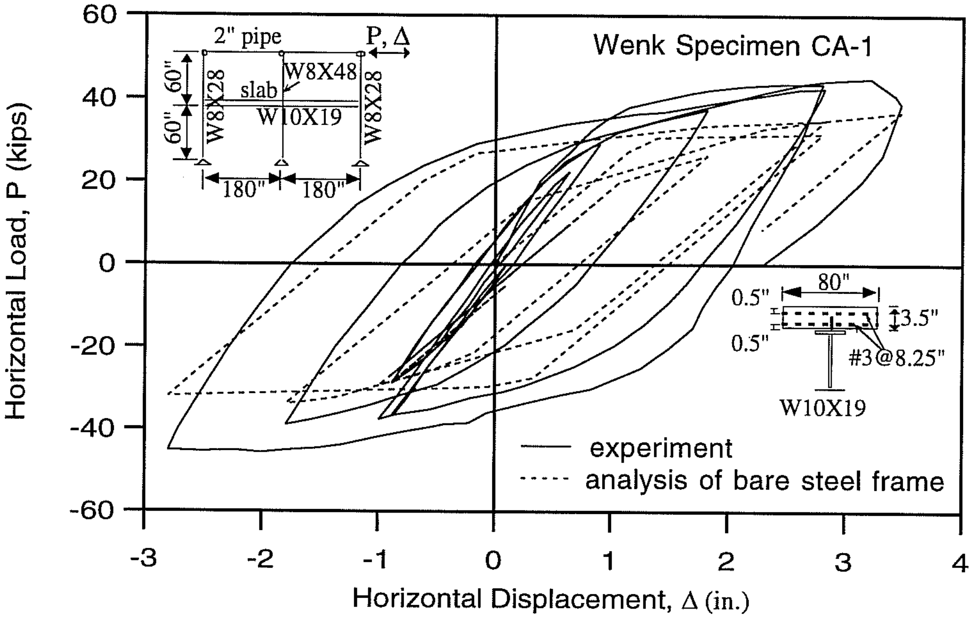

Fig. 7.21: Comparison of Overall Response Obtained by the Test and the Analysis Modeling Composite Beams as Bare Steel Beam Elements for Wenk Specimen CA-1 (Wenk 1977).

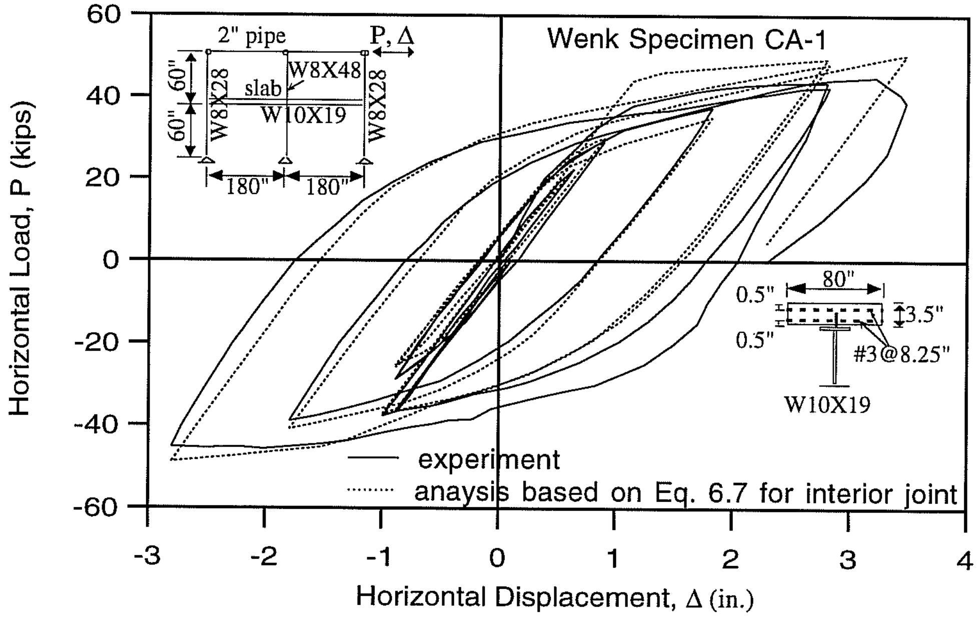

Fig. 7.22a: Comparison of Overall Response Obtained by the Test and the Analysis Using the Ultimate Moment Obtained by Assuming Compression Yield of Reinforcing Bars at Interior Joint.

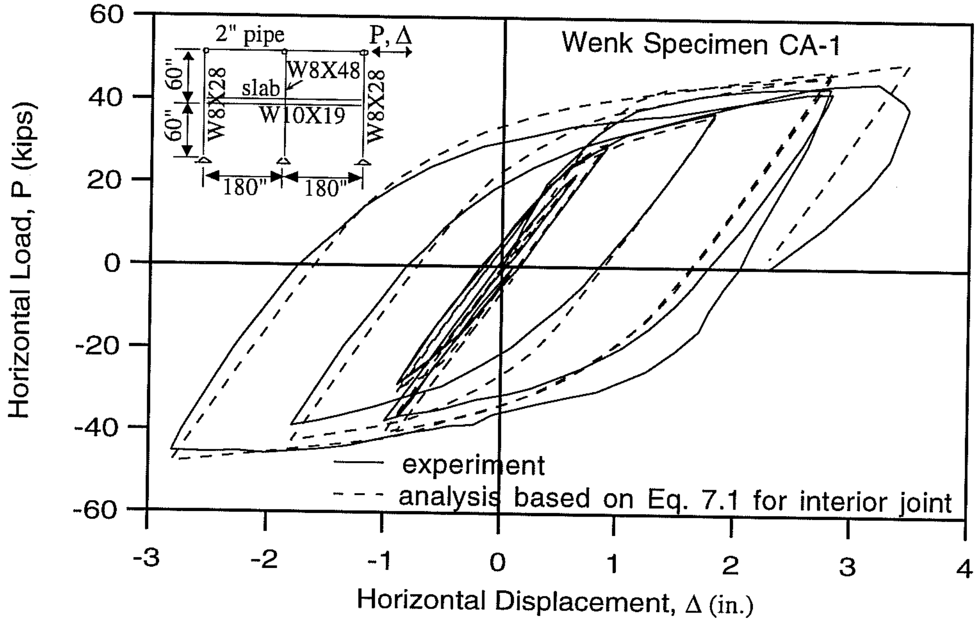

Fig. 7.22b: Comparison of Overall Response Obtained by the Test and the Analysis Using the Ultimate Moment Obtained by Assuming Tension Yield of Reinforcing Bars at Interior Joint.

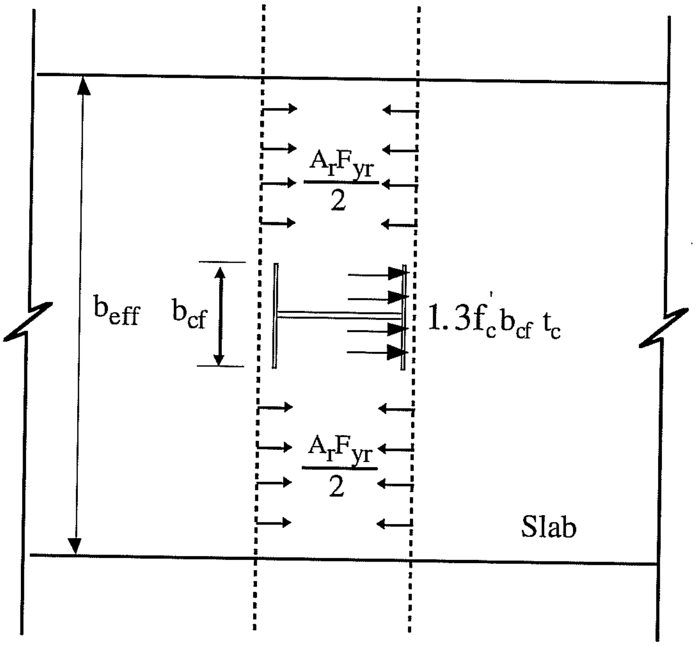

Fig. 7.23a: Maximum Slab Forces at Interior Joint (Wenk 1977).

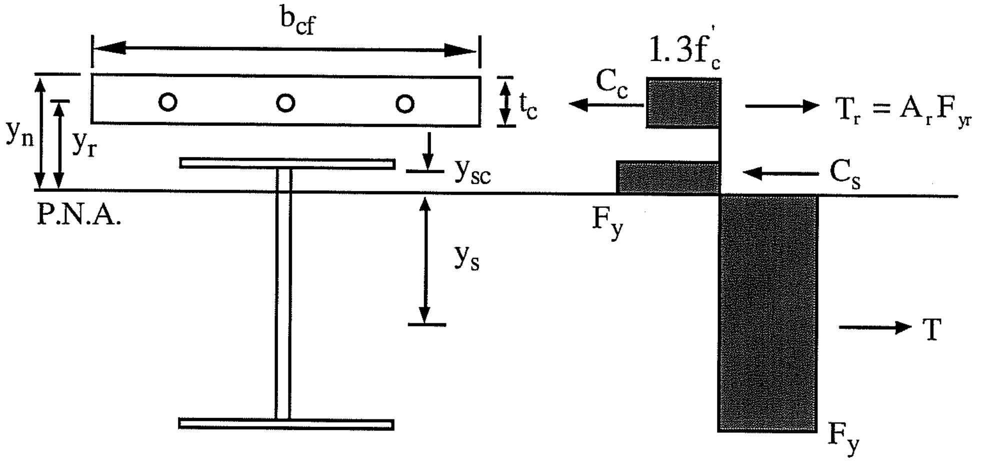

Fig. 7.23b: Maximum Stress at Positive Moment Region of Interior Joint (Wenk 1977).

In the following paragraphs, the effect of a moving inflection point on the one component series model is discussed. The one component series model proposed by Giberson (1967) for the stiffness formulation of a beam element consists of an elastic element with two plastic hinges at the ends. All inelastic rotations within a member length are lumped into these two plastic hinges. In order to estimate the characteristics of these two plastic hinges, moment distribution along a member must be predetermined and the inelastic stiffness of sections along the beam must be known. It is often assumed for members with uniform stiffness that the inflection point is in the middle of the member and the member end moments are of the same magnitude but have opposite signs (fixed inflection point during loading history). The inelastic characteristics of the two plastic hinges are determined such that the plastic hinges represent all the inelastic rotation within the member. This assumption is not always justified. In reality, the yield condition at one end of a member depends on rotation at the other end. However, it has been found that the multi-linear hinge model (Section 7.2) and other one component series models (Giberson 1967; Goel 1968; Emori 1981; Banon 1981), which are based on the anti-symmetric moment distribution assumption, are fairly accurate for prismatic girders of frames subjected to strong earthquake motions or large lateral forces.

In the previous chapter, two bilinear skeleton models and hysteretic rules for composite beams were developed for an equivalent cantilever composite beam with a fixed length. However, when a one component series model using the developed hysteretic rules is applied to model composite beams, difficulties arise because the anti-symmetric moment distribution assumption is not valid. This assumption is not valid due to the unsymmetric cross-section of composite beams and the fact that the stiffness of a composite beam varies as a function of the moving inflection point during loading history.

In this work, to account for the change of the length of an equivalent cantilever beam due to varying inflection point locations during the loading history, the equivalent cantilever beam lengths for positive and negative moments obtained from the linear moment distribution at the end of the previous load step are applied to determine the stiffness of two plastic hinges for the next load step (Eq. 6.12). The overall response predicted by this approach (Analysis A) for Wenk Specimen CA-1 is compared with the experimental results in Fig. 7.24a. The agreement between the experimental and analytical responses is reasonable.

Also, the overall response predicted by the analysis using a fixed inflection point during entire load steps (Analysis B) is compared with the experimental data and the response predicted by Analysis A in Fig. 7.24a. In Analysis B, the lengths of equivalent cantilever beams for positive and negative moments are taken equal to 0.7L and 0.3L (Lee 1987), respectively, where L is the length of the composite beam. The overall response predicted by Analysis B matches reasonably well with the experimental data. In Figs. 7.24b and 7.24c, the local composite beam response predicted by Analysis A is compared with that by Analysis B. From these figures, it can be seen that although there is some difference between the analytical local responses, the difference between the analytical overall responses is almost negligible. The effect of moving a inflection point during the loading history on the local and overall responses of the test frame is not significant.

In general, it appears that if the one component series model employs hysteretic rules to properly model structural characteristics of its structural component under strong earthquake motions, the analytical response is not significantly affected by the assumed inflection point, even if the structural component has unsymmetric cross-section, or the movement of inflection point between subsequent load or time steps is relatively large.

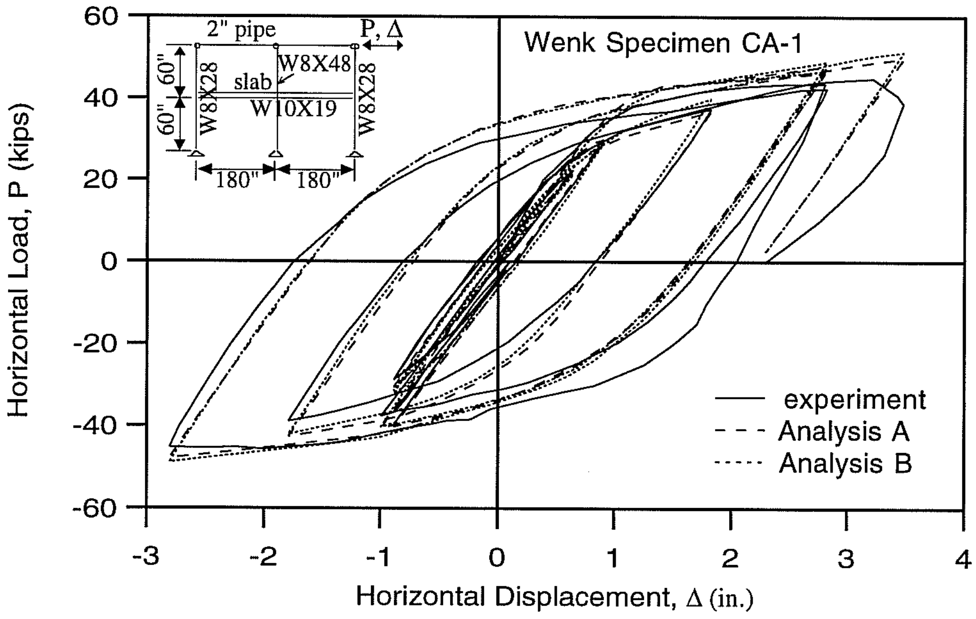

Fig. 7.24a: Comparison of Overall Responses Obtained by the Test and the Analyses Using Different Methods to Consider Changing Inflection Point for Wenk Specimen CA-1 (Wenk 1977).

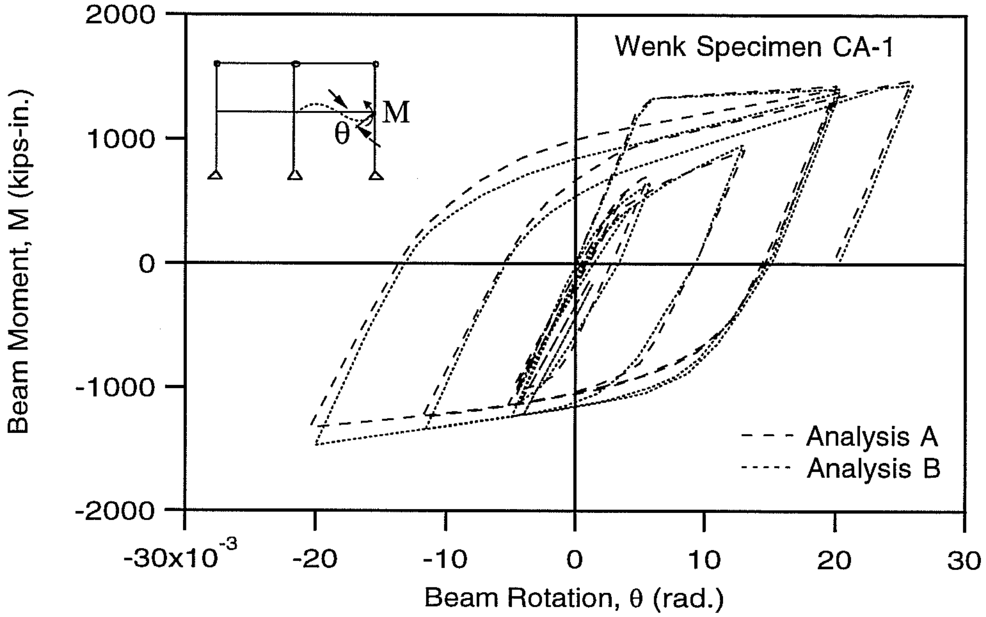

Fig. 7.24b: Comparison of Beam Moment-Rotation Relations of Right Composite Beam Obtained by the Analyses Using Different Methods to Consider Changing Inflection Point for Wenk Specimen CA-1 (Wenk 1977).

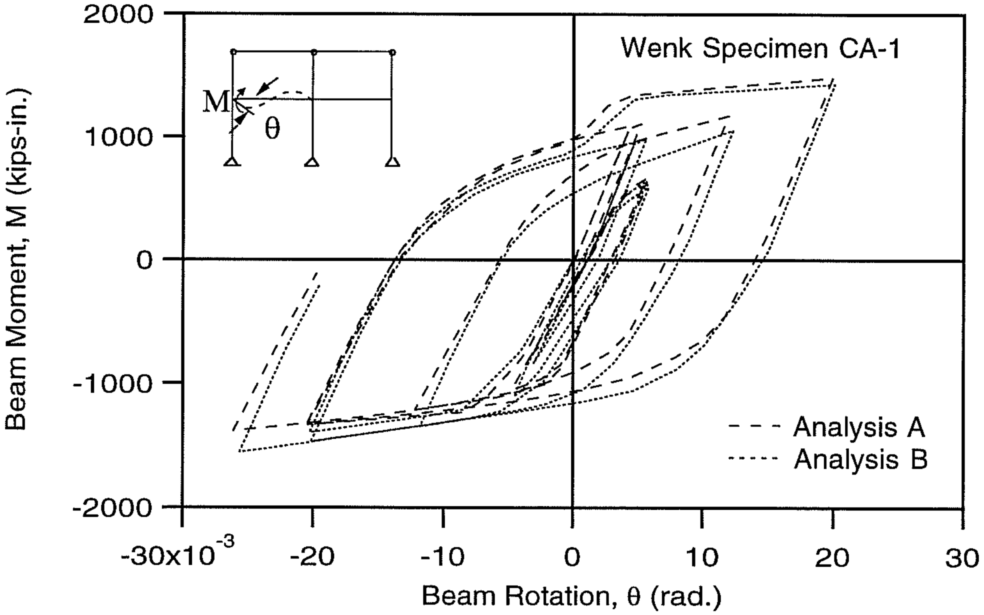

Fig. 7.24c: Comparison of Beam Moment-Rotation Relations of Left Composite Beam Obtained by the Analyses Using Different Methods to Consider Changing Inflection Point for Wenk Specimen CA-1 (Wenk 1977).

7.4 Summary

In this chapter, the multi-linear hinge element and the nonlinear panel zone element developed for bare steel beams and columns, and column panel zones, respectively, were combined into eleven bare steel subassemblages and four bare steel frames to investigate their local and overall response. The analytically predicted overall responses matched reasonably well with the experimental data. The analyses by the multi-linear hinge elements and the nonlinear panel zone elements produced better local and overall response predictions than the analyses by the bilinear hinge elements and the bilinear panel zone elements. The composite beam elements, combined with the multi-linear hinge elements and the nonlinear panel zone elements, were applied to analyze two steel subassemblages with composite slabs and one steel frame with composite slabs. The analytical predictions of overall response matched reasonably well with the experimental data.

Chapter 8: CONCLUSIONS AND RECOMMENDATIONS

8.1 Conclusions

In this study, a multi-linear hinge element, nonlinear panel zone element, and composite beam element were developed to model bare steel beams and columns, column panel zones, and composite beams. These elements are intended for use in the analysis of steel moment resisting frames under earthquake loading.

The multi-linear hinge element can be considered as a one component series hinge type model. It employs multilinear force deformation relationships, and accounts for the effects of beam end connection types. Cases of fully welded as well as welded flange-bolted web type connections are modeled. The element also models plastic axial deformations and changes in axial stiffness due to hinge formation under combined bending and axial force. Hardening rules handle monotonic, cyclic or random loading. The beam behavior of the model was investigated. For all welded connections, the predicted results by the model were compared with experimental data for five test specimens. The agreement was good. The model was also applied to eight test specimens with welded flange-bolted web connections. The correlation between the predicted results and experimental data was acceptable. The predictions made by the model employing the weighting factor matched well with the analytical results obtained by the fiber model. The column behavior of the model was also investigated. The multi-linear hinge model considering plastic axial deformations exhibited reasonable performance in the first and second order analyses. In general, the multi-linear hinge model showed significantly better performance than the commonly used bilinear hinge model and could reasonably model the beam-column behavior of bare steel members in moment resisting frames.

The nonlinear panel zone element, which is essentially a rotational spring element, was developed to describe cyclic panel zone behavior of bare steel beam-to-column joints. From the comparison of the analytical results with test results for the specimens with a doubler plate, it was found that doubler plates were only partially effective in resisting the panel zone shear. In spite of the simplicity of the model, reasonable agreement was established between model predictions and test results for panel zones with no doubler plates. For panel zones with doubler plates, the predictions of the simple model are not as reliable.

A composite beam element, which is a one component series hinge type model, was developed by improving the model proposed by Lee. In the hysteretic model of the developed element, a smooth transition from the elastic stage to the inelastic stage and the strength deterioration at the linear crack closing stage were considered. The capability to account for a moving inflection point was added to the element. The member behavior predicted by the developed element matched reasonably well with the experimental results before local buckling dominated the experimental response.

The multi-linear hinge element and the nonlinear panel zone element were combined into eleven bare steel subassemblages and four bare steel frames to investigate their local and overall response. The analytically predicted overall responses matched reasonably well with the experimental data. Since the multi-linear hinge and nonlinear panel zone elements have the capability to more accurately model the mechanical behavior of the structural components, the analyses by the multi-linear hinge elements and the nonlinear panel zone elements produced better local response predictions than the analyses by the bilinear hinge elements and the bilinear panel zone elements. The composite beam elements, combined with the multi-linear hinge elements and the nonlinear panel zone elements, were applied to analyze two steel subassemblages with composite slabs and one steel frame with composite slabs. The analytical predictions of overall response matched reasonably well with the experimental data. In general, it appeared that if the one component series model employed hysteretic rules to properly model structural characteristics of its structural component under strong earthquake motions, the analytical response was not significantly affected by the assumed inflection point, even if the structural component had an unsymmetric cross-section, or the movement of inflection point between subsequent load or time steps was relatively large.

8.2 Recommendations for Future Research

For the multi-linear hinge model to be employed to describe the behavior of a member in the direction of weak axis bending, weak axis bending moment-rotation relations and weak axis bending moment-axial force interaction relations need calibration to experimental data and predictions made by other more sophisticated analytical models.

The thickest column flange used in the study of the column panel zone was t_{cf} = 1.775". In actual design practice, even thicker column flanges may be used, perhaps on the order of 3 to 5 inches. Additional test or FEM predictions for such column sections are needed to further verify the monotonic panel zone moment-rotation relations and hysteretic rules suggested in Chapter 5.

From the study of the column panel zones with doubler plates, it has been found that reliable model predictions are difficult to obtain for cases where doubler plates have a yield stress significantly different than the column web, and that the effectiveness of doubler plates is affected by the method used to connect them to the column (one side attachment, both sides attachment, welding details, etc.). Additional test or FEM predictions for the column panel zones with doubler plates are needed to further study the effectiveness of doubler plates.

There was little experimental data to model the panel zone behavior of composite beam-to-column joints. This study therefore did not attempt to develop a panel zone element for composite beam-to-column joints. Rather, the parameters to define the hysteretic rules for the panel zone of bare steel beam-to-column joints were adjusted such that analytical panel zone strengths matched well with the experimental panel zone strengths for the limited number of test specimens with composite beams. More tests for the panel zone of composite beam-to-column joints are needed to further investigate and to model this situation.

Additional improvements are needed for models of composite beams. This is among the most difficult of modeling problems for steel moment frames. It is also an important problem, since most steel moment frames are constructed with composite beams. The complexities of this problem include difficulties in establishing effective width, and in accurately modeling the slip between the concrete slab and steel beam under cyclic load. Additional experimental data and three dimensional finite element analyses are required to support the development of improved composite beam models.

Finally, it is noted that the models developed in this study have been calibrated using currently available experimental data. As additional experimental data becomes available, the model parameters should be continually reevaluated to assure that the models provide a realistic representation of structural response.

References

Adams, J. (1973), "Nonlinear Behavior of Steel Frames," Ph.D. Thesis, Dept. of Civil Eng., Massachusetts Institute of Technology, June 1973.

American Institute of Steel Construction, Inc., *Manual of Steel Construction-Allowable Stress Design*, 9th Edition, Chicago, Illinois, 1989.

American Institute of Steel Construction, Inc., *Seismic Provisions for Structural Steel Buildings, Load and Resistance Factor Design,* 2nd Edition, Chicago, Illinois, 1994.

American Institute of Steel Construction, Inc., *Supplement 1 to the LRFD Specification for Structural Steel Buildings,* 2nd Edition, Chicago, Illinois, 1994.

Ansourian, P. (1975), "An Application of the Method of Finite Elements to the Analysis of Composite Floor Beams," Institution of Civil Engineers, Vol. 59, pp. 699-726, 1975.

Bäcklund, J. (1976), "Large Deflection Analysis of Elasto-Plastic Beams and Frames," Journal of Mechanical Science, Vol. 18, 1976, pp. 269-277.

Becker, E.R. (1971), "Panel Zone Effect on the Strength and Stiffness of Rigid Steel Frames," Research Report, Mechanical Lab., University of Southern California, June 1971.

Carol, I., Murcia, J. (1989), "Nonlinear Time-Dependent Analysis of Planar Frame Using an 'Exact' Formulation-II. Computer Implementation for R. C. Structures and Examples," Computer & Structures, Vol. 33, No. 1, 1989, pp. 89-102.

Carpenter, L.D. and Lu, L.W. (1973), "Reversed and Repeated Load Tests of Full-Scale Steel Frames," Steel Research for Construction, AISI, Bulletin No. 24, April, 1973.

Chen, P.F. and Powell, G.H. (1982), "Generalized Plastic Hinge Concepts for 3D Beam-Column Elements," EERC Reports No. 82/20, University of California, Berkeley, Nov. 1982.

Clough, R.W., Benuska, K.L., and Wilson, E.L. (1966), “FHA Study of Seismic Design Criteria for High Rise Buildings," HUDTS-3, Aug. 1966, Federal Housing Administration, Washington D.C.

Cofie, N. G. and Krawinkler, H. (1985), "Uniaxial Cyclic Stress-Strain behavior of Structural Steel," Journal of Engineering Mechanics, Vol. 111, No. 9, Sept. 1985, pp. 1105-1120.

Dafalias, Y. F. (1975), "On Cyclic and Anisotropic Plasticity: I) A General Model Including Material Behavior Under Stress Reversals, II) Anisotropic," Ph.D. Thesis, Dept. of Civil Eng., University of California, Berkeley, 1975.

Dafalias, Y. F. and Popov, E. P. (1975), "A Model of Nonlinearly Hardening Materials for Complex Loading," Acta Mechanica, ASME, Vol. 21, 1975, pp. 173-192.

Dafalias, Y. F. and Popov, E. P. (1976), "Plastic Internal Variables Formalism of Cyclic Plasticity," Journal of Applied Mechanics, ASME, Vol. 43, Dec. 1976, pp. 645-651.

Daniels, J.H., Kroll, G.D., and Fisher, J.W. (1970), "Behavior of Composite Beam-to-Column Joints," Journal of Structural Division, ASCE, Vol. 96, No. ST3, pp. 671-685, March 1970.

Drucker, D.C. (1960), "Plasticity," Structural Mechanics, pp. 407-488, Pergamon Press, London, 1960.

duPlessis, D.P. (1974), "The Interaction of Floors and Frames in Multi-Story Buildings," Ph. D. Thesis, Dept. of Civil Eng., Lehigh University, 1974.

duPlessis, D.P. and Daniels, J.H. (1972), "Experiments on Composite Beams Under Positive End Moment," Fritz Engineering Laboratory, Report No. 374.2, Lehigh University, 1972.

duPlessis, D.P. and Daniels, J.H. (1972), "Strength of Composite Beam-to-Column Connections," Fritz Engineering Laboratory, Report No. 374.3, Lehigh University, 1973.

Elias, Z. M. (1986), "Theory and Methods of Structural Analysis," John Wiley & Sons, 1986.

Engelhardt, M.D. (1992), "Cyclic Tests on Large Scale Steel Moment Connections," Research Report PMFSEL 92-2, Dept. of Civil Eng., University of Texas, Austin, June 1992.

Engelhardt, M.D. and Sabol, T.A. (1994), "Testing of Welded Steel Moment Connections in Response to the Northridge Earthquake," Progress Report to the AISC Advisory Subcommittee on Special Moment Resisting Frame Research, Dept. of Civil Eng., University of Texas, Austin, Oct. 1994.

Fielding, D.J. and Chen, W.F. (1973), "Steel Frame Analysis and Connection Shear Deformation," Journal of Structural Division, ASCE, Vol. 99, No. ST1, January 1973.

Fielding, D.J. and Huang, J.S. (1971), "Shear in Steel Beam-to-Column Connections," Welding Journal, Vol. 50, No. 7, Research Supplement, pp. 313-s to 326-s, 1971.

Firmansjah, J. and Hanson, R.D. (1992), "Behavior of 3-D Steel Moment Frame Structures Under the Influence of Bi-Directional Ground Excitation," Research Report UMCEE 92-4, Dept. of Civil Eng., University of Michigan, May 1992.

Giberson, M.F. (1969), "Two Nonlinear Beams with Definition of Ductility," Journal Structural Division, ASCE, Vol. 95, No. ST7, July 1969.

Grant, J.A., Fisher, J.W., and Slutter, R.G. (1977), "Composite Beams with Formed Steel Deck," Engineering Journal, AISC, Vol. 14, No. 1, pp. 24-43, 1977.

Hill, R. (1950), "The Mathematical Theory of Plasticity," Oxford University Press, Oxford, England 1950.

Hsu, L.W. (1974), "Behavior of Multi-Story Reinforced Concrete Walls During Earthquakes," Ph.D. Thesis, Dept. of Civil Eng., University of Illinois, Urban, 1974.

International Conference of Building Officials (1988),*Uniform Building Code*.., Whittier, California, 1988.

Iwan, W.D. (1967), "On a Class of Models for the Yielding Behavior of Continuous and Composite Systems," Journal of Applied Mechanics, Vol. 34, Transaction ASME Vol. 89, Series E, 1967, pp. 163.

Kaba, S.A. and Mahin, S.A. (1984), "Refined Modeling of Reinforced Concrete Columns for Seismic Analysis," EERC Reports No. 84/03, University of California, Berkeley, April. 1984.

Kanaan, A.E. and Powell, G.H. (1973), "DRAIN-2D- A General Purpose Computer Program for Dynamic Analysis of Inelastic Plane Structures- With User's Guide," EERC Reports No. 73/6 and 73/22, University of California, Berkeley, April 1973.

Kang, Y.J. and Scordelis, A.C. (1980), "Nonlinear Analysis of Prestressed Concrete Frames," Journal Structural Division, ASCE, Vol. 106, No. ST2, Feb. 1980.

Kato, B., Chen, W.F., and Nakao, M. (1988), "Effects of Joint-Panel Shear Deformation on Frame," Journal of Constructional Steel Research, Vol. 10, pp. 269-320, 1988.

Kato, B. and Tagawa, Y. (1985), "Strength of Composite Beams Under Seismic Loading," Composite and Mixed Construction, ASCE, New York, 1985.

Keshavarzian, M. and Schnobrich, W. (1985), "Inelastic Analysis of RC Coupled Shear Walls," Earthquake Engineering and Structural Dynamics, Vol. 13, 1985, pp. 427-448.

Kim, W.K. (1992), "Seismic-Response Analysis and Design of Composite Building Structures," Ph.D. Thesis, Dept. of Civil Eng., Lehigh University, Bethlehem, 1992.

Krawinkler, H. (1978), "Shear in Beam-Column Joints in Seismic Design of Steel Frames," Engineering Journal, AISC, Third Quarter, 1978.

Krawinkler, H., Bertero, V.V., and Popov, E.P. (1971), "Inelastic Behavior of Steel Beam-to-Column Subassemblages," EERC Reports No. 71/07, University of California, Berkeley, October. 1971.

Latona, R.W. and Roesset, J.M. (1970), "Nonlinear Analysis of Building Frames for Earthquake Loading," Research Report R70-65, Dept. of Civil Eng., Massachusetts Institute of Technology, 1970.

Lee, S.J. (1987), "Seismic Behavior of Steel Building Structures with Composite Slabs," Ph.D. Thesis, Dept. of Civil Eng., Lehigh University, Bethlehem, 1987.

Lee, S.J. and Lu, L.W. (1989), "Cyclic Tests of Full-Scale Composite Joint Subassemblages," Journal of Structural Division, ASCE, Vol. 115, No. 8, Aug. 1989, pp. 1977-1998.

Lu, L.W. and Carpenter, L.D. (1978), "Hysteretic Behavior of Full-Scale Steel and Composite Frames," Proceedings of Sixth European Conference on Earthquake Engineering, Dubrovnik, Yugoslavia, 1978.

Lu, L.W., Slutter, R.G., and Yen, B.T. (1980), "Research on Composite Structures for Building and Bridges Application," Developments in Composite and Mixed Construction, Edited by Kato, B. and Lu, L.w., U.S.A.-Japan Seminar on Composite Structures and Mixed Construction Systems, Gihodo Shuppan Co., 1980.

Lui, E.M. (1985), "Effects of Connection Flexibility and Panel Zone Deformation on the Behavior of Panel Steel Frames," Ph.D. Thesis, Purdue University West Lafayette, Indiana, USA, 1985.

Lui, E.M. and Chen, W.F. (1986), "Analysis and Behavior of Flexibly-Jointed Frames," Engineering Structures, Butterworth, Surrey, UK, Vol. 8, No. 2, pp. 107-118, April 1986.

Mari, A. and Scordelis, A.C. (1982), "Nonlinear Geometric Material and Time Dependent Analysis of Three Dimensional Reinforced and Prestressed Concrete Frames," SESM Report 82-12, University of California, Berkeley.

Mark, K.M. (1976), "Nonlinear Dynamic Response of Reinforced Concrete Frames," Ph.D. Thesis, Dept. of Civil Eng., Massachusetts Institute of Technology, August 1976.

Meyer, C., Roufaiel, M.S., and Arzoumandis, S.G. (1983), "Analysis of Damaged Concrete Frames for Cyclic Loads," Earthquake Engineering and Structural Dynamics, Vol. 11, 1983, pp. 207-228.

Mondkar, D.P. and Powell, G.H. (1975), "ANSR 1- General Purpose Program for Analysis of Nonlinear Structural Response," EERC Reports No. 75/37, University of California, Berkeley, December 1975.

Moon, J.H. (1994), "Time-Dependent Analysis of Behavior and Strength for Prestressed Concrete Members with Bonded or Unbonded Tendons," Ph.D. Thesis, Dept. of Civil Eng., University of Texas, Austin, May 1994.

Mosaddad, B. and Powell, G.H. (1982), "Computational Models for Cyclic Plasticity Rate Dependence, and Creep in Finite Element Analysis," EERC Reports No. 82/26, University of California, Berkeley, Nov. 1982.

Mroz, Z. (1967), "An Attempt to Describe the Behavior of Metals under Cyclic Loads Using a More General Workhardening Model," Acta Mechanica, Vol. 7, Nos. 2-3, 1969, pp.199-212.

Mroz, Z. (1967), "On Description of Anisotropic Workhardening," Journal of Mechanical Physics and Solid, Vol. 15, 1967, pp.163-175.

Newmark, N.M., Siess, C.P., and Viest, I.M. (1951), "Tests and Analysis of Composite Beams with Incomplete Interaction," Proceedings of the Society for Experimental Stress Analysis, Vol. 9, No. 1, 1951.

Ollgaard, J.G., Slutter, R.G., and Fisher, J.W. (1971), "Shear Strength of Stud Connectors in Lightweight and Normal Concrete," Engineering Journal, AISC, Vol. 8, No. 2, pp. 55-64, 1971.

Otani, S. (1974), "Inelastic Analysis of R/C Frame Structures," Journal Structural Division, ASCE, Vol. 100, No. ST7, July 1974.

Peterson, H. and Popov, E. P. (1977), "Constitutive Relations for Generalized Loadings," Journal of the Engineering Mechanics Division, ASCE, Vol. 103, No. EM4, Aug. 1977, pp. 611-627.

Popov, E. P., Bertero, V.V., and Chandramouli, S. (1975), "Hysteretic Behavior of Steel Columns," EERC Reports No. 75/11, University of California, Berkeley, September 1975.

Popov, E. P. and Peterson, H. (1978), "Cyclic Metal Plasticity: Experiments and Theory," Journal of the Engineering Mechanics Division, ASCE, Vol. 104, No. EM6, Dec. 1978, pp. 1371-1388.

Popov, E.P. (1987), "Panel Zone Flexibility in Seismic Moment Joints," Journal of Construction and Steel Research, Vol. 8 pp. 91-118, 1987.

Popov, E.P. (1988), "Seismic Moment Connections for Moment Resisting Frames," Journal of Construction and Steel Research, Vol. 10 pp. 163-198, 1988.

Popov, E.P. and Stephen, R.M. (1972), "Cyclic Loading of Full-Size Steel Connections," Steel Research for Construction, AISI, Bulletin No. 21, February, 1972.

Popov, E.P., Amin, N.R., Louie, J.C., and Stephen, R.M. (1985), "Cyclic Behavior of Large Beam-Column Assemblies," Earthquake Spectra, Vol. 1, No. 2, Feb. 1985.

Prager, W., "A New Method of Analyzing Stresses and Strains in Work-Hardening Plastic Solids," Journal of Applied Mechanics, Vol. 78, 1956, pp. 493.

Ramm, E. (1980), "Strategies for Tracing the nonlinear Response Near Limit Points," Nonlinear Finite Element Analysis in Structural Mechanics Proceedings of the Europe-U.S. Workshop, Ruhr-Universitat, Bochum, Germany, July 28-31 1980.

Riks, E. (1979), "An Incremental Approach to the Solution of Snapping and Buckling Problems," International Journal of Solids Structures, Vol. 15, 1979, pp.529-551.

Robinson, H. (1969), "Composite Beam Incorporating Cellular Steel Decking," Journal of Structural Division, ASCE, Vol. 95, No. ST3, March 1969.

Roufaiel, M.S. and Meyer, C. (1987), "Analytical Modeling of Hysteretic Behavior of R/C Frames," Journal Structural Division, ASCE, Vol. 113, No. 3, March 1987.

Sarkisian, M.P. (1985), "Beam-to-Column Connections Subjected to Seismic Loads," Master Thesis, Dept. of Civil Eng., Lehigh University, Bethlehem, 1985.

Schiff, S.D. (1988), "Seismic Design Studies of Low Rise Steel Frames," Ph.D. Thesis, Dept. of Civil Eng., University of Illinois, Urban, 1988.

Schneider, S.P., Roeder, C.W., and Carpenter, J.E. (1991), "Seismic Performance of Weak-Column Strong-Beam Steel Moment Resisting Frames," Research Report, Dept. of Civil Eng., University of Washington, Seattle, Sept. 1991.

Slutter, R.G. (1981), "Tests of Panel Zone Behavior in Beam-Column Connections," Fritz Engineering Laboratory, Report No. 403.1, Lehigh University, 1981.

Slutter, R.G. and Driscoll, G.C. (1965), "Flexural Strength of Steel-Concrete Composite Beams," Journal of Structural Division, ASCE, Vol. 91, No. ST2, April 1965.

Soleimani, D., Popov, E.P., and Bertero, V.V. (1979), "Nonlinear Beam Model for R/C Frame Analysis," Seventh Conference on Electronic Computation, St. Louis, Missouri, Aug. 1979, ASCE, New York 1979.

Structural Engineers Association of California (1988), *Recommended Lateral Force Requirements*, San Francisco, California, 1988.

Tagawa, Y., Aoki, H., and Kato, B. (1986), "Composite Effect of Concrete Slabs and Strength of Composite Girders Under Seismic Loading," Proceedings of the Pacific Structural Steel Conference, New Zealand, 1986.

Tagawa, Y., Kato, B., and Aoki, H. (1989), "Behavior of Composite Beams in Steel Frame Under Hysteretic Loading" Journal of Structural Division, ASCE, Vol. 115, No. 8, Aug. 1989, pp. 2029-2045.

Takayanagi, T. and Schnobrich, W.C. (1979), "Nonlinear Analysis of Coupled Wall Systems," Earthquake Engineering and Structural Dynamics, Vol. 7, 1979, pp. 1-22.

Taucer, F., Spacone, E., and Filippou, F.C. (1991), "A Fiber Beam-Column Element for Seismic Response Analysis of Reinforced Concrete Structures," EERC Reports No. 91/17, University of California, Berkeley, Dec. 1991.

Tsai, K.C. and Popov, E.P. (1988), "Steel Beam-Column Joints in Seismic Moment Resisting Frames," EERC Reports No. 88/19, University of California, Berkeley, Nov. 1988.

Uang, C.M. (1985), "Experimental and Analytical Study of the Hysteretic Behavior of Steel Composite Girders," CE 299 Report, Dept. of Civil Eng., University of California, Berkeley, April 1985.

Uang, C.M., and Bertero, V.V. (1986), "Earthquake Simulation Tests and Associated Studies of a 0.3 Scale Model of a Six-Story Concentrically Braced Steel Structure," EERC Research Report, No. 86/10, University of California, Berkeley, Dec. 1986.

Wakabayashi, M., Matsui, C., Minami, K., and Mitani, I. (1974), "Inelastic Behavior of Steel Frames Subjected to Constant Vertical and Alternating Horizontal Loads," Fifth World Conference on Earthquake Engineering, Vol. 1, pp. 1194, Rome 1974.

Wallace, B.J. and Krawinkler, H. (1989), "Small-Scale Model Tests of Structural Steel Assemblies" Journal of Structural Division, ASCE, Vol. 115, No. 8, Aug. 1989, pp. 1999-2015.

Wang, S.J. (1988), "Seismic Response of Steel Building Frames with Inelastic Joint Deformation," Ph.D. Thesis, Dept. of Civil Eng., Lehigh University, Bethlehem, 1988.

Wenk, T. and Daniels, J.H. (1977), "Composite Assemblage Experiments," Fritz Engineering Lab. Report No. 403.2, Lehigh University, Bethlehem, May 1977.

Ziegler, H. (1959), "A Modification of Prager's Hardening Rule," Quarterly of Applied Mathematics, Vol. 17, 1959, pp. 55.